Concepts and Modelling in Geomorphology: International Perspectives

Concepts and Modelling in Geomorphology

International Perspectives

Edited by
I. S. Evans, R. Dikau, E. Tokunaga, H. Ohmori
and M. Hirano



TERRAPUB, Tokyo

Concepts and Modelling in Geomorphology: International Perspectives
Edited by I. S. Evans, R. Dikau, E. Tokunaga, H. Ohmori and M. Hirano
ISBN No. 4-88704-132-2

Published by TERRAPUB, 2003 Sansei Jiyuugaoka Haimu, 27-19 Okusawa 5-chome, Setagaya-ku, Tokyo 158-0083, Japan.
Tel: +81-3-3718-7500 Fax: +81-3-3718-4406
URL http://www.terrapub.co.jp/

All rights reserved

© 2003 by TERRAPUB, Tokyo

No part of the material protected by this copyright notice may be reproduced or utilized in any form or by any means, electronic or mechanical, including photo-copying, recording or by any information storage and retrieval system, without written permission from the copyright owner.

(This book is partly supported by Grant-in-Aid for Publication Scientific Research Results of the Japan Society for the Promotion of Science.)

Printed in Japan

Preface

In the last two decades, the prospects for geomorphological modelling have been drastically improved by advances in Information Technology, especially by greatly increased processing speeds and storage capacities. The development of new processing tools in Geographic Information Systems (GIS), the production and availability of comprehensive spatial data from remote sensing and of high-resolution digital landform data such as Digital Elevation Models (DEMs), plus ongoing progress in statistical and mathematical methods, resolve many difficulties and permit new problems to be tackled. In the various branches of geomorphology, analyses and models based on these new opportunities have tested many of the existing concepts and generated new concepts. Both landforms and processes have been quantified, but they have also been interrelated and models have been developed to cover feedbacks, time lags and connections between different scales, so that we come closer to modelling systems and predicting landform development.

Among the varied tools employed are distributed modelling, entropy and energy expenditure, exploratory and inferential statistics, partial differential equations, finite elements, threshold recognition, fractals, and response-time analysis. The present book summarizes many basic concepts and ideas of landforms and their development, and provides a view of conceptual challenges and developments in geomorphology at the start of the 21st century. Most of the papers are concerned with both theoretical concepts or modelling, and comparisons with real-world data. They can be grouped into four sections:

Landform modelling, general considerations;
Material transport in landform modelling;
Fluvial landform structure: mathematical and physical laws; and
DEMs, GIS and modelling in geomorphology.

In **Part 1, Landform modelling, general considerations**, ideas are reviewed that have permeated modern geomorphology in the 20th century, especially for the modelling of landforms and processes in recent decades. These four papers critically review and extend geomorphological concepts such as peneplains, phase boundaries, morphostructures and scale.

Walther Penck recognised the importance of tectonism and denudation occurring simultaneously (Chorley *et al.*, 1973): this is clearly the case for Japan, where the Davisian concept of rapid uplift followed by prolonged stability seems singularly inappropriate. Like the Davisian scheme, however, the Penckian consists of theoretical possibilities, and these do not necessarily materialise when we make comparisons with observational data. **Ohmori** is able to show that Penck's concept of the primary peneplain (primärrumpf) is inapplicable to any

orogenic area. This is because, based on Japanese measurements of denudation and uplift, a low-relief surface would have a denudation rate so low that it could not balance an appreciable uplift rate: only crustal stability could maintain low relief. Even quite slow uplift would lead to surface dissection, and depression would either submerge the plain or bury it in sediments. Thus a 'primary peneplain' would be indistinguishable from a Davisian 'end peneplain'. Actual landscape development in Japan and other orogenic areas is quite different to that predicted by either Davisian or Penckian models.

Blair suggests how geomorphology can broaden its horizons to match the global perspectives of earth system science. Expanding from the traditional focus on subaerial exogenic processes at scales from centimetres to hundreds of kilometres, geomorphology should consider boundaries between media such as atmosphere, lithosphere and ocean at all scales from mineral surface microtopography to continental scale morphology. Such a focus reveals the general concept of 'sympathetic boundaries' in the media on either side of the main boundary. It also prevents neglect of the importance of mass transfer and gravity, and of the dependence of resistance on molecular forces.

From the boundaries emphasised by Blair, **Ilyin** expands on the importance of the ocean: lithosphere boundary. He distinguishes rifted morphology, that can be related to active sea-floor spreading from Mid-Ocean ridges, from volcanic block morphology not so related, consisting of seamounts, lava plateaus, rises and major islands. Similar acoustic basement morphology shows, however, that the latter has developed from the former. Ocean floor morphometry and structure change steadily with age, as tectonism transforms the initially mainly volcanic morphology.

Much recent work in geomorphology and hydrology has emphasised the importance of scaling between two related properties, for example when linear fractal plots show a power relation between properties. **Evans** shows that there are often limits to this behaviour, where thresholds change the nature of relationships between properties of the land surface. Thus the size or spacing of landforms is scale-specific, either globally, regionally or locally. Examples can be given both from bedforms such as dunes and drumlins, and from erosional forms such as landslides and cirques. The processes involved include the tectonic, volcanic, fluvial, gravitational, glacial and aeolian.

Part 2, Material transport in landform modelling, deals with material movements, landform processes and essential characteristics included in magnitude-frequency distribution of landform processes. Three papers discuss the characteristics of patterns in material movements in landform processes and the typical landforms peculiar to each movement. The subjects discussed in this part are basic ones for all aspects of geomorphology.

Nishimori and Tanaka provide a simple model for aeolian dune dynamics. Based on Hack's three dominant factors (wind regime, available sand, and surface cover by plants), it simulates dunes of the various shapes observed. With qualitative resemblance to real systems, the results are especially useful in studying the interactions between vegetation and dunes.

Transport of material is central to modelling landform change. **Hirano** views the transport of mass in terms of both downward movement and diffusion. This is analysed in terms of Green's Function, with varied coefficients for the two components representing different processes. The Function is integrated to give topographic change. Rate of erosion is proportional to surface convexity and gradient, and depth of sediment varies with a normal (Gaussian) distribution.

Another aspect of landform development is the variation of processes over time: **Schmidt and Preston** consider the frequency and magnitude of processes relevant to sediment flux over the Holocene. Different systems can be linked as components in a sediment flux model at regional scale. Starting from landscape units, this is an upscaling approach to modelling landscape development.

Part 3, Fluvial landform structure: mathematical and physical laws, includes three papers discussing the mathematical and physical meanings of landform structure. Using considerable mathematical and physical methodology, they synthesise the presently prevailing knowledge of landforms and comment on future developments in the application of numerical methods in geomorphology as a natural science. In particular, the physical processes implicated by morphological characteristics of landforms are discussed.

Cudennec, Fouad and Sumarjo-Gatot analyse river networks in terms of lengths of water paths to the outlet, defined as the sums of link lengths of different Strahler orders. Consistent with the fractal nature of river networks, probability distributions of link lengths show strong scaling especially for lower orders. Truncated hydraulic lengths (summed up to a given order) are negatively skewed and some follow a gamma distribution, which is hidden in basin-scale functions.

Tokunaga considers the fractal nature of drainage basins in terms of Horton's law of stream numbers, redefined as an asymptotic law of self-similar networks. This can be expressed by a three-term recurrence formula, with some properties similar to those of one-dimensional quasi-crystals. The fractality arises from the nesting of most probable states as the potential energy of water is expended.

Peckham also considers the fluvial landscape in steady state. He understands it in relation to Hamilton's Principle, optimizing the difference between kinetic and potential energy dissipation, while conserving mass. A local equation relates surface elevations to those of neighbours in a grid. Finite-element solutions to the partial differential equations lead to local features such as peaks, ridges, saddles, slopes and forks, but not pits: the numerical solutions are hydrologically sound, and exhibit the features of real fluvial landscapes.

In **Part 4, DEMs, GIS and modelling in geomorphology**, three papers focus on digital methods in geomorphology using digital elevation models (DEMs) and geographical information systems (GIS). Even in 1984, the Japanese Geomorphological Union held a symposium on "Geomorphology and Data-Processing" (Japanese Geomorphological Union, 1985). It focused on the nature of numerical data (DEMs) and methods (GIS) for their application in geomorphology. Knowledge of and techniques for DEMs and GIS have recently developed remarkably, all over the world. From these methodological developments the papers propose some new methods for landform analysis,

terrain analysis and natural hazard analysis. Basic problems for the future development of numerical treatment and applications in geomorphology are discussed. These papers build on those in Pike and Dikau (1995), from a previous IAG Conference.

As modelling advances, it can be used to improve prediction. This is important especially for landslides, which are intimately related to surface form and materials as well as weather conditions. **Pike, Graymer and Sobieszczyk** use digital maps of geology and ground slope gradient in combination with previous landslides to provide an index of landslide susceptibility. This automates earlier less quantitative indices, and provides a spatial prediction of future landsliding. The index is applied to detailed data for a large Californian urban area.

Ground slope is measured from Digital Elevation Models (DEMs) at the appropriate scale of resolution, and is important also in **Guth**'s study of the geomorphometry of the USA. Considering DEMs at three different grid spacings (for continental, regional and local DEMs), Guth shows that quadrangle averages of elevation and slope gradient are very well correlated, though mean gradients vary inversely with spacings. Results for a third major variable, degree of terrain organization, are more variable between different DEMs, especially where relief is low. Analysis of geomorphometric bivariate plots or histograms provides effective assessment of DEM quality (outliers are normally defects), and should be integrated in the process of producing and editing DEMs.

Sulebak and Hjelle also use DEMs to analyse terrain at different scales. Most existing multi-resolution models are based on triangulations and optimised for visualisation. For terrain analysis, better models are provided by hierarchies of spline surfaces at different levels of resolution. These can be used at appropriate scales in GIS applications.

It is difficult to provide a balanced international view of the broad field addressed here. However, with four papers each from the USA, Japan and western Europe (France, Germany, Norway and UK), one from Russia, and some representation from Indonesia, New Zealand and Australia (Sumarjo-Gatot, currently Schmidt and Preston), this volume does provide a good representation of the current distribution of work on theoretical geomorphology, and gives a truly international perspective. New concepts are developed, and old concepts are expressed in new ways. We hope that, together with the volumes edited by Lane, Richards and Chandler (1998) and Hergarten and Neugebauer (1999), it provides many pointers to future work. Although this field is not an easy one, the development of ever-better tools (in GIS, IT and mathematics), and DEM data that are more accurate and at higher resolution, permit improved models and better applications. Many exciting possibilities remain to be exploited.

Ian S. EVANS (Univ. Durham, UK)
Richard DIKAU (Univ. Bonn, Germany)
Eiji TOKUNAGA (Chuo Univ., Japan)
Hiroo OHMORI (Univ. Tokyo, Japan)
Masashige HIRANO (Osaka City Univ., Japan)

REFERENCES

Chorley, R. J, Beckinsale, R. P. and Dunn, A. J. (1973) *The History of the Study of Landforms, Vol. 2: The Life and Work of William Morris Davis*. Methuen, London.

Hergarten, S. and Neugebauer, H. J. (eds.) (1999) *Process Modelling and Landform Evolution, Lecture Notes in Earth Sciences, 78*. Springer, Berlin.

Japanese Geomorphological Union (1985) Special Issue on Geomorphology and Data-Processing. *Trans. Japan. Geomorph. Union*, Vol. 6, No. 3.

Lane, S. N., Richards, K. S. and Chandler, J. H. (eds.) (1998) *Landform Monitoring, Modelling and Analysis*. John Wiley & Sons, Chichester.

Pike, R. J. and Dikau, R. (eds.) (1995) Geomorphometry. *Zeitschrift für Geomorphologie, N.F.* Supplement-Band **101**.

Acknowledgements

The starting point of this book was the Fifth International Conference on Geomorphology which was held on 23–28 August, 2001, in Tokyo, Japan. At the conference, Symposium 19: New Concepts and Modelling in Geomorphology, and Symposium 20: Geomorphometry, DEMs and GIS were organized. Symposium 19 focused on concepts, broad themes, and development or testing of geomorphological models, while Symposium 20 dealt with themes more specifically on geomorphometric results, DEMs, and GIS-related techniques in geomorphology. At the conference, important concepts and modelling techniques for geomorphology were presented, opening new horizons in fundamental geomorphology. Some publishers were interested in disseminating the outstanding concepts and techniques widely, and established an editorial board for publication of a book. The editors of this book selected several presentations among those in the symposia and sessions of the conference, and asked the authors to contribute their articles to the book. This book contains refereed presentations selected from the above two symposia and from Session 14: Theories, Methods and Techniques in Geomorphology. The editors are grateful to the contributors for their cooperation and productivity, without which the book would never have progressed beyond the drawing board.

Throughout the planning, preparation and production of this book many people became involved, some substantially, others peripherally. To all of these people the editors extend their gratitude; a particular expression of thanks is due to all the reviewers for their friendly cooperation, and to Mr. K. Oshida and Ms. K. Kono of TERRAPUB publisher for their hard work in editorial processes.

The publication of this book was financially supported by Grant-in-Aid for Publication of Scientific Research Results, Grant-in-Aid for Scientific Research, Japan Society for the Promotion of Science (No. 155304; Representative: Hiroo Ohmori).

Editorial Board

Ian S. Evans
Reader in Geography, University of Durham, U.K.

Richard Dikau
Professor of Geography, University of Bonn, Germany

Eiji Tokunaga
Professor of Earth Sciences, Chuo University, Japan

Hiroo Ohmori
Professor of Natural Environmental Sciences, University of Tokyo, Japan

Masashige Hirano
Professor of Earth Sciences, Osaka City University, Japan

Contributors

Robert W. Blair, Jr.
Department of Geosciences, Fort Lewis College, U.S.A.

Christophe Cudennec
Ecole Nationale Supérieure Agronomique de Rennes, France

Ian S. Evans
Earth Surface Systems Research Group, University of Durham, U.K.

Youssef Fouad
Ecole Nationale Supérieure Agronomique de Rennes, France

Russell W. Graymer
U.S. Geological Survey, U.S.A.

Peter L. Guth
Department of Oceanography, U.S. Naval Academy, U.S.A.

Masashige Hirano
Graduate School of Science, Osaka City University, Japan

Øyvind Hjelle
SINTEF Applied Mathematics, Norway

Alexander V. Ilyin
N. N. Andreyev Acoustics Institute, Russia

Hiraku Nishimori
Department of Mathematical Sciences, Osaka Prefecture University, Japan

Hiroo Ohmori
Department of Natural Environmental Studies, Graduate School of Frontier Sciences, University of Tokyo, Japan

Scott D. Peckham
INSTAAR, University of Colorado, U.S.A.

Richard J. Pike
U.S. Geological Survey, U.S.A.

Nicholas J. Preston
Geographisches Institut, Universität Bonn, Germany

Jochen Schmidt
Geographisches Institut, Universität Bonn, Germany

Steven Sobieszczyk
U.S. Geological Survey, U.S.A.

Jan R. Sulebak
SINTEF Applied Mathematics, Norway

Irianto Sumarjo-Gatot
Center for Soil and Agroclimate Research, Indonesia

Hirohisa Tanaka
Department of Mathematical Sciences, Osaka Prefecture University, Japan

Eiji Tokunaga
Faculty of Economics, Chuo University, Japan

Contents

Preface v
Acknowledgements x
Editorial Board xi
Contributors xiii

Part 1. LANDFORM MODELLING, GENERAL CONSIDERATIONS

The Paradox of Equivalence of the Davisian End-Peneplain and Penckian Primary Peneplain
Hiroo OHMORI 3
Geomorphology: Boundaries between Media
Robert W. BLAIR, Jr. 33
Evolution of the Ocean Floor Morphostructure: Actualistic Model
Alexander V. ILYIN 43
Scale-Specific Landforms and Aspects of the Land Surface
Ian S. EVANS 61

Part 2. MATERIAL TRANSPORT IN LANDFORM MODELLING

Simple Model for the Complex Dynamics of Dunes
Hiraku NISHIMORI and Hirohisa TANAKA 87
Green's Function of Mass Transport and the Landform Equation
Masashige HIRANO 101
Towards Quantitative Modelling of Landform Evolution through Frequency and Magnitude of Processes: A Model Conception
Jochen SCHMIDT and Nicholas James PRESTON 115

Part 3. FLUVIAL LANDFORM STRUCTURE: MATHEMATICAL AND PHYSICAL LAWS

Planar Organization of River Networks: A Hidden Gamma Law Structure
Christophe CUDENNEC, Youssef FOUAD and Irianto SUMARJO-GATOT 133
Tiling Properties of Drainage Basins and Their Physical Bases
Eiji TOKUNAGA 147
Mathematical Modeling of Landforms: Optimality and Steady-State Solutions
Scott D. PECKHAM 167

Part 4. DEMs, GIS AND MODELLING IN GEOMORPHOLOGY

A Simple GIS Model for Mapping Landslide Susceptibility
Richard J. PIKE, Russell W. GRAYMER and Steven SOBIESZCZYK 185
Eigenvector Analysis of Digital Elevation Models in a GIS: Geomorphometry and Quality Control
Peter L. GUTH 199
Multiresolution Spline Models and Their Applications in Geomorphology
Jan Rasmus SULEBAK and Øyvind HJELLE 221

Author Index 239

Subject Index 241

Place Index 253

Concepts and Modelling in Geomorphology: International Perspectives,
Eds. I. S. Evans, R. Dikau, E. Tokunaga, H. Ohmori and M. Hirano, pp. 3–32.
© by TERRAPUB, Tokyo, 2003.

The Paradox of Equivalence of the Davisian End-Peneplain and Penckian Primary Peneplain

Hiroo OHMORI

Department of Natural Environmental Studies, Graduate School of Frontier Sciences, The University of Tokyo, 7-3-1 Hongo, Bukyo-ku, Tokyo 113-0033, Japan
e-mail: ohmori@k.u-tokyo.ac.jp

Abstract. The Davisian model elucidates landscape development through an orogeny by denudation processes, postulating prolonged still-stand of a landmass following rapid tectonic uplift, ultimately resulting in a peneplain. The Penckian model emphasizes that landscape is shaped by concurrent tectonics and denudation, and includes the primary peneplain as an antithesis against the Davisian end-peneplain by assuming a steady state between tectonic uplift and denudation from the beginning of orogenesis. Every ordinary landscape development through an orogeny has been expected to follow a course located between the two distinctive courses of landscape development. On the basis of the relationships between mountain altitude, local relief and denudation rate observed in Japan, denudation rate increases with local relief and the local relief increases with mountain altitude. A mountain range is considerably denuded even during the uplift phase. As denudation rate approaches tectonic uplift rate with an increase in mountain altitude by tectonic uplift, a steady state between denudation and uplift appears, and the mountain range attains a critical altitude that remains constant, in spite of continuous tectonic uplift. If tectonic uplift ceases, the mountain range is lowered by denudation, resulting in a subdued low relief landscape, ultimately a peneplain. The primary peneplain requires a low uplift rate to keep a balance with the low denudation rate due to its low altitude. Based on the observed data in Japan whose denudation rates are among the highest class in the world, the tectonic uplift rate must be 0.05 mm/yr or lower for a mountain range with an altitude of 100 m above sea level to maintain its low altitude. This low uplift rate should be classified not as an orogenic crustal movement but as crustal stability. Thus, the Penckian primary peneplain must be an irrelevance. A low relief landscape recognized as a primary peneplain must be formed originally as a Davisian end-peneplain. The sequence of ordinary landscape development is outside the two courses of the Davisian and Penckian models.

Keywords: Uplift, Denudation, Orogeny, Peneplain, Davisian Model, Penckian Model

INTRODUCTION

Two basic, classic and famous models of landscape development have greatly influenced and promoted modern macroscale geomorphology. One is the Davisian model (Davis, 1899) and the other is the Penckian model (Penck, 1924). One of the most important results of the models is the illustration of sequential changes in landscape during an orogeny, as expressed by Davis (1899); initial form, youth, maturity, old age, and peneplain. The sequential changes in landscape are

extremely different between the two, resulting from remarkably different geomorphic processes associated with tectonic uplift and denudation. Each of them, however, produced the most basic sequence. It was necessary, therefore, for most of the textbooks of geomorphology to make reference to the two models for describing macroscale landscape development, including many arguments about the geomorphic processes in the models, and proposing many models modifying, rectifying and extending them (e.g. Geikie, 1913; Tsujimura, 1922; Cotton, 1922, 1942; Lobeck, 1939; Worcester, 1939, 1949; Inoue *et al*., 1940: Thornbury, 1954; Maull, 1958; Sheidegger, 1961; King, 1962; Chorley *et al*., 1964; Tricart, 1965; Chorley, 1965; Chorley *et al*., 1973; Twidale, 1976; Büdel, 1977; Bloom, 1978, 1991; Louis and Fischer, 1979; Chorley *et al*., 1984; Summerfield, 1991, 2000; Beaumont *et al*., 2000; Hovius, 2000).

One of the most significant differences between the two models is the position of a peneplain in the sequence of landscape development, that is, the end-peneplain of the Davisian model and the primary peneplain of the Penckian model. The two peneplains are located at opposite ends of the sequence. Is the difference, however, a true difference? Textbooks of geomorphology have consumed many pages to argue the problems included in the "Geographical Cycle", especially the rapid uplift without serious denudation postulated in the Davisian model, or to examine practical applications of the "Morphological Analysis", especially the steady state of the Penckian model. The difference seems to have been accepted as a natural result coming from the different models. The question; "Is the difference physically true or not true?", however, must be a basic and conceptual problem in the geomorphology of macroscale landscape development (Ohmori, 2001a).

This paper first introduces some problems of the Davisian and Penckian models, and then provides estimates of denudation rates observed in Japan. The relationship between denudation rate and local relief is then assessed, and the change in mountain altitude resulting from concurrent tectonics and denudation is modelled. Finally the paper discusses the relationship between the Davisian end-peneplain and the Penckian primary peneplain on the basis of the concurrent tectonics and denudation model.

THE DAVISIAN AND PENCKIAN MODELS

Landscape changes at any time with changes in physical condition of the forces working on and in an area. The activities of the forces, in turn, are controlled under dynamic relationships between tectonics, denudation process and the landscape itself. An essential problem of present-day geomorphology must be to deduce the temporal changes in landscape; not only the temporary changes during a relatively short time but also the sequential changes during an orogeny. In particular, it is desirable for a conceptual model of landscape development to illustrate a general sequence of landscape changes during an orogeny as a basis for understanding the landscape and its nature. It seems as if we want to know not about the histories of individual persons, but about the

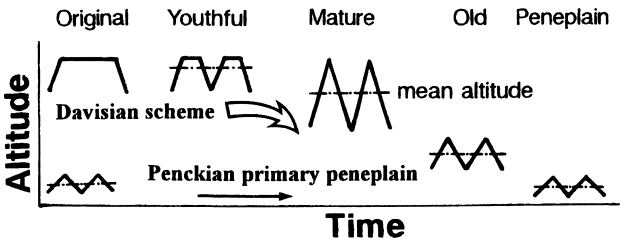


Fig. 1. Two courses of landscape development in orogenesis inferred from the Davisian scheme and Penckian model. Stages are referred to the Davisian scheme (Ohmori, 2001b).

generalized sequential changes in the life of a human being without interruptions by accidental events, as a basis for understanding the human being and our lives.

There have been many arguments against the Davisian model and Davis himself made additional explanations of his model (Davis, 1901, 1905, 1909, 1912, 1922, 1923, 1926, 1932, etc.). When a model, however, has once been proposed, it becomes relatively independent of the person who proposed it, even if the person has other ideas about it. The “interruption”, “episode” and “event” may be caused by temporary actions of tectonics and denudation and must occur more or less in most mountain ranges. These are, however, side issues for the essential sequence of landscape development. The elementary framework of a model must represent the most basic concept and should be a target for discussing and examining the problems included in the model.

In terms of summarizing the landscape changes in drainage basins by the denudation processes discussed by Powell (1875), Gilbert (1877), Davis (1889, 1890) and others, the Geographical Cycle (or the Cycle of Erosion) model was proposed by Davis (1899) in a scientific journal. It was the first systematic introduction of a genetic model of landscape development into geomorphology. In the basic scheme of the Davisian model of the Ideal Geographical Cycle, the original surface is rapidly uplifted without serious denudation (Fig. 1; Ohmori, 1993, 2001b). The mountain range is therefore uplifted to the highest position at first. Then the mountain range continuously decreases in altitude by the ensuing denudation. Local relief, however, is significantly low at first. In particular, when the uplifted initial landform is assumed to be a peneplain or a flat surface emerged from the sea, the local relief is the lowest of any in the sequence of landscape development. Local relief increases with progressive dissection during the youthful and mature stages. It is not until the mountain range has passed full maturity that local relief starts decreasing. After full maturity, local relief decreases together with altitude. The mountain range is lowered by prolonged denudation, it approaches base level, and finally results in a low relief landscape. This low relief denudational landscape is a peneplain (Fig. 1). The peneplain as a technical term was proposed by Davis (1889) for the first time, and was later called the “end-peneplain (Endrumpf)” by Penck (1924).

The Penckian model emphasizes that change in surface altitude is controlled under the relationship between tectonic uplift rate and denudation rate. The difference between the two rates determines the direction (up or down) and rate of change in altitude. On the basis of the Penckian model, when denudation rate is equal to tectonic uplift rate, altitude does not change. This is a steady state between tectonic uplift and denudation. When the steady state appears and continues from the beginning of orogenesis, a region which is expected to be a mountain range can not increase in altitude, and a low relief landscape should be maintainable through the orogenic period. This low relief denudational landscape is the primary peneplain (Primärrumpf) (Fig. 1). The sequence of landscape development resulting from the steady-state process was proposed by Penck (1924) as an extreme case against the other extreme case of the Davisian scheme. The primary peneplain, therefore, is an antithetic landscape to the end-peneplain.

As introduced above, the two models have deduced two different sequences of macroscale landscape development following the first set of initial landforms. The changes in landscape were described in terms of altitude and local relief. The end-peneplain and primary peneplain are both a low altitude and low relief landscape, resulting from denudation processes, but with different relations to tectonic uplift. Their courses in the sequence of landscape development are poles apart; an up at first and slowly down curve in the Davisian model and a low horizontal line in the Penckian model (Fig. 1). Every ordinary landscape development resulting from concurrent tectonics and denudation has been expected to follow a course between the two. A mountain range is uplifted to some altitude through a course between the two, then decreases in altitude, and is finally reduced to peneplain. How does the local relief, however, change with change in altitude through this course? What relationship is observed between altitude and local relief through a mountain building? Do all sequences of landscape development resulting from concurrent tectonics and denudation truly follow a course between the two?

Now, the Penckian model is mathematically expressed by the following equation:

$$\frac{\partial H}{\partial t} = -\varepsilon\left(\frac{\partial H}{\partial x}\right) \tag{1}$$

where H is the altitude, x is the horizontal distance, t is the time and ε is a constant. The term $\partial H/\partial x$ indicates surface gradient, and therefore, Eq. (1) means that denudation rate is proportional to surface gradient. It implies that denudation rate is zero when the surface is flat. On the basis of Eq. (1), therefore, the denudation rate working on the primary peneplain must be low throughout an orogeny. Nevertheless, the primary peneplain requires a denudation rate equal to the tectonic uplift rate in the orogenesis to keep it at low altitude.

Here, a question is raised. Is it physically possible that a low relief landscape such as peneplain has a denudation rate to keep a balance with the tectonic uplift

rate expected for orogenesis? What relationship can be induced between local relief and denudation rate in macroscale landscapes on the earth? Is the primary peneplain actually able to exist on the earth? This question was suggested by Ohmori (1978) and clearly emphasized by Yoshikawa (1985b, p. 102–103) on the basis of the quantitative relationships between tectonics, denudation, and morphometric attributes in Japan. Two questions will be examined on the basis of the data observed in Japan; what relationships are there between denudation rate, local relief, and altitude, and how does local relief change through an orogeny?

DENUDATION RATES IN RELATION TO LOCAL RELIEF IN JAPAN

Present-day denudation rates for macroscale landscape in Japan have been estimated mainly based on the sediment delivery rates to reservoirs (Tanaka and Ishigai, 1951; Tanaka, 1955; Namba and Kawaguchi, 1965; Ishigai, 1966; Yoshikawa, 1974; Ohmori, 1978, 1983b, 1983c; Mizutani, 1981; Tanaka, 1982; Fujiwara *et al*., 1999, 2001). In contrast to variations in temporary denudation rate due to individual landslides and floods, denudation rates calculated from total sediment supply for reasonably long periods show stable values for individual drainage basins of reservoirs (Yoshikawa, 1974; Ohmori, 1978, 1983b, 1983c, 2000; Fujiwara *et al*., 1999, 2001). In Japan, there are 116 reservoirs each of which has a drainage basin area larger than 20 km^2 together with a data set of annual sedimentation rate. For estimating the denudation rates in drainage basins, 82 reservoirs were selected among the 116 reservoirs (Fujiwara *et al*., 1999, 2001; Ohmori, 2001a). Each satisfies the criteria of sedimentation such as sediment volume over 50,000 m^3, water storage capacity over 2,000,000 m^3, sedimentation ratio to water storage capacity less than 25%, and observation duration longer than 10 years. Trap efficiency of sediment in the reservoir satisfying the criteria is estimated to be more than 90% (Ezaki, 1966; Ashida, 1971). Most of them are the upper-most ones in a sequence of reservoirs through individual rivers. The mean observation duration is about 30 years, with a longest duration of 66 years, including many typhoons and a number of heavy rainfall events.

The denudation rate E in the drainage basin of reservoir is given by:

$$E = \frac{1}{S}\left(\frac{V}{T}\right)\left(\frac{\rho}{\sigma}\right) \tag{2}$$

where V is the total sediment volume in each reservoir, T is the observation duration, ρ is the mean sediment density, σ is the crustal density, and S is the drainage basin area. The values of ρ and σ are assumed to be 1,750 kg/m^3 and 2,500 kg/m^3, respectively. Denudation rates in drainage basins of the 82 reservoirs are shown in Fig. 2 (Ohmori, 2001a). They show values ranging from 0.06 to 7.04 mm/yr (Fujiwara *et al*., 1999, 2001; Ohmori, 2001a).

A conspicuous characteristic of the distribution of denudation rates is a marked difference between drainage basins even in the same district. For some

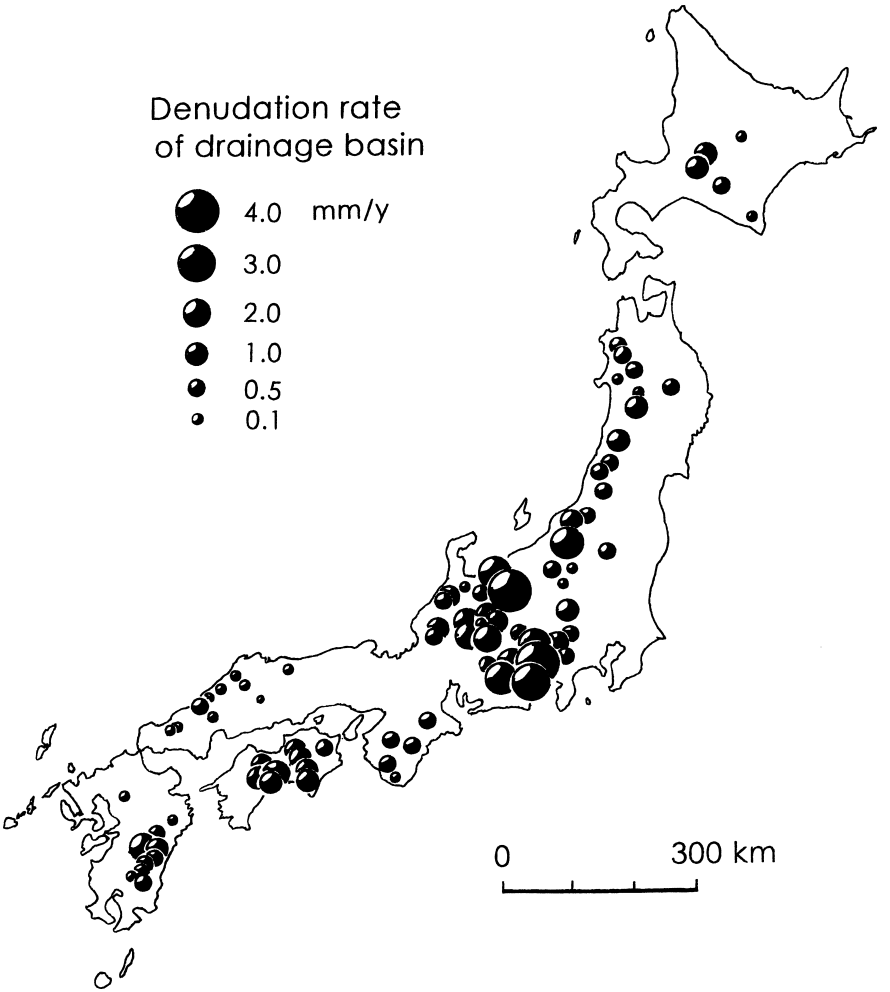


Fig. 2. Denudation rates in drainage basins of reservoirs in Japan. The rate indicates the value calculated by dividing the total sediment volume accumulated in a reservoir by the area of drainage basin of the reservoir and by the observation duration (Ohmori, 2001a).

mountain ranges, the highest rate is ten times or higher than the lowest one. Such local variations in denudation rate depend predominantly not on local differences in precipitation and rock type but on local differences in local relief as examined below.

The dispersion of altitude (altitude dispersion) D is defined as the standard deviation of the frequency distribution of surface altitude in a unit area of specific size (Ohmori, 1978):

$$D = \left[\frac{\sum_{i=1}^{n} (h_i - H)^2}{n-1} \right]^{1/2} \tag{3}$$

where h_i is the altitude of point i, n is the number of points in a unit area, and H is the mean altitude given by:

$$H = \frac{\sum_{i=1}^{n} h_i}{n} \tag{4}$$

The altitude dispersion is a measure of local relief (Evans, 1972; Ohmori, 1978; Ohmori and Hirano, 1984; Ohmori and Sugai, 1995). It is directly proportional to mean surface gradient (Ohmori, 1978; Ohmori and Sohma, 1983; Ohmori and Hirano, 1984) and indicates the dispersion of potential energy of the surface materials with a high relation to landslide occurrence (Ohmori and Sugai, 1995). In Japan, altitude dispersion in a certain unit area varies regionally, and in each region throughout Japan it increases with size of unit area at approximately the same rate (Ohmori, 1978). This indicates that the altitude dispersion in a unit area with any specific size can be used to describe regional characteristics of local relief in Japan. The altitude dispersion of a unit square with an area of 1 km^2 is called the "basic dispersion of altitude (basic altitude dispersion)".

The relationship between altitude dispersion and denudation rate has been expressed empirically by a power function for drainage basins larger than some tens of km^2 in Japan (Ohmori, 1978, 1982, 2001a; Fujiwara *et al*., 1999, 2001). The "50 m DEM" published by Geographical Survey Institute of Japan is a data set of surface altitudes of lattice points in a grid system with horizontal intervals of about 50 m, 1.5″ (ca. 46 m) in latitude and 2.25″ (ca. 49–63 m) in longitude: it covered all of Japan by 2000. Using the 50 m DEM which has about 450 lattice points in each unit area of 1 km^2, basic altitude dispersion was calculated. The relationship between denudation rate E (mm/yr) and mean basic altitude dispersion D (m) of drainage basins of the 82 reservoirs is given by:

$$E = \alpha D^{\beta} \tag{5}$$

where α and β are constants. The correlation coefficient is 0.94, and $\alpha = 4.4 \times 10^{-5}$ and $\beta = 2.2$ for the best-fit function (Fig. 3; Fujiwara *et al*., 1999, 2001; Ohmori, 2001a).

The relationships between denudation rate and rainfall condition in individual drainage basins of the 82 reservoirs are shown in Fig. 4 (Fujiwara *et al*., 1999,

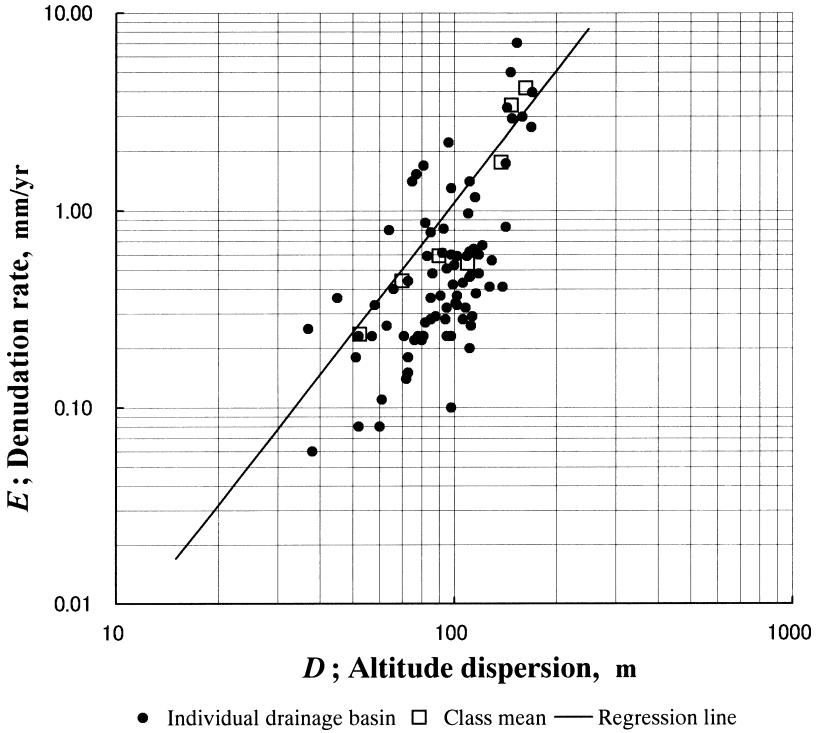


Fig. 3. Relationship between altitude dispersion and denudation rate for 82 selected reservoirs in Japan (Fujiwara *et al.*, 1999, 2001; Ohmori, 2001a). Closed circles are denudation rates for individual reservoirs, open squares show mean denudation rates for individual classes of altitude dispersion, and solid line indicates a non-biased regression line.

2001; Ohmori 2001a). In Fig. 4, open squares indicate the relationship between denudation rate and mean annual rainfall, and closed circles indicate the relationship between denudation rate and intense rainfall which is represented by the mean yearly total volume of individual rainfalls over 100 mm a day. Neither relationship shows any clear trend. Thus, concerning not the temporary denudation rate but the mean short-term denudation rate for some tens years, denudation rate does not have any strong relationships to rainfall conditions in Japan.

On the other hand, among the 82 drainage basins, 59 drainage basins, each of which has a dominant rock type occupying over 70% of the area of drainage basin, were selected for examining the effect of rock type on denudation. Rock types were classified into Cenozoic volcanic rocks, Neogene sedimentary rocks, Granitic rocks, Mesozoic-Palaeozoic sedimentary rocks, and Metamorphic rocks. Figure 5 shows the relationship between mean basic altitude dispersion and denudation rate by each rock type for the 59 drainage basins (Fujiwara *et al.*, 1999, 2001; Ohmori 2001a). Metamorphic rocks show a denudation rate a little

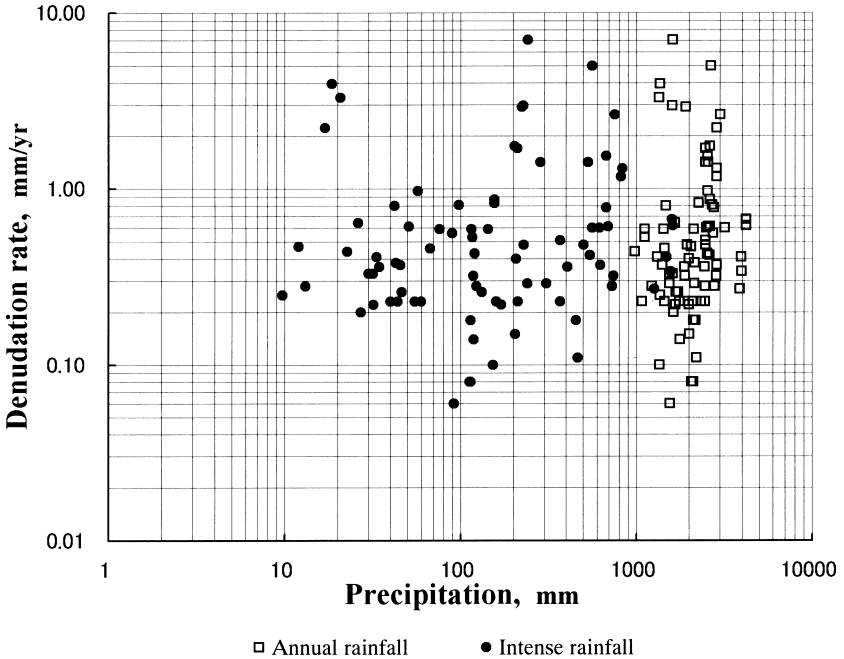


Fig. 4. Relationship between denudation rate and rainfall (Fujiwara *et al*., 1999; Ohmori 2001a). Open squares indicate mean annual rainfall in drainage basins, and closed circles indicate the amount of intense rainfall (mean yearly total volume of individual rainfall over 100 mm a day).

higher than that of Granitic rocks for the same altitude dispersion. Remarkable differences in denudation rate, however, are not recognized among the rock types, and denudation rate increases with altitude dispersion at similar rates for all the rock types. The principal factor, therefore, causing local variations in denudation rate is judged to be the altitude dispersion, that is, the local relief (Ohmori, 1978, 1983a, 2001a; Tokunaga and Ohmori, 1989; Fujiwara *et al*., 1999, 2001).

Using mean basic altitude dispersion over a whole mountain range, mean denudation rates of individual mountain ranges in Japan have been calculated from Eq. (5) (Fig. 6; Fujiwara *et al*., 1999, 2001; Ohmori, 2001a). Numerals in Fig. 6 indicate the long-term denudation rates in drainage basins for ten thousands years or longer. They were estimated from the morphometric analysis of mountain slopes and/or volume of alluvial fans formed since the late Pleistocene including the Last Glacial Age (Iso *et al*., 1980; Akojima, 1983; Nakano, 1989; Yoshinaga *et al*., 1989; Oguchi, 1991; Yoshiyama and Yanagida, 1995). The mean short-term denudation rates estimated for mountain ranges correspond well with these, although it has been sometimes presumed that climatic changes might cause remarkable changes in denudation rate (e.g. Yoshikawa *et al*., 1981; Yoshikawa, 1985a). Water flow, glacial and periglacial processes, rock weathering and vegetation coverage might be changed by climatic change. Some of them,

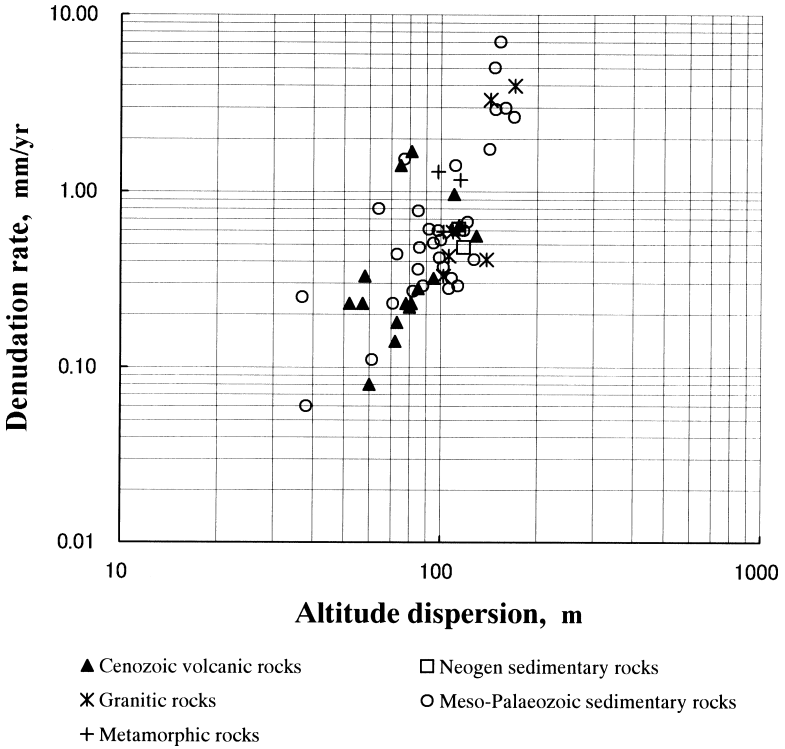


Fig. 5. Relationship between altitude dispersion and denudation rate for each rock type (Fujiwara *et al.*, 1999; Ohmori 2001a). Drainage basins are categorized on the basis of a dominant rock type occupying over 70% of each drainage basin.

however, have positive responses to a climatic change, while others show negative responses. Thus, it is not easy to estimate how denudation rate changes with climatic change. The change in denudation rate with climatic change might be small due to complex responses of the agencies, and denudation rate might be maintained on an average in proportion to the magnitude of local relief in Japan.

The resulting variations in estimated denudation rate for individual mountain ranges show contrasts between morphotectonic terrains with different Quaternary vertical displacements (Fig. 7; Research Group for Quaternary Tectonic Map, 1968, 1969, 1973; Ohmori, 1978, 1995, 2000). The denudation rates are high in Central Japan, the outer belt of Southwest Japan and the inner belt of Northeast Japan, and low in the inner belt of Southwest Japan, the outer belt of Northeast Japan and the mainland of Hokkaido. In particular, values greater than 1.0 mm/yr are indicated for the central Japanese mountain ranges whose mean altitudes are about 1000 m above sea level with peaks of about 3000 m. These rates are almost equal to the mean Quaternary uplift rates of individual mountain ranges

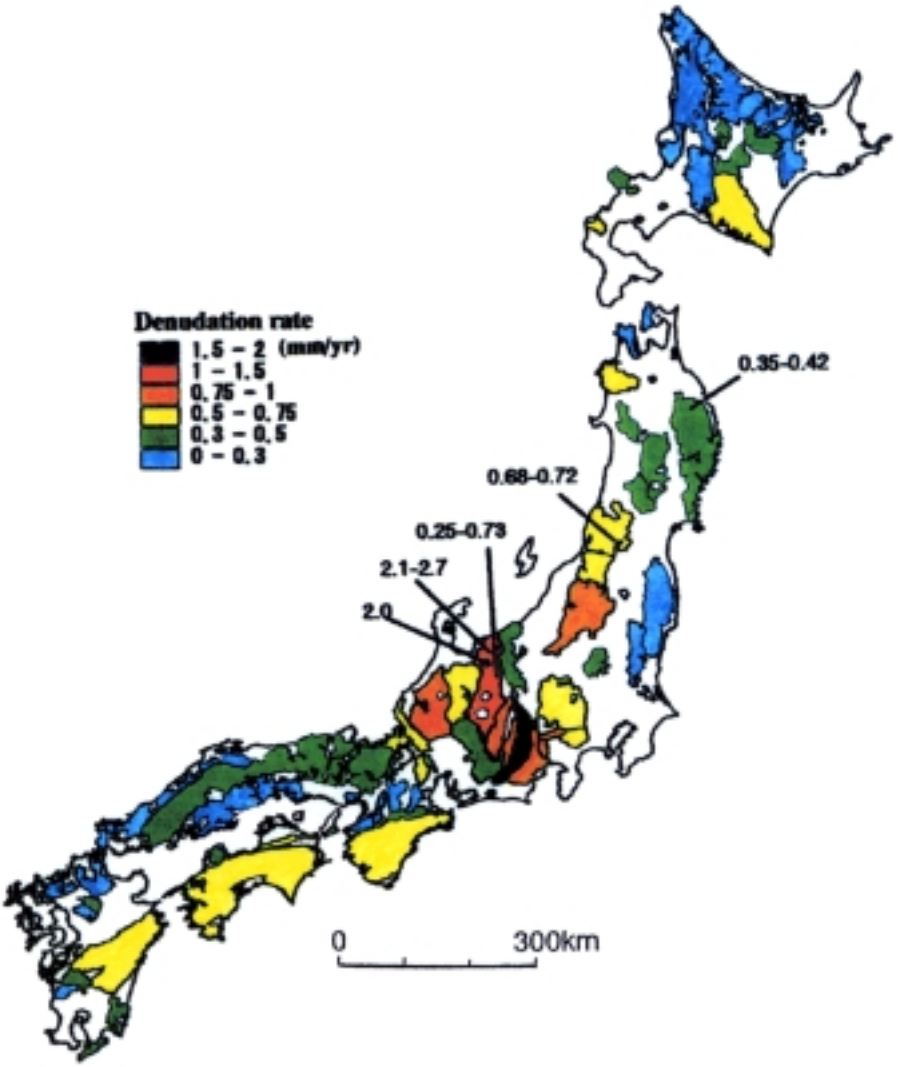


Fig. 6. Denudation rates in individual mountain ranges in Japan estimated from Eq. (5) (Fujiwara *et al*., 1999, 2001; Ohmori, 2001a). Numerals are the long-term denudation rates which were estimated from the morphometric analysis of mountain slopes and volume of alluvial fans formed since the late Pleistocene.

inferred from the Quaternary vertical displacements (Yoshikawa, 1974, 1985a, 1985b; Ohmori, 1978, 1987).

In detail, using the mean basic altitude dispersion, denudation rates were calculated from Eq. (5) for individual squares with an area of 36 km^2; 6 km (ca. 3′15″) in latitude by 6 km (ca. 3′35″–4′35″) in longitude, in Japan (Fig. 8,

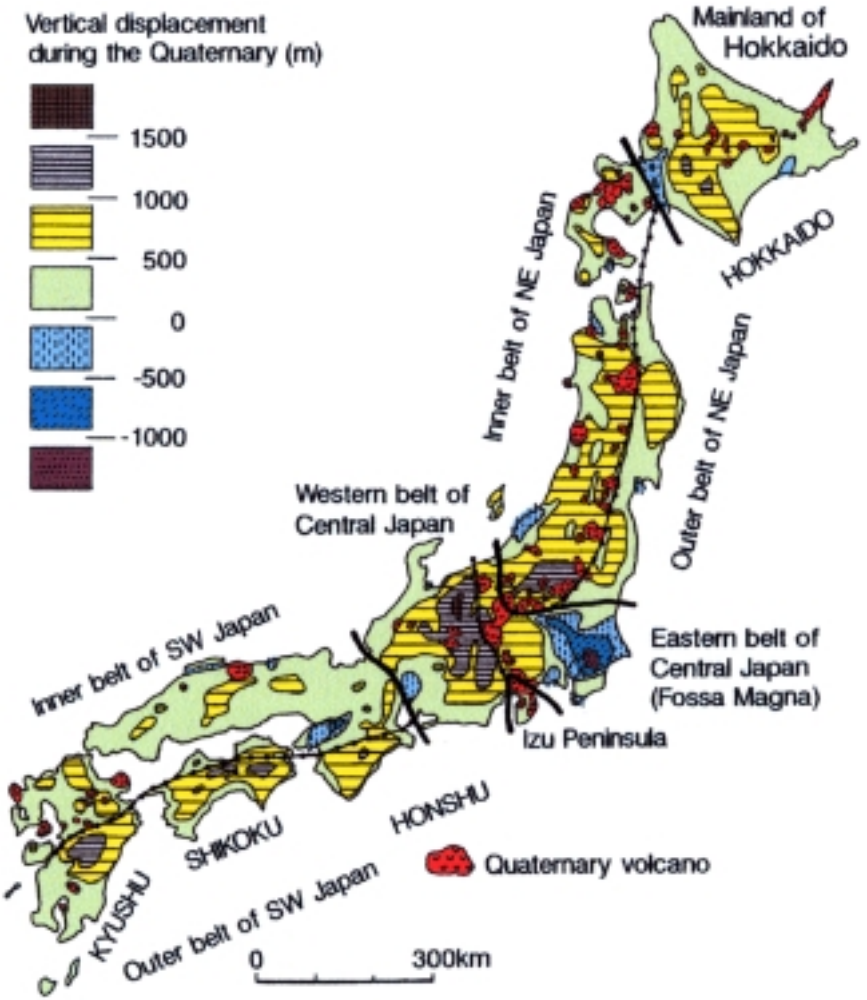


Fig. 7. Morphotectonic divisions of Japan and vertical displacement during the Quaternary (Ohmori, 2000, compiled from Okayama, 1953; Research Group for Quaternary Tectonic Map, 1968, 1969, 1973; Research Group for Active Faults, 1980; Yoshikawa *et al*., 1981; Ohmori, 1995).

Fujiwara *et al*., 1999, 2001). The estimated denudation rates are high in the central part with high peaks, and decrease outward with decreasing altitude in individual mountain ranges. The denudation rates are around 5.0 mm/yr for squares with peaks of about 3000 m above sea level, around 3.0 mm/yr for squares with peaks of about 2000 m, and around 1.0 mm/yr or less for squares with peaks of about 1000 m. These facts suggest that there are strong relationships between altitude, altitude dispersion, and denudation rate.

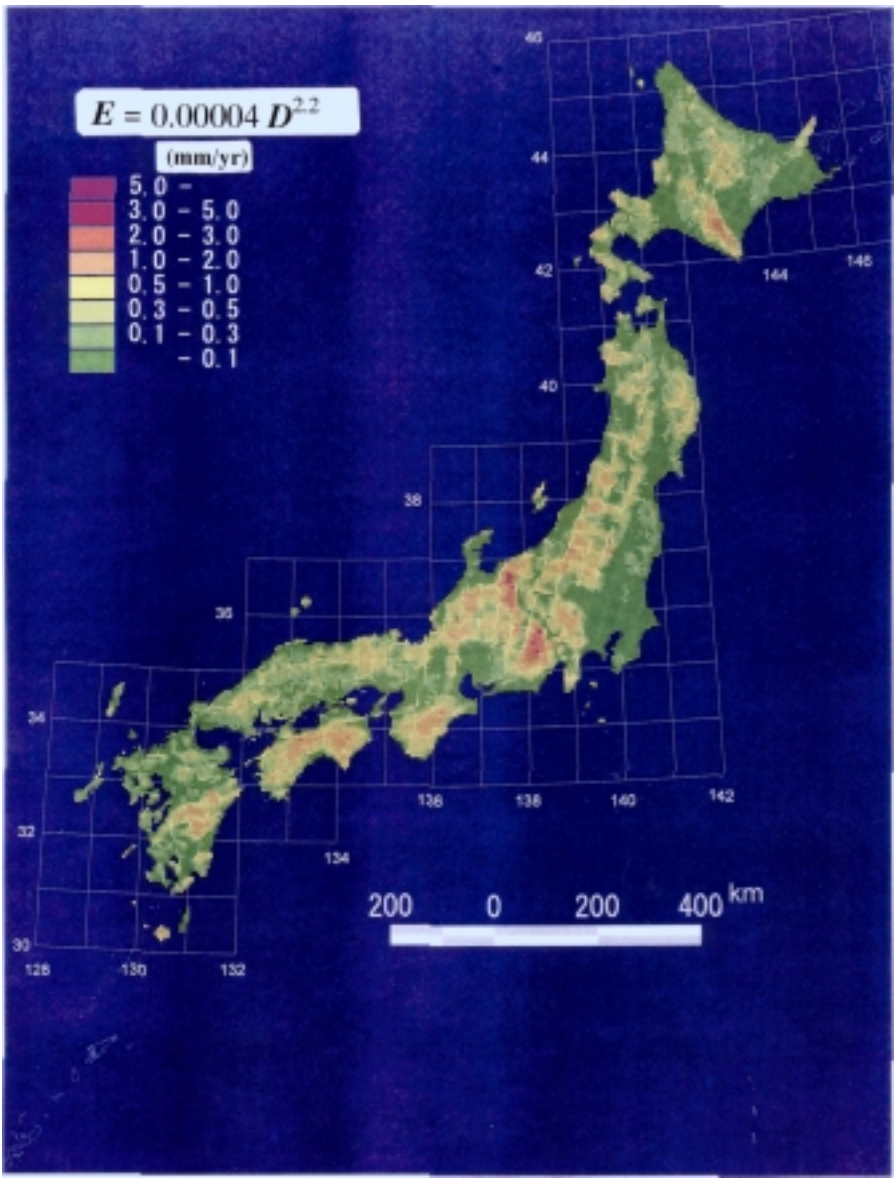


Fig. 8. Denudation rates in individual squares of 36 km^2 in Japan estimated from Eq. (4). Each square is 6 km (ca. 3′15″) in latitude by 6 km (ca. 3′35″–4′35″) in longitude (Ohmori *et al*., 1999).

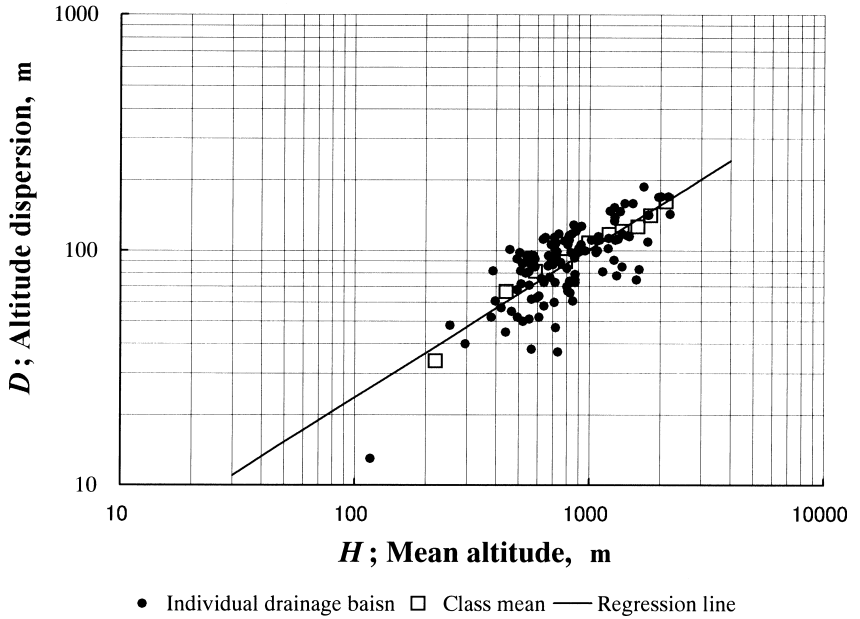


Fig. 9. Relationship between mean altitude and mean altitude dispersion for drainage basins of 116 reservoirs with an area larger than 20 km^2 (Ohmori, 2001a).

LANDSCAPE DEVELOPMENT RESULTING FROM CONCURRENT TECTONICS AND DENUDATION

1. Relationships between altitude, altitude dispersion, and denudation rate

For the Japanese mountain ranges, the relationship between altitude H (m) and altitude dispersion D (m) is expressed by a power function with high correlation:

$$D = aH^b \tag{6a}$$

where a and b are constants (Ohmori, 1978, 1982, 1983b; Ohmori and Hirano, 1984; Tokunaga and Ohmori, 1989; Oguchi, 1991; Sugai *et al*., 1994; Ohmori and Sugai, 1995; Fujiwara *et al*., 1999, 2001). Using mean altitude and mean basic altitude dispersion in drainage basins of the 116 reservoirs in Japan with precise geomorphometric data sets, Eq. (6a) has shown $a = 1.300$ and $b = 0.63$ for the best-fit function with a correlation coefficient of 0.89 (Fig. 9; Ohmori, 2001a).

Here, by differentiating Eq. (6a) by H, we have:

$$\frac{\partial D}{\partial H} = baH^{b-1} \tag{6b}$$

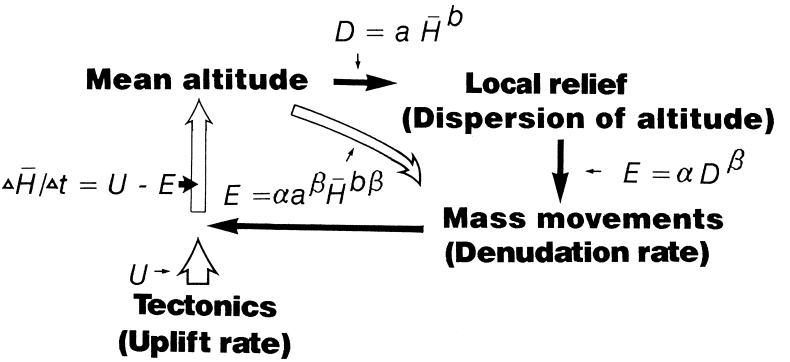


Fig. 10. Schematic relations between uplift rate, morphometry (altitude and local relief) and denudation (Ohmori, 2000)

Equation (6b) can be transformed by transposing after dividing both sides by D:

$$\frac{\partial D}{D} - b\left(\frac{\partial H}{H}\right) = 0 \tag{6c}$$

Equation (6c) is an expression showing a quasistatic process, implying that when H is changed by tectonics and denudation, D changes with H satisfying a dynamic equilibrium state between H and D (Ohmori, 1984, 1985; Ohmori and Hirano, 1984). It indicates mathematically that the ratio of change in altitude dispersion is proportional to about 63% of that in mean altitude. For example, when a mountain range increases in mean altitude from 500 m to 550 m above sea level, basic altitude dispersion increases from about 65 m to 69 m. The increment ratio in altitude dispersion is 6%. It corresponds to 63% of the increment ratio in mean altitude, that is, 10%. It indicates that for intensely denuded regions, local relief changes functionally in relation to the change in altitude.

Now, by coupling Eqs. (5) with (6a), denudation rate is also expressed by a power function of altitude. Substituting Eq. (6a) into Eq. (5) yields the equation:

$$E = \alpha\left(aH^b\right)^\beta = \gamma H^\delta \tag{7}$$

where $\gamma (=\alpha a^\beta)$ is 7.8×10^{-5} and $\delta (=b\beta)$ is 1.39 when E and H are expressed in mm/yr and m, respectively. Regression analysis between denudation rate and altitude directly calculated from the observed data for the 82 reservoirs has shown $\gamma = 9.7 \times 10^{-5}$ and $\delta = 1.32$ with a correlation coefficient of 0.83, indicating that Eq. (7) is a reasonable result (Ohmori, 2001a). On the basis of Eq. (7), the denudation rate is only 0.047 mm/yr for a mean altitude of 100 m, 1.15 mm/yr for a mean altitude of 1000 m, and 5.31 mm/yr for a mean altitude of 3000 m. Indeed,

landslides which are the dominant denudation process in the Japanese mountain ranges are very rare at lower altitudes and increase in volume with altitude dispersion which, in turn, is functionally related to altitude (Sugai *et al*., 1994; Ohmori and Sugai, 1995).

The relationships between tectonic uplift rate, denudation rate, altitude and local relief (altitude dispersion) expressed by Eqs. (5), (6a) and (7) are illustrated in Fig. 10. Rate of increase in altitude is determined by subtracting denudation rate E from tectonic uplift rate U. Denudation rate is controlled by local relief, and local relief is controlled by mountain altitude. The mountain altitude, in turn, is determined by the difference between tectonic uplift rate and denudation rate. A feedback system is therefore recognized between tectonics, denudation and morphometric attributes (altitude and local relief), although the tectonic movements associated with plate motion may be relatively independent of the other factors in Japan (Ohmori, 2000).

2. *Changes in altitude and local relief resulting from concurrent tectonics and denudation*

Sequential changes in altitude resulting from concurrent tectonic uplift and denudation have been discussed on the basis of Eq. (7) (Ohmori, 1978, 1983a, 1984, 1985, 1993, 2000; Yoshikawa, 1984, 1985a, 1985b). Values of coefficients of Eqs. (5), (6a) and (7) presented in this paper differ from those of Ohmori (1978). The function types and results of simulation, however, are not seriously different. Using the new values of the coefficients of Eq. (7), landscape development is discussed in this paper.

Temporal change in altitude is controlled by the difference between tectonic uplift rate and denudation rate. It is expressed by:

$$\frac{\partial H}{\partial t} = U - E \tag{8}$$

From Eq. (8), the time necessary for mean altitude to increase from h_1 to h_2 is given by:

$$t = \int_{h_1}^{h_2} \frac{1}{U - E}\, dH \tag{9}$$

By substituting Eq. (7) into Eq. (9):

$$t = \int_{h_1}^{h_2} \frac{1}{U - \gamma H^{\delta}}\, dH \tag{10}$$

where the measurement units of U, H and t are mm/yr, m, and year, respectively.

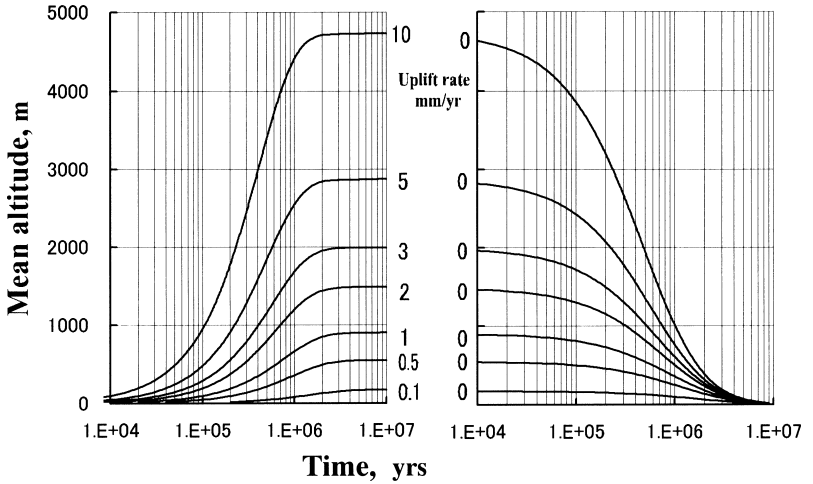


Fig. 11. Changes in mean altitude resulting from concurrent tectonics and denudation from an initial altitude at sea level.

Though the model does not require a constant uplift rate, assuming that the tectonic uplift rate is constant, and that the presently observed relationship between denudation rate and altitude dispersion is valid over time, the change in mean altitude can be simulated as a simplest case (Fig. 11). Using Eq. (6a), local relief can also be estimated for any mean altitude. The resulting landscape development can be divided into developing, culminating and declining stages (Ohmori, 1978, 1985, 1993, 2000; Yoshikawa *et al.*, 1981; Yoshikawa, 1984, 1985a, 1985b).

In the developing stage, the mean altitude of a mountain range increases due to the tectonic uplift rate exceeding the denudation rate. Denudation rate increases with mean altitude, as altitude dispersion becomes greater. As it approaches the tectonic uplift rate, rate of increase in mean altitude is progressively slower. When the denudation rate catches up with the tectonic uplift rate, a steady state appears, and the mountain range enters the culminating stage. The culminating stage indicates that a time-independent landscape is maintained in dynamic equilibrium between tectonic uplift and denudation. Mean altitude attains a critical altitude and then remains constant, in spite of continuous tectonic uplift. Altitude dispersion also reaches a maximum and keeps a constant sediment yield. Parallel retreat of slope is a dominant process maintaining the landscape (Ohmori, 1983a, 1984), resulting in accordance of summit level, which may correspond to the "oberes Denudationsniveau" of Penck (1894, 1919) (Ohmori, 1978, 1985, 2000; Yoshikawa *et al.*, 1981; Yoshikawa, 1984, 1985a, 1985b). The critical altitude H_c (m) is uniquely determined by tectonic uplift rate, and given by:

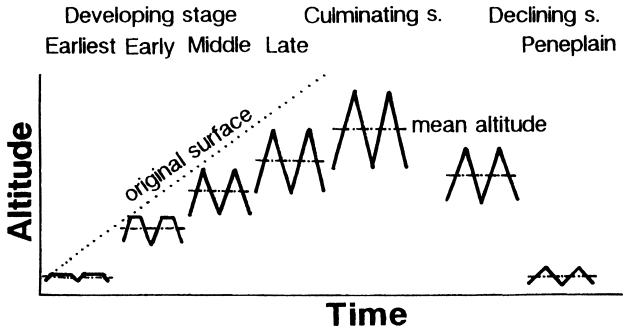


Fig. 12. Landscape development in orogenesis resulting from concurrent tectonics and denudation (Ohmori, 1985, 2001b).

$$H_c = \left(\frac{U}{\gamma}\right)^{1/\delta} \tag{11}$$

For example, when the tectonic uplift rate is 1 mm/yr, a complete steady state appears at the critical altitude of about 900 m above sea level in about 3 million years. The basic altitude dispersion is estimated to be about 95 m. When the tectonic uplift rate is 3 mm/yr, the critical altitude of about 2000 m above sea level, with a basic altitude dispersion of about 150 m, is attained in about 2 million years. The critical altitude becomes greater with a higher uplift rate, and the higher the uplift rate, the earlier the mountain ranges attain their critical altitudes.

During the declining stage, when the uplift rate declines, mean altitude falls and there is a decrease in altitude dispersion and sediment yield. The higher areas with high altitude dispersions are lowered more rapidly than the lower areas characterized by lower altitude dispersions. A decline in slope plays a significant part in the decrease in altitude in comparison with the parallel retreat of slopes (Ohmori, 1983a, 1984), resulting in a subdued landscape. The mean altitude is lowered to 100 m above sea level, with a basic altitude dispersion of about 25 m, in about 10 million years, regardless of its initial altitude. This low relief denudational landscape should be in the latest old stage, an end-peneplain. The landscape development discussed above is illustrated in Fig. 12 (Ohmori, 1985, 2001b).

On the basis of the model represented by Eq. (10), it is possible to assess the impact of changes in tectonic uplift rate on the sequence of landscape development. This produces a sequential change in mean altitude composed of several phases with different uplift rates. In such a case, there is not significant difference between a mean altitude calculated by the integrated uplift of individual uplift rates for 1 million years or longer, and a mean altitude calculated using the mean uplift rate, u (the mean weighted uplift rate):

$$u = \frac{\left(\sum_{i=0}^{n} u_i t_i \right)}{T} \tag{12a}$$

where t_i is the duration of each uplift rate of u_i, n is the number of the changes in uplift rate, and T is the total duration of simulation; $\sum t_i$ (Ohmori, 1987, 1990a, 1990b). When the uplift rate is constant throughout the total duration, n is 0. The mean uplift rate is practically estimated by:

$$u = \frac{H_n}{T} \tag{12b}$$

where H_n is the cumulative vertical displacement of land surface without denudation during the total duration of T. The cumulative vertical displacement must be estimated on the basis of the altitude of a reference surface such as an uplifted depositional surface or uplifted peneplain remnant, geologically and chronologically confirmed.

As the same way, it is also possible to assess the impact of changes in denudation rate with climatic change on the sequence of landscape development. Values of the coefficients γ and δ may be peculiar to each climatic phase. As examined in the previous section, however, denudation rate might be maintained on an average in proportion to the magnitude of local relief, in spite of climatic changes, in Japan. For avoiding the "simulation game", therefore, the change in denudation rate seems better to be ignored in the simulation until reliable denudation rate in each climatic phase is revealed.

The changes in altitude and local relief in the developing stage have been discussed on the basis of morphometric analyses and chronological data for the mountain ranges in central Japan (Sugai and Ohmori, 1999). Having formed during the late Pliocene and early Pleistocene, the original low-relief surfaces have been progressively dissected by valley deepening from the increase in altitude by tectonic uplift. The original surface on an interfluve disappears due to intersection of the valleys that eroded both flanks, when the original surface attains about 1600–2000 m above sea level. The shape of cross-section of an interfluve changes from trapezoidal to triangular, indicating that the mountain range enters into the full mature stage in the Davisian sense. At this time, the local relief expressed by the altitudinal difference between ridge top and foot reaches about 1000 m. Even after the original surface disappears, ridge top altitude and local relief still increase as a result of tectonic uplift. When the mountain range ultimately attains its own critical altitude, the shape of an interfluve approaches a steady state, and remains the same until relative rates of tectonic uplift and denudation change. These results agree well with the model discussed above.

The relationship between sediment yield and stage of landscape development has been discussed on the basis of the relationship between stage of mountain

range and alluvial fan development at the mountain foot (Saito, 1988, 1989a, 1989b) as follows. In Japan, 586 alluvial fans with an area larger than 2 km^2 formed since the late Pleistocene are counted. Regional variations in distribution of alluvial fans show contrasts between morphotectonic terrains. On the basis of multiple discriminant analysis, the principal factor controlling regional variations is the relief ratio of the drainage basin. The relief ratio is a measure of local relief and functionally related to altitude dispersion (Oguchi and Ohmori, 1994). It is also related to the stage of landscape development of a mountain range (Saito, 1989a, b). Using the stages of individual mountain ranges evaluated by Ohmori (1978), mountain ranges in the advanced stages with high mean altitudes and high altitude dispersions have extensive and well-developed alluvial fans with thick deposits at their foot. Mountain ranges in the early stages with low mean altitudes and low altitude dispersions have small alluvial fans with thin deposits or no conspicuous alluvial fan at their foot. The proportion of drainage basins having alluvial fans in individual mountain ranges increases with advance in stage of mountain landscape: Mountain ranges in the more advanced stage have a higher proportion of drainage basins with alluvial fans. Depositional landforms in the lowlands, therefore, have been developed in connection with the dissection processes in mountain ranges controlled by altitude and altitude dispersion, both of which change with advance in stage (Saito, 1988, 1989a, 1989b).

3. Differences in the course of landscape development between the three models

The model discussed above is now called the RAD model (the Relief-Altitude-Denudation model). The Penckian model is also a model for landscape development resulting from concurrent tectonics and denudation, although it was originally developed for describing hill-slope development. What difference is there between these two models? For the RAD model, we can assume arbitrarily any possible values only for tectonic uplift rate. Denudation rate is determined by mean altitude that is, in turn, functionally related both to rates of tectonic uplift and denudation. On the basis of the empirical relationships between denudation rate, local relief and mean altitude, the course of landscape development can have only one course for a value of tectonic uplift, although the values of $\gamma(=\alpha a^{\beta})$ and δ $(=b\beta)$ may be different between tectonic or climatic regions. The tectonic movements associated with plate motion may be relatively independent of the other factors during the developing and culminating stages, while those associated with isostasy during the declining stage may be related to denudational unloading (Ohmori, 2000).

For the Penckian model, however, there is no functional relationship between denudation rate and altitude, although denudation rate is assumed to be proportional to surface gradient which may be a measure of local relief. We can, therefore, assume arbitrarily and independently any values for both rates of tectonic uplift and denudation. On the basis of the Penckian model, we can deduce any courses of landscape development in terms of using the tectonic uplift rate and denudation rate assumed, at our own convenience. From this kind of simulation, we can not

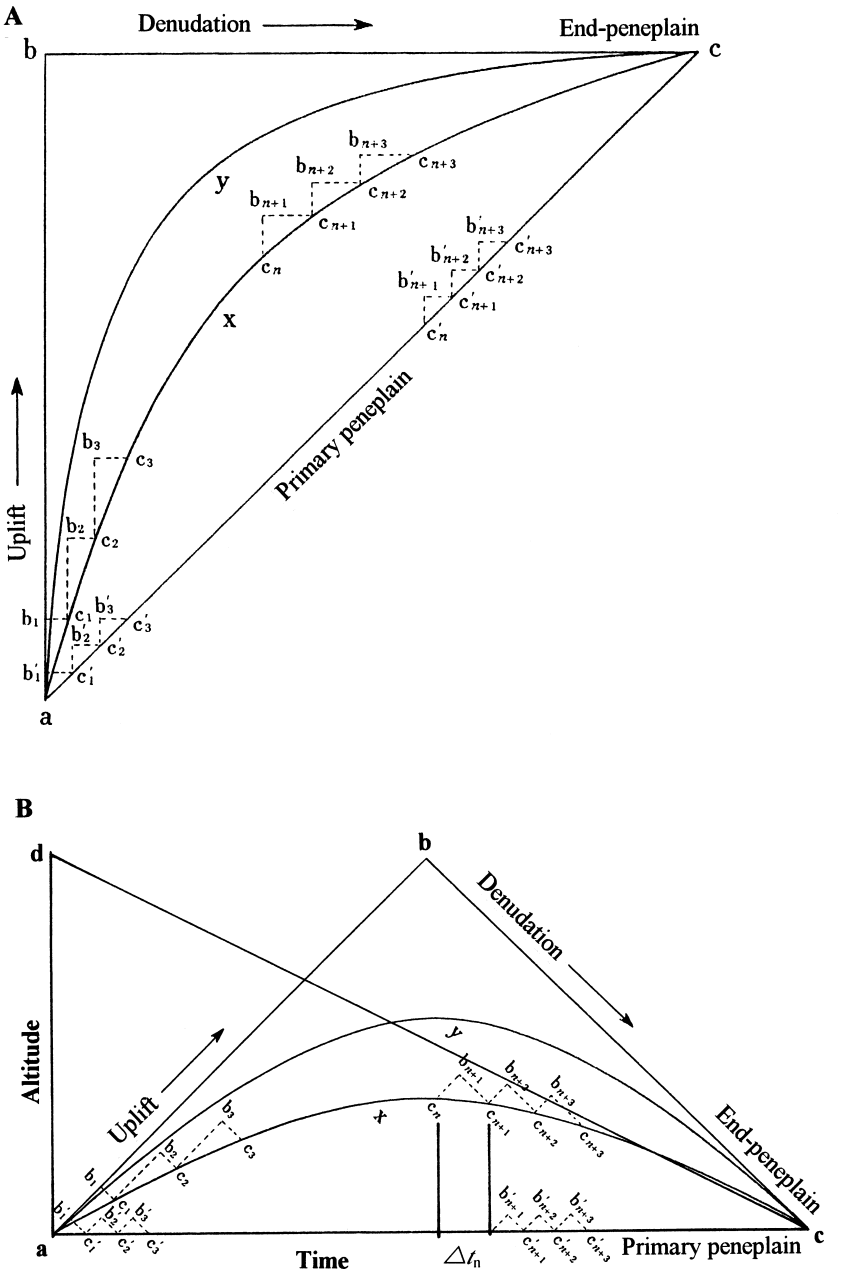


Fig. 13. Change in altitude for cases of different relationship between tectonic uplift and denudation. **A**: Penckian diagram (Penck, 1924, p. 11; transformed by Yoshikawa (1985b) to express tectonic uplift and denudation by the same measurement scale). The lengths of $c_n b_{n+1}$ and $b_{n+1}c_{n+1}$ are the uplift and denudation in a short time span, respectively. **B**: Rotated diagram of **A** for expressing the course in terms of the time-altitude relationship. The lengths of $(c_n b_{n+1})\sin(\pi/4)/\Delta t_n$ and $(b_{n+1}c_{n+1})\sin(\pi/4)/\Delta t_n$ are respectively the uplift rate and denudation rate in Δt_n.

confirm which course among a number of simulated courses is adequate as a basis for understanding landscape and its nature. A model with a high degree of freedom for determining values of its constituent elements is not always a superior model. The freedom sometimes implies that we can not determine actually any possible values of the elements. With imaginary and arbitrary values, the model may sometimes deduce meaningless results.

Figure 13-**A** is a diagram which was transformed by Yoshikawa (1985b, figure 2.3, p. 37) from the diagram of Penck (1924, figure 1, p. 11) to express tectonic uplift and denudation on the same scale. In the diagram, W. Penck intended to express the Davisian model by the lines **ab** and **bc**, and the primary peneplain by the line **ac**. The two curves ***x*** and ***y*** are example courses of the sequence resulting from concurrent tectonics and denudation. Total amount of tectonic uplift is the same as that of denudation for each course, and they are also the same for all the courses. It means that each curve ***x*** and ***y*** expresses a sequence of landscape development throughout an orogeny. Every course of the sequence resulting from concurrent tectonics and denudation has been considered to be necessarily in the triangle **abc** (Penck, 1924). This may be an origin of the idea that every ordinary landscape development is expected to follow a course between the Davisian sequence **a–b–c** and the Penckian primary peneplain sequence **a–c**.

The Penckian diagram can be rotated into Fig. 13-**B** for expressing the courses in terms of the time-altitude relationship. Figure 13-**B** is not mathematically accurate expression, but is convenient for explanation. In Fig. 13-**B**, Δt_n, the time span, varies with course and changes with time except for the line **ac**. The lengths of $c_n b_{n+1}$ and $b_{n+1} c_{n+1}$ indicate not time length but relative rates of tectonic uplift and denudation in Δt_n. To be exact, $(c_n b_{n+1})\sin(\pi/4)/\Delta t_n$ and $(b_{n+1} c_{n+1})\sin(\pi/4)/\Delta t_n$ indicate tectonic uplift rate and denudation rate, respectively. It is clear that the **a–b–c** course does not show the correct course of the Davisian model with respect to time. This is from lack of the adequate concept of time in the Penckian diagram. For this kind of comparison, the course of the Davisian model must be expressed by the course **a–d–c**, because the Davisian model starts from the highest position in the sequence.

In Fig. 13-**B**, each central part of the curves ***x*** and ***y*** shows a steady state keeping a balance between uplift rate and denudation rate for a short time span. In the RAD model, the culminating stage appears when both the mean altitude and the local relief remain constant due to dynamic equilibrium between tectonic uplift and denudation, while in the Davisian model the mountain altitude continuously decreases. It is sure that the dynamic equilibrium state is outside the Davisian model (Hack, 1960; Ahnert, 1970; Ohmori, 1978, 1985; Yoshikawa, 1984, 1985a, 1985b).

For examining the differences in sequence between the RAD model and the Davisian model, it is difficult to compare altitude between the models, because altitude was not quantitatively expressed in relation to time in the Davisian model. If denudation rate changes with time, the Davisian model could show many courses of the sequence of landscape development. Figure 13-**B**, however, suggests that many mountain ranges among those following the sequence resulting from concurrent tectonics and denudation may exceed in altitude the mountain

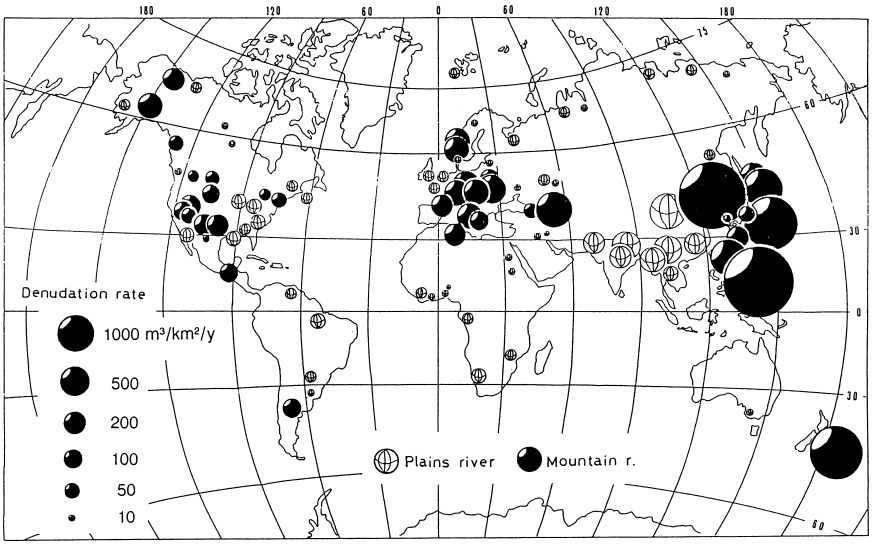


Fig. 14. Distribution of denudation rates in drainage basins of rivers in the world (Ohmori, 1983c).

range following the Davisian model in the later stage of orogeny, for the same condition of total tectonic uplift and total denudation. It is also difficult to compare the local relief between the models, because in the Davisian model local relief was not quantitatively expressed in relation to altitude. For a mountain range in the full maturity of the Davisian model, local relief is at its maximum but mean altitude is significantly lower than the initial altitude. Local relief of the RAD model, however, continues increasing with an increase in altitude by tectonic uplift even after the mountain range has entered the full maturity until it reaches the critical altitude. Even if the mean altitude in the full maturity is equal to the critical altitude, local relief must be maintained by continuous tectonic uplift and exceeds that of the Davisian model sooner or later, because local relief in the Davisian model decreases continuously after the full maturity. This is also another case of the RAD model coming out of the Davisian model. These indicate that the Davisian model draws not an extension of the sequence of landscape development but just a special case. Much of the sequence of landscape development resulting from concurrent tectonics and denudation must lie outside the sequence of the Davisian model.

RELATIONSHIP BETWEEN THE END-PENEPLAIN AND PRIMARY PENEPLAIN

The distribution of denudation rates in drainage basins of rivers in the world is shown in Fig. 14 (Ohmori, 1983c). It shows that denudation rates in Japan are among the highest class in the world. It indicates that the denudation rates estimated from Eqs. (5) and (7) must also be among the highest class in the world. Even in the areas of high denudation rates such as Japan, when mean altitude is 100 m above

sea level, with a basic altitude dispersion of about 25 m, the denudation rate is calculated to be about 0.05 mm/yr from Eqs. (5) and (7). The tectonic uplift rate, therefore, must be about 0.05 mm/yr or less to keep a balance with the denudation rate working on a peneplain for maintaining it at low altitude. A tectonic uplift rate of 0.05 mm/yr means that the land surface is tectonically uplifted only 5 mm in a hundred years, 5 m in a hundred thousand years, and 50 m in a million years. If the mean altitude of an imaged primary peneplain is considerably lower than 100 m above sea level, the tectonic uplift rate for maintaining the primary peneplain needs to be much lower than 0.05 mm/yr in any regions in the world. Such a low uplift rate could not be measured by our surveying techniques, and in practice must be recognized as a stable stand as noted by Yoshikawa (1985b, p. 102–103). Essentially it cannot create a mountain range, even though there is little denudation, and it should be out of orogenic processes. It hardly needs saying that an initially low relief landscape maintained at low altitude not by denudation but by a vertically stable stand, by a lack of crustal movement, is not a Penckian primary peneplain. The origin of the initially low relief landscape itself is the very problem with respect to a peneplain.

On the basis of the changes in altitude and local relief for the mountain ranges in Japan, interfluve cross-section shape transforms from trapezoidal to triangular in the late developing stage and remains the same during a steady state of culminating stage (Ohmori, 1990a, b; Sugai and Ohmori, 1999). If the stages occur at a low altitude, the landscape may show a low relief landscape similar to a peneplain. Maintaining the culminating stage at a low altitude for a considerably long term needs also an extremely low tectonic uplift rate. It necessarily accompanies a considerably long-term youthful stage in the Davisian sense. The sequence of landscape development with the long-term youthful stage due to a low tectonic uplift rate is also quite different from the concept of the primary peneplain.

On the contrary, the tectonic uplift rate in orogenesis should easily exceed such a low denudation rate, and altitude and local relief must become high. The observed lowest denudation rate among the 82 reservoirs in Japan is 0.06 mm/yr. The mean altitude of the drainage basin with the lowest denudation rate is 565 m above sea level, and the mean basic altitude dispersion is 38 m. The mean altitude and altitude dispersion are relatively higher than those expected from the observed denudation rate. The basic altitude dispersion of 38 m, however, is considerably lower than the 70 m expected from the mean altitude. The drainage basin is located in the Chugoku Mountains famous for “uplifted peneplain remnants” in the inner belt of Southwest Japan. Extensive low relief denudational surfaces formed during the late Tertiary and early Quaternary are widely distributed on ridge tops in and around the drainage basin (Okazaki, 1967; Yoshikawa *et al*., 1981; Ohmori, 1984). They have been dissected by deep but narrow valleys. The Quaternary vertical displacement of the Chugoku Mountains is about 400–800 m (Research Group for Quaternary Tectonic Map, 1968, 1969, 1973; Fig. 7), indicating that the mean Quaternary tectonic uplift rate is about 0.2–0.4 mm/yr (Ohmori, 1978). Though the absolute value of the tectonic uplift rate is among the

lowest class in Japan, the uplift rate has overcome the denudation rate, causing the high mean altitude. As dissection processes could not follow the tectonic uplift, extensive peneplain surfaces remain on ridge tops, resulting in the relatively low altitude dispersion. This is an exceptional case in Japan. The case, however, indicates that the denudation rate working on a peneplain must be significantly low, being easily exceeded by the tectonic uplift rate in orogenesis.

The primary peneplain must be formed under a condition with some high uplift rate expected for orogenesis and also with some high denudation rate equivalent to the uplift rate for maintaining it at low altitude. As examined above, however, such a place can not be found in the world, especially in the orogenic zones even with significantly high denudation rates like Japan. The primary peneplain imaged by W. Penck, therefore, cannot actually exist on the earth.

If a low relief denudational landscape has been kept at low altitude for a considerably long term, it should have been formed originally not as a primary peneplain under the steady state of the Penckian model, but as an end-peneplain of the Davisian model. It must have been maintained at low altitude due to a vertically stable stand of the crust. Therefore, it can be practically, physically and conceptually said that the Penckian primary peneplain must be the same as the Davisian end-peneplain.

CONCLUSIONS

On the basis of the relationships between denudation rates, mountain altitude and local relief observed in Japan, the landscape development resulting from concurrent tectonics and denudation can be divided into developing, culminating and declining stages. In the developing stage, mean altitude increases together with local relief due to the tectonic uplift exceeding the denudation. During the culminating stage in a steady state between tectonic uplift and denudation, mean altitude attains a critical altitude and remains constant, in spite of continuous tectonic uplift. Local relief reaches a maximum and maintains a constant sediment yield. In the declining stage, mean altitude, local relief and sediment yield decrease. As higher areas with high local relief lowered more rapidly than lower areas with lower local relief, a peneplain of a subdued and rolling landscape finally appears.

The culminating stage does not exist in the Davisian model. It must be sure also that many mountain ranges among those following the sequence resulting from concurrent tectonics and denudation exceed in altitude a mountain range following the Davisian model. On the other hand, the relationships between denudation rate, altitude, and local relief observed in Japan indicate that the tectonic uplift rate for keeping a balance with the denudation rate working on a peneplain must be much lower than 0.05 mm/yr. Such a low uplift rate cannot create a mountain range and should be outside orogenic processes. A low relief denudational landscape maintained at low altitude should have been formed originally not as a primary peneplain under the steady state of the Penckian model, but as an end-peneplain of the Davisian model. It can be conclusively said that the primary

peneplain imaged by W. Penck cannot actually exist on the earth and that it must be the same as the Davisian end-peneplain. The sequence of landscape development resulting from concurrent tectonics and denudation, therefore, can not always stay within the framework bounded by the Davisian model and the Penckian primary peneplain.

For a physical mode of landscape formation process constructed on the basis of the dynamic relationships between tectonics, denudation process and landscape, it sometimes appears that no assumptions are necessary for the simulation. Even such a physical model, however, can not estimate any landscape changes in the future, even for the past, without any assumptions of the changes in tectonics or denudation process, or in the landscape itself. When an assumption is conceptually recognized to be typical of cases, for example, an abrupt uplift, a constant uplift, a gradual uplift or a stable stand, the assumption itself must not be criticized. The model may show an imaginable case. It is important to examine whether or not the model and assumption give us a comprehensive, realistic and basic sequence of landscape development for understanding landscape and its nature. "How do we use it" depends on the level of our geomorphology.

We should remember, however, that a model deductively given on the basis of a mathematical or physical assumption indicates the result at the same time as it is proposed, if the equation has been mathematically solved already. For one of the simplest examples, when a model that denudation rate (dH/dt) is assumed to be proportional to altitude (H) is proposed, the model is mathematically expressed by $dH/dt = -\lambda H$, and at once the solution is given by $H = H_0 e^{-\lambda t}$, where H_0 is the initial altitude, t is the time, and λ is a constant. The locus drawn by the equation indicates the sequence of changes in altitude, and the characteristics of the locus have been mathematically established already, too. For such a model, the assumption itself needs to be examined whether or not it is adequate for understanding geomorphic processes going on the actual field, because the assumption includes both geomorphic processes and results themselves. Examining the results from such a model can not explore a new horizon further than the mathematical meanings that have been discovered already. If a model, even if it appears to have a physical basis, is not tested on the basis of the data actually observed on the earth, further discussion including simulation sometimes induces not better understandings but awful misunderstandings about landscape development.

The Davisian and Penckian models seemed to have indicated the fundamental courses of landscape development through an orogeny. They provided a new world of geomorphology. The actual sequence of landscape development in orogenesis, however, lies outside these two models.

Acknowledgements—The author wishes to express many thanks to all those who gave helpful comments on this research at the Symposium "New Concepts and Modeling in Geomorphology", the Fifth International Conference on Geomorphology held in Tokyo, 2001. He also gratefully acknowledges Ian S. Evans, Eiji Tokunaga and Masashige Hirano for their critical and fruitful comments on an early version of the manuscript.

REFERENCES

Ahnert, F. (1970) Functional relations between denudation rate, relief, and uplift in large midlatitude drainage basins: *Amer. Jour. Sci.*, **268**, 243–268.

Akojima, I. (1983) Comparison between the past and the present denudation rate of mountains around the Yamagata Basin, Northeast Japan: *Trans. Japan. Geomorph. Union*, **4**, 97–106 (in Japanese with English abstract).

Ashida, K. (1971) Sedimentation in reservoirs: In K. Yano (ed.), *Science on Disasters Caused by Water*, pp. 522–554. Gihodo, Tokyo (in Japanese).

Beaumont, C., Kooi, H. and Willett, S. (2000) Coupled tectonics-surface process models with applications for rifted margins and collisional orogens: In M. A. Summerfield (ed.), *Geomorphology and Global Tectonics*, pp. 29–55. John Wiley & Sons, Chichester.

Bloom, A. L. (1978) *Geomorphology*. Prentice Hall, Englewood Cliffs, 510 pp.

Bloom, A. L. (1991) *Geomorphology*. Prentice Hall, Englewood Cliffs, 532 pp.

Büdel, J. (1977) *Klima-Geomorphologie*. Gebrüder Borntrager, Berlin, 304 pp.

Chorley, R. J. (1965) A re-evaluation of the geomorphic system of W. M. Davis: In R. J. Chorley and P. Haggett (eds.), *Frontiers in Geographical Teaching*, pp. 147–163. Methuen, London.

Chorley, R. J., Dunn, A. J. and Beckinsale, R. P. (1964) *The History of the Study of Landforms, Vol. 1: Geomorphology before Davis*. Methuen and John Wiley & Sons, London, 678 pp.

Chorley, R. J., Beckinsale, R. P. and Dunn, A. J. (1973) *The History of the Study of Landforms, Vol. 2: The Life and Work of William Moris Davis*. Methuen, London, 874 pp.

Chorley, R. J., Schumm, S. A. and Sugden, D. E. (1984) *Geomorphology*. Methuen, London, 605 pp.

Cotton, C. A. (1922) *Geomorphology of New Zealand*. Dominion Museum, Wellington, 462 pp. (reprint in 1926).

Cotton, C. A. (1942) *Geomorphology* (3rd ed.). Whitcombe & Tombs, Christchurch, 505 pp.

Davis, W. M. (1889) The rivers and valleys of Pennsylvania: *Natl. Geogr. Mag.*, **1**, 183–253.

Davis, W. M. (1890) The rivers of northern New Jersey with notes on the classification of rivers in general. *Natl. Geogr. Mag.*, **2**, 81–110.

Davis, W. M. (1899) The geographical cycle: *Geogr. Jour.*, **14**, 481–504.

Davis, W. M. (1901) Peneplains of central France and Brittany: *Bull. Geol. Soc. Amer.*, **12**, 481–483.

Davis, W. M. (1905) Complications of the geographical cycle: *Rept. Eighth Int. Geogr. Cong., Washington*, 1904, 150–163 (in *Geographical Essays*, 1909, 279–295).

Davis, W. M. (1909) *Geographical Essays* (reprinted in 1954). Dover Pub. Inc., Boston, 777 pp.

Davis, W. M. (1912) *Die erklärende Beschreibung der Landformen*. Druck und Ver. Teubner, Leipzig, 565 pp.

Davis, W. M. (1922) Peneplains and geographical cycle: *Bull. Geol. Soc. Amer.*, **33**, 587–598.

Davis, W. M. (1923) The cycle of erosion and summit level of the Alps: *Jour. Geol.*, **31**, 1–41.

Davis, W. M. (1926) The value of outrageous geological hypothesis: *Science*, **58**, 463–469.

Davis, W. M. (1932) Piedmont benchland and Premärrumpfe: *Bull. Geol. Soc. Amer.*, **43**, 399–440.

Evans, I. S. (1972) General geomorphometry, derivatives of altitude, and descriptive statistics: In R. J. Chorley (ed.), *Spatial Analysisi in Geomorphology*, pp. 19–90. Methuen & Co., London.

Ezaki, K. (1966) The studies on sedimentation in reservoirs: *Rept. Public Works Res. Inst., Ministry of Construction*, No. 129, 55–83 (in Japanese).

Fujiwara, O., Sanga, T. and Ohmori, H. (1999) Regional distribution of erosion rates over the Japanese Islands: *Japan Nuclear Cycle Technical Review*, **5**, 85–93 (in Japanese with English abstract).

Fujiwara, O., Sanga, T. and Ohmori, H. (2001) *Regional Distribution of Erosion Rates over the Japanese Islands* (CD-ROM version). Nuclear Cycle Technical Research Inst., Tokyo, 25p. + CD-ROM (in Japanese with English abstract).

Geikie, J. (1913) *Mountains: Their Origin, Growth and Decay*. Oliver and Boyd, Edinburgh, 311 pp.

Gilbert, G. K. (1877) *Report on the Geology of the Henry Mountains. U.S. Geogr. Geol. Survey of the Rocky Mountain Region*. Government Printing Office, Washington, D.C., 160 pp. (in 2nd ed., 1880, 170 pp.).

Hack, J. T. (1960) Interpretation of erosional topography in humid temperate climate: *Amer. Jour. Sci*., **258-A**, 80–97.

Hovius, N. (2000) Macroscale process systems of mountain belt erosion: In M. A. Summerfield (ed.), *Geomorphology and Global Tectonics*, pp. 76–105. John Wiley & Sons, Chichester.

Inoue, S., Hanai, J., Okayama, T., Fukui, E., Tada, F., Yoshimura, S. and Watanabe, A. (1940) *Physical Geography* (1st vol.). Chijin-shokan, Tokyo, 684 pp. (in Japanese).

Ishigai, H. (1966) Study on sedimentation of clastic sediments in reservoirs: *Rept. Tech. Res. Lab. Central Res. Inst. Electric Power Industry*, No. 66010, 95 pp. (in Japanese with English abstract).

Iso, N., Yamakawa, K., Yonezawa, H. and Matsubara, T. (1980) Accumulation rates of alluvial cones, constructed by debris-flow deposits, in the drainage basin of the Takahashi river, Gifu Prefecture, central Japan: *Geogr. Rev. Japan*, **53**, 699–720 (in Japanese with English abstract).

King, L. C. (1962) *The Morphology of the Earth*. Oliver and Boyd, Edinburgh, 699 pp.

Lobeck, A. K. (1939) *Geomorphology: An Introduction to the Study of Landscape*. McGraw-Hill Books Com., New York, 731 pp.

Louis, H. and Fischer, K. (1979) *Allgemeine Geomorphologie*. Walter de Gruyte, Berlin, 814 pp.

Maull, O. (1958) *Handbuch der Geomorphologie*. Ver. Franz Deuticke, Vienna, 600 pp. + 44 plates.

Mizutani, T. (1981) Drainage basin characteristics affecting sediment yield from steep mountain drainage basin: *Shin-Sabo*, No. 119, 1–9 (in Japanese with English abstract).

Nakano, S. (1989) Geology of Washiba-Kumonotaira volcano, Japan Alps, central Japan: *Bull. Volcanol. Soc. Japan*, **34**, 197–211 (in Japanese with English abstract).

Namba, S. and Kawaguchi, T. (1965) Influences of some factors upon soil losses from large mountain watersheds: *Bull. Government Forest Experiment Station*, No. 173, 93–116 (in Japanese with English abstract).

Oguchi, T. (1991) Quantitative study of sediment transport in mountain drainage basins since the Late Glacial: *Trans. Japan. Geomorph. Union*, **12**, 25–39 (in Japanese with English abstract).

Oguchi T. and Ohmori, H. (1994) Analysis of relationships among alluvial fan area, source basin area, basin slope, and sediment yield: *Zeit. Geomorph. N.F.*, **38**, 405–420.

Ohmori, H. (1978) Relief structure of the Japanese mountains and their stages in geomorphic development: *Bull. Dept. Geogr., Univ. Tokyo*, **10**, 31–85.

Ohmori, H. (1982) Functional relationship between the erosion rate and the relief structure in the Japanese mountains: *Bull. Dept. Geogr., Univ. Tokyo*, **14**, 65–74.

Ohmori, H.(1983a) A three dimensional model for the erosional development of mountain on the basis of relief structure: *Trans. Japan. Geomorph. Union*, **4**, 107–120.

Ohmori, H. (1983b) Characteristics of the erosion rate in the Japanese mountains from the viewpoint of climatic geomorphology: *Zeit. Geomorph. N.F.*, Suppl. Bd., **46**, 1–14.

Ohmori, H. (1983c) Erosion rates and their relation to vegetation from the viewpoint of world-wide distribution: *Bull. Dept. Geogr., Univ. Tokyo*, **15**, 77–91.

Ohmori, H. (1984) Change in the earth's surface altitude with absolute time simulated from the relation between mean altitude and dispersion, and between dispersion and denudation rate: *Bull. Dept. Geogr., Univ. Tokyo*, **16**, 5–22.

Ohmori, H. (1985) A comparison between the Davisian scheme and landform development by concurrent tectonics and denudation: *Bull. Dept. Geogr., Univ. Tokyo*, **17**, 18–28.

Ohmori, H. (1987) Mean Quaternary uplift rates in the central Japanese mountains estimated by means of geomorphological analysis: *Bull. Dept. Geogr., Univ. Tokyo*, **19**, 29–36.

Ohmori, H. (1990a) Quaternary uplift rate and its relation to landforms of Mts. Shikoku, Japan: In N. Yonekura, A. Okada and A. Moriyama (eds.), *Tectonic Landforms*, pp. 60–86. Kokon-Shoin, Tokyo (in Japanese).

Ohmori, H. (1990b) Geomorphogenetic crustal movement and the altitudinal limitation of peneplain remnants of the Shikoku Mountains, Japan: *Bull. Dept. Geogr., Univ. Tokyo*, **22**, 17–34.

Ohmori, H. (1993) Changes in the hypsometric curve through mountain building resulting from concurrent tectonics and denudation: *Geomorphology*, **8**, 263–277

Ohmori, H. (1995) Geological and geomorphological characteristics of Japan: In Editorial Committee of the History of Civil Engineering in Japan (ed.), *The History of Japanese Civil Engineering from*

1966 to 1990: Memorial Publication of the Eightieth Anniversary of the Japan Society of Civil Engineers, pp. 16–20. Japan Society of Civil Engineers, Tokyo (in Japanese).

Ohmori, H. (2000) Morphotectonic evolution of Japan: In M. A. Summerfield (ed.), *Geomorphology and Global Tectonics*, pp. 146–166. John Wiley & Sons, Chichester.

Ohmori, H. (2001a) Dynamics of uplift and erosion in the Japanese mountains: *Chikyu* (*The Earth*), No. 32, 14–21 (in Japanese).

Ohmori, H. (2001b) A paradox of concurrency of the Davisian end-peneplain and the Penckian primary peneplain: *Special Pub. Geogr. Inform. Sys. Ass.*, **1**, 4–5.

Ohmori, H. and Hirano, M. (1984) Mathematical explanation of some characteristics of altitude distributions of landforms in an equilibrium state: *Trans. Japan. Geomorph. Union*, **5**, 293–310.

Ohmori, H. and Sohma, H. (1983) Landform classification in mountain region and geomorphic characteristic values: *J. Japan Cartgr. Asso.*, **21**(3), 1–12 (in Japanese with English abstract).

Ohmori, H. and Sugai, T. (1995) Toward geomorphometric models for estimating landslide dynamics and forecasting landslide occurrence in Japanese mountains: *Zeit. Geomorph. N.F.*, Suppl. Bd., **101**, 149–164.

Ohmori, H., Sanga, T., Fujiwara, O. and Sugai, T. (1999) Distribution of erosion rates over the Japanese Islands and its regional characteristics. *Proceedings of Korea-Japan Geomorphological Conference*, 52–53.

Okayama, T. (1953) The geomorphic structure of Japan: *Jour. Histor. Assoc. Meiji Univ.*, **13**, 28–38 (in Japanese).

Okazaki, S. (1967) A consideration on the characteristics and genesis of the eroded flat surfaces found in the mountain lands non-volcanic area in Japan: *Ochanomizu Univ. Studies in Arts and Culture*, **20**, 193–204 (in Japanese with English summary).

Penck, A. (1894) *Morphologie der Erodoberfläche I, II*. Ver. J. Engelhorn, Stuttgart, 471 pp., 696 pp.

Penck, A. (1919) Die Gipfelflur der Alpen: *Sitz. Preuss. Akad. Wiss. Berlin*, **32**, 256–268.

Penck, W. (1924) *Die Morphologische Analyse*. Ver. J. Engelhorns Nachf., Stuttgart, 283 pp.

Powell, J. W. (1875) *Exploration of the Colorado River of the West and Its Tributaries*. U.S. Government Printing Office, Washington, D.C., 291 pp.

Research Group for Active Faults (1980) *Active Faults in Japan—Sheet Maps and Inventories*. Univ. Tokyo Press, 363 pp. (in Japanese with English summary).

Research Group for Quaternary Tectonic Map (1968) Quaternary tectonic map of Japan: *Daiyonki Kenkyu* (*The Quat. Res.*), **7**, 182–187 (in Japanese with English abstract).

Research Group for Quaternary Tectonic Map (1969) *Quaternary Tectonic Map of Japan*. National Research Center of Disaster Prevention, Tokyo, 6 sheets.

Research Group for Quaternary Tectonic Map (1973) *Explanatory Text of the Quaternary Tectonic Map of Japan*. National Research Center of Disaster Prevention, Tokyo, 167 pp.

Saito, K. (1988) *Alluvial Fans in Japan*. Kokon-shoin, Tokyo, 280 pp. (in Japanese).

Saito, K. (1989a) Dominant factors influencing the distribution of alluvial fans in the Taiwan Island: *J. Hokkai-Gakuen Univ.*, No. 53, 19–36 (in Japanese with English abstract).

Saito, K. (1989b) Geomorphic development of mountains in the Taiwan Island: *Ann. Hokkaido Geogr. Soc.*, No. 63, 9–16 (in Japanese with English abstract).

Scheidegger, A. E. (1961) *Theoretical Geomorphology*. Springer Ver, Berlin, 333 pp.

Sugai, T. and Ohmori, H. (1999) A model of relief forming by tectonic uplift and valley incision in orogenesis: *Basin Res.*, **11**, 43–57.

Sugai, T., Ohmori, H. and Hirano, M. (1994) Rock control on magnitude-frequency distribution of landslide: *Trans. Japan. Geomorph. Union*, **15**, 233–251.

Summerfield, M. A. (1991) *Global Geomorphology*. Longman, Essex, 537 pp.

Summerfield, M. A. (2000) Geomorphology and global tectonics: introduction: In M. A. Summerfield (ed.), *Geomorphology and Global Tectonics*, pp. 3–12. John Wiley & Sons, Chichester.

Tanaka, H. (1955) Geological and topographical studies on the sedimentation of reservoirs in Japan: *Jour. Technical Res. Lab.*, **5**(2), 163–198.

Tanaka, H. and Ishigai, H. (1951) On the relation of sedimentation of reservoirs to configuration and nature of rocks of catchment area (1st report): *Jour. Japan Soc. Civil Engineers*, **36**, 173–177

(in Japanese with English abstract).
Tanaka, M. (1982) A map of regional denudation rate in the Japanese mountains: *Trans. Japan. Geomorph. Union*, **3**, 159–167.
Thornbury, W. D. (1954) *Principles of Geomorphology*. John Wiley & Sons, New York, 618 pp.
Tokunaga, E. and Ohmori, H. (1989) Drainage basin geomorphology: *Trans. Japan. Geomorph. Union*, **10-A**, 35–46.
Tricart, J. (1965) *Principes et Méthodes de la Géomorphologie*. Masson & Cie, Paris, 496 pp.
Tsujimura, T. (1922) *Geomorphology*. Kokon-shoin, Tokyo, 700 pp. (in Japanese).
Twidale, C. R. (1976) *Analysis of Lamdforms*. John Wiley & Sons Australia, Sydney, 572 pp.
Worcester, G. G. (1939) *A Textbook of Geomorphology*. D. van Nostrand Co., New York, 565 pp.
Worcester, G. G. (1949) *A Textbook of Geomorphology* (2nd ed.). D. van Nostrand Co., New York, 584 pp.
Yoshikawa, T. (1974) Denudation and tectonic movement in contemporary Japan: *Bull. Dept. Geogr., Univ. Tokyo*, **6**, 1–14.
Yoshikawa, T. (1984) Geomorphology of tectonically active and intensely denuded regions: *Geogr. Rev. Japan*, **57A**, 691–702 (in Japanese with English abstract).
Yoshikawa, T. (1985a) Landform development by tectonics and denudation: In Pitty, A. (ed.), *Themes in Geomorphology*, pp. 194–210. Croom Helm, London.
Yoshikawa, T. (1985b) *Geomorphology in Tectonically Active and Intensely Denuded Region*. Univ. Tokyo Press, Tokyo, 132 pp. (in Japanese).
Yoshikawa, T., Kaizuka, S. and Ota, Y. (1981) *The Landforms of Japan*. Univ. Tokyo Press, Tokyo, 222 pp.
Yoshinaga, S., Saijyo, K. and Koiwa, N. (1989) Denudation process of mountain slope during Holocene based on the analysis of talus cone aggradation process: *Trans. Japan. Geomorph. Union*, **10**, 179–193 (in Japanese with English abstract).
Yoshiyama, A. and Yanagida, M. (1995) Uplift rates estimated from relative heights of fluvial terrace surfaces and valley bottoms: *Jour. Geogr.*, **104**, 809–826 (in Japanese with English abstract).

Concepts and Modelling in Geomorphology: International Perspectives,
Eds. I. S. Evans, R. Dikau, E. Tokunaga, H. Ohmori and M. Hirano, pp. 33–42.
© by TERRAPUB, Tokyo, 2003.

Geomorphology: Boundaries between Media

Robert W. BLAIR, Jr.

Department of Geosciences, Fort Lewis College, Durango, CO 81301, U.S.A.
e-mail: blair_r@fortlewis.edu

Abstract. An earth boundary surface is the interface between two media, such as the atmosphere-lithosphere, atmosphere-ocean, and lithosphere-ocean. These boundary surfaces separate different density media with their own energy dynamics, composition, and strength. The advantages of an earth-system, boundary strategy in geomorphology is that it is less limiting and brings forth the importance of several concepts, which are intuitively obvious, but are often overlooked or assumed. Thus, a more complete understanding of the nature and origin of landscapes is possible. First, all surface morphology is created from the transfer of mass in 3-d space; second, gravity is the dominant driving force of both exogenous and endogenous processes at meso- and megascales; third, a medium's resistance to change (viscosity or rigidity) is dependent on the strength of the molecular forces holding the medium together, its thermal state and the presence of structural discontinuities; fourth, sympathetic boundaries are commonly found adjacent to the studied surface in one or both media; and fifth, the application of earth-system boundaries is not scale limiting and includes a range from continental scale morphology to mineral surface microtopography.

Keywords: Gravity, Boundary Surfaces, Scale, Geomorphology, Landscape Development

INTRODUCTION

The early development of geomorphology in the late 1800's focuses on two paradigms, one process oriented, developed by G. K. Gilbert, and one historically based, championed by W. M. Davis and others. As circumstances would have it, the focus on physiography, classification and history of landscapes dominates during the first half of the 20th Century. In the latter half of this century, the emphasis shifts toward a study grounded on basic principles of mechanics and fluid dynamics of specific processes (e.g. fluvial, eolian, mass wasting) that form landscapes (Strahler, 1952; Ritter, 1988). Now with the easy availability of satellite imagery to study megascale landforms and scanning electron microscopes to study the very small, it is proposed that geomorphology expand its field of study to surfaces and processes not typically addressed in order to provide a more integrated view and understanding of earth systems. Recent publications by Summerfield (2000) and Allen (1997) reflect this trend.

Traditionally, geomorphologists focus their study of the earth's landforms on exogenic processes at mesoscopic scales (centimeter to hundreds of kilometers range) operating upon 30 percent (sub aerial portion) of the planets surface

(Thorn, 1988, p. 25). Earth surface morphology, governed by endogenic processes, microscopic activity and 70 percent of the earth's surface that lies below the ocean, tends to be ignored by geomorphologists. These subjects are generally left to geologists, geophysicists, chemists and oceanographers, but, unfortunately, these practitioners often ignore the interpretation and ramifications of surface morphologic signatures. By redefining a geomorphic surface, a more integrated and expanded view of earth phenomena is possible.

BOUNDARY SURFACES

1. Definition

A physical boundary surface is an interface between two defined media. Generally these media display different physical and chemical properties and exhibit different energy states. Megageomorphic surfaces, with areas greater than 10^8 square meters (>100 sq km), include air-ocean, air-land, and ocean-seafloor surfaces (Fig. 1). Mesogeomorphic surface morphology, with areas between 10^7 to 1 square meters, embody not only exposed pediments and inselbergs, but hidden surfaces such as sediment-ice boundaries found at the sole of a glacier, soil-rock interfaces below regolith and water table surfaces associated with cave formation.

The most common microgeomorphic surface boundaries studied, with areas less than 10^{-2} square meters, are weathering horizons, but any geomorphic

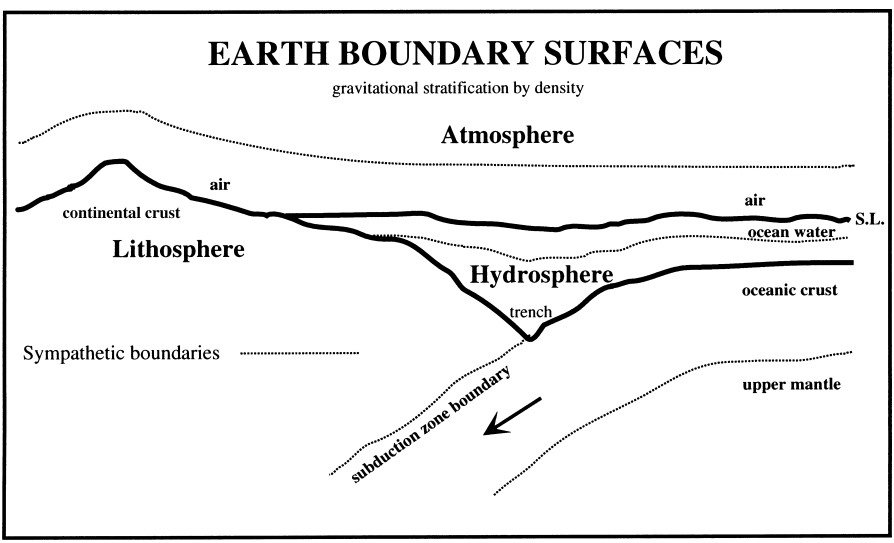


Fig. 1. Earth Boundary Surfaces. Shows megascale primary and sympathetic boundaries found on the earth's surface generated through gravitational segregation by density.

surface can also be studied at molecular scales. The major differences between studying these different scales of landforms are the tools we use. For megascopic landscapes we use aerial photography and satellite imagery, for mesoscopic landforms field observations with the naked eye and for microscopic surfaces optical and scanning electron microscopes (SEM).

2. Geometry

Geomorphologists typically address processes operating upon single surfaces shared between two media, such as wind on sand, or water on sediment. Although, these simple systems have only two general physical components, the inter-media dynamics and resultant morphological signatures are complex because of surface roughness and complicated feedback loops (e.g. Wiggs, 2001; Lawless and Robert, 2001).

When two planar surfaces intersect they share a line. Such is the case when the ocean surface intersects the land surface to produce a shoreline. The shoreline represents the intersection of four media: air, water, water-saturated rock and "dry" rock. This linear zone is subject to energy dispersion by processes from all of the respective media. Multiple lithologies only complicate the system. As such, the shoreline is one of the most dynamic and complex geomorphic regions studied and is influenced by wave action, wind shear, springs, and life from two entirely different ecological habitats. Organic entities, from bacteria, to humans and up to elephants, represent media and processes that need to be addressed as system components (Westbroek, 1991). Without defining the geometry and all the media involved, an investigator could easily overlook the interaction and input each medium might have on the resultant landscape.

3. Exogenous versus endogenous

The boundary surface is where energy is dispersed, reflected and absorbed. The energy can come from either side of the boundary to drive geomorphic processes that modify the morphology. Geomorphologists traditionally use the term, exogenic processes, as those processes operating at or near the earth's surface while endogenic processes are derived from within the earth (Bates and Jackson, 1987).

These definitions are adequate when addressing mega- and most mesoscale landscapes but they break down when describing processes operating on surfaces in general. Thus, it is useful to use the more general English word, exogenous, that means operating externally while endogenous means operating internally (American Heritage Dictionary). In this paper the surface is the reference plane and the medium with the greatest viscosity or rigidity is considered endogenous. Therefore, at a water-ice contact the water medium is the exogenous medium and the ice is considered the endogenous medium. Solar energy (exogenous) that passes through the atmosphere to the earth's surface is absorbed and emitted from within the rock as thermal energy (endogenous). Seismic energy dissipating at the earth's surface is considered endogenous energy.

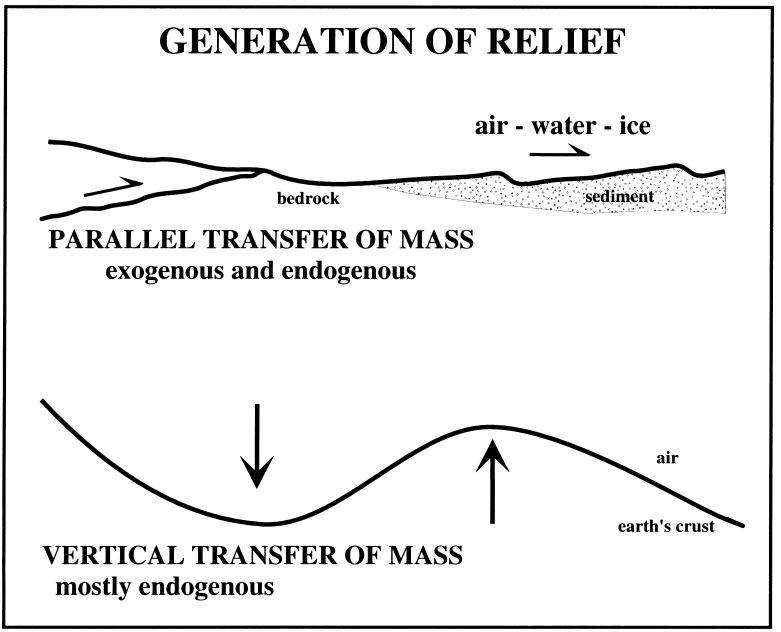


Fig. 2. Generation of Relief. Depicts the lateral and horizontal transfer of mass in 3-d space.

MASS AND ENERGY EXCHANGE AT BOUNDARY SURFACES

1. Gravity forces

Earth surface morphology evolves from the transfer of mass in 3-d space (Fig. 2). At mega and mesoscopic scales, processes under the constant pull of gravity drive this transfer. Gravity can work directly on a surface by pulling denser matter toward the earth's center and allowing less dense material to rise or by indirectly pulling fluid or solid masses across a surface to do work. Examples of mass transfer include horizontal and vertical plate movements to create mountains ranges, erosion of highlands that generates isostatic uplift, wind friction by air across a dune surface to produce wind ripples, and glacial ice dragging stones across bedrock to form scour marks. In these instances, the deposition and erosion tend to create surfaces that, statistically, are near perpendicular to the gravitational pull. In stratigraphy this translates to the law of horizontality.

2. Molecular forces

At microscopic scales, molecular forces control the migration and activity of molecules across microtopographic surfaces. Physicists have further defined these molecular forces. They have identified four fundamental forces in nature:

strong, weak, electromagnetic and gravity (Capra, 1982; Davies, 1983). The strong force is responsible for holding the nucleus of an atom together. The weak force is associated with beta decay in unstable isotopes and the electromagnetic force, which generates the positive and negative force fields, creates molecular bonding and radiation. Recently physicists have shown these three forces, excluding gravity, are permutations of a single-integrated force, described by the Standard Model (Gell-Mann, 1994, p. 125).

The strong and electromagnetic forces hold matter together and create the resistance to morphologic change. Gravity at molecular scales is insignificant compared to the strong and electromagnetic force fields; thus, the microtopographic signature is governed by processes that fall in the realm of surface physics and chemistry (Hochella, 1995; MacDonald *et al*., 1996). Differential solution of mineral surfaces, microscopic plucking and deposition all leave signatures that can provide clues to surface environmental history (see Potential Applications below).

3. Thermal energy

The viscosity and/or rigidity of a medium such as air, water, ice or rock is related to its internal kinetic energy or heat. As kinetic energy increases, molecular vibrations drive molecules apart, which weaken bonding and decrease viscosity and rigidity. The thermal state of the exogenous medium is a factor in the aggressiveness of erosion and the endogenous medium's resistance. How a material behaves under stress is a function of its temperature and the time over which the stress is applied. For example, water at 4°C has a density of 1 g/cm^3 and a slightly higher viscosity than water at 20°C water with a density of 0.998 g/cm^3. This generates a greater shear on a sandy bed and under plain bed energy conditions that can create sand ripples not possible with the warmer less viscous water. More relevant, however, are variations in the temperatures of glacial ice. Ice at 0°C has a Moh's hardness of 1.5 while ice at –80°C has a hardness of 6 (Martini *et al.*, 2001, p. 14). The power flow law is one model that describes ice creep in glaciers and includes a temperature factor:

$$\varepsilon = A\tau^n$$

Where ε = strain rate, A = temperature dependent constant, τ = effective shear stress related to thickness of ice, and n = exponent with a mean value of 3.

The temperature-dependent, constant, *A*, can change over two orders of magnitude between 0°C and –13°C (Summerfield, 1991, p. 265). It is well known that warm-based glaciers found in temperate latitudes are more effective erosional agents than polar cold-based glaciers (Martini *et al.*, 2001, p. 70).

4. Structural discontinuities

It is rare that crystalline materials are homogeneous to any extent without faults, joints, micofractures and mineral dislocations. Thus, as emphasized by

Davis (1899), structure has a profound impact on earth surface morphology both directly and indirectly. It is obvious that structural discontinuities will directly influence the texture and competence of the endogenous media surface. For example, convergent plate boundaries create mountain morphology. Joints control drainage patterns and microfractures allow accelerated erosion rates. Mineral dislocations are targets for chemical weathering.

DISCUSSION

1. Boundary surface interplay

Ritter *et al.* (1995, p. 8) define landforms as representing the interaction between driving forces (climate, gravity and internal heat) and resistance (lithology and structure). This relationship is recognized and described by G. K. Gilbert in 1877 (Ritter, 1988). He describes the interplay between geologic driving forces, primarily running water and the resistance of materials on geomorphic surfaces in the Henry Mountains. Because the dominant exogenous processes at mesoscopic scales are fluids, Strahler (1952) calls fluid dynamics the cornerstone of geomorphology. This is especially true at mesoscales. However, at megascopic and microscopic scales tectonics and molecular forces respectively, become more important.

2. Safety ratio and boundary surface

Engineering geologists and geomorphologists have long recognized the importance of defining the failure threshold or safety ratio that defines slope stability (Rahn, 1996). The safety ratio (SR) is defined empirically as the sum of resisting forces divided by the sum of driving forces (Fig. 3). The prime driving force in the formula is gravity and the resisting forces are defined in terms of friction and cohesion (Derringh, 1998, p. 82). Friction of a free body object is also governed by gravity, hence, the gravity term in the numerator. In essence, the SR at mega and mesoscales is the ratio of the strong/electromagnetic forces that hold matter together, against gravity, which is trying to move matter closer to the center of the earth.

When the resisting forces are greater than the driving forces, the system retains its integrity with little or no observed change. Changes are indeed taking place because matter is in constant motion at the molecular scale. When the ratio becomes less than 1, then gravity overwhelms the molecular forces. The system becomes unstable and a transfer of mass occurs (e.g. slope failure) toward a more stable geometry.

SYMPATHETIC BOUNDARIES

Landform surfaces are part of a system and are influenced by or create other boundaries. Invariably, there are adjacent surface boundaries that are hidden in one or both of the bounding media (Fig. 1). For example, the Andean Mountain chain is a distinct landscape whose morphology reflects the convergent plate

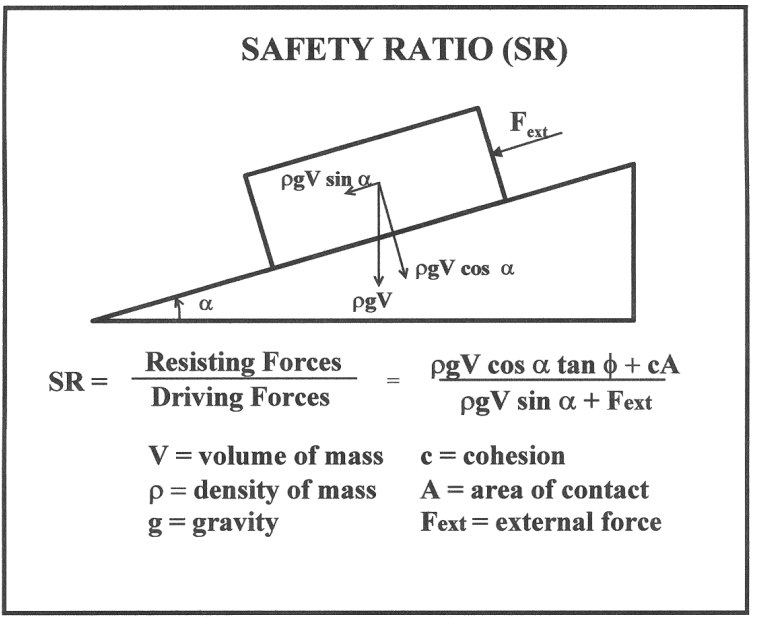


Fig. 3. Safety Ratio. Shows the geometry and forces of a free-body object resting on a solid surface.

boundary between the Nasca and South American plates. The Andean mountain system exists in direct response to the subsurface west-plunging subduction zone. The mountain range, in turn, diverts atmospheric flow and is reflected in cloud layers. Crevasses on the convex surface of a glacier are mirrored at depth by bedrock steps. Pressure release joints in granite on Half Dome in Yosemite National Park parallel the exposed cliff face surface.

These sympathetic boundaries, therefore, can reveal or even control the nature and origin of the primary study surface.

POTENTIAL APPLICATIONS

1. Endogenous landforms

Seismic body waves (Shear and Pressure waves) generated within the earth radiate in all directions, and when they reach the earth's surface they reflect most of that energy back into the earth. But some of this energy is dissipated at the density boundary interface between the crust and the atmosphere to create complex surface waves known as Love and Rayleigh waves (Fowler, 1990, p. 80). These surface waves form short-lived landforms (giant rapidly moving ripples) that can rearrange the earth's surface in minutes by creating landslides, liquifaction and altered drainages (Bolt, 1993). The physical morphology of these fleeting landforms is not well understood, but considering that few places on earth have

been exempt from earthquakes, it is surprising that they have not been addressed in greater detail.

Endogenous energy is important in the larger scheme of landscapes and geomorphic processes. All uplift is in response to endogenous processes such as plutonism and isostasy that generate greater potential energy in the landscape that later is converted to kinetic energy via exogenous processes. In fact, without the endogenous input and subsequent uplift, landscapes would have long ago eroded away. Scheidegger (1998) notes the importance of endogenous processes in the Chinese Himalayan landscape and laments over the lack of respect these processes have been given.

2. Microscopic surfaces

Geomorphologists can benefit from the close examination of microtopography because unique environmental signatures are often scribed on these surfaces. For example, thermal spalling of quartzites form a unique fracture signature as seen on SEM microphotographs (Willard, 1968). Mahaney *et al.* (1996) found that the microtexture on quartz grains from Antarctica can be used to differentiate till transported over long distances under thick ice from thinner outlet glaciers traveling over shorter distances. Micromorphology of sand and silt grains using SEM from the Lower Cambrian sediments in Estonia was studied by Kurvits *et al.* (2000). They were able to construct transport history that indicated eolian and/or fluvial suspension was dominant.

3. Ocean floor

The ocean and the ocean floor are the last frontiers of earth exploration. Because ocean water obscures our view of 70 percent of our planet, we know more specific detail about the surfaces of Mars and Venus than we do of Earth. This is because the Mars Global Surveyor satellite provided imagery of the Martian surface with resolutions about one meter (http://nssdc.gsfc.nasa.gov.html). On Venus the Magellan satellite radar penetration through the thick Venetian atmosphere has given us less than 300 meter object resolution. On Earth, satellite radar cannot penetrate ocean water and we are relegated to interpreting the ocean floor from radar altimetry of the ocean surface that gives us about a 1 to 2 km resolution. Gravity variations, due to the distribution of submarine topography, mold the seawater surface to reflect an approximation of the ocean floor thousands of meters below. This is another example of a surface interpretation from a sympathetic boundary. At present, modern side-scan sonar imagery with sub meter resolution has covered less than a few percent of the ocean floor surface. If the ocean floor has as much diversity as the land, it follows that we have an extensive information gap to close.

CONCLUSIONS

The purpose of this paper is to break down the inherent, or perhaps unintended, limits of geomorphic study by focusing on boundary surfaces, their adjacent

media, and the fundamental forces driving geomorphic processes. Geomorphic studies should have no scale limits. By defining a geomorphic surface as simply an interface between two media, a few basic concepts are revealed: 1) earth surface morphology evolves from the transfer of mass in 3-d space, 2) at mega- and mesoscopic scales gravity is the dominant force driving geologic processes to shape the landscape, 3) at molecular scales gravity plays a minor role compared to the electromagnetic/strong forces holding matter together and 4) sympathetic boundaries found with the primary surface of study can add insight to the nature and origin of both surfaces. The boundary concept can be expanded to the study of both continental-scale, as well as, molecular-scale surfaces. Geomorphology viewed in this larger context then becomes a subject of study that should be the cornerstone of all Earth system curricula.

REFERENCES

Allen, P. A. (1997) *Earth Surface Processes*. Blackwell Science Ltd., Oxford, 404 pp.

Bates, R. L. and Jackson, J. A. (eds.) (1987) *Glossary of Geology*, 3rd ed. American Geological Institute, Alexandria, VA, 788 pp.

Bolt, B. E. (1993) *Earthquakes*. W. H. Freeman and Co., New York, 331 pp.

Capra, F. (1982) *The Turning Point*. Bantam Books, New York, 464 pp.

Davies, P. (1983) *God and the New Physics*. Touchstone, New York, 255 pp.

Davis, W. M. (1899) The geographic cycle: *Geogr. Jour.*, **14**, 481–504.

Derringh, E. (1998) *Computational Engineering Geology*, Prentice Hall, Upper Saddle River, New Jersey, 323 pp.

Fowler, C. M. R. (1990) *The Solid Earth, an Introduction to Global Geophysics*. Cambridge University Press, New York, 472 pp.

Gell-Mann, M. (1994) *The Quark and the Jaguar—Adventures in the Simple and the Complex*. W. H. Freeman and Co., New York, 392 pp.

Hochella, Jr., M. F. (1995) Mineralogy scratches new surfaces: *Geotimes*, **40**(9), 16–18.

Kurvits, T., Mahaney, W. C. and Kalm, V. (2000) Grain micromorphology in the Rannamoisa section, Lower Cambrian, Estonia: *Proceeding of the Estonian Academy of Sciences, Geology—Eesti Teaduste Akadeemia Toimetised, Geoloogia*, **49**(1), 17–27.

Lawless, M. and Robert, A. (2001) Scales of boundary resistance in coarse-grained channels: Turbulent velocity profiles and implications: *Geomorphology*, **39**, 221–238.

MacDonald, R. J., Taglauer, E. C. and Wandelt, K. R. (eds.) (1996) *Surface Science: Principles and Current Applications*. Springer-Verlag, Berlin, 372 pp.

Mahaney, W. C., Claridge, G. and Campbell, I. (1996) Microtextures on quartz grains in tills from Antarctica: *Palaeogeography, Palaeoclimatology, Palaeoecology*, **121**(12), 89–103.

Martini, I. P., Brookfield, M. and Sadura, S. (2001) *Principle of Glacial Geomorphology and Geology*. Prentice Hall, NJ, 381 pp.

Rahn, P. H. (1996) *Engineering Geology, an Environmental Approach*, 2nd ed. Prentice Hall PTR, New Jersey, 656 pp.

Ritter, D. F. (1988), Landscape analysis and the search for geomorphic unity: *Geological Society of America*, **100**, 160–171.

Ritter, D. F., Kochel, R. C. and Miller, J. R. (1995) *Process Geomorphology*, 3rd ed. Wm. C. Brown Purblishers, Dubuque, IA, 546 pp.

Scheidegger, A. E. (1998) Tectonic predesign of mass movements, with examples from the Chinese Himalaya: *Geomorphology*, Elsevier, **24**(1-3), 37–46.

Strahler, A. N. (1952) Dynamic basis of geomorphology: *Geological Society of America*, **63**, 923–938.

Summerfield, M. A (1991) *Global Geomorphology*. Longman Scientific & Technical, Esssex, England, 537 pp.

Summerfield, M. A. (2000) *Geomorphology and Global Tectonics*. John Wiley & Sons, New York, 367 pp.
Thorn, C. E. (1988) *Introduction to Theoretical Geomorphology*. Unwin Hyman, Boston, 247 pp.
Westbroek, P. (1991) *Life as a Geological Force*. W. W. Norton & Co., New York, 240 pp.
Wiggs, G. F. S. (2001) Desert dune processes and dynamics: *Progress in Physical Geography*, **25**(1), 53–79.
Willard, R. J. (1968) Scanning electron microscope: *Geotimes*, **13**(7), 16–17.

Concepts and Modelling in Geomorphology: International Perspectives,
Eds. I. S. Evans, R. Dikau, E. Tokunaga, H. Ohmori and M. Hirano, pp. 43–59.
© by TERRAPUB, Tokyo, 2003.

Evolution of the Ocean Floor Morphostructure: Actualistic Model

Alexander V. ILYIN

N.N. Andreyev Acoustics Institute, Shvernik str., 4, Moscow 117036, Russia
e-mail: alexander_ilyin@mail.ru

Abstract. The ocean floor morphostructure, in its main features, is represented by two varieties—rift-geneous and volcanic blocks. The first one is characteristic for mid-ocean ridges (MORs), while the second one—for peripheral ocean areas. Both morphostructure types co-exist within the framework of uniform ocean crust, an integral process of the ocean floor spreading. Hence, the morphostructure division into two parts is an evidence of a complex evolutionary transformation of the ocean floor structure. The morphometric analysis of the rift-geneous and volcanic-block morphostructure points to a clear interrelation between structural relief parameters and the geological age of spreading centers. Values of rift zones' relief ruggedness in spreading centers of the juvenile and relatively old age can reach the relation of 1:2. According to petrology data, structural relief in MOR segments with the young spreading center is formed under the influence of intensive deep-seated volcanism, while the segments with relatively old spreading centers are formed under the influence of a tectonic factor. Morphometric characteristics of the acoustic basement relief on the MOR periphery and on ocean margins, point to a great resemblance to parameters of present-day rift zones conjugate with young spreading centers. For that reason, volcanic-block morphostructure of peripheral ocean zones can be considered as a paleoanalogue of present-day rift zones with young spreading centers. That offers a possibility to suggest an evolutionary model of the oceanic earth's crust, which will be in full conformity with the principle of actualism. Morphometric parameters and other structural peculiarities of the ocean floor change with the geological age of spreading centers. This process reflects a gradual transformation of the mainly volcanic stage of the morphostructure development into a mainly tectonic one.

Evolution of the ocean morphostructure is a direct result of the upper mantle evolution under the ocean—from rich to depleted.

Keywords: Evolution, Morphostructure, Morphometric Parameters, Spreading, Sea Floor Age, Volcanic Blocks

EVOLUTION OF THE OCEAN FLOOR MORPHOSTRUCTURE

The ocean floor morphostructure is represented by two types—rift-geneous and volcanic blocks in its main features (Fig. 1). Rift-genous morphostructure is a deeply echeloned system of rift ridges and valleys, inherited from spreading centers and rift zones of mid-ocean ridges (MORs). Volcanic block morphostructure is the combination of oceanic rises, major islands, seamounts, lava plateaus and plains, which is not directly related to present-day MORs. Rift-geneous morphostructure is typical of MORs, while the volcanic-block one is

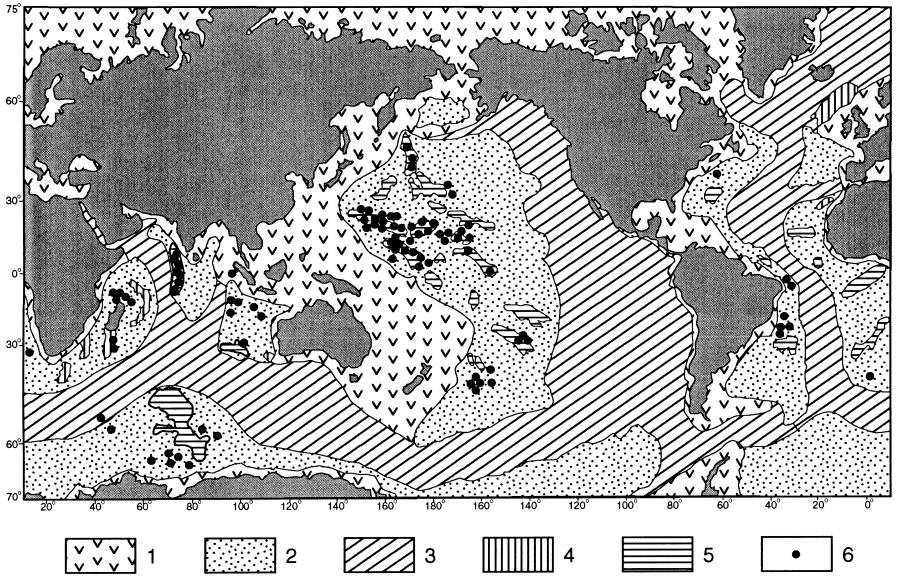


Fig. 1. The scheme of different-age ocean earth crust distribution. 1 - different-age earth crust of a continent-to-ocean transition zone; 2, 3 - earth crust of the Mesozoic (2) and Cenozoic (3); 4 - microcontinents; 5 - volcanic blocks; 6 - seamounts with flat summit.

typical for peripheral ocean areas. Both varieties of morphostructure coexist within the framework of uniform ocean crust, an integral process of ocean floor spreading. That means that the ocean floor has undergone a complex evolution in its development.

To reveal the main evolutionary stages of morphostructure one needs an effective approach to analyzing relief by means of quantitative assessments and new approaches to data interpretation. It is also necessary to make a broad correlation between data on the acoustic basement relief and other structural peculiarities of the ocean floor. The problem is in finding a common principle admitting a gradual transformation or a transfer from one type of morphostructure into another one. For this, it is necessary to make an independent analysis of rift-geneous relief on the one hand, and volcanic blocks—on the other. In each case, it is important to reveal such peculiarities of spatial variability of the structural relief that would point to general tendencies in its development. Analysis of rift-geneous morphostructure seems rather promising in this respect.

Interrelation between parameters of rift zone relief and the geological age of the MOR spreading centers engages one's attention among the variety of factors that determine the formation of rift-geneous relief (Ilyin, 2000, 2001). By the age of spreading centers we mean the geological age of oceanic basins, in which those centers exist and develop.

The Mid-Atlantic Ridge (MAR) is a classical example of different-age

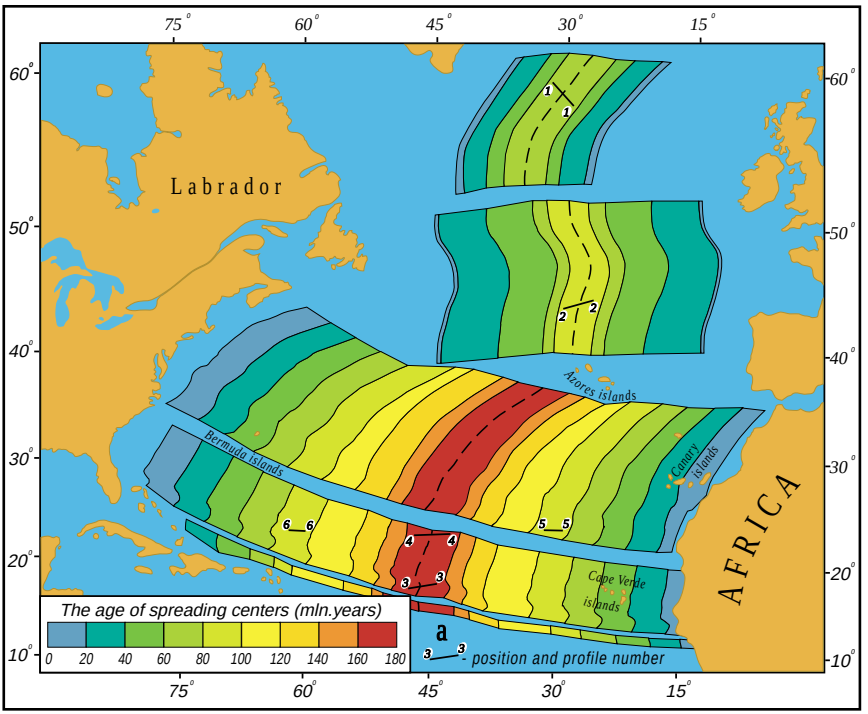
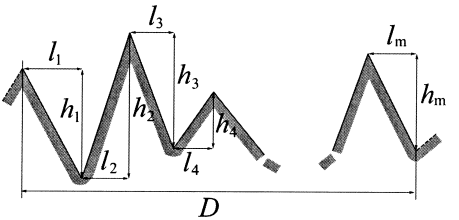


Fig. 2. Modern rifts with spreading centers started at different geological age and the sequence of the earth crust formation in the North Atlantic. The age of spreading centers is the age of plate formation after initiation of rift. a - position of echo sounding profiles, shown in Fig. 4.

prograding rifts. In the North Atlantic, it is characterized by three main segments—the Reykjanes Ridge, the Azores ridge and the tropical ridge (Fig. 2).

They are divided by major fracture zones, called demarcation transform faults (Pusharovsky, 1996). The geological age of the segments makes up respectively 60, 90 and 180 million years. The maximum age difference reaches 120 million years. Such time interval is comparable to the duration of major geological epochs and periods. For that reason, the above-mentioned segments present an ideal possibility for comparing them with each other and revealing peculiarities in the evolution of the morphostructure and the MOR geological structure on the whole.

Evolutionary changes of morphostructure can be clearly seen through comparison studies of structural relief parameters as evidenced by morphometric analysis of the three above-mentioned segments. The analysis was based on echosounding profiles running across rift zones' strike. Such analysis makes it possible to reveal the degree of relief ruggedness. Horizontal ruggedness (l) is a total of slopes' projections onto a horizontal plane. Vertical ruggedness (h) is a sum of slope projections onto a vertical plane, and shows relief amplitudes.



$$l_{mean} = \frac{1}{m}\sum_{i=1}^{m} l_i = \frac{1}{m} D$$

$$h_{mean} = \frac{1}{m}\sum_{i=1}^{m} h_i$$

Fig. 3. Definition of the horizontal (l_m) and vertical (h_m) bottom relief ruggedness.

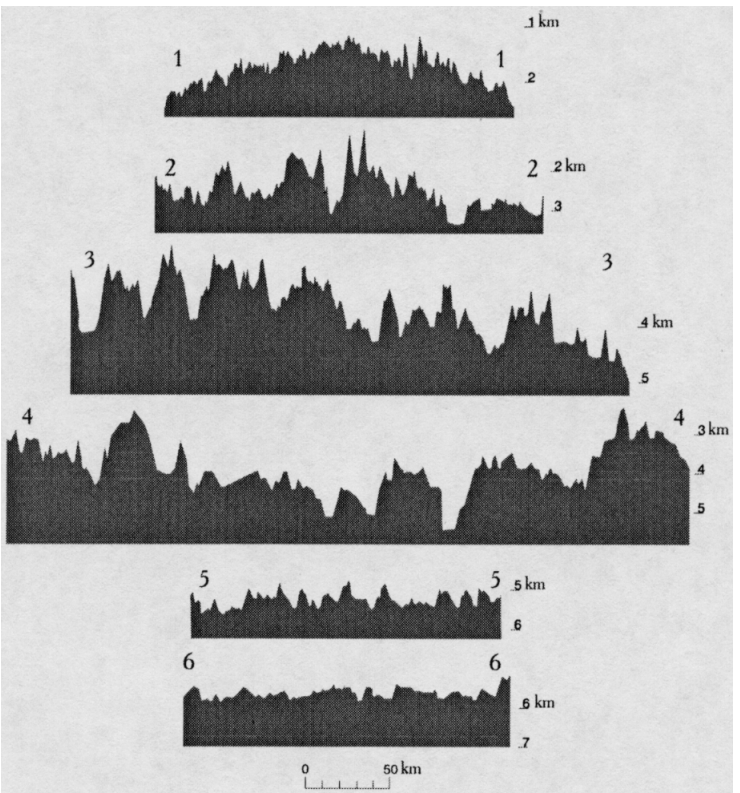


Fig. 4. Echo sounding profiles of the Mid-Atlantic Ridge rift zones. Position and profile numbers are shown on Fig. 2. Profile 1-1 was obtained in expedition of R/S "Anton Dohrn" and "Gauss" (Ulrich, 1962).

Average values of *l* and *h* are used to analyze general tendencies of the relief evolution, as they make it possible to assess general energy of relief (Fig. 3).

The morphometric analysis was made within the boundaries of magnetic anomaly 5 (Fig. 4). It is within these relatively narrow axial zones of MOR that

Table 1. Parameters of the rift zones MAR ruggedness in the North Atlantic.

Segments of MAR and echo sounding profile numbers (Fig. 2 and 4)		Geological age of the spreading center (mln. years)	l_{mean}, km	h_{mean}, m	Ages of measured portion since the born (mln. years)
Reykjanes Ridge	1-1	~ 60	2.0	180	0-20
Azores	2-2	~ 90	2.0	235	0-20
Tropical	3-3	~ 180	3.5	340	0-20
Tropical	4-4	~ 180	4.2	360	0-20
Tropical	5-5	~ 90	2.1	170	80-100
Tropical	6-6	~ 90	2.3	115	80-100

the ocean earth's crust is formed. Such zones are most representative for studying structural relief, as they are only slightly veiled by bottom sediments and represent the structural carcass of the earth's crust on the ocean floor.

The results of the analysis are shown in Table 1. It is evident that structural relief characteristics vary from segment to segment. The minimal relief energy is typical of the Reykjanes ridge's axial zone, the intermediate one—of the Azores segment, while the maximum one—of the tropical segment. Two groups of the tropical (3–4 and 5–6) are distinguished in relation to ages since the born.

Differences in the MOR relief are usually explained by the rates of the ocean floor spreading. It is commonly supposed that the maximum rate of spreading on the East Pacific Rise (EPR) forms a slightly rugged relief. At the same time, more contrasting structural relief is formed on MAR at a low spreading rate.

Data on MAR morphometry in the northern areas of the Atlantic Ocean reverse the picture. Minimal spreading rate in the Reykjanes ridge rift zone produces slightly rugged relief. An increased rate in the tropical part of the Atlantic Ocean (~2 cm a year) produces intensive and contrasting structural relief ruggedness. Moreover, in conditions of markedly polar spreading rates (about 1 cm a year on the Reykjanes ridge and up to 18 cm a year on the EPR) the relief of these MOR segments is very much the same. Apparently, the reasons behind those differences in the rift zone relief are ambiguous.

The formation of structural relief in rift zones and spreading centers comes under the influence of volcanic and tectonic processes. By their nature, volcanic processes produce smoothed forms of relief, while tectonic process produces more rugged forms. Judging by morphometric analysis results, ratio between volcanic and tectonic factors naturally changes with the change of the age of the spreading centers and rift zones. From this point of view, the present-day relief of the Reykjanes ridge was formed under the deciding influence of volcanic processes, while the relief of tropical Atlantic Ocean's rift zone—under the influence of tectonic processes. Direct relationship between parameters of relief ruggedness in the MAR rift zones and geological age of spreading centers is supported by peculiarities in the distribution of other structural characteristics,

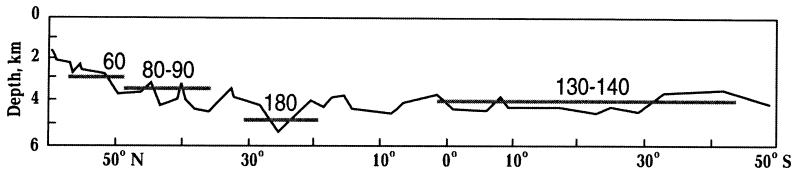


Fig. 5. Relation between MAR average depths and the geological age of spreading centers. Age in million years.

including petrological, geophysical and geodynamic. The author wishes to emphasize the volcanic effect there in addition to contraction of plate by cooling.

According to Dmitriyev (1998), there are several types of ocean basalts in the rift zone of the North Atlantic. TOR-1 type basalt is typical for the Reykjanes ridge. The same type of basalt with certain modifications prevails in the Azores sector. TOR-1 type basalts rise from the depth of 500 to 700 kilometers and get separated from the mantle at the temperature of about 1,270°C and the pressure of 8–10 kb. Differences in basalt composition are explained by the depth and intensity of magmatic processes. The most deep magmatic processes are typical of the Reykjanes ridge rift zone, which develops under the influence of powerful mantle plume. On the contrary, minimal depth and relatively weak magmatic intensity are typical for the tropical Atlantic Ocean's rift zone.

In other words, the more the mantle is enriched in chemical elements abundant at great depths, the more active it is, and the bigger amounts of volcanic basalt it brings to the ocean floor. Depleted mantle makes minimal contribution to the ocean earth's crust accretion. Such petrology data produce satisfactory explanation for peculiarities in the evolution of the rift zone relief within the above-listed segments. The poorly rugged relief of the Reykjanes ridge axial zone is a result of intensive volcanic processes that substantially suppress tectonic processes. There are suggestions that high bathymetric position of the Reykjanes ridge is in itself a result of excessive volcanism, an increase in the thickness of the earth crust's second layer (Langmuir *et al.*, 1992). On the contrary, the multiple-rugged large-block relief of the tropical North Atlantic rift zone should be considered a result of weak volcanic processes and an intensive tectonic disintegration of the earth crust.

Cumulative effect of the MAR rift zone relief evolution in the North Atlantic can be easily expressed in quantitative terms. An average bathymetric level of the Reykjanes ridge is about twice as high as the same level of the MAR tropical segment (Fig. 5). Ruggedness of the rift zone relief in those segments also has twofold parameters, as it has been shown.

There is a close correlation between geomorphologic data and data on geodynamics, seismicity, distribution of gravity anomalies and heat flow of MAR. The listed data vary along the MAR as distinctly as morphometric characteristics of the structural relief. Namely, the Reykjanes ridge is characterized

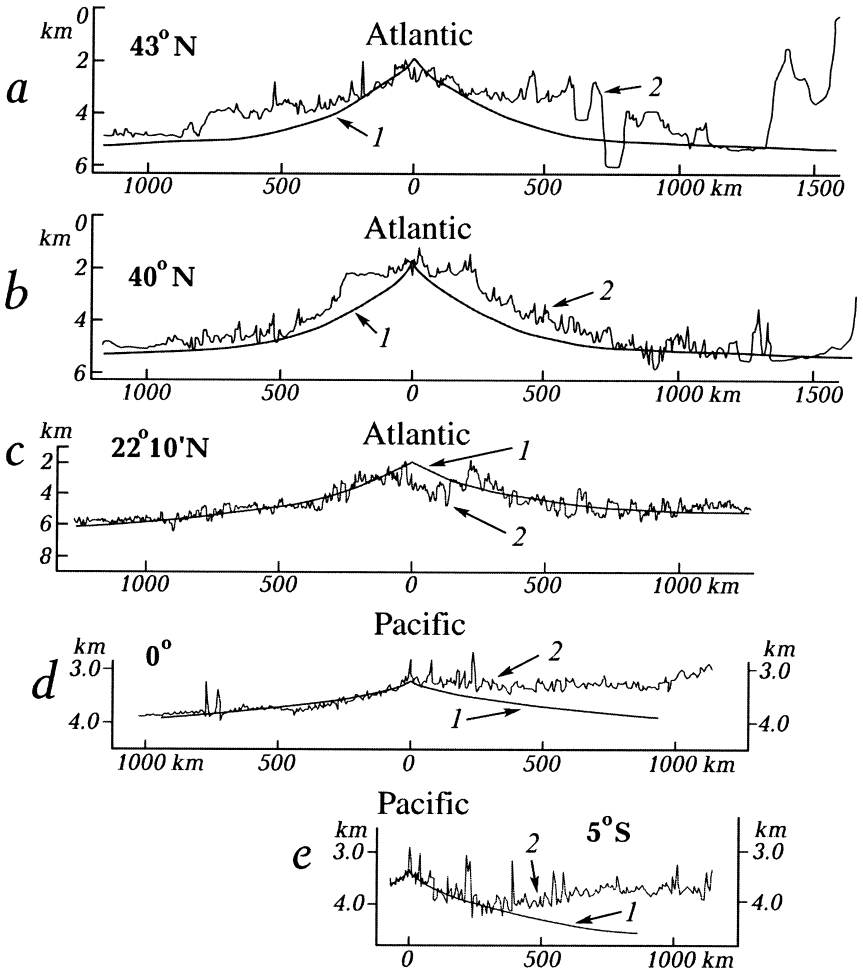


Fig. 6. Relation between the thermal contraction curve (1) and the regional component of mid-ocean ridges' relief (2) (Laughton *et al*., 1975; Lonsdale, 1977; Ilyin, 1978).

by increased free-air gravity anomalies in the free air reduction and decreased—in the Bouguer reduction. It indicates to seal failure characteristic of volcanic material accumulated there in big volumes. The pattern is absolutely different in the MAR tropical zone. Intensity of volcanism is reduced, while free-air gravity anomalies in the free air reduction have close to zero values.

Geodynamic aspect of the MOR morphostructure evolution is best of all manifested when one compares the rated curve of thermal contraction with real bathymetry. The above-listed curve results from relation $H = k\sqrt{t}$, where H stands for ocean depth, and t stands for the age of the earth crust in million years. The depth increase rate is controlled by coefficient of thermal conductivity (k) of

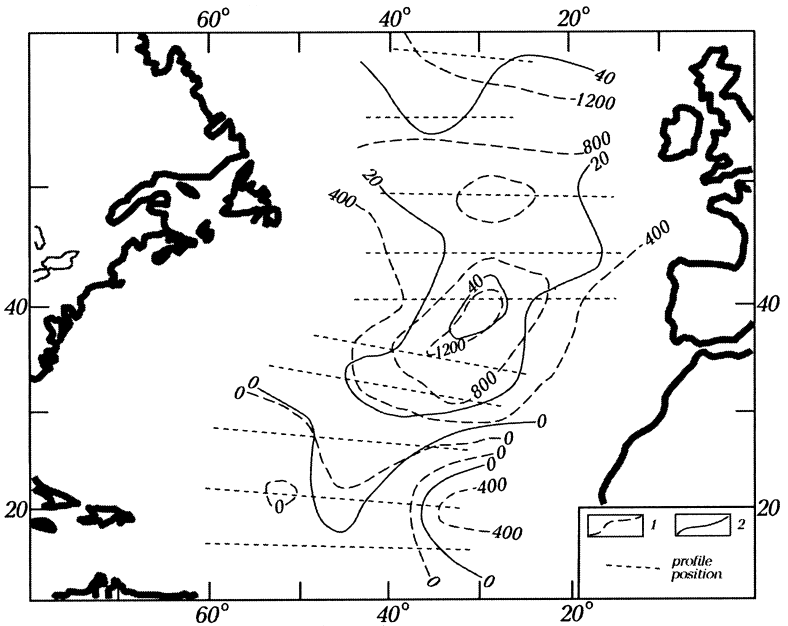


Fig. 7. Excess of the regional component of Mid-Atlantic Ridge relief over the thermal contraction curve (dotted line) and gravity anomaly in free air reduction (continuous line) (Sclater *et al.*, 1975).

rocks formed in the MAR rift zone. Under that model, the regional MOR relief is approximated by concave curve that shows a regular sinking of the earth crust as its geological age increases. The sinking results from the cooling of lithospheric plates' rear segments, moving away from the MOR spreading center.

MAR segments in the North Atlantic are characterized by different correlation between the thermal contraction curve and the existing relief, that is to say that approximation degree is different (Fig. 6). In the MAR tropical part that curve almost ideally approximates the relief of MAR flanks—from the axial zone to the foot (Ilyin, 1978). In the Reykjanes ridge area, the smoothed relief exceeds thermal contraction curve by 1,200 meters on the average. Relief anomalies characteristic of the Azores segment are somewhat less—up to 800 meters. The checking of that trend for different isochrones has shown that positive relief anomalies can reach 1,000 to 1,500 meters (Laughton *et al.*, 1975). The above-mentioned authors believe the relief anomalies come as a result of high lithospheric temperatures in the MAR area.

It is important to note that an excess of relief over the level of thermal contraction curve is in strict correlation with gravity anomalies in the free air reduction (Fig. 7). That clearly indicates that the earth crust is formed there by big amounts of volcanic matter. A different situation is typical for the MAR tropical zone, where excess of relief over the thermal contraction curve and gravity

anomalies are reduced to minimum.

The authors of the thermal contraction hypotheses consider relief and gravity anomalies a result of dynamic prop of lithospheric plates at the level of isostatic compensation that is on the border with astenosphere. It seems that both factors—high temperatures and dynamic prop of lithosphere plates are the result of an influence by anomalous mantle that generates intensive manifestation of magmatic processes on the ocean floor surface. Such phenomenon is also characteristic for EPR (Lonsdale, 1977). A sharp asymmetry of its regional form has been revealed in some pacific regions (Fig. 6). Such discrepancy between the ridge shape and the thermal contraction curve is explained by an increased volcanic productivity on the eastern flank of the elevation situated over a vast "hot spot" in the Galapagos region. The earth crust forms there a visible excess of mass over the thermal contraction curve.

The degree of MOR relief approximation to the thermal curve is directly linked with the age of spreading centers. The maximal level of approximation is characteristic of the MAR tropical part. Approximation is either incomplete or is nil in the areas of the Reykjanes ridge, the Azores segment and the equatorial Pacific, where anomalous conditions in the formation of the ocean floor structure exist. It is important to note variability of seismicity parameters along the MAR in the North Atlantic. Earthquakes with increased magnitude are more typical for tropical segments, and those with decreased magnitude are typical of the Reykjanes ridge and Azores segment.

Heat flow within MAR is characterized by major variations, but the region of increased values is situated on the Reykjanes ridge (Udintsev, 1989–1990). When one compares different groups of data, it becomes evident that there is a common factor in the ocean floor structural evolution that defines a directed development of the morphostructure, seismicity, as well as petrological, geochemical, thermal, gravimetric and geodynamic characteristics. Dmitriyev *et al*. (1999) believe that the reason behind discreteness of petrological parameters is discreteness of some external geodynamic conditions with their nature not clear yet. For these reasons different-level geodynamic situations can co-exist synchronously. Paying adequate to a cautious assessment of the reasons behind discreteness of structure-forming processes in the MOR rift zones, it is necessary to say that synchronal existence of different geodynamic situations is a regular phenomenon rather than mysterious. It manifests itself in the fact that profoundly different magmatic and other structural processes take place in modern MOR rift zones conjugate with spreading centers of the same age difference. When speaking about the age of the center of spreading we mean the age of the oceanic basin, where this center has been existent since the formation of the basin and is still active. It is the age of the spreading center that determines the duration of interaction between the earth crust and the upper mantle under the ocean. That is to say that structural processes in MOR axial zones develop under the influence of the upper mantle, which undergoes different stages of its own evolution. Long-term mantle evolution in the MAR tropical zone, where the spreading center has the maximum age of about 180 million years, has resulted in the formation there

of "cold" lithosphere blocks and segments of "dry" spreading (Bonatti *et al.*, 1993). The scale of earth crust formation in such MOR segments is considerably reduced by possibilities of depleted earth mantle. That's why the earth crust there has symbolical thickness, and the exposure of mantle rocks is fixed on the floor surface. Apparently, such correlation in magmatism intensity along the MOR strike comes because a sequential rift intrusion propagation into continental earth crust opens a "valve" into enriched mantle. It is the enriched mantle that forms highly productive plume magmatic associations at the initial stages of riftogenesis and determines all the other peculiarities of the oceanic earth crust structure.

Morphostructure, as one of the structural elements of the ocean's earth crust, evolves in the same sequence. That is to say, evolution is determined by a damping of volcanic process intensity and relative activisation of tectonic processes.

In the North Atlantic, such evolution manifests itself in the decrease of an average bathymetric level of the MAR rift zone, deepening of the rift valley that acquires a sharper morphological outline and isolation of large morphostructural blocks. That is how the MAR morphostructure develops in that region. As the geological age of spreading centers increases, tectonization and disintegration of the earth crust become the prevailing process of the relief formation.

ACTUALISTIC MODEL

If this is the case, such tendency should somehow also make itself evident across MOR. The age of the earth crust changes most quickly in that direction. However, it is difficult to make structural relief analysis in this case, as a cover of bottom sediments veils acoustic basement on MOR peripheries. Quantitative relief assessment can be made only in the regions where sediments are not thick. Such is for example the tropical MAR segment in the North Atlantic, where average thickness of the sediments' cover does not exceed 100 meters (Udintsev, 1989–1990).

Relief ruggedness parameters revealed in the area of isochrones aged 90 million years are at least twice as low as relief ruggedness of the MAR rift zone at the same latitudes (see Figs. 2 and 4). Similar results were obtained when calculations were made on morphometric indices of structural relief, buried under the sediments' cover (Fig. 8). Trans-ocean seismo-acoustic profile across the South Atlantic was used for calculation (Van Andel, 1970). Ratio between the indices of vertical ruggedness *h* on the ridge riftzone and in one of the sections of MAR's western flank, with the earth crust aged 70 to 80 million years, is about 2:1. One can trace analogy with morphometric analysis results on the MAR relief at 22°30′ N in the North Atlantic (Fig. 4, Table 1).

Progressive decrease of acoustic basement relief ruggedness towards the continental margin testifies to a transformation of the ocean floor structure relief. The rift-geneous relief component, which is so evident within axial zones and upper steps of MAR flanks, comes to the background. Volcanic block rises and islands, major volcanic mountains and plains become the prevailing relief forms.

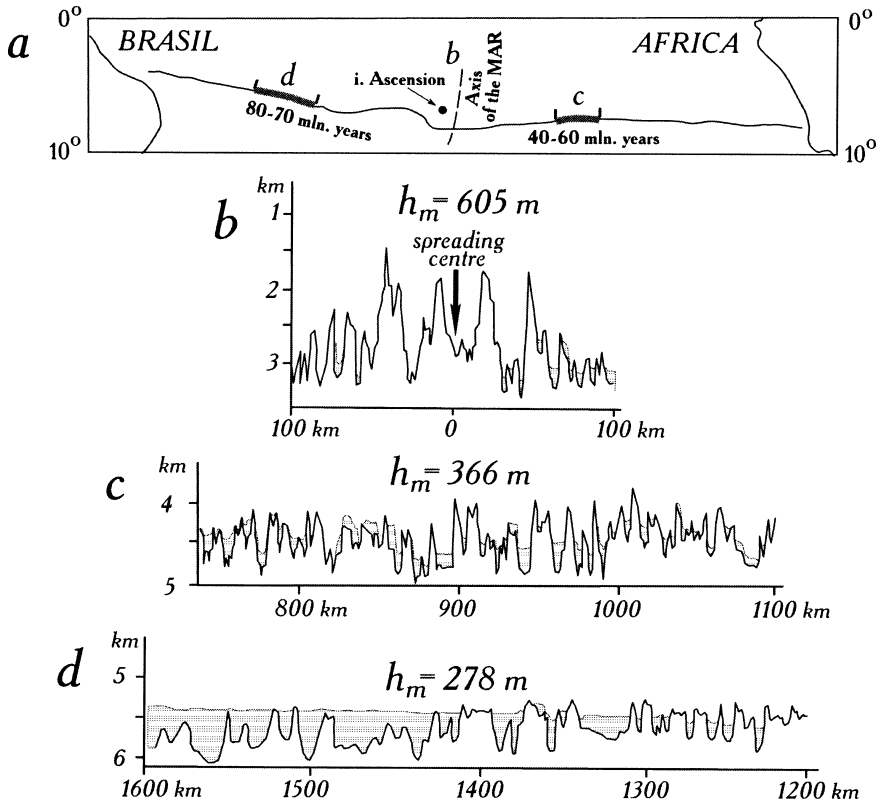


Fig. 8. Relation between the vertical structural relief ruggedness (*h*) and the geological age of the oceanic earth crust.

The influence of tectonics as a relief-forming factor weakens, ceding to versatile eruptive manifestations. The distribution of major seamounts best of all testifies to a prevailing role of volcanic factor in the earth crust formation in the deep-sea ocean floor regions as well as in those situated near the continents. Most of them are situated in deep-sea basins. The highest mountains rise from great depths. There are 50 large mountains, 4.5 to 5 kilometers high, in Pacific Ocean basins. There are no major mountains on the East Pacific rise. Similar distribution of mountains according to their size is typical of the Atlantic Ocean (Ilyin, 1976). Such regularity is confirmed by statistical mountain analysis within major regions as well as the entire World Ocean (Batiza, 1982; Marova, 2000). Oceanic rises and numerous volcanic islands are also widespread on a remote periphery of mid-ocean ridges.

Generalization of data on major seamounts and rises shows that most of them are concentrated on the Mesozoic earth crust (Fig. 1). The maximum number of mountains and rises falls on the Cretaceous period. Large mountains in the Pacific

Ocean are situated mainly in the northwestern area. The total area of the Pacific Ocean floor with Mesozoic earth crust makes up about 60 percent.

On the face of it, the existence of two general morphostructure types—riftogeneous and volcanic blocks, testifies to the absence of obviously inherited forms of sea floor structure. However, the inheritance can be traced in some hidden forms. Both morphostructure varieties have distinct geographical boundaries and specific morphological parameters. The geographical border between them generally coincides with the MOR foot, which divides the earth crust into the Mesozoic and Cenozoic. The origin of that border is one of the main objects in sea floor morphostructure studies.

According to some data, this border is marked by regional tectonic dislocations at the foot of MOR in the Atlantic and Indian Oceans, and by the Great Geological Division in the Pacific Ocean (Krasnyi, 1978; Odinokov *et al*., 1990). However, there are still questions. It is to a great extent unclear why one morphostructure variety transforms into another one. Analysis of a consistent development of the ocean floor acoustic basement structure can give an answer to that.

The initial stage of the morphostructure evolution is linked with the formation of the earth crust on the ocean periphery. The biggest volcanic clusters appeared there as dominating relief forms. It is evident that volcanism that has resulted in such grandiose relief forms, was exceptionally intensive and productive. That conclusion is first of all confirmed by seismic study data. Looking at transatlantic profiles, one can see that the 2nd and 3rd layers of the ocean's earth crust are progressively built up towards continents' borderland. They are at least twice as thick as the crust within MAR (Udintsev, 1989–1990). The East-Indian ridge structure testifies to the increased thickness of volcanic layer in the regions adjacent to the continent (Neprochnov *et al*., 2000). The upper Cretaceous stage of trappean magmatism is registered in the development of the East-Indian ridge. It resembles continental trappean magmatism in intensity and geochemical characteristics (Kashintsev *et al*., 2000). Geochemical data testify to the decrease of magmatism intensity with time (Rundkvist *et al*., 1998). An intensive volcanic activity at the early stage of the ocean crust formation is confirmed by evolution of foraminifera types variety in the late Phanerozoic (Lukashina, 2000). According to other parameters, Jurassic and Cretaceous lithosphere of the ocean floor radically differs from MOR lithosphere. Vast floor areas are characterized by zones of calm magnetic field. Where it is possible to identify linear magnetic anomalies, they have local occurrence. Short "snatches" of anomalies, often of a non-inversion type, are characteristic for the Mesozoic earth crust of the entire World Ocean (Karasik *et al*., 1981; Gurevich *et al*., 1987). Comparison between Mesozoic and Cenozoic magnetic anomalies shows that the rates of the floor spreading are twice as high in Cenozoic ones. That means that with the present-day spreading rates in the tropical segment of the North Atlantic (up to 3 cm a year), spreading rate at the same latitude in the Mesozoic period was 1–1.5 cm a year. Such spreading rates contributed to accumulation of already gigantic volumes of volcanic matter per unit area.

In that respect data on the Pacific Ocean are most representative. High

volcanic activity was typical of the periods covering 110–95 million years and 80–65 million years. In comparison with other time periods volcanic intensity in those periods was significantly higher (Rea and Vallier, 1983). Then major volcanic rises of the western Pacific formed on the area of 30 million square kilometers. The volume of volcanic piling was so great that Cretaceous epicontinental transgression is now linked with their formation. Similar picture is characteristic of the Atlantic and Indian Oceans, where most major seamounts and rises appeared within the Cretaceous period. Iceland, the Azores and the Galapagos Islands are a modern analogue of intensive Cretaceous volcanism.

Composition of Mesozoic volcanic rock was also different as compared with MOR rock. Apatite-type rock enriched with phosphorus has been located in the Marcus-Necker arch area. Abyssal alkaline magmatic processes are typical of many other areas, in particular the Cape Verde Islands in the Atlantic Ocean (Pusharovsky, 1990). Some samples of potassic rock have been retrieved from the Reykjaness Ridge (Kharin and Chernysheva, 1997; Kharin, 1999).

Judging from the analysis of potassic nephelinites in the central basin of the Pacific Ocean and the volcanic chain of the Line Islands Natland (1973) has related them to the rock typical of the areas characterized by slow opening, such as African rifts. He believes that the bottom area from the Line rise to the Wake atoll may be at all coeval, that is having no signs of horizontal displacement. Such situation contributed to accumulation of grandiose volcanic masses, so typical of the central Pacific Ocean.

According to DSDP materials, episodes of powerful volcanism are particularly characteristic of the period covering 110–90 Ma and 80–65 Ma million years. However, volcanic processes were also rather productive in other Mesozoic time intervals (Winterer, 1973). In effect, the World Ocean undergoes a continuous stage of intensive volcanism. With due regard for the stages fixed by geophysical data, it covers the period of up to 100 million years.

The totality of morphostructural, geophysical, petrologic, paleonthological and geodynamic data suggests that the ocean's earth crust on MOR periphery drastically differs from the earth crust of MOR itself. It was formed by more deep-seated high intensity magmatic processes, not typical of many MOR areas. It is obvious that the principle of bottom structure inheritance on ocean periphery from MOR spreading centers is not observed. It becomes particularly obvious if one compares volcanic block relief of those regions and MOR's rift-geneous relief.

A "hot spot" hypothesis is sometimes used to smoothen the above contradictions. However, that concept does not produce necessary effect, as gigantic isometric areas of sea mountains and rises reaching thousands of kilometers in width go beyond the border of linear volcanic structures created by "hot spots". The width of volcanic relief belts formed by "hot spots" should not exceed 300 kilometers (Epp, 1984).

Before making an attempt to reveal a general tendency in the formation of morphostructure of major volcanic mountains and rises on the ocean periphery, one should note that from the point of view of ocean floor spreading, the split of

continents in the Jurassic-Cretaceous period predetermined two types of earth crust—continental and oceanic. All processes of the morphostructure formation as well as the formation of the entire geological structure in the present-day World Ocean took place within the framework of oceanic earth crust. An assessment that oceanic earth crust blocks could be formed as a result of continental earth crust contamination can be accepted with reservation. It seems likely that the process of continental crust contamination was restricted within the early stages of the ocean crust formation.

Three such stages are usually considered. The first one is linked with the rise of mantle matter and the thinning out of continental earth crust. The second one is characterized by rifting accompanied by earth crust rupture as well as the sinking and upthrusting of separate blocks. The third stage is characterized by a complete split of continents and marks the beginning of an independent existence of oceanic earth crust (Pegrum and Mounteney, 1978). In line with such division, the first two stages should be considered as preparatory for a final split of continental crust. It is believed that those stages may have continued for about 20 million years (Nairn and Stehli, 1974). At that stage, continental lithosphere was stripping and breaking open. It was broken by numerous rift cracks spreading out in different directions. In other words, there was no single spreading center, and the spreading was dispersed. An intensive contamination of the continental earth crust with the splitting of separate fragments by most developed rifts was one of the major events at that stage. The Rockoll Rise in the Atlantic Ocean, separated from the continent by an early-Cretaceous rift situated at the site of the present-day Irish basin, is a vivid example of such separation. That rift existed until the Eocene, when a new rift became active west of the Rockoll Rise, and an entire block of continental crust found itself between two blocks of oceanic earth crust (Laughton, 1975). However, examples of continental earth crust contamination are still exceptionally rare. They are not found in structures, which, in view of their proximity to continents, should have contained continental rock. In particular, geochemical research data on the Cape Verde Islands show the absence of continental rock contamination, as no xenoliths or any other indications of continental earth crust have been found there (Pusharovsky, 1990). No fragments of continental rock have been found in the super-thick oceanic crust of the Agulhas Plateau (Uenzelman *et al*., 1999).

One may anticipate that the most likely contamination of the earth crust in the central North Atlantic could take place on the ocean floor between the present-day coastal line and anomaly M 25, identified in eastern and western parts of that region. A final split of the continental or sub-continental crust, the appearance of oceanic type crust and stable linear spreading center are linked with anomaly M 25.

From the point of view of ocean floor spreading, rift-geneous relief of acoustic basement exists everywhere—from continents' boundaries to present-day MOR spreading zones. However, volcanic blocks dominate on the ocean periphery. They suppress tectonic relief that was formed in MOR rift zones. A prevailing role of volcanic process in the formation of structural relief outside

present-day MORs becomes apparent if we compare independent data on the ocean floor structure. According to data received in morphological, geodynamic, petrological, geochemical, geophysical and paleonthological research, volcanism was most intensive and productive on ocean periphery. Volcanism was gradually loosing strength with distance from continents' margin. Such a clear tendency in volcanism evolution gives grounds to assume the same evolution of the upper mantle.

At the rifting or dispersed rifting stage, enriched continental mantle initiated a powerful deep-seated and possibly plume volcanism. The influence of enriched mantle continued even after a final splitting of continents and the formation of oceanic earth crust. It was so effective that major volcanic massifs and mountains were appearing on the ocean crust much later after it had finally formed. The new earth crust was becoming a stable foundation for younger volcanic constructions.

Cretaceous stage volcanoes can be encountered within Jurassic crust of the Pacific Ocean floor, while Cenozoic stage ones can be encountered on Cretaceous crust (Heezen and Fornari, 1975). A typical example of intra-plate volcanism in the Atlantic is the Bermuda rise, which appeared 40 to 50 million years ago on the crust aged about 120 million years. Volcanic and tectonic processes created there a powerful basalt layer, several times thicker than standard oceanic crust (Udintsev, 1989–1990).

Gigantic rises and sea mountains could appear only on thick solid lithosphere that formed long before they appeared. Such volcanic massifs cannot exist directly in the rift zone, because according to isostatic models, the young ocean crust cannot serve as a safe mechanic prop for them (Vogt, 1974). Zones of MOR's triple junctions where the earth crust of increased thickness is formed are an exception. Here, we can cite areas of Island, the Azores, the Bowe Island and a vast area of the North Atlantic, between 12° and 20°N.

If we consider physical models which describe processes of intra-plate rises formation, concepts about spontaneous and localized deep-seated intrusions seem to be promising (Sychev *et al*., 1993).

In conclusion, it is worth noting that the ocean morphostructure, like the entire earth crust, is formed by the processes of the ocean floor spreading. Riftogeneous relief is found everywhere. At the same time, it was considerably, we can even say radically, transformed by volcanic processes in areas situated close to continents and in deep basins. Volcanic relief forms dominate and form volcanic-block structure. It is the degree in which volcanic or tectonic processes dominate that determines the morphostructure type. Taking present-time rift zones with spreading centers of different geological age as an example, one can see how volcanic processes subdue tectonic manifestation in the Reykjanes ridge and the Azores rift zone. On the contrary, tectonics plays a determining role in the central North Atlantic, where the spreading center is relatively old.

It is not difficult to imagine that a massive volcanic morphostructure of islands, oceanic rises and big sea mountains on the ocean periphery is a paleoanalogue of volcanic blocks in contemporary rift zones conjugate to geologically young spreading centers. That analogy completely fits into the

actualistic model of the ocean floor morphostructure evolution (Ilyin, 2001).

In other words, the existence of two general morphostructure types is not linked with radical differences in the ocean earth crust structure, but it reflects a change over from the mainly volcanic stage of the morphostructure evolution to the mainly tectonic one. The very evolution of the oceanic morphostructure is a direct result of an evolution of upper mantle under the ocean. A long-term transition period from enriched mantle to its depleted state has determined the existence of two main morphostructure types, as well as the entire geological structure of the ocean floor.

Acknowledgements—The author is grateful to Sergey Averianov for preparing the illustrations and the text for publication.

REFERENCES

Batiza, R. (1982) Abundances, distribution and sizes of volcanoes in the Pacific Ocean and implications for the origin of nonhotspot volcanoes: *Earth and Planet Sci. Lett*., **69**, 195–206.

Bonatti, E., Seyer, M. and Sushevskaya, N. M. (1993) A cold suboceanic mantle belt at the Earth's equator: *Science*, **261**, 315–320.

Dmitriyev, L. V. (1998) Variations in the composition of mid-ocean ridge basalts as the function of geodynamic situation and their shaping: *Petrology*, **6**(4), 340–362 (in Russian).

Dmitriyev, L. V., Sokolov, S. Y., Melson, V. G. and O'Hirn, T. (1999) Plume and spreading association of basalts and their reflection in petrological and geophysical parameters of the northern Mid-Atlantic Ridge: *Russian Magazine on Earth Sciences*, **1**(6), 15–33 (in Russian).

Epp, D. (1984) Possible perturbations to hotspot traces and implications for the origin and structure of the Line Islands: *J. Geophys. Res*., **89**(B13), 11273–11286.

Gurevich, N. I., Sokolov, B. A. and Lovchikova, T. L. (1987) Certain features of the Pacific Ocean's central basin evolution based on magnetometric data: In VIEMS' Publication of Express Information, *Marine Geology and Geophysics*, Issue 2, pp. 1–13 (in Russian).

Heezen, B. C. and Fornari, D. J. (1975) Geological Map of the Pacific Ocean: *Init. Rep. DSDP*, **30**.

Ilyin, A. V. (1976) *Geomorphology of the Atlantic Ocean Floor*. Science, Moscow, 232 pp. (in Russian).

Ilyin, A. V. (1978) Morphostructure of the ocean floor and some questions of new global tectonics: *Geotectonics*, **6**, 17–35 (in Russian).

Ilyin, A. V. (2000) Actualistic model of the ocean floor relief evolution: *Reports of the Academy of Sciences*, **371**(1), 70–74 (in Russian).

Ilyin, A. V. (2001) Actualistic model of the ocean floor relief evolution: *Special Publication of the Geographic Information Systems Association*, **1**, 6–7.

Karasik, A. M. and Sochevanova, N. A. (1981) Axes of magnetic anomalies on the World Ocean water area. Collection of articles: *Electromagnetic Studies of the Earth Crust and the Upper Mantle in Ocean and Seas*, pp. 205–212. IZMIRAN, Moscow (in Russian).

Kashintsev, G. L., Neprochnov, Y. P. and Grinko, B. N. (2000) Genesis and evolution of the East-Indian Ridge: *Oceanology*, **40**(6), 901–906 (in Russian).

Kharin, G. S. (1999) Periodicity of magmatic rock transformation and ocean lithosphere formation: *Petrology*, **6**, 611–630 (in Russian).

Kharin, G. S. and Chernysheva, E. A. (1997) Tuffs of alkaline pikritoides in the transition zone of the Reykjaness Ridge (North Atlantic): *Reports of the Academy of Sciences*, **357**(1), 112–116 (in Russian).

Krasnyi, L. I. (1978) On great Pacific geological division: *Reports of the Academy of Sciences*, **242**(5), 1148–1151 (in Russian).

Langmuir, C. H., Klein, E. M. and Plank, T. (1992) Petrologic systematics of Mid-Ocean Ridge Basalts: Constraints of melt generation beneath ocean ridges: In J. P. Morgan *et al*. (eds.),

Mantle Flow and Melt Generation at Mid-Ocean Ridges, pp. 183–280. AGU, Washington., D.C.
Laughton, A. S. (1975) Tectonic evolution of the Northeast Atlantic Ocean: Review. *Norges Geol. Unders*, **316**, 169–193.
Laughton, A. S., Roberts, D. G. and Graves, R. (1975) Bathymetry of the Northeast Atlantic: Mid-Atlantic Ridge to Southwest Europe: *Deep-Sea Research*, **22**(12), 791–810.
Lonsdale, P. (1977) Regional shape and tectonics of the equatorial East Pacific rise: *Marine Geophys. Res*., **3**(3), 295–315.
Lukashina, N. P. (2000) Volcanic activity in oceans and foraminifer evolution in the late Phanerozoic on the example of the North Atlantic: *Oceanology*, **40**(1), 97–103 (in Russian).
Marova, N. A. (2000) Main peculiarities of volcanic sea mountains' distribution in the World Ocean: *Reports of the Academy of Sciences*, **375**, 249–251 (in Russian).
Nairn, A. E. M. and Stehli, F. G. (1974) A model for the North Atlantic: In A. E. M. Nairn and F. G. Stehli (eds.), *The Oceans Basins and Margins, 2, The North Atlantic*, pp. 1014. Plenum Press, New York.
Natland, J. H. (1973) Petrology of volcanic rocks dredged from seamounts in the Line Islands: *Init. Rep. DSDP*, **33**, 749–787.
Neprochnov, Y. P., Grinko, B. N. and Ganzha, O. Y. (2000) East-Indian Ridge earth crust structure: *Oceanology*, **40**(1), 85–96 (in Russian).
Odinokov, Y. Y., Udintsev, G. B. and Beresnev, A. F. (1990) Peculiarities of the Mid-Atlantic Ridge edge dislocation zone morphology: *Geotectonics*, **1**, 97–103 (in Russian).
Pegrum, R. M. and Mounteney, N. (1978) Basins Flanking North Atlantic Ocean and Their Relation to the North Sea Area: *Am. Assoc. of Petroleum Geologists Bull*., **62**(3), 419–441.
Pusharovsky, Y. M. (ed.) (1990) *Tectonics and Magmatism of the Cape Verde Islands*. Science, Moscow, 246 pp. (in Russian).
Pusharovsky, Y. M. (1996) Comparative tectonics of the Atlantic and Indian oceans: *Geotectonics*, **5**, 3–14 (in Russian).
Rea, D. K. and Vallier, T. L. (1983) Two Cretaceous volcanic episodes in the western Pacific Ocean: *Geophys. Soc. Am. Bull*., **94**, 1430–1437.
Rundkvist, D. V., Ryakhovsky, V. M., Mironov, Y. V. and Pustovoi, A. A. (1998) Direction and rhythm of the global development of the World Ocean magmatism: *Reports of the Academy of Sciences*, **363**(4), 523–526 (in Russian).
Sclater, J. G., Lawver, L. A. and Parsons, B. (1975) Comparison of long wavelength residual elevation and free air gravity anomalies in the North Atlantic and possible implications for the thickness of the lithospheric plate: *J. Geophys. Res*., **80**(8), 1031–1052.
Sychev, P. M., Soinov, V. V., Veselov, O. V. and Volkova, N. A. (1993) Isostasy of arched uplifts, ridges and sea mountains: thermal models: *Pacific Geology*, **1**, 3–15 (in Russian).
Udintsev, G. (ed.) (1989–1990) *International Geological and Geophysical Atlas of the Atlantic Ocean*. Moscow, 124 pp. (in Russian and English).
Uenzelman, N. G., Gohl, K., Erhardt, A. and Seargent, M. (1999) Agulhas Plateau, SW Indian Ocean evidence for excessive volcanism: *Geophysical Abstracts*, **9**(6), p. 3.
Ulrich, J. (1962) Echolotprofile der Forschundsfahrten von F.F.S. "Anton Dohrn" und V.F.S. "Gauss" im Internationalen Geophysikalischen Jahr 1957/1958: *Erg nzungsheft Reihe*, **B-40**(6) zur Deutschen Hydrographischen Zeitschrift, 194–240.
Van Andel, T. H. and Heath, G. R. (1970) Tectonics of the Mid-Atlantic Ridge, 6–8° South Latitude: *Marine Geophysical Researches*, **1**, 5–36.
Vogt, P. R. (1974) Volcanic height and plate thickness: *Earth and Planet Sci. Lett*., **23**(3), 235–253.
Winterer, E. L. (1973) Bathymetry and regional tectonic setting of the Line Islands Chain: *Init. Rep. DSDP*, **33**, 731–747.

Concepts and Modelling in Geomorphology: International Perspectives,
Eds. I. S. Evans, R. Dikau, E. Tokunaga, H. Ohmori and M. Hirano, pp. 61–84.
© by TERRAPUB, Tokyo, 2003.

Scale-Specific Landforms and Aspects of the Land Surface

Ian S. EVANS

Earth Surface Systems Research Group, University of Durham, England;
Department of Geography, Science Laboratories,
South Road, Durham, England DH1 3LE, U.K.
e-mail: i.s.evans@durham.ac.uk

Abstract. The land surfaces of Earth, of other planets and of moons show both scale-specific and scaling behaviour. Size and spacing of landforms often show clustering around characteristic scales or between limits related to process thresholds or to the space available. This is clearest for various bedforms, in dynamic equilibrium with the last dominant flow or several flows. It is also clear for glacial cirques and for some types of landslides, sinkholes, abyssal hills and volcanoes.

Strong scale-specificity as in cirques may be global. Weaker forms of scale specificity are also recognised, limited by either material or process variations to regions or to locales. The implications of global, regional and local scale-specificity are explored. Even the weaker forms of scale-specificity are not expected on surfaces generated by fractal models.

The contrast between efficiency of surface flow and of consistently channelled flow imposes a lower characteristic scale (length of slope, drainage density) on fluvial erosional topography. The most common horizontal scales observed in the Earth's topography are (1) tens or hundreds of m for slopes to (minor) streams; (2) km for major slopes, relevant to deep bedrock landsliding; and (3) tens to hundreds of km for broader tectonic and volcanic relief features. The internal properties of the Earth's lithosphere and mantle impose limits to relief.

Scaling may involve statistical self-similarity or self-affinity (fractal behaviour) over a few orders of magnitude, but is bounded by both upper and lower limits. Scaling is also found, over more limited ranges, for the characteristics of scale-specific features such as cirques and dunes. Scaling may be isometric (constant shape) or allometric (shape changes with size). Clear thresholds in the impact cratering process give changes in morphology and breaks of slope in depth: diameter scaling plots; these vary in orderly fashion between different planets and moons. Given the number of scale thresholds evident in geomorphology, it is dangerous to use scaling relationships for extrapolation beyond the data on which they are based.

Keywords: Fractal, Scaling, Relief, Bedforms, Landslides, Cirques, Craters

INTRODUCTION

The scale-specific nature of the land surface cannot be denied: nor can the scaling relationships between geometric attributes over certain ranges. Wherever landforms can be defined, there is an upper and a lower limit to their size. At the least the upper limit is less than the whole Earth and the lower limit is greater than

sedimentary grain size. Taken globally, features such as river channels, landslides, alluvial fans and volcanic cones cover broad ranges of size, but others such as cirques, drumlins and dolines cover narrower ranges, typically one decimal order of linear magnitude—a factor of 10 difference between the widest and the narrowest. The geomorphometry of specific landforms often demonstrates specific scales, especially for equilibrium forms (mainly bedforms). Non-equilibrium forms, by definition growing or decaying, are likely to cover broader size ranges, but they too are limited by thresholds.

Most landform sizes and spacings show large numbers of small values and smaller numbers of large ones. Thus it is natural to view them on logarithmic scales, and to consider their log-normality—their fit to the log-Gaussian probability distribution. Among the many right-skewed unimodal models for frequency distributions, the main simple alternatives to the log-normal are the exponential and Pareto (power function) distributions, where the most frequent values are at the lowest magnitude. The distribution at middle to high values may differ little between the three models: thus large data sets are needed to provide discrimination, but these are infrequent even today. Johnson *et al.* (1994) provided comprehensive information on all the distribution models considered here: Cox (1992) discussed the use of probability plots in choosing between right-skewed distributions (specifically the exponential and gamma). What is most crucial in distinguishing the log-normal is the existence of a left-hand declining limb, so that on a log scale of magnitude the smaller values are of declining frequency. Testing this requires careful consideration of completeness of inclusion of smaller values, since a phased truncation or censoring of the data might create a spurious declining limb.

It may be misleading to consider the global distribution of sizes. Although cirques are globally scale-specific, there are other landforms which are scale-specific in a given region or locality. Lineation and streamlining are usually associated with scale-specificity. Landforms such as yardangs (streamlined forms eroded by the wind) are locally similar in size, but vary tremendously between areas, mainly because they are eroded into different materials over different time-spans.

Scale-specificity involves not only size frequency distributions, but also breaks in slope in power and other plots which otherwise exhibit fractal-like scaling. Such breaks relate to process thresholds, whereas size limits may reflect either thresholds or constraints on the space available. When a threshold is crossed a new feature emerges, such as a slip face in a pile of aeolian sand, or a central peak in an impact crater. Such thresholds limit positive feedbacks (from form to process and back) that would produce runaway, scale-free forms. Negative feedbacks, on the other hand, directly provide limits to the scale of landforms. Thus scale-specificity is found in both exogenetic and endogenetic process—form relationships, and on both moons and planets.

Landform scale-specificity and scale-dependency is recognised by geomorphologists either implicitly or explicitly (Evans, 1972; Wood, 1996; Wilson and Gallant, 2000, p. 31). One may wonder at the necessity for a review

such as this; but many other scientists and engineers are now concerned with the land surface as represented in Digital Elevation Models and find scale-free fractal models a seductive approach. Hence there is a need to be explicit, to compile and to analyse hard evidence for scale-specificity. Here we first consider scale-specificity in bedforms (aeolian, fluvial and glacial), then in some specific erosional forms (glacial cirques, karst sinkholes, landslides and fluvial slopes) and finally in tectonism, isostasy, volcanoes and meteorite impact craters. It is not possible to be comprehensive, but consideration of contrasting process-systems provides revealing comparisons. Specific scales are shown to be related to thresholds or to space constraints.

AEOLIAN BEDFORMS

Both yardangs and dunes are aeolian bedforms, formed by the interaction of a fluid current with erodible and transportable land surface material. Mini-yardangs, of centimetric scale, form rapidly on sandy beaches as initially wet sand dries and is eroded by moderate wind. Yardangs form over centuries when lake sediments dry out and are eroded by unidirectional winds: those in Egyptian lake sediments at Kharga are 0.5 to 8.7 m high (Goudie, 1999). In the Holocene diatomites of Chad, their crests are spaced (transverse wavelength) 20 to 50 m apart (Mainguet, 1972, plates LXXIV and LXXVI). Nearby crests and corridors in Palaeozoic sandstone have a 1.6 km spacing and can be considered as long mega-yardangs: illustrations in Hagedorn (1971, Abb. 74–82) show that the long ridges grade into shorter yardangs and are sometimes oblique to structure. The landscape is dominantly aeolian and implies that the Northeast Trades have been stronger and persistent through much of the Quaternary, amplified by deflection around the Tibesti massif. The lake sediments with yardangs penetrate the corridors between the mega-yardangs (Mainguet, 1972), but there are no intermediate features. Yardangs are not found on the backs of the larger features, and they do not have mini-yardangs on their sides or tops: the microrelief is quite different from the broader form (Whitney, 1983). Apart from the relation to material erodibility, it is hard to explain the variation in yardang size, and its regional regularity. Yardangs are found even in resistant granites and marbles in Egypt.

Mini-yardangs are superimposed on beaches that are smooth for hundreds of metres. Thus none of these landscapes can be described as self-similar or fractal: they are ordered, and their scale is clear. The yardang family as a whole is not globally scale-specific except in its upper size limit: it is, however, locally or regionally scale-specific. It can also be found on other planets. Greeley and Iversen (1985, pp. 143–144) illustrate some very regular lineations in the equatorial regions of Mars, which are likely to be due to wind erosion. Their transverse spacing is 2 km in the western Tharsis region (about 92 ridges in 181 km) and 280 m in the Aeolis region (46 in 13 km).

Among aeolian landforms, the regularity of sand dunes is well known (Cooke *et al.*, 1993), although size and spacing do vary regionally and some

'hierarchies' are recognised. At the edge of a dune field, the change in surface properties is abrupt. Sand dunes are often superimposed at two different scales. In a given region, however, both dunes and megadunes (draa) of a particular type vary little in height and spacing (Lancaster, 1988). Where dunes are superimposed on draa, there is an order of magnitude difference in scale between the two (Lancaster, 1988, figure 2). There is a clear gap in size and spacing between the two types, and some qualitative differences between dunes and draa, so the relationship is not gradational. Both the dunes and the draa are regionally scale-specific, each covering half an order of magnitude or less. The contrast between them is strongest in the time taken to move one wavelength: this is three orders of magnitude greater for Namib draa than for their superimposed dunes.

Desert dunes are spaced hundreds of metres apart, up to several km. Considering transverse and longitudinal dues in the northern Sahara, Wilson (1971, 1972) distinguished dunes, with wavelengths of 3 to 100 m, from draa (megadunes) with wavelengths of 300–5500 m. He maintained (1972, p. 185) that ripples, dunes and draa are distinct, and do not grow or shrink into one of the other two. For each, the greater wavelengths are in coarser sand, so that for a given material the ranges of wavelengths are well under one order of magnitude. Apparently this relationship is regional: later workers such as Wasson and Hyde (1983a, b) and Lancaster (1988) did not find a general relation between dune spacing and grain size in Australia or southern Africa.

Within ten different regions and dune types, spacing varies less than an order of magnitude (Lancaster, 1988, figure 1). Simple barchan dunes are mainly 1–12 m high and 25–100 m wide: or, according to Allen (1982, vol. 1, p. 320), "Most barchans have a height of 2–20 m and are usually homogeneous in scale within any one area." Not only are they scale-specific, but also within their limited size range their shape changes systematically with size. A slip face is formed when a dune reaches a threshold height, of the order of a metre. In larger barchans, the slip face and the horns become relatively more important (Sauerman *et al.*, 2000).

A full survey of Australia's desert dunes, which are mainly linear and without draa, shows a mean transverse spacing of 560 m (mode 270 m) (Wasson *et al.*, 1988, figure 10). The cores of most dune-fields show spacings less than 300 m. Greater spacings are most common on coarser sands, toward the periphery of dune-fields.

Star dunes are among the highest: in some regions they show two clear scales, an order of magnitude apart. In the Namib Desert, their heights are unimodal and mainly 50–200 m; widths are 400–1000 m and spacings 600 to 1800 m, averaging 1330 m. Comparative figures for a range of studies on different continents, by different authors, are height mainly 50–350 m, width 200–3000 m, and spacing 160–4000 m (Lancaster, 1989). Thus star dunes are scale-specific, especially regionally. They develop under multidirectional winds, with abundant sand supply but little net movement: seasonal variations in sand flow cancel out.

Dunes in general are at least regionally scale-specific in their dimensions and spacings. The lower size limit reflects the ease with which small sand patches are dissipated. Upper limits to height may reflect exposure to greater wind forces.

GLACIAL AND FLUVIAL BEDFORMS

Currents in water and in ice also produce bedforms, which tend to be lineated or streamlined as well as scale-specific. Fluvial and marine dunes, antidunes and sand waves cover at least two orders of magnitude, but their dimensions increase with depth of current (Allen, 1982 vol. 1, pp. 331–334, 410 and 456) and are thus locally scale-specific.

Drumlins and flutings form beneath glaciers, and sand ribbons and sand waves form on continental shelves. Drumlins have regionally consistent spacings, heights and widths, although lengths are more variable. Mean widths in 17 drumlin fields studied by Mills (1987) in the USA were between 110 and 437 m (mainly 200 to 360 m): studies in Europe extend this range of means to 128 to 755 m. Mean height varied only from 6 to 24 m in the USA study, but from 4 to 52 m in European studies. For individual drumlins, the overall width ranges over one order of magnitude; drumlins can be regarded as globally scale-specific. There are trends in size and shape within drumlin fields, so that locally drumlins are highly scale-specific. In some areas, drumlins merge into more elongate fluting forms: in Alberta, these have transverse wavelengths around 100 or 200 m (Gravenor and Meneley, 1958) whether in bedrock, till or water-laid sediments.

At a different scale, the flutings observed on many glacier forelands show striking regularity as well as parallelism. For example, those in front of one Norwegian glacier are around 0.3 m high (range 0.07 to 1.13) and 3 m wide (range 0.5 to 9.7) (Gordon *et al.*, 1992, pp. 717–718). These are unlikely to show transitions to drumlins or the related large flutes. They may relate to deforming debris-rich basal ice, rather than to deforming sediments.

Bedforms of mobile material, such as dunes and many drumlins, are limited in size either by the negative feedback of stronger currents at the crests of higher forms, or by instabilities tending to split them more often than merging them.

GLACIAL CIRQUES

A different category includes erosional features such as landslides, dolines and glacial cirques, none of which are bedforms. Evans and McClean (1995) demonstrated scale-specificity in glacial cirques, and their evidence is extended in Table 1 to four large data sets. Cirque lengths and widths approximate Gaussian distributions on the logarithmic scales that are appropriate to most size measurements. The reduction of skewness to near zero confirms the appropriateness of the logarithmic scale, and the similarity of median and geometric mean confirms symmetry on that scale. The consistently low standard deviations (SD) demonstrate strong regional scale-specificity; the range within each region is only one order of magnitude. Means vary little, supporting the concept of cirques as globally scale-specific. Evans and McClean (1995, table 1) gave logarithmic (base 10) standard deviations, all of them low, for further size measures, six in all.

The minimum size is related to thresholds for glacier formation: the maximum, to available space on slopes or at valley heads. Width across a valley head is more obviously limited than length downvalley, yet both width and length of cirques

Table 1. Length and width of Glacial Cirques. The geometric mean, the antilog of the mean on the logarithmic scale, is the most appropriate measure of central tendency for frequencies that are log-normally distributed.

Range	*N*	$\log_{10}$ *scale*		*median*	*geometric*	*skewness:*	
		mean	*SD*		*mean*	*initial*	$\log_{10}$ *scale*
CIRQUE LENGTH :							
Bendor , B.C.	186	2.87	0.186	735 m	741 m	1.42	0.10
Cayoosh, B.C.	198	2.85	0.206	670 m	708 m	1.67	0.04
Wales (provisional)	228	2.80	0.192	620 m	631 m	2.03	0.29
Lake D., England	158	2.75	0.190	535 m	562 m	1.36	0.18
CIRQUE WIDTH :							
Cayoosh, B.C.	198	2.82	0.215	625 m	658 m	1.79	0.42
Wales (provisional)	228	2.84	0.181	686 m	656 m	1.41	0.19
Lake D., England	158	2.79	0.187	600 m	621 m	0.85	-0.02

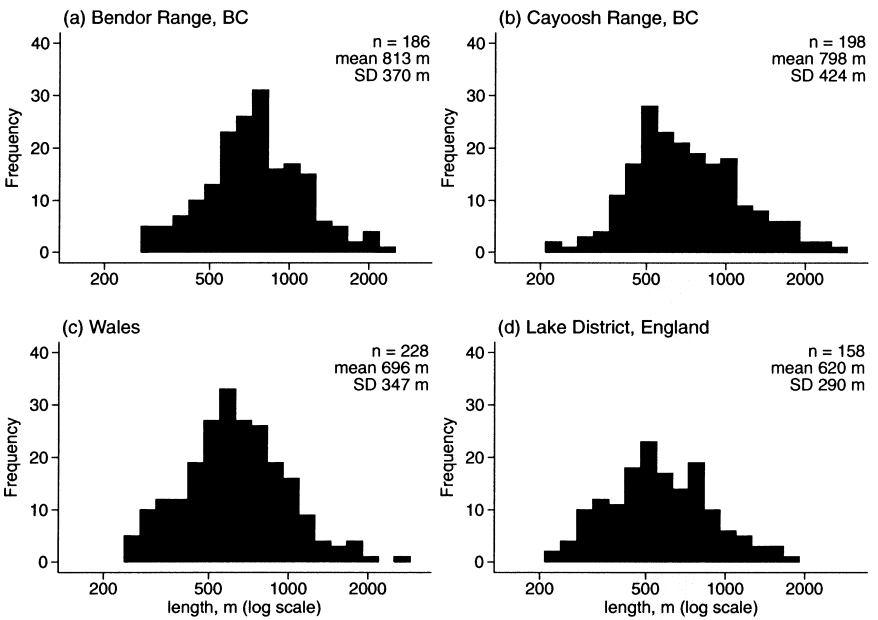


Fig. 1. Logarithmic histograms of cirque lengths in British Columbia and in Britain: (a) Bendor range, B.C.; (b) Cayoosh Range, B.C.; (c) Wales; and (d) the Lake District, England. Note the symmetry between left and right limbs, not suggesting truncation.

are scale-specific. Histograms of cirque length (Fig. 1) on a logarithmic scale show clear declining limbs on both upper and lower sides. Quantile-quantile plots (e.g. Evans and McClean, 1995, figure 2) confirm the excellent fit of log-normal distributions to length, width and wall height for all four sets of cirques in Table 1. De Blasio (2002) shows that this size distribution can be modelled by stipulating that much of the surface is unsuitable for cirque development: otherwise (on his assumption, of growth from small hollows) there would be a proportion of small, recently formed cirques. I prefer the interpretation that snow-patches are not effective erosion agents (Evans, 1997), and cirque development only starts when threshold thickness and horizontal dimensions permit development of a glacier, with significant basal movement.

Within their specific range of scales, cirques do show power-function relations, for example between vertical and horizontal dimensions (Evans and McClean, 1995) there is allometry (change in shape with size: Church and Mark, 1980). Scaling may thus be complementary, not contradictory, to scale-specificity.

KARST

Unlike depressions in fractal surfaces, karst depressions do not give size and shape distributions that mirror those of elevations. Sinkholes or dolines are the most common type of karst depression, and they are produced by solution of limestone, gypsum or sodium chloride, often followed by subsidence of overlying rocks. Sinkhole depths (Troester *et al*., 1984) and diameters (White and White, 1987) approximate exponential frequency distributions. Log-log plots are decidedly non-linear: sinkhole populations are not fractal. On carbonate in Kentucky, a typical width is around 200 m: on gypsum in Uzbekistan, depressions are tightly clustered around a width of 10 m. The 2800 dolines plotted by Gorbunova (in Klimchouk and Andrejchuk, 1996) cover two orders of magnitude, but are developed on a range of cover rock thicknesses.

Karst towers in northern Puerto Rico range in height from 5 to 52 m. For 149 measured by Day (1978), the modal height is 12 m, the median 16 m and the mean 19 m: the standard deviation is 10.7 m. The frequency distribution (Day, 1978, figures 3 and 4) seems close to log-normal.

On a narrower scale, the width and length of clints on limestone pavements, and the depth and width of the grikes separating them, are log-normally distributed with limited variation (Goldie and Cox, 2000). This is an example of characteristic scales in rock structure producing similar scales in the land surface. Solution flutes (Rillenkarren) on limestone show limited variation in each area: for example, those measured by Mottershead (1996) in Majorca average 17 mm wide, with a standard deviation of only 3.2 mm for the means of 30 sets of flutes.

LANDSLIDES

Landslides are a very broad category and range over about 4 orders of linear magnitude globally (metres to tens of kilometres: note that two orders of area equate to one order of length). However, in a particular region a specific type of

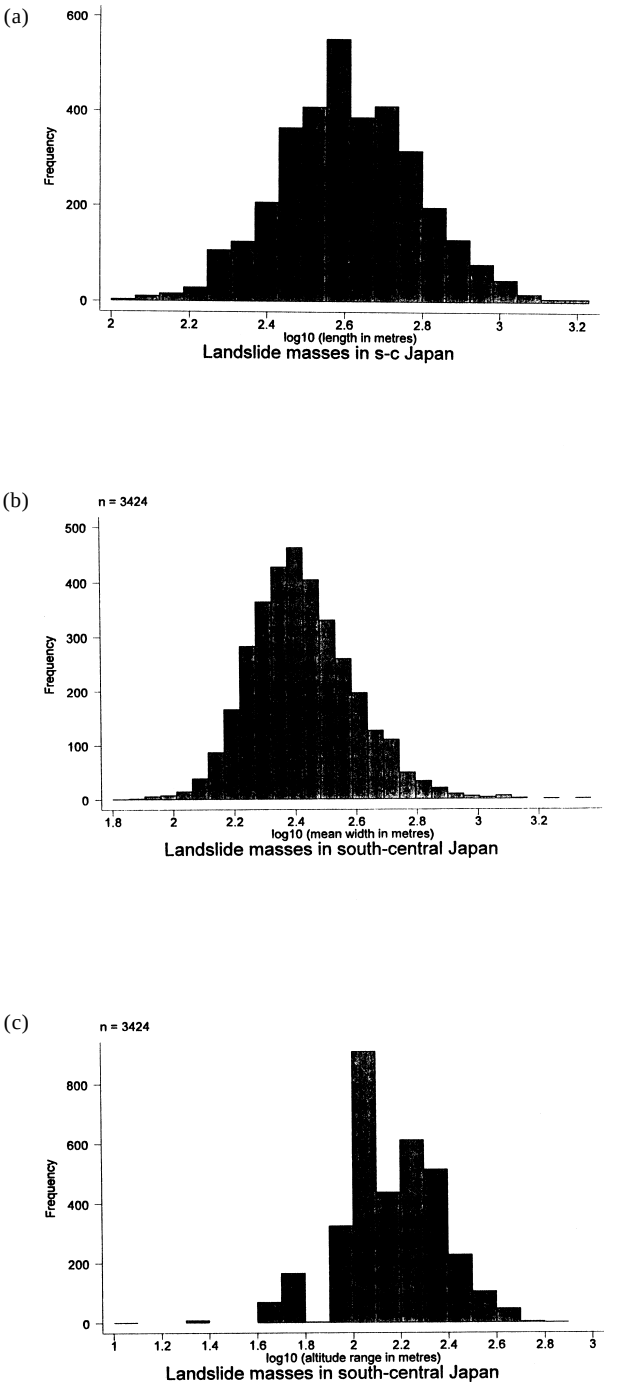


Fig. 2. Logarithmic histograms of (a) length; (b) mean width and (c) altitude range of 3424 landslide masses in south-central Japan (data supplied by Sugai and Ohmori).

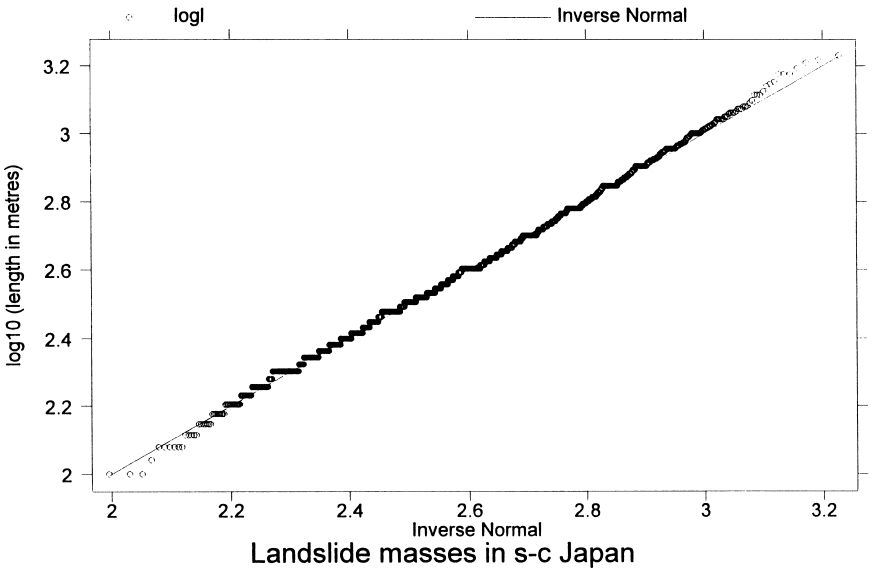


Fig. 3. Logarithmic quantile-quantile plot of landslide mass length in south-central Japan (data supplied by Sugai and Ohmori). The quantiles are the data ordered by magnitude. Each quantile is plotted against the corresponding quantile of the Gaussian frequency distribution with the same mean, standard deviation and sample size. Linearity shows the excellent match of this large data set to the log-normal frequency distribution.

landslide may have a characteristic scale, depending mainly on material properties and slope form. Testing this concept requires large data sets based on regional inventories. One of these covers 3424 landslide masses in the Akaishi Range, south-central Japan (Sugai *et al*., 1994). As for most landforms, the size distribution is positively skewed: the mode and median length are 400 m and the mean is 446 m. There is some rounding to a 50 m interval. Logarithmic transformation provides an excellent symmetrical distribution (Fig. 2), tightly clustered around the geometric mean of 409 m, 2.61 on the scale $\log_{10}$ (metres). On the same scale the standard deviation is 0.18, very similar to the cirques of Table 1. For mean width, defined as area/length, the standard deviation is 0.17 and for range in altitude of the landslide mass (excluding the scar) it is 0.21 (Fig. 2). The quantile-quantile plot (Fig. 3) shows how closely the data fit the log-normal distribution.

In fact the landslide masses are at a broad range of altitudes, and on 11 different geological formations for which mean lengths vary from 387 to 505 m (Ohmori and Sugai, 1995, table 1): for these more tightly defined groups, standard deviations are less. These authors stated that they "tried not to miss any of the masses larger than 10,000 m^2" (Ohmori and Sugai, 1995, p. 153): "landslide masses smaller than 10,000 m^2 were not counted" (Sugai *et al*., 1994, p. 237), corresponding to a linear dimension of about 100 m. It is safer to assume that coverage is near-complete for masses over 200 m long, and on this basis I

infer that the decline in frequency below a length of 400 m is not an artefact due to under-sampling. Hence these landslide masses in the Japanese Alps are regionally scale-specific.

Stark and Hovius (2001) come to different conclusions for landslides in mountainous parts of New Zealand and Taiwan. Their size range from 100 to 300,000 m^2, corresponding to 10 to 550 m linearly, is rather less than two orders of magnitude. Modal frequency on a logarithmic scale is around 1000 m^2 in each case, suggesting a dominance of smaller landslides than in Japan. Stark and Hovius (2001) suggest that the decline in frequency for smaller landslides results from under-sampling, which seems more likely for their linear dimensions below 30 m than for those below 400 m in Japan. They fit power functions to the right-hand limbs of the frequency distributions, but admit (p. 1081) that the power law fit is adequate only for part of the distribution with 25% of the observations. They are able to simulate observed distributions on the assumption that landslides are under-sampled according to a positive quasi-power-law relationship, below apparent mapping resolutions of 28 m and 42 m for two air-photo-based studies in New Zealand. To confirm that under-sampling occurs in this way requires a very detailed field study.

Montgomery *et al*. (1998) mapped 3224 shallow landslides in western Washington and Oregon, mainly between 20 and 220 m across. They found a roughly exponential distribution of landslide areas, with a median of 3386 m^2 and a mean of 8152 m^2. The general conclusion that landslides follow power-law scaling for all size ranges ("scale invariance is a general property of the landslide mechanism"; Hovius, 2000, p. 83) may be premature. It is likely that more precisely defined landslide types follow log-normal or exponential distribution models. Their lower size limits are thresholds specific to the type. Their upper size limits (a length of 1 km in New Zealand; Hovius, 2000) are controlled by slope height and length, characteristics of the topography in a particular region. Each landslide type is regionally scale-specific, even though landslides globally cover a wide range of scales and exhibit scaling behaviour over limited ranges. Recognition of this may require classification of types, at the level of rotational slumps, debris flows and rock avalanches: the category 'landslide' may be too broad. If too diverse a group are pooled, some essential scale-specific aspect may be lost, e.g. the transition from simple to complex landslides, or single movements to multiple movements.

FLUVIAL SLOPES

Some aspects of the land surface appear similar in form when viewed at different scales—notably the dendritic drainage channel networks found in many regions. However, these are not scale-free because the initiation of a channel requires runoff from a threshold area: this varies as a function of rainfall, slope gradient and soil properties. Measurement of channel density necessarily implies mean spacing and thus scale-specificity. Tarboton *et al*. (1992) defined this basic length scale of the (fluvial) landscape as the point where domination by stable diffusive processes (such as creep) gives way to unstable channel-forming

processes. Dietrich *et al*. (1993) considered thresholds of slope stability and of saturation, but found that the main threshold for channel initiation is in the critical shear stress of erosion by overland flow. The critical support area to generate a channel declines with increasing local valley slope (Montgomery and Dietrich, 1992), over a length range from about 30 to 300 m in coastal California and Oregon. Thus for each region there is a characteristic horizontal scale related to channel initiation; channel density is a useful concept even though the network of flow expands and contracts in response to weather events. There are various ways of measuring this characteristic horizontal dimension (reviewed in Evans, 1972, pp. 33–36) and it is not easy to agree on a single figure.

Channel initiation depends on resistance and gradient as well as discharge, so there is considerable inter-regional variation in this scale-specificity. For example, Vandekerckhove *et al*. (2000) found the threshold drainage area for gully initiation in Iberia and Greece to vary between the squares of 6 m and 200 m. The area was less on steeper slopes and varied also with vegetation, land use history and antecedent moisture. One complication pointed out by Dietrich and Montgomery (1998, p. 40) is that the fundamental hillslope for deep landsliding is much bigger than that for fluvial processes.

Furthermore, in some regions with steep slopes, landsliding limits the height and gradient of slope which can be supported, giving a distinctive scale to valley-side relief. Thus stream heads, valley spacing, slope height and gradient are regionally scale-specific features. Gullies on lateral moraines form within clear geometric constraints. These constraints cause regularity in length, in width and thus in spacing (Blair, 1994, figure 9). This local scale-specificity is further maintained by slope collapse if moraine height exceeds a threshold, between 120 and 132 m for the Tasman Glacier (Blair, 1994). Further processes that can produce impressively regular grooves include tephra avalanches, passing radially down the slopes of volcanoes. Allen (1982, vol. 2, p. 420, after Richards) illustrated a large and very regular set, 1–3 m deep and 3–7 m wide, on the upper flanks of Bárcena Volcano in Mexico. Alluvial fans have a wide range of areas (over four orders, or two linear orders), but within a region their length, width and vertical range each vary over one to two linear orders (Blair and McPherson, 1994).

Hovius (1996) demonstrated regular spacing of the main streams (those rising near the main divide) in ten different mountain ranges. Spacing at the mountain front (the Himalaya are an exception) averages just over twice the distance between the front and the main divide. For seven ranges, spacing varies essentially between 3 and 35 km.

For several areas in southern France, Vergne and Souriau (1994) found lineation of detrended topography at scales greater than 2 or 3 km, related to lineation of the main drainage. At shorter scales the topography tends to isotropy and a fractal interpretation may be considered. In the mountains of central Japan, Oguchi (1997) found that total drainage density varied only between 8 and 13 km km^{-2} over a range of igneous, volcanic and sedimentary rock types with relief (in 500 m squares) of 50–550 m. Standard deviations within each type were low, 1.2

to 3.3 km km^{-2}. He related this to uniform spacing of ridges, i.e. 'grain'.

The classic geomorphic concept of 'grain' was defined by Pike *et al*. (1989, p. 129) as "the characteristic horizontal spacing of major rivers and valleys", and shown by them to be equivalent to the concept of 'range' in geostatistics. Either range or standard deviation of altitude is plotted against circle diameter or area, and it is assumed that a single point is reached where the increase (in relief) flattens out. This diameter should be the length of major slopes, and can be used to define a characteristic vertical dimension, relief over a natural rather than an arbitrary area. Note that fractal surfaces will not give such a break point.

With real data, convex plots or multiple break points are often found, but the resulting subjectivity can be reduced by fitting all possible pairs of regression lines (starting from high and from low values) and taking the intersection of the pair that minimise root mean square deviations (Pike *et al*., 1989). This gave 'grain' (valley spacing) values of 1 to 3 km for the Montara Mountain area of San Mateo County, California. Previous manual studies showed grain varying from 2 to 13 km in southern New England, New York and Georgia, USA and from 3 to 24 km in central Europe, but from 3 to 48 km in the Alps. The latter surely exceeds the fundamental hillslope length even for deep landsliding. Such long grain distances may reflect the 3-D nature of glacially-modified valley networks, and broader tectonic forms. The initially 2-D concept of grain needs to be replaced by the expectation of multiple breaks in plots of relief v. diameter—and in variograms.

Dietrich and Montgomery (1998) recognised four specific scales in the fluvial landscape: the channel head, as discussed above in relation to drainage density; channel width and meander wavelength, not discussed here; the change from straight channel slopes to concave-up ones, reflecting a change in the ratio between classic process coefficients m and n (at a drainage area of some 0.8 km^2 in their figure 2.6 for north-western California—i.e. major slopes or valley-sides); and erosional unloading producing isostatic compensation at wavelengths from 100 to 1,000 km because of crustal rigidity (see below). They consider that drainage density sets (minor) hillslope length, which in turn influences hillslope height (local relief). I suggest, however, that relief and grain relate to their third scale rather than their first.

Attempts to fit scale-free fractal models to the land surface have instead established further scale-specific features. Fractal dimensions estimated at broad scales (around 200 km) are about 2.66, considerably higher (rougher surfaces) than those of 2.1 to 2.4 obtained at the erosional landscape scale (around 200 m) (McClean and Evans, 2000). Mark and Aronson (1984) found convex-up scale breaks at 330 to 1800 m, in variograms for mountainous parts of the USA at separations from 150 m to 5 km. I interpret the breaks as lengths of characteristic slopes, the topographic 'grain' beyond which altitude variance increases little: i.e. they are half the major ridge spacing. Estimated fractal dimensions over shorter separations averaged 2.2, while those above the scale break exceeded 2.5. At broader scales, for variogram analyses of large islands with generally high apparent fractal dimensions, McClean and Evans (2000, table 3) observed two

scale breaks, at 8–54 km and at 75–290 km. For continents, Australia and South America show breaks around 100 km (but North America does not). These breaks may relate to broad-scale relief, limited by isostasy and tectonism.

TECTONIC AND RELIEF

Tectonic and isostatic processes are responsible for broader specific scales in topography. The 5 km mean altitude of the Tibetan Plateau may be the highest supportable by current tectonic stresses balanced against lateral spreading in the asthenosphere (Bird, 1991): potential energy increases as the square of altitude, imposing a vertical scale limit. The flexural rigidity of the Earth's crust spreads isostatic depression due to loads of volcanoes over distances such as 200 km for Hawaii. The wavelength varies with the load and with effective elastic thickness of the crust, which varies between 4 and 130 km in North America as lithospheric thickness and temperature vary (Bechtel *et al*., 1990). Thus wavelengths of displacement vary both within and between oceans and continents, providing at best regional scale specificity.

The relief (vertical range or dispersion of altitude) in any region has an upper limit, due to the interaction between uplift, erosional processes and rock strengths. Globally, the subaerial maximum range is in the Himalaya, about 6,500 m around Nanga Parbat and Dhaulagiri. From variogram analyses (reflecting considerable averaging), the standard deviation of altitude differences increases to a maximum (in Asia) of about 1,900 m, at separations in excess of 1,200 km (McClean and Evans, 2000, p. 376).

Brozovic *et al*. (1997) note that in the northwestern Himalaya mean altitude varies with snowline (ELA). They infer that glaciation and frost action above the snowline are faster than fluvial erosion below (Hallet *et al*., 1996; Evans, 1997): only a small proportion of the topography can exceed altitudes 2 km above ELA. In such high relief areas, slopes (above streams or glaciers) have reached limiting gradients and heights maintained by landsliding (Schmidt and Montgomery, 1995; Burbank *et al*., 1996).

VOLCANIC

Globally, volcanoes cover a wide size range, but more specifically, continental stratovolcanoes (cones composed of both lava and ash) are several km across and mainly 500 to 3000 m high (above their bases); a chain of 46 in the central Andes (de Silva and Francis, 1991) are spaced on average 30 km apart. Francis and Abbott (1973) plotted height above base for all 181 continental conical composite volcanoes and found a clear mode around 1750 m (Table 2). They suggested that caldera formation, and possibly a limit to the sustainable height of a magma column, make it difficult for volcanoes on land to exceed a relative height of 3500 m. Parasitic cones, of which there may be dozens on a stratovolcano and more on a shield volcano, have a distinct scale of hundreds of metres. Scales vary between planets: the main volcanic centres on Mars and Venus are hundreds of km across. For young oceanic (hot spot) volcanoes on Earth, Vogt (1974b) found that height

Table 2. Relative heights of volcanoes, from figures in Vogt (1974) and Francis and Abbott (1973): frequency distributions for oceanic and continental volcanoes.

Height, km (lower class limit)	*0*	*1*	*2*	*3*	*4*	*5*	*6*	*7*
oceanic (adjusted)	1	5	16	12	9	7	4	2
continental conical	35	85	42	17	1	1		

(1 to 7.5 km, corrected for buoyancy of submerged bases of the volcanoes: Table 2) increased with the square root of age of the basement crust. For a given basement age, there is only a two-fold range in volcano height. Relative height is thus limited by lithospheric thickness and temperature, but support from seawater permits oceanic volcanoes such as Hawaii to reach greater heights than continental ones.

Pike (1978) recognised 20 classes in a population of 655 terrestrial volcanic edifices and gave geometric means of their dimensions. Ranges of one standard deviation above and below the mean are around four-fold, implying logarithmic standard deviations a little greater than those for cirques given above (Table 1) but still consistent with scale-specificity. As in the case of landslides, classification (on criteria other than size) may be a prerequisite to recognition of scale-specificity.

Vogt (1974a) gave histograms for volcano spacing in various tectonic settings: spacing averages 40–100 km along subduction zones or hot-spot tracks and is approximately equal to lithosphere thickness. Median separations are 55 km in island arcs, 70 km in continental subduction zones. 'Hot spot' volcanoes in young lithosphere are 35 km apart for the New England seamounts, 42 km in Galapagos, and 52 km in the Azores. The Hawaii-Emperor chain lies on older (Cretaceous) crust and median spacing is 72 km, while on still older crust the Cape Verde, Canary and Cameroon volcanoes are 80 km apart. These differences support the importance of lithospheric age (and thus thickness) rather than plate velocity, in controlling volcano spacing. For eastern Africa Mohr and Wood (1976) confirmed the importance of lithospheric thickness, but disagreed with Vogt's hypothesis of fracture control. Spacings of 10 and 19 km in the very young crust of Erta-ali and Dubbi in Afar rise to 42 km along the Ethiopian and Gregory Rifts, 70–75 km in the Harar and eastern Uganda plateaux and Addis Ababa region, and 109 km on the Ethiopian Plateau (Oligocene and Miocene volcanoes). They also found that composition (basaltic, silicic or alkaline-carbonatitic) did not affect spacing. Both size and spacing of volcanoes are thus regionally scale-specific, and median spacing varies globally by one order of magnitude. Much greater spacing (over 500 km) on Mars suggests very thick lithosphere (Vogt, 1974a).

Where crust is rifting in the Red Sea, points of high heat flow about 50 km apart become the initial sites of oceanic crust formation (Bonatti, 1985). These 'asthenospheric diapirs' relate to instability in the upper mantle. Schouten *et al.* (1985, p. 225) found that "the volcanism that forms the oceanic crust along the

spreading-plate boundaries is concentrated at regular intervals related to spreading rate. ... the boundaries ... have a fairly rigorous cellular structure on a 30–80 km length scale." This seems to bear some relation to the volcano spacing discussed above. The spacing depends, however, on the one-third power of the magma production rate, and thus increases with Mid-Ocean Ridge spreading rate (Bonatti, 1985) to 140–180 km for the equatorial East Pacific Rise. A hierarchical series of overlapping along-ridge segment scales is recognised by Macdonald (1998): discontinuities between his third-order segments, 30 to 100 km long, correspond with breaks in magma chambers and are considered to be short-lived. His second-order discontinuities break Mid-Ocean Ridges into segments 50–230 km long that persist for several million years and are comparable to the cells discussed by Bonatti: they relate to overlapping spreading centres where magma supply is low.

Lava flows are also scale-specific. Walker (1973) demonstrated log-normal distributions of length for each chemical/viscosity group of flows. Median length is 4.1 km for basaltic and 1.3 km for acidic flows, but rate of effusion during the first few days is more important than viscosity as a control of length. Later work (in Chester, 1993, pp. 89–92) confirmed and extended Walker's conclusions. Pinkerton and Wilson (1994) developed a fuller model, and dealt with data sets showing a little over one order of magnitude variation in flow length. They confirmed Walker's conclusions, but demonstrated the effects of flow duration and gradient. Pelletier (1999), however, found a power-law distribution of areas of basaltic regions in western North America, between separation distances of 3 and 150 km: and of Hawaiian cinder cones, from 150 m to 7.5 km. He viewed the clustering of magmatism and volcanism as statistically self-similar in space and time.

Measuring the shape of lava flow outlines, Bruno *et al*. (1994) found fractal behaviour for basaltic flows on gentle slopes, but not for silicic flows. The latter showed convex fractal plots with clear scale breaks at 300 m or 2 km (in their figure 10 examples). This scale specificity is attributed to the higher viscosities and yield strengths, suppressing shortwave irregularity in silicic-flow outlines.

OCEAN FLOOR (TECTONIC AND VOLCANIC)

Young ocean floor on the flanks of Mid-Ocean Ridges shows transverse and strong longitudinal lineation, at regionally specific scales. Near-axis stretching of lithosphere produces lengthening normal faults perpendicular to spreading direction, giving multiple horsts and grabens. Perfit and Chadwick (1998) illustrated a number of Ridge flanks with kilometric-scale lineation. On the East Pacific Rise, Lonsdale (1977, p. 271 and figure 6) demonstrated "... marginal grabens spaced fairly regularly at 1.5 km intervals". He also illustrated (p. 255, figure 2) linear highs spaced c. 4 km apart.

Herzfeld *et al*. (1993) applied residual variograms to high-precision profiles 30 and 80 km long across two Pacific Mid-Ocean Ridges. Both showed clear scale dependence, with linear and Gaussian-linear geostatistical models applicable at different scales. Specific scales (ranges at which the increase of variance with separation levels out) of 6.75 and 10 km were found for the Juan de Fuca Ridge,

and 14 and 32 km for the faster-spreading East Pacific Rise. Herzfeld and Overbeck (1999) found apparent fractal dimensions around 2.3 for separations below 2 km, but around 2.54 from 2 to 10 km, results surprisingly similar to those for subaerial fluvial topography. The sea floor is smoother at local than at broader scales and is clearly anisotropic. Thus even though the spreading sea-floor of Mid-Ocean Ridges provides an environment where fewer processes are important than in sub-aerial topography, models of low dimensionality do not fit the complexity observed.

Carbotte and Macdonald (1994) found that fault scarp lengths and spacings in all their study areas followed exponential frequency distributions. For three areas in the Ecuador Rift and on the East Pacific Rise, characteristic lengths from the fitted exponential models were 5.8, 5.32 and 4.52 km; characteristic spacings were 1.21, 1.13 and 0.85 km. Mean lengths or spacings were rather greater in each case.

Fault scarp heights average 90 m: fault growth lasts for about 700 ka and often interacts with volcanism (Macdonald, 1998). This produces abyssal hills, covering over 30% of the ocean floor, and typically 50–300 m high, 2–5 km wide and 10–20 km long. Different models of interaction of faulting and volcanism apply to Mid-Ocean Ridges with different spreading rates and magma supplies. Detailed studies by ALVIN submersible on the fast-spreading, high-axis East Pacific Rise demonstrate that the abyssal hills there are essentially faulted volcanic structures, elongated parallel to Ridge axes (Macdonald *et al*., 1996). They develop asymmetrically as the outward-facing scarps are episodically draped by lava flows; these 'volcanic growth faults' are almost complete within 6 km of the Ridge axis. The inward-facing slopes are simpler fault scarps sloping 60–90° and continuing activity until over 30 km from the axis. Where spreading rates are low or magma in short supply, back-tilted fault blocks form the dominant abyssal hills. With more magma, intermediate spreading rates and a high axis, axial volcanoes are split as they move away from the axis, giving asymmetric abyssal hills even without tilting. Whole volcanoes are preserved mainly near axial discontinuities on fast-spreading Ridges (Macdonald *et al*., 1996).

Smith and Jordan (1987) proposed an exponential frequency distribution for large Pacific seamounts (submerged volcanoes). Wessel and Lyons (1997), however, preferred a power-law, assuming data inadequacy below 2 km height even in their improved satellite-geodesy-based data. They did show that many seamounts line up in 'hot-spot' chains, with height and density varying with age of oceanic crust: this suggests regional scale-specificity.

IMPACT CRATERS

Meteorite impact craters cover a broad range of scales, but when dimensions are plotted against each other there are breaks where power-law relations change. In fact, this may be the clearest example of scale-specificity bounding two scaling regimes. On the Moon, Pike (1967) observed a threshold depth of 2 km (diameter 15 km) beyond which rim-floor relative relief diminishes and central peaks appear. Rugged arcuate structural and slump terraces are found where crater

diameter exceeds 20 to 25 km. Further work established eleven changes in shape between diameters of 10 and 30 km, averaging 18.7 km on the Moon. Work on Mars found similar morphological transitions, but at a diameter of about 5 km (Pike, 1980, 1988): on Earth it averages 3 km and on Mercury 16 km (later revised to 10 km: Pike, 1988). Ejecta on Mars show signs of flow for craters 4 to 60 km in diameter: this probably comes from incorporation of subsurface volatiles (water, carbon dioxide). The huge energy involved in producing craters over 80 km in diameter probably evaporates the volatiles, or masks their flow effects.

The depth: diameter break in slope (intersection of lines fitted to simple and to complex craters) was refined to 1.9 km on Earth, 3.1 on Mars, 10 on Mercury (later revised to 4.7 km) and 10.9 km for the Moon (Pike, 1980, 1988, table XI). Figure 4 shows log-log scaling plots for Mars, the Moon and a comparison of planets. The transition is at smaller diameters in sedimentary rocks and in the layered lavas of lunar maria and Martian plains. Thus the transition size is negatively related to gravity and to rock layering and weakness. Clearly we are dealing here with a major process threshold. The fact that central peaks appear in smaller craters than do rimwall terraces was used by Pike (1980) to argue against centripetal slumping and deep sliding as the initiating process: deformation is shallow and in large complex craters inertially-driven central rebound occurs during impact, generating the inward displacement and rimwall failure.

Studies of large features established a further transition, to basins with concentric multiple rings. Pike (1985, 1988) observed a 'root-two times diameter' scaling of ring spacing for multi-ring basins on all planets and moons examined. In that a given wavelength dominates a region, this is a regional scale-specificity even though many wavelengths (above a threshold) are globally possible. Pike (1988, figure 10) provided fuller information on the simple to complex crater transition, and recognised a progression with size from simple through modified-simple and immature-complex to complex craters, then protobasins, two-ring basins and multiring basins. He also updated comparisons between planets (and moons).

Recently Schenk (2002) has made further use of these relationships, on three of Jupiter's moons. The transition from simple to complex occurs at 250 m on Ganymede, and 300 m on both Callisto and Europa. The next transition, to ringed structures, comes at 26 km on the first two, but at 8 km on Europa. Finally, Ganymede and Callisto show a further transition (at 60 km on older craters, 150 km in younger) to anomalous domes with poor rims; this is found at 30 km on Europa, but has not been found elsewhere. Schenk's interpretation is that warmer ice at depth is weaker than brittle, very cold ice near the surface. At greater depth, this warm ice completely covers an 'ocean'. Schenk infers that the warm ice is at 16 to 22 km depth on the first two moons and the ocean is over 80 km down: the figures for Europa are 7–8 km and 19–25 km respectively. Hence it is possible to constrain models of structure by establishing specific scales in morphology.

Like other artificial landforms, artificial craters produced in a given period are much more scale-specific in size. Westing and Pfeiffer (1972) estimated that 26 million craters were produced in Indochina from 1965 to 1971, mainly in South

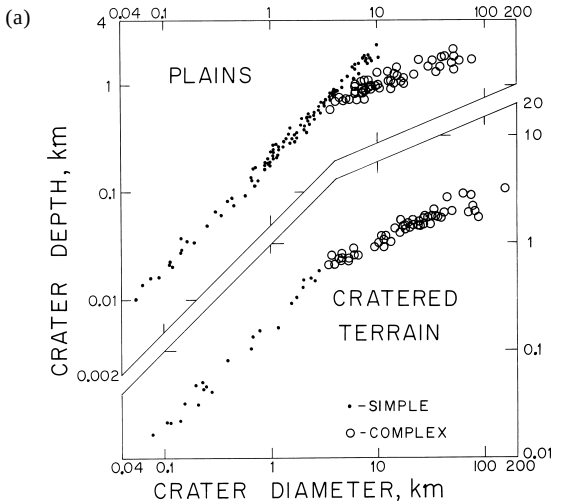


Fig. 4. Breaks in the crater depth: diameter scaling relation, illustrating the morphologic transition from simple to complex craters, from Pike (1980, figures 6, 9 and 2). (a) 230 craters on Mars, showing larger simple craters on plains than on 'cratered terrain'. (b) Based on 203 mare craters and 136 upland craters on the Moon. Simple craters follow a similar relation for maria and for uplands (as for the two divisions of Mars), but complex craters average 12% deeper in uplands. (c) Summary of the relationships on three planets and the Moon. The transition size increases as gravity decreases.

Vietnam. Most were from 500-pound bombs, and the craters were 1.5 to 6 m deep and 6 to 12 m in diameter.

DISCUSSION AND CONCLUSION

"... we ignore scale-dependency at our peril" (Wood, 1999). Iwahashi *et al*. (2001, p. 853) agree that "Geomorphic phenomena are scale-dependent, commonly irregular—even random—at high resolution, but exhibiting order at coarser scales." Frequent references by geomorphologists to typical landform sizes and various types of spatial regularity imply that the land surface is not scale-free (self-affine). If all landforms scale over broad ranges, why do we so often mention size in our initial description of a landform type? My literature search for hard evidence of size distributions has often been disappointing in that consistent measurements of large sets of landforms, producing frequency distributions, are much less common than vague assertions about size or spacing. Some evidence from different authors is conflicting, authors rarely compare power, exponential and log-normal models of frequency distributions, and the existence of a declining frequency of smaller forms needs careful testing when distributions are skewed. Progressive omission of smaller features is always a question, but does not explain the bimodality found in some dune size-frequency distributions. Our understanding of many landform types is incomplete: we need many more

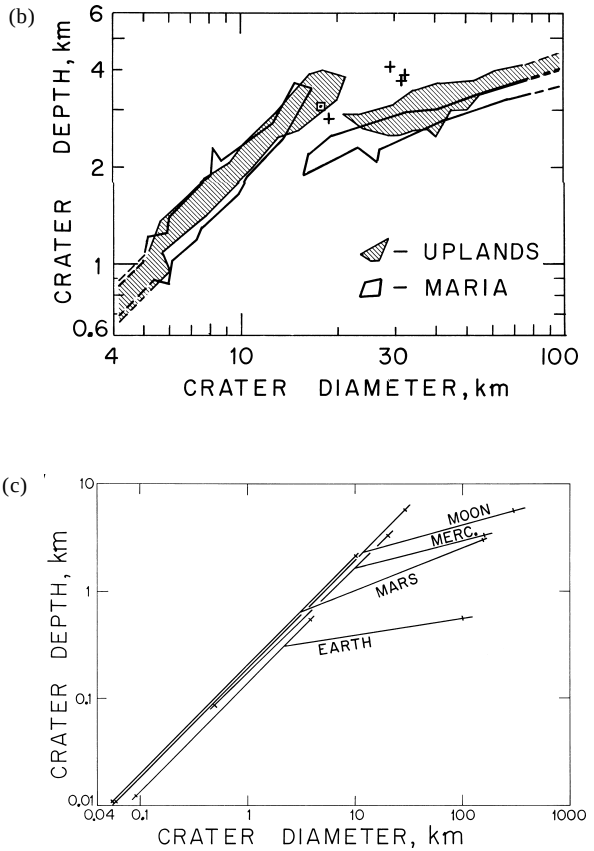


Fig. 4. (continued).

comprehensive frequency distributions of landform size and spacing to distinguish the very different models proposed and to establish the extent of scale-specificity (as manifest in log-normal or exponential distributions)—global, regional or local.

Scale-specificity has nevertheless been demonstrated for the size and spacing of specific landforms in aeolian, glacial, karst, tectonic, volcanic and meteoritic geomorphology, and for certain aspects of fluvial and slope geomorphology. It is found on a range of planets and moons. Juxtaposition of results from diverse branches of geomorphology has been valuable in demonstrating the scope for cross-fertilization in concepts and methods. I do not have space here to discuss the excellent examples of scale-specificity in coastal and periglacial geomorphology, or in patterned ground or microrelief. The pingos of permafrost areas are scale-specific. There are of course very clear examples of local scale-specificity in channel forms such as meanders, bars and pool-riffle sequences.

Further scales, etched into topography by erosion, are inherited from structural features such as jointing, faulting and bedding.

Only a mention can be made of the importance attached to scale considerations in (largely fluvial) process studies (e.g. Church, 1996), relevant though that is to development of scaled bedforms. However, the concept of 'Representative Elementary Area', "a fundamental scale for catchment modelling at which continuum assumptions can be applied" (Wood *et al.*, 1990) appears to be an explicit recognition of scale specificity. Dietrich and Montgomery (1998) and Beven (1995) discussed the importance of including realistic scale effects in landscape modelling and hydrological modelling respectively. Process modellers are forced to take scale into account both by the reality of specific scales in the land surface (as discussed here) and by practical data and modelling considerations.

Scale specificity of landforms is common in both the land surface and the sea floor, and arises in several different ways. Each specific scale raises questions of the processes or constraints responsible: some scales in different thematic fields (process systems) are interrelated. For example, cirques and landslides are constrained spatially by the dimensions of the slopes or valleys in which they develop. Processes exhibit thresholds of depth, width or velocity, or sizes of circulation cells, which may relate to scale-specific landforms (especially bedforms). Whether the specificity is global, regional or local, it is a clear feature of the land surface and a deviation from general mathematical models of the surface. Yet our precise knowledge of size and spacing is surprisingly limited: geomorphologists have become more sensitive to issues of temporal scale, but they should not lose sight of related issues of spatial scale (Phillips, 1988).

Scale dependence involves scaling (either isometric or allometric), scale breaks (thresholds) and scale-specific frequency distributions. Both the establishment of scaling relationships over certain ranges, and the recognition of scale-specific features and processes, are among the important tasks of geomorphology. The concept of 'scaling' remains valuable if the range of scales over which it applies is clearly specified: commonly this is between one and three decimal orders of linear magnitude. As Mark and Aronson (1984, p. 681) put it, for their study of variograms for Appalachian and western USA regions, "In a certain sense ... both conventional geomorphic wisdom ('landscapes have characteristic scales') and the fractals model ('geomorphic surfaces are statistically self-similar') are 'correct' ".

The existence of thresholds, breaks in slope and other limits means that, in earth sciences, scaling never applies over unlimited ranges: it is thus foolish to extrapolate. This rules out the use of scaling relationships to make up for limited measurement resolution or to 'extend the range' of data: their use should be confined to interpolation and estimation within the range of the data. Where characteristic scales can be established, they provide important clues to process and basic concepts for a discipline, parts of its broader framework and connective tissue. I assert that most recognisable landform types are scale-specific, at least regionally or locally.

Acknowledgements—Based on a presentation to 5th International Geomorphological Conference, Tokyo August 2001, S19: New concepts and modelling in geomorphology. Comments by Nick Cox, David Higgitt and Richard Pike have led to significant improvements. Hiroo Ohmori and Toshihiko Sugai kindly provided their landslide data file. Figure 4(a)–(c) is reproduced with kind permission of Richard Pike. This review is dedicated to the memory of Richard J. Chorley (1927–2002), who turned British geomorphology from an introspective art into an outward-looking science.

REFERENCES

Allen, J. R. L. (1982) Sedimentary structures: their character and physical basis: *Developments in Sedimentology*, **30**, 2 vols., Elsevier, Amsterdam, 593 + 663 pp.

Bechtel, T. D., Forsyth, D. W., Sharpton, V. L. and Grieve, R. A. F. (1990) Variations in effective elastic thickness of the North American lithosphere: *Nature*, **343**, 636–638.

Beven, K. (1995) Linking parameters across scales: subgrid parameterisations and scale dependent hydrological modelling: In J. D. Kalma and M. Sivapalan (eds.), *Scale Issues in Hydrological Modelling*, pp. 263–282. J. Wiley, New York.

Bird, P. (1991) Lateral extrusion of lower crust from under high topography, in the isostatic limit: *J. Geophys. Res.*, **96**, 10275–10286.

Blair, R. W. (1994) Moraine and valley-wall collapse due to rapid deglaciation in Mount Cook National Park, N.Z.: *Mountain Research and Development*, **14**, 347–358.

Blair, T. C. and McPherson, J. G. (1994) Alluvial fan processes and forms: In A. D. Abrahams and A. Parsons (eds.), *Geomorphology of Desert Environments*, pp. 354–402. Chapman & Hall, London.

Bonatti, E. (1985) Punctiform initiation of sea-floor spreading in the Red Sea during transition from a continental to an oceanic rift: *Nature*, **316**, 33–37.

Brozovic, N., Burbank, D. W. and Meigs, A. J. (1997) Climatic limits on landscape development in the Northwestern Himalaya: *Science*, **276**, 571–574.

Bruno, B. C., Taylor, G. J., Rowland, S. K. and Baloga, S. M. (1994) Quantifying the effect of rheology on lava-flow margins using fractal geometry: *Bulletin of Volcanology*, **56**, 193–206.

Burbank, D. W., Leland, J., Fielding, E., Anderson, R. S., Brozovic, N., Reid, M. R. and Duncan, C. (1996) Bedrock incision, rock uplift and threshold hillslopes in the northwestern Himalayas: *Nature*, **379**, 505–510.

Carbotte, S. M. and Macdonald, K. C. (1994) Comparison of seafloor tectonic fabric at intermediate, fast and superfast spreading ridges: influence of spreading rate, plate motions, and ridge segmentation on fault patterns: *J. Geophys. Res.*, **99**(B7), 13,609–13,631.

Chester, D. (1993) *Volcanoes and Society*. Edward Arnold, London, 351 pp.

Church, M. (1996) Space, time and the mountain—how do we order what we see?: In B. L. Rhoads and C. E. Thorn (eds.), *The Scientific Nature of Geomorphology: Proc. 27th Binghamton Symposium in Geomorphology*. J. Wiley, New York.

Church, M. and Mark, D. M. (1980) On size and scale in geomorphology: *Progress in Physical Geography*, **4**(3), 342–390.

Cooke, R. U., Warren, A. and Goudie, A. S. (1993) *Desert Geomorphology*. UCL Press, London, 526 pp.

Cox, N. J. (1992) Precipitation statistics for geomorphologists: variations on a theme by Frank Ahnert: *Catena*, Supplement, **23**, 189–212.

Day, M. J. (1978) Morphology and distribution of residual limestone hills (mogotes) in the karst area of northern Puerto Rico: *Geol. Soc. Am. Bull.*, **89**, 426–432.

De Blasio, F. V. (2002) Note on simulating the size distribution of glacial cirques: *Earth Surf. Processes Landf.*, **27**, 109–114.

de Silva, S. L. and Francis, P. W. (1991) *Volcanoes of the Central Andes*. Springer, Berlin.

Dietrich, W. E. and Montgomery, D. R. (1998) Hillslopes, channels and landscape scale: In G. Sposito (ed.), *Scale Dependence and Scale Invariance in Hydrology*, pp. 30–60. Cambridge U.P.

Dietrich, W. E., Wilson, C. J., Montgomery, D. R. and McKean, J. (1993) Analysis of erosion thresholds, channel networks, and landscape morphology using a Digital Terrain Model: *Journal of Geology*, **101**, 259–278.

Evans, I. S. (1972) General geomorphometry, derivatives of altitude, and descriptive statistics: Ch. 2 In R. J. Chorley (ed.), *Spatial Analysis in Geomorphology*, pp. 17–90. Methuen, London.

Evans, I. S. (1997) Process and form in the erosion of glaciated mountains: Ch. 7 In D. R. Stoddart (ed.), *Process and Form in Geomorphology*, pp. 145–174. Routledge, London.

Evans, I. S. and McClean, C. J. (1995) The land surface is not unifractal; variograms, cirque scale and allometry: *Zeitschrift für Geomorphologie*, N.F. Supplement-Band, **101**, 127–147.

Francis, P. W. and Abbott, B. M. (1973) Sizes of conical volcanoes: *Nature*, **244**, 22–23.

Goldie, H. S. and Cox, N. J. (2000) Comparative morphometry of limestone pavements in Switzerland, Britain and Ireland: *Zeitschrift für Geomorphologie*, N.F. Supplement-Band, **122**, 85–112.

Gordon, J. E., Whalley, W. B., Gellatly, A. F. and Vere, D. M. (1992) The formation of glacial flutes: assessment of models with evidence from Lyngsdalen, North Norway: *Quaternary Science Reviews*, **11**, 709–731.

Goudie, A. S. (1999) Wind erosional landforms: yardangs and pans: In A. S. Goudie, I. Livingstone and S. Stokes (eds.), *Aeolian Environments, Sediments and Landforms*, pp. 167–180. J. Wiley, Chichester.

Gravenor, C. P. and Meneley, W. A. (1958) Glacial flutings in central and northern Alberta: *American Journal of Science*, **256**, 715–728.

Greeley, R. and Iversen, J. D. (1985) Wind as a geological process; on Earth: *Mars, Venus and Titan*. Cambridge U.P., 333 pp.

Hagedorn, H. (1971) Untersuchungen über Relieftypen arider Räume an Beispielen aus dem Tibesti-Gebirge und seiner Umgebung: *Zeitschrift für Geomorphologie*, N.F. Supplement-Band, **11**, 251 pp.

Hallet, B., Hunter, L. and Bogen, J. (1996) Rates of erosion and sediment evacuation by glaciers: a review of field data and their implications: *Global & Planetary Change*, **12**, 213–235.

Herzfeld, U. C., Kim, I. I., Orcutt, J. A. and Fox, C. G. (1993) Fractal geometry and sea-floor topography: theoretical concepts versus data analysis for the Juan de Fuca Ridge and the East Pacific Rise: *Annales Geophysicae*, **11**(6), 531–541.

Herzfeld, U. C. and Overbeck, C. (1999) Analysis and simulation of scale-dependent fractal surfaces with applications to seafloor morphology: *Computers and Geosciences*, **25**, 979–1007.

Hovius, N. (1996) Regular spacing of drainage outlets from linear mountain belts: *Basin Research*, **8**, 29–44.

Hovius, N. (2000) Macroscale process systems of mountain belt erosion: In M. A. Summerfield (ed.), *Geomorphology and Global Tectonics*, pp. 77–105. J. Wiley, New York.

Iwahashi, J., Watanabe, S. and Furuya, T. (2001) Landform analysis of slope movements using DEM in Higashikubiki area, Japan: *Computers & Geosciences*, **27**, 851–865.

Johnson, N. L., Kotz, S. and Balakrishnan, N. (1994) *Continuous Univariate Distributions*, Vol. 1, 2nd ed., J. Wiley, New York, 719 pp.

Klimchouk, A. and Andrejchuk, V. (1996) Breakdown development in cover beds, and landscape features induced by intrastratal gypsum karst: *Int. Jour. Speleology*, **25**(3–4), 127–144.

Lancaster, N. (1988) Controls of eolian dune size and spacing: *Geology*, **16**, 972–975.

Lancaster, N. (1989) Star dunes: *Progress in Physical Geography*, **13**, 67–91.

Lonsdale, P. (1977) Structural geomorphology of a fast-spreading rise crest—the East Pacific Rise near 3.25 S.: *Marine Geophys. Res.*, **3**, 251–293.

Macdonald, K. C. (1998) Linkages between faulting, volcanism, hydrothermal activity and segmentation on fast spreading centres: In W. R. Buck, P. T. Delaney, J. A. Karson and Y. Lagabrielle (eds.), *Faulting and Magmatism at Mid-Ocean Ridges*, pp. 27–58. American Geophysical Union, Washington, D.C.

Macdonald, K. C., Fox, P. J., Alexander, R. T., Pockalny, R. and Gente, P. (1996) Volcanic growth faults and the origin of Pacific abyssal hills: *Nature*, **380**(6570), 125–129.

Mainguet, M. (1972) *Le modelé des grès: problèmes généraux*. Institut Géographique National, Paris.

McClean, C. J. and Evans, I. S. (2000) Apparent fractal dimensions from continental scale digital elevation models using variogram methods: *Transactions in GIS*, **4**(4), 361–378.

Mark, D. M. and Aronson, P. B. (1984) Scale-dependent fractal dimensions of topographic surfaces: an empirical investigation, with applications in geomorphology and computer mapping: *Mathematical Geology*, **16**(7), 671–683.

Mills, H. H. (1987) Morphometry of drumlins in the northeastern and north-central USA.: In J. Menzies and J. Rose (eds.), *Drumlin Symposium*, pp. 131–147. A. A. Balkema, Rotterdam.

Mohr, P. A. and Wood, C. A. (1976) Volcano spacings and lithospheric attenuation in the Eastern Rift of Africa: *Earth & Planetary Science Letters*, **33**, 126–144.

Montgomery, D. R. and Dietrich, W. E. (1992) Channel initiation and the problem of landscape scale: *Science*, **255**, 826–830.

Montgomery, D. R., Sullivan, K. and Greenberg, H. M. (1998) Regional test of a model for shallow landsliding: *Hydrological Processes*, **12**, 943–955.

Mottershead, D. (1996) A study of flutes (Rillenkarren) at Lluc, Majorca: *Zeitschrift für Geomorphologie*, N.F. Supplement-Band, **103**, 215–241.

Oguchi, T. (1997) Drainage density and relative relief in humid steep mountains with frequent slope failure: *Earth Surf. Processes Landf.*, **22**, 107–120.

Ohmori, H. and Sugai, T. (1995) Toward geomorphometric models for estimating landslide dynamics and forecasting landslide occurrence in Japanese mountains: *Zeitschrift für Geomorphologie*, N.F. Supplement-Band, **101**, 149–164.

Pelletier, J. D. (1999) Statistical self-similarity of magmatism and volcanism: *J. Geophys. Res.* **104**(B7), 15,425–15,438.

Perfit, M. R. and Chadwick, W. W. (1998) Magmatism at Mid-Ocean Ridges: constraints from volcanological and geochemical investigations: In W. R. Buck, P. T. Delaney, J. A. Karson and Y. Lagabrielle (eds.), *Faulting and Magmatism at Mid-Ocean Ridges*, pp. 59–115. American Geophysical Union, Washington, D.C.

Phillips, J. D. (1988) The role of spatial scale in geomorphic systems: *Geographical Analysis*, **20**(4), 308–317.

Pike, R. J. (1967) Schroeter's Rule and the modification of lunar crater impact morphology: *J. Geophys. Res.*, **72**(8), 2099–2106.

Pike, R. J. (1978) Volcanoes on the inner planets: some preliminary comparisons of gross topography: *Proceedings, Lunar & Planetary Science Conference, 9th*, 3239–3273.

Pike, R. J. (1980) Control of crater morphology by gravity and target type: Mars, Earth, Moon: *Proceedings, Lunar & Planetary Science Conference, 11th*, 2159–2189.

Pike, R. J. (1985) Some morphological systematics of complex impact structures: *Meteoritics*, **20**(1), 49–68.

Pike, R. J. (1988) Geomorphology of impact craters on Mercury: In F. Vilas, C. R. Chapman and M. S. Matthews (eds.), *Mercury*, pp. 165–273. Univ. of Arizona Press, Tucson AZ.

Pike, R. J., Acevedo, W. and Card, D. H. (1989) Topographic grain automated from digital elevation models: *Proceedings, Auto-Carto 9, ASPRS/ACSM Baltimore MD, 2–7 April 1989*, 128–137.

Pinkerton, H. and Wilson, L. (1994) Factors controlling the lengths of channel-fed lava flows: *Bulletin of Volcanology*, **56**, 108–120.

Sauerman, G., Rognon, P., Poliakov, A. and Herrmann, H. J. (2000) The shape of the barchan dunes of southern Morocco: *Geomorphology*, **36**, 47–62.

Schenk, P. M. (2002) Thickness constraints on the icy shells of the Galilean satellites from a comparison of crater shapes: *Nature*, **417**(6887), 419–421.

Schmidt, K. M. and Montgomery, D. R. (1995) Limits to relief: *Science*, **270**, 617–620.

Schouten, H., Klitgord, K. D. and Whitehead, J. A. (1985) Segmentation of Mid-Ocean Ridges: *Nature*, **317**(6034), 225–229.

Smith, D. K. and Jordan, T. H. (1987) The size distribution of Pacific seamounts: *Geophys. Res. Letters*, **14**, 1119–1122.

Stark, C. P. and Hovius, N. (2001) The characterization of landslide size distributions: *Geophys. Res. Letters*, **28**, 1091–1094.

Sugai, T., Ohmori, H. and Hirano, M. (1994) Rock control on magnitude-frequency distribution of landslide: *Trans., Japan Geomorph. Union*, **15**, 233–251.

Tarboton, D. G., Bras, R. L. and Rodriguez-Iturbe, I. (1992) A physical basis for drainage density: *Geomorphology*, **5**, 59–76.

Troester, J. W., White, E. L. and White, W. B. (1984) A comparison of sinkhole depth frequency distributions in temperate and tropic karst regions: In B. F. Beck (ed.), *Sinkholes: Their Geology, Engineering and Environmental Impact*, pp. 65–73. A. A. Balkema, Rotterdam.

Vandekerckhove, L., Poesen, J., Oostwoud Wijdenes, D., Nachtergaele, J., Kosmas, C., Roxo, M. J. and de Figueiredo (2000) Thresholds for gully initiation and sedimentation in Mediterranean Europe: *Earth Surf. Processes Landf.*, **25**(11), 1201–1220.

Vergne, M. and Souriau, M. (1994) A multi-scale analysis of continental relief in southern France: *Int. Jour. Remote Sensing*, **15**(2), 2409–2419.

Vogt, P. R. (1974a) Volcano spacing, fractures, and thickness of the lithosphere: *Earth & Planetary Science Letters*, **21**, 235–252.

Vogt, P. R. (1974b) Volcano height and plate thickness: *Earth & Planetary Science Letters*, **23**, 337–348.

Walker, G. P. L. (1973) Lengths of lava flows: *Philosophical Trans., Royal Soc. London*, **A274**, 107–118.

Wasson, R. J. and Hyde, R. (1983a) Factors determining desert dune type: *Nature*, **B304**, 337–339 [Discussion (1984) *Nature*, **309**, 91–92].

Wasson, R. J. and Hyde, R. (1983b) A test of the granulometric control of desert dune geometry: *Earth Surf. Processes Landf.*, **8**, 301–312.

Wasson, R. J., Fitchett, K., Mackey, B. and Hyde, R. (1988) Large-scale patterns of dune type, spacing and orientation in the Australian continental dunefield: *Australian Geographer*, **19**, 89–104.

Wessel, P. and Lyons, S. (1997) Distribution of large Pacific seamounts from Geosat/ERS-1: implications for the history of intraplate volcanism: *J. Geophys. Res.*, **102**(B10), 22,459–22,475.

Westing, A. H. and Pfeiffer, E. W. (1972) The cratering of Indochina: *Scientific American*, **226**(5), 20–29.

White, W. B. and White, E. L. (1987) Ordered and stochastic arrangements within regional sinkhole populations: In B. F. Beck and W. L. Wilson (eds.), *Karst Hydrology: Engineering and Environmental Applications*, pp. 85–90. A. A. Balkema, Rotterdam.

Whitney, M. (1983) Eolian features shaped by aerodynamic and vorticity processes: In M. E. Brookfield and T. S. Ahlbrandt (eds.), *Eolian Sediments and Processes, Developments in Sedimentology*, **38**, pp. 223–245. Elsevier, Amsterdam.

Wilson, I. G. (1971) Desert sandflow basins and a model for the development of ergs: *Geographical Journal*, **137**, 180–199.

Wilson, I. G. (1972) Aeolian bedforms—their development and origins: *Sedimentology*, **19**, 173–210.

Wilson, J. P. and Gallant, J. C. (eds.), (2000) *Terrain Analysis: Principles and Applications*. J. Wiley, New York, 479 pp.

Wood, E. F., Sivapalan, M. and Beven, K. (1990) Similarity and scale in catchment storm response: *Reviews of Geophysics*, **28**(1), 1–18.

Wood, J. (1996) Scale-based characterization of digital elevation models: Ch. 13 In D. Parker (ed.), *Innovations in GIS 3*. Taylor and Francis, London.

Wood, J. (1999) Visualisation of scale dependencies in surface models: *Paper Presented at the International Cartographic Association Annual Conference, Ottawa 1999*.

Concepts and Modelling in Geomorphology: International Perspectives,
Eds. I. S. Evans, R. Dikau, E. Tokunaga, H. Ohmori and M. Hirano, pp. 87–100.
© by TERRAPUB, Tokyo, 2003.

Simple Model for the Complex Dynamics of Dunes

Hiraku NISHIMORI and Hirohisa TANAKA

Department of Mathematical Sciences, Osaka Prefecture University,
Sakai 599-8531, Japan
e-mail: nishimor@ms.osakafu-u.ac.jp

Abstract. A simple model for the dynamics of dunes is introduced. The model simulates formation processes of typical shapes dunes: transverse dunes, barchans, seif dunes, star dunes, parabolic dunes and elongated parabolic dunes according to several environmental factors. The results have qualitative correspondence to the real systems. Considering the simplicity of the algorithm and the consequent easiness of handling, this model is expected to provide us with wide applicability for the investigation of various dynamics of dunes, especially the interplay between vegetation and dunes.

Keywords: Dunes, Dynamics, Simulation, Vegetation, Morphology

INTRODUCTION

It is well known that the shape of dunes depends upon several environmental factors surrounding them, for example, the amount of available sand in each desert area, wind directional variability, vegetation density covering sand surface, etc. Among all, the interplay between the dynamics of dunes and the growth of plants remains unexplained because of the complex nature of the dynamics of the system and the difficulty of the inspection of the theoretical hypothesis through direct observations. On the other hand, many valuable observational studies have been conducted and have provided us with detailed environmental conditions at individual arid areas in which typical types of vegetated dunes are seen (Hack, 1941; Pye, 1982; Tsoar *et al.*, 1982; Halsey *et al.*, 1990; Thomas *et al*., 1990; Cook *et al*., 1993). One of the pioneering studies among them was made by Hack (1941) in which he introduced a phase diagram to show the relation between the wind condition, available sand, the ratio of surface covered by plants and the dominant type of dunes observed in each and (or semiarid) area. Here, taking previous observational studies and computational studies (de Castro, 1995) into consideration, we propose a minimal model which realizes the qualitative dynamics of dunes in mildly vegetated arid areas (Nishimori *et al*., 2001). Thereafter, the formation processes of transverse dunes, parabolic dunes and elongate parabolic dunes are simulated. Effectively, Hack's phase diagram of vegetated dunes is numerically testified. Below, we make a brief explanation of our model. Firstly, the outline of our previous model (Nishimori *et al*., 1998) for 'un-vegetated' dunes is introduced which is shown to reproduce various types of

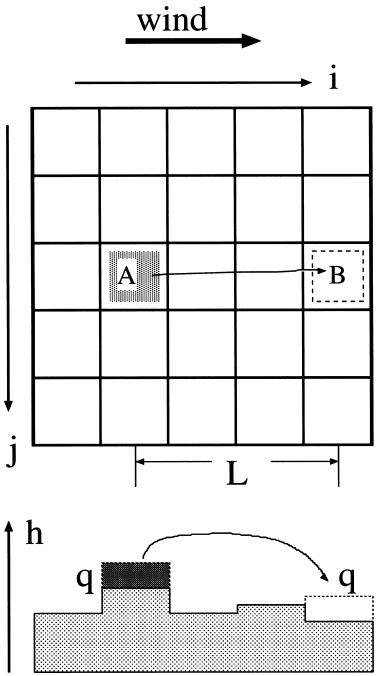


Fig. 1. Top: Top view of 2-dimensional lattice used for the present model. At each cell, field variable h (i, j), height of sand surface, is allocated. Wind is blowing from the right to the left. At a saltation step sand grains at cell A in the top figure will jump into cell B. In this process the surface height at A decreases by q and the height at B increases by q. Bottom: The corresponding profile. Note the size of each cell is sufficiently larger than individual sand grains, thus, each saltation step in this model represents the movement of a large number of sand grains.

dunes according to environmental factors. Secondly, a simple extension of the above model is made to simulate the evolution process of vegetated dunes. Afterwards, we make discussions on the methodology how to investigate complex phenomena using minimal models.

MODEL FOR UNVEGETATED DUNES

The model consists of horizontally extended 2-dimensional lattice (Fig. 1) Each cell of the lattice corresponds to the area of the ground sufficiently larger than individual sand grains. At each cell (i, j), at each coarse-grained time step n, a continuous field variable $h_n(i, j)$ is allocated to denote the average height of the sand surface within the cell. Therefore, the evolution of $h_n(i, j)$ at one time step does not express the movement of individual sand grains. It rather describes the resulting surface height change after the collective motion of many grains during the unit time period sufficiently shorter than the characteristic time of a dune formation but much larger than the time scale of individual sand grains dynamics.

According to Bagnold the elementary dynamics of individual sand grains consists of creep and saltation (Bagnold, 1941). Creep is the process where sand grains move along sand surface by sliding or rolling. Saltation is the process in which sand grains make short jumps typically in the order of 10 cm. However, in the real process of dune formation the distinction between creep and saltation is not clear. For example, in the ripple formation model by Anderson *et al.* (Anderson, 1987), they stressed the important role of small jumps called reptation with the intermediate scale between saltation and creep. Apart from the above processes, suspension process plays an important role for sub-aqueous dunes, but is not a decisive factor for the desert dunes because of the large difference of the mass density between the air and sand grains.

Here, we construct a phenomenological model at the space-time scale much larger than these elementary processes. We divide the dynamical process into two:

i) The *inertial* or *advection* process: This describes the accumulated transport effect by saltation over the unit time scale and the unit space scale of our coarse grained model.

ii) The *frictional* (or *diffusion*) process: There must be fluctuation effects around the average motion due to erratic wind directions, irregularities of the dune surface, etc. This erratic 'Brownian' motion is modified by the slope effect as the chemical potential does in the microscopic Brownian motion. The actual dynamics of our model are as follows:

In the frictional process, we may assume a local conservation law of the amount of sand in the coarse grained space mesh. Therefore, the conservation equation

$$h_{n+1}(i,j) = h_n(i,j) + \left[\sum_{(i',j')\in NN} j_n^{NN}(i',j':i,j) + \sum_{(i',j')\in NNN} j_n^{NNN}(i',j':i,j) \right] \tag{1}$$

holds. Here, *NN* are nearest cells of (i, j) and *NNN* are 2nd nearest cells of (i, j), the quantity $j_n^{NN}(i', j':i, j)$ and $j_n^{NNN}(i', j':i, j)$ are the net flux of sand from (i', j') to (i, j). This flux is the horizontal component of the flow which is assumed to be proportional to the gravitational force along the slope. Hence, if the local slope is sufficiently gentle, the relations

$$\begin{aligned} j_n^{NN}(i',j':i,j) &= a\big(h_n(i',j') - h_n(i,j)\big) + b\delta_{j',j} \quad (i > i') \\ &= a\big(h_n(i',j') - h_n(i,j)\big) - b\delta_{j',j} \quad (i' > i) \end{aligned} \tag{2}$$

$$j_n^{NNN}(i',j':i,j) = \frac{a}{\sqrt{2}}\big(h_n(i',j') - h_n(i,j)\big) \tag{3}$$

hold, where a and b are positive constants. The symbol δ in the right hand side of

Eq. (2) means Kronecker's delta, and the terms proportional to b in these equations describe the constant drift in the wind direction. However, they are ineffective in this model because of the conservation relation (1).

The advection process is modeled as follows.

$$h_{n+1}(i,j) = h_n(i,j) + \sum_{(i',j)} q_n(i',j)\left(\delta_{i'+L_n(i',j),i} - \delta_{i',i}\right) \tag{4}$$

Here $L_n(i, j)$ is the average transport length (note that this is not the saltation length) of sand grains which take off from (i, j), whereas $q_n(i, j)$ is the 'height transfer' associated with the grains transfer from (i, j) to $(i + L_n(i, j), j)$ by the inertial process (Fig. 1). The symbol δ in the right hand side of Eq. (4) means Kronecker's delta, and the 2nd and the 3rd terms express the incoming advection flux to (i, j) and the outgoing one from (i, j), respectively. The transport length $L_n(i, j)$ depends on many factors which are mutually coupled in a complicated manner. For example, the flow field of the wind directly affects the saltation length of individual sand grains, whose accumulation results in the transport length. On the other hand, the flow field sensitively depends on the present profile of the sand surface. At the same time the surface profile varies with time through the transport of sand grains. In the same way, the specification of the amount of the height transfer $q_n(i, j)$ in terms of possible relevant factors, also, is not an easy task.

Here, to make a minimal model for the large scale dynamics of dunes, we ignore the details of actual systems and assume a set of rather simple rules for the transport length $L_n(i, j)$ and the height transfer $q_n(i, j)$ as

$$L_n(i, j) = L_0\,(\tanh(\nabla_i h_n(i, j)) + 1) \tag{5}$$

$$q_n(i, j) = q_0(-\tanh(\nabla_i h_n(i, j)) + 1 + \varepsilon) \tag{6}$$

Here, $\nabla_i h_n(i, j)$ means $h_n(i + 1, j) - h_n(i, j)$, i.e., the local slope in i-th (wind) direction, where L_0, q_0 and ε are positive constants. The above rules reflect the following observations (Rassmussen, 1989):

(i) In the windward side of a sand hill, the wind velocity is higher than the flat area.

(ii) Particularly around the crest of the real sand hill, a sharp peak of the surface wind velocity is observed.

(iii) At the lee side of the hill a drastic decrease of the wind velocity is observed.

The relation between Eqs. (5) and (6) and (i), (ii), (iii) are schematically explained in Fig. 2.

Apart from the above dynamical rules, seasonal change of wind directions and other geological conditions play very important roles in dunes evolution. To investigate the relation between such factors and dunes' morphology, we introduced two control parameters; i) the amount of available sand in a desert area, ii) the

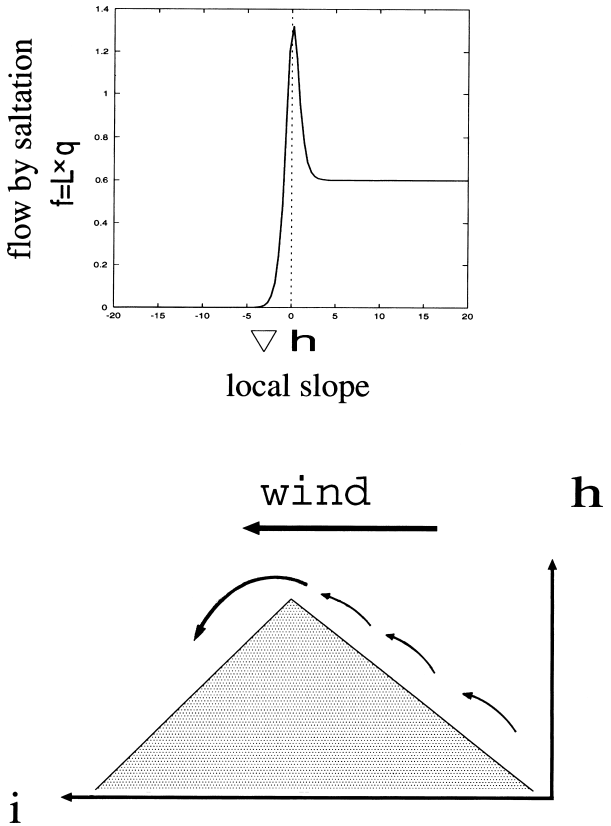


Fig. 2. Saltation flux $f = L \times q$ for the present model as the function of local slope ∇h in wind direction (i-direction). Here, L_0 and q_0 are 1 and ε is 0.3 (see Eqs. (5) and (6)). It reflects the observational fact, namely, large bed load in the windward particularly around the crest (indicated by the arrow), whereas sharply it decreases in the lee side of a dune. This situation is schematically shown in the bottom figure.

directional variability of wind in the desert area. Typical shapes of simulated dunes under various pairs of above control parameters are shown in Fig. 3. The correspondence between the morphology obtained in our simulations and that of real systems (Wasson *et al.*, 1983) seems fairly good as seen in Fig. 4. It means the present simple set of rules is available to study the morphodynamics of various types of dunes.

MODEL FOR VEGETATED DUNES

Here we make a simple extension of the above model to plant trees on the sand surface. For this purpose, in addition to $h_n(i, j)$, a new field variable $c_n(i, j)$, the local density of vegetation is allocated at each site. These two field variables

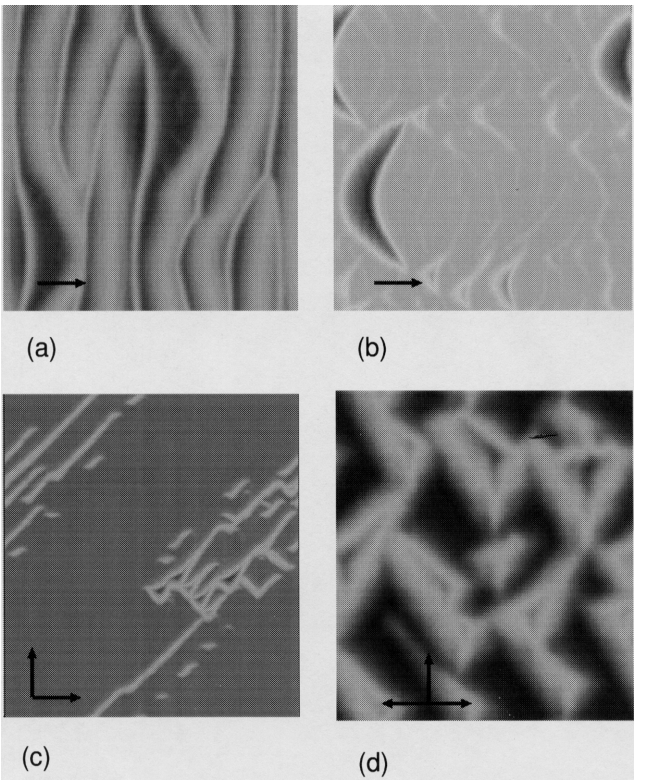


Fig. 3. Various shapes of simulated dunes; (a) transverse dunes, (b) barchans, (c) seif dunes, and (d) star dunes. Arrows indicate wind directions which can change depending on seasons.

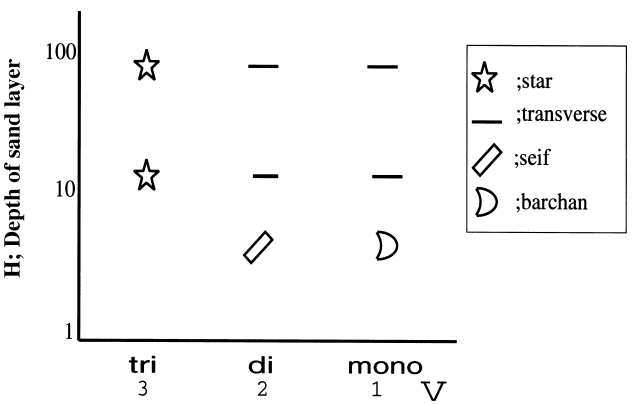


Fig. 4. Types of dunes formed at several points in the control parameters space. The control parameter V is the wind directional variability and H is the average depth of sand layer.

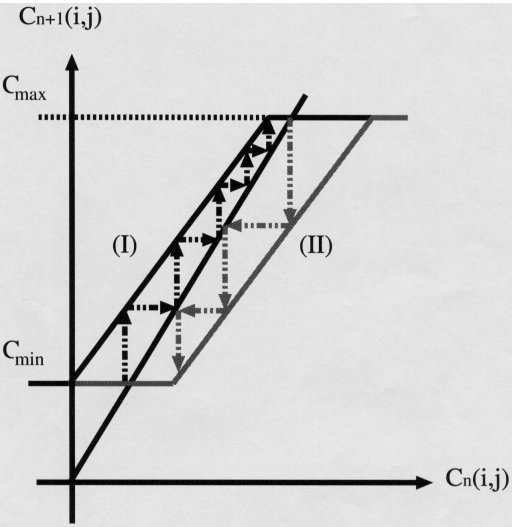


Fig. 5. Schematic explanations of the present model; (I) The Map $c_n(i, j) \to c_{n+1}(i, j)$ to describe the discretized time evolution of plants density. Without the temporal change $b_n(i, j)$ of surface height, plant density monotonically increases up to the saturation value $c_{\max}$. (II) With more than a certain speed of surface rise or deflation, plants at the surface are, more or less, damaged because they are buried or cut away, then, $c_n(i, j)$ will decrease with time with the lower limit $c_{\min}$.

are set to interact each other through a suppression factor $a_{\beta,n}(i, j)$. The specific rules are as follows:

(i) For the evolution of $c_n(i, j)$, the local density of plants, we adopt a set of simple rules. Firstly in an extreme case such that the profile of the sand surface is kept unchanged, plants will grow up to the saturation density without being cut away if the drastic deflation of the ground does not occurs nor are buried by the rapid accumulation of sands, that is, $c_n(i, j)$, will increase until the maximum value $c_{\max}$. Unlike such a cases, if the temporal change of surface height is very fast, the growth rate of plants is suppressed or some of them may wither and die, then $c_n(i, j)$, decreases down to the minimum density $c_{\min}$. To reflect the above situation, we use a discrete set of dynamics which is a sectional linear map as shown in Fig. 5. Specifically, the dynamics are expressed as

$$\left.\begin{array}{ll} c_{n+1}(i,j) = A\big(c_n(i,j) - b_n(i,j)\big) + c_{\min} & \big(b \le c \le (c_{\max} - c_{\min})/A + b\big) \\ c_{n+1}(i,j) = c_{\max} & \big((c_{\max} - c_{\min})/A + b < c\big) \\ c_{n+1}(i,j) = c_{\min} & (c < b) \end{array}\right\} \quad (7)$$

here $b \equiv b_n(i, j) \equiv |h_n(i, j) - h_{n-1}(i, j)|$, $c \equiv c_n(i, j)$ and A is a constant to determine the growth rate of plants.

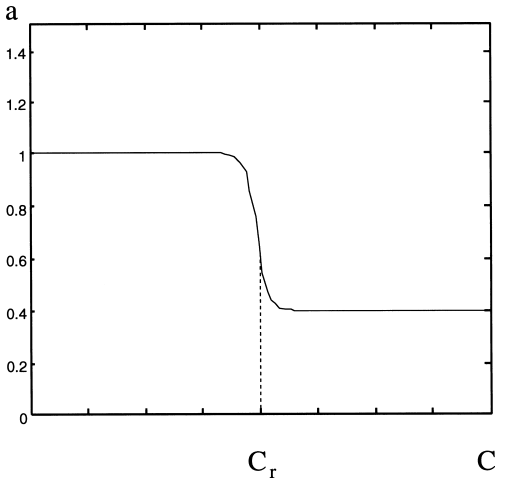


Fig. 6. Suppression factor a of sand flux as a function of local density of vegetation c. Above a critical density c_{cr} of vegetation, the flux of sand drastically decreases as described in Eq. (8).

(ii) For the evolution of $h_n(i, j)$. The crucial effect caused by permitting the growth of plants is such that the sand transport sharply decreases when the cover ratio of sand surface by plants exceeds a critical value. To realize the situation in a simple expression, the suppression factor $a_{\beta,n}(i, j)$ is introduced,

$$a_{\beta,n}(i,j) = \frac{1}{2}\left(\tanh \beta\left(c_{\mathrm{cr}} - c_n(i,j)\right) + 1\right) \tag{8}$$

Here, c_{cr} is the critical vegetation density over which the movement of sand sharply decreases, and β determines the maximum efficiency of suppression (Fig. 6). The value of β depends on whether it is for the saltation flux or for the creep flux. With the suppression factor, the height transfer $q_n(i, j)$ in Eq. (4) and, subsequently, the saltation flux $j_n^{\mathrm{sal}}(i, j) \equiv L_n(i, j) \times q_n(i, j)$ are forced to decrease as

$$q'_n(i, j) = a_{\beta,n}(i, j)^2 q_n(i, j) \tag{9}$$

$$j'^{\mathrm{sal}}_n(i, j) = a_{\beta,n}(i, j)^2 j_n^{\mathrm{sal}}(i, j) \tag{10}$$

where $q'_n(i, j)/j'^{\mathrm{sal}}_n(i, j)$ and $q_n(i, j)/j_n^{\mathrm{sal}}(i, j)$ are, respectively, the height transfer/local saltation flux with vegetation and without vegetation. In the same way, by the vegetation, the diffusional flux (1) is suppressed as

$$j'^{NN}_n(i', j' : i, j) = a_{\beta,n}(i, j)^2 j_n^{NN}(i', j' : i, j) \tag{11}$$

$$j'_n{}^{NNN}(i', j':i, j) = a_{\beta,n}(i, j)^2 j_n{}^{NNN}(i', j':i, j) \quad (12)$$

where the left hand sides are the diffusional flux with vegetation. The time evolution of sand surface is, like the previous model for unvegetated dunes, governed by Eqs. (1) and (2) though with the modified sand flux by the vegetation mentioned above. This suppressed sand dynamics affects the growth of vegetation through the variable b introduced in Eq. (7). In such way, the sand dynamics and the vegetation growth are competing each other in this model to reflect real systems.

To compare the simulation outputs with Hack's (1941) diagram, two kind of quantities are chosen as the control parameters. One is the amount of sand at the source. Namely, the average height, $<h_{\text{source}}>$, of the sand surface at the source site, $\{(i, j) | i = 1, 2\ 1 \le j \le N\}$. Specifically, uniformly random numbers between $2<h_{\text{source}}>$ and 0 are allocated to these sites at each time step. The other control parameter is the wind strength which should be a monotonically increasing function of saltation flux. Specifically, the variable q_0 in Eq. (6) is adopted as the index of wind strength. Note that the vegetation density, which is one of the axes in the diagram by Hack (1941), is not adopted as a control parameter because it is rather a resultantly attained quantity after the above two control parameters are fixed.

Except for the source area, simulations are initiated from flat sand surface, while the initial vegetation density $c_0(i, j)$ at each site is set randomly around the average value $<c_0(i, j)>$ which is between $c_{\max}$ and $c_{\min}$. Note the boundary condition in j direction, which is perpendicular to the wind direction, is set periodic to decrease the boundary effect, and the leeward boundary in i direction is set as the free boundary. Below the initial level 0 of sand surface, erosion of sand surface is inhibited to realize the existence of the hard ground or the ground water table. Using these rules, spontaneous formation processes of typical types of dunes are observed.

RESULTS

Typical snapshots of simulated dune field are shown in Fig. 7. In all figures, sand is supplied from the most windward 2 rows, and steady wind is blowing from the left to the right as indicated by an arrow. Parameters to control the amount of sand at the source $<h_{\text{source}}>$ and the index of wind strength $f_0 \equiv L_0 \times q_0$ are described under each figure. The left part in each figure shows the spatial distribution of vegetation density $c_n(i, j)$. The darker tone indicates the more densely vegetated place, whereas white parts indicates the areas with bare sand surfaces. The right part in each figure shows the surface height distribution $h_n(i, j)$, where the darker position means the higher surface.

The specific conditions for the appearance of individual steady states are as follows. First of all, when the wind force is too weak, regardless of the amount of sand supply at the source, clearly shaped dunes will not appear in the system (Fig. 7(a)). This is also the case where the amount of sand supply is too small.

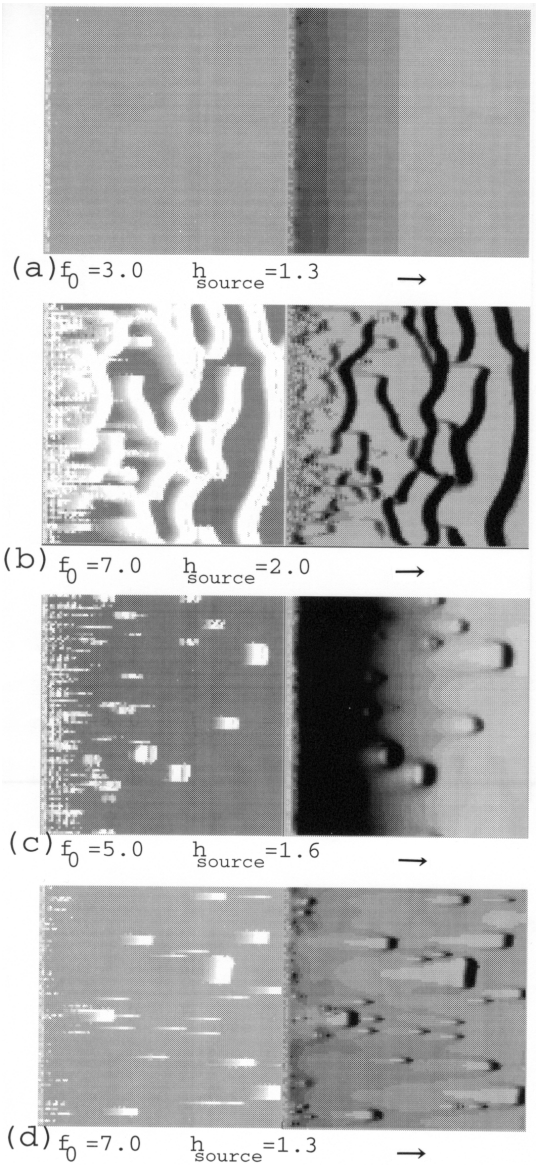


Fig. 7. Snapshots of simulated dunes under various pairs of control parameters, wind force and sand supply. (a) When the wind force is too weak no distinguishable dune is formed. It is also the case for too small amount of sand supply at the source. (b) Under stronger wind with sufficient amount of sand supply transverse dunes prevail while small parabolic dunes are seen just lee of the sand source. The latter will soon grow up to the former. (c) Parabolic dunes, the arms of which extend in the windward direction, are formed under mildly blowing wind with intermediate amount of sand at the source. (d) If the amount of sand is comparatively small within this regime, thin and long parabolic dunes, namely, elongate parabolic dunes will grow. They look like rather linear dunes if without their noses.

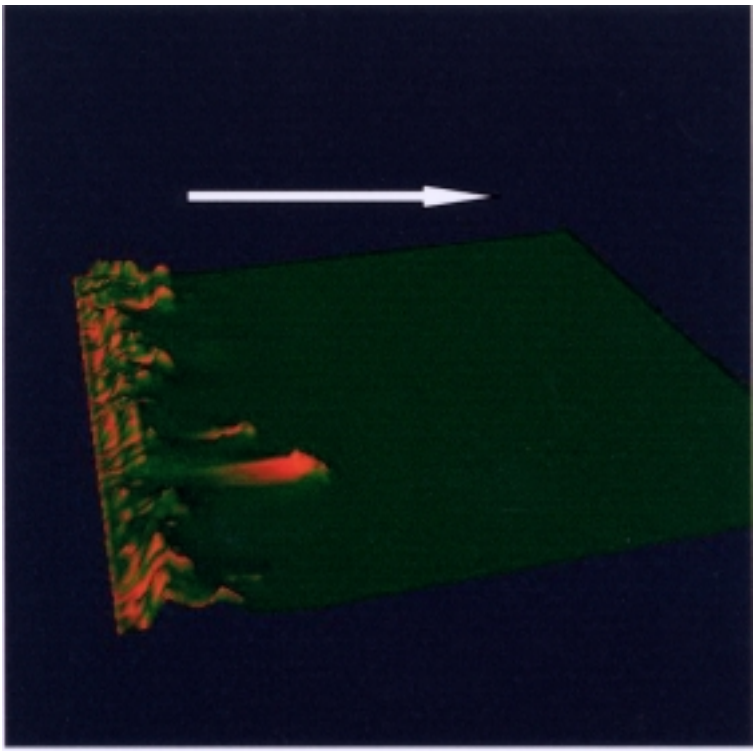


Fig. 8. Under mildly blowing wind (from the left to the right) with proper amount of sand at the source (the left-most area), parabolic dunes will be generated to penetrate into the vegetated inland area. Green color means vegetated area whereas khaki color means bare sand surface.

However, with a stronger wind force and a greater amount of sand supply, two types of clearly shaped active dunes are formed:

i) When a sufficiently large amount of sand is supplied under strong wind, transverse dunes, barchan dunes or both will dominate in the system. In more detail, small parabolic dunes formed just the lee of the sand source soon develop into barchan dunes, which connect to each other and grow larger as they move, to form transverse dunes the crests of which extend roughly perpendicular to the direction of wind (Figs. 7(b) and 8).

ii) If the amount of sand supply or the wind force is slightly less than the above, parabolic dunes will prevail in the system (Figs. 7(c) and (d)). They have arms extending to the windward direction. At the centre of each parabolic dune, a hollow develops in which surface erosion proceeds until the unerodible surface appears. The sand at the hollow will move to constitute the crest of the dune. There we can see the tendency that the length of the arms varies depending on the wind force, namely, the arms extend further under a stronger wind. In the case with rather small amounts of sand, elongate parabolic dunes (Pye, 1982) with the

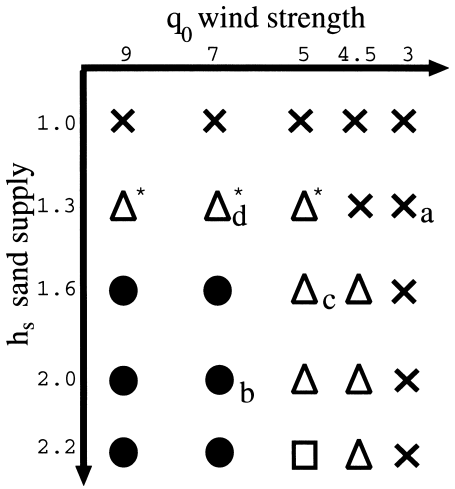


Fig. 9. Phase diagram to show the dominant types of dunes under various pairs of control parameters. Here the directions of axes are set for the easiness to compare with Hack's (1941) phase diagram. The alphabets in the diagram indicate the conditions corresponding to respective snapshots in Fig. 7. Symbols △s and ●s indicate, respectively, parabolic dunes, and, barchan (or transverse) dunes, whereas ×s mean the conditions for no dune formation. The △s accompanied by * mean the conditions for the development of rather thin parabolic dunes with long arms. At the condition with the symbol □ many irregular mounds are formed which are not clearly categorized as particular type of dunes.

shapes like hair-pins will appear (Fig. 7(d)). The arms of such elongate dunes, if without their noses, may appear to be pairs of linear dunes.

The above results are summarized in a phase diagram as shown in Fig. 9. This diagram is not directly compared with that of Hack (1941) because of the fewer axes in our diagram. Also, in the diagram, an ambiguous area is left in which condition irregular mounds of sand are formed, which are not easily categorized into other dominant types of dunes. There is, however, good qualitative correspondence to the previous observational studies including that of Hack (1941), especially, regarding the systematic change of the dunes' morphology from the transverse (or barchan) dunes to the parabolic or the elongate parabolic dunes according to the amount of available sand (or to the wind force). Moreover no dune formation is realized under very light winds or under very small amounts of sand supply.

DISCUSSION

The above results indicate that our simple model of dunes contains intrinsic dynamics by which the morphodynarnics of dunes are decisively affected, and that through this model time evolution of dune systems under various situations are expected to be effectively simulated. Also, the simplicity of the model would

enables us to make analytical investigations of the system. On the other hand, it should be noted that, in modeling the 'minimal' dynamics of the system, several aspects of them were intendedly cut away which may cause some degrees of discrepancies between the reality and simulated dunes.

To fill the gap between the reality and the minimal model, recently, several models have been proposed some parts of which dynamics are deduced from detailed fluid model. Especially a simple analytical expression of turbulent boundary layer near dunes surface (Jackson *et al*., 1975) has been incorporated into numerical models to catch some quantitative features of real barchans (Sauermann *et al*., 2001; Kroy *et al*., 2002; Andreotti *et al*., 2002). Yet, calculations under more complex and interesting boundary conditions, e.g., unsteady wind in strength and directions, naturally or artificially vegetated sand surface, etc. are still far beyond to be fulfilled on the basis of the detailed models. Also the interaction between isolated dunes and their collective dynamics in large time and spatial scales are of great interest but hard to be solved if one try to start from the details of the underlying systems. It is supposed the difficulty to treat such complex situations is staying not only in the amount of the accompanying calculations but rather in the-entangled relationship between what are engaged in the whole dynamics the degree of which is not clearly estimated. In other words, we hardly know what equations we should calculate before starting and accomplishing the calculations.

Considering the above facts and the present results of our model, heuristic approaches of exploring minimal rules are expected to play a certain role for the study of dunes. Especially, the investigation of universal natures which do not depend on the details of the underlying systems, seems the most effectively performed by this kind of approach. The methodology for the minimal model approach is yet to be developed (Werner, 1995; Momiji *et al*., 2000; Kroy and Herrmann, 2002) for the efficient understanding of complex dynamics of dunes.

Acknowledgements—This research was supported by the Grant-in-Aid for Scientific Research of JSPS (c11837017).

REFERENCES

Anderson, R. S. (1987) A theoretical model for aeolian impact ripples: *Sedimentology*, **34**, 943–956.

Andreotti, B. and Claudin, P. (2002) Selection of shapes and velocities. Part2: A two-dimensional modeling: *cond-matt*. 0201105.

Bagnold, R. A. (1941) *The Physics of Blown Sand and Desert Dunes*. Mathuen, London, 265 pp.

Cook, R., Warren, A. and Goudie, A. (1993) *Desert Geomorphology*. UCL press, London, 526 pp.

de Castro, F. (1995) Computer simulation of the dynamics of a dune system: *Ecological Modeling*, **78**, 205–217.

Hack, J. T. (1941) Dunes of the western Navajo Country: *Geographical Review*, **31**, 240–263.

Halsey, L. A., Catto, N. R. and Rutter, N. W. (1990) Sedimentology and development of parabolic dunes, Grande Prairie dune field, Alberta: *Canadian Journal of Earth Sciences*, **27**, 1762–1772.

Jackson, P. S. and Hunt, J. C. R. (1975) Turbulent wind flow over a low hill: *J. R. Met. Soc*., **101**, 929–955.

Kroy, K. and Herrmann, H. J. (2002) Minimal model for sand dunes: *Phys. Rev. Lett*., **88**, 0540301-1-4.

Momiji, H., Carretero-Gonzalez, R., Bishop, S. R. and Warren, A. (2000) Simulation of the effect

of wind speedup in the formation of transverse dune fields: *Earth Surf. Process. Landform*, **25**, 905–918.

Nishimori, H. and Tanaka, H. (2001) A simple model for the formation of vegetated dunes: *Earth Surf. Process. Landforms*, **26**, 1143–1150.

Nishimori, H., Yamasaki, M. and Anderson, K. H. (1998) A simple model for the various pattern dynamics of dunes: *International Journal of Modern Physics B*, **12**, 257–272.

Pye, K. (1982) Morphological development of coastal dunes in a humid tropical environment, Cape Bedford and Cape Flattery, North Queensland: *Geografiska Annaler*, **64A**, 213–227.

Rassmussen, K. (1989) *Proc. of Symposium* '*Coastal Sand Dunes*'. Royal Society Edinburgh, **B96**, 129–147.

Sauermann, G., Kroy K. and Herrmann, H. J. (2001) A continuum saltation model for sand dunes: *Phys. Rev. E*, **64**, 031305-1-10.

Thomas, D. S. G. and Tsoar, H. (1990) The geomorphological role of vegetation in desert dune systems: In J. B. Thornes (ed.), *Vegetation and Erosion*, pp. 471–489. John Wiley and Sons, Chichester.

Tsoar, H. and Moller, J.-T. (1982) *Aeolian Geomorphology*, pp. 75–97. Allen and Unwin, Boston.

Wasson, R. J. and Hyde, R. (1983) Factors determining desert dune type: *Nature*, **304**, 337–339.

Werner, B. T. (1995) Eolian dunes: Computer simulations and attractor interpretation: *Geology*, **23**, 1107–1110.

Concepts and Modelling in Geomorphology: International Perspectives,
Eds. I. S. Evans, R. Dikau, E. Tokunaga, H. Ohmori and M. Hirano, pp. 101–114.
© by TERRAPUB, Tokyo, 2003.

Green's Function of Mass Transport and the Landform Equation

Masashige HIRANO

Graduate School of Science, Osaka City University,
Sugimoto 3-3, Sumiyoshi-ku, Osaka 558-8585, Japan
e-mail: hirano-h@kcc.zaq.ne.jp

Abstract. Transport of the earth surface material associated with diffusion brings a landform change, and the resulted sediment or debris thickness is approximated by a normal distribution. The essential feature of this geomorphic process is described in terms of the transport distance and the spatial spreading of the masses. A unit mass on a slope may move at a rate b downward and spread at a diffusivity a, simultaneously. Thus, we may introduce a kind of Green's function which gives the diffusion over the area at and the transportation over the distance bt of the unit mass situated on a given point at $t = 0$ during the time t. The Green's function is applied to any kind of mass movement, though the constants a and b may change by the processes. Topographic change due to the masses distributed continuously in the source area is derived by integration of the Green's function of mass transport, and the result gives the general solution of the landform equation which means that the rate of erosion is proportional to the convexity and gradient of land surface. The solution derived from the landform equation shows the retreat and subduing of a vertical scarp at $x = 0$ with time in the simplest case. Application of the Green's function to such a present day mass movement as the Ontake landslide in 1984 is also possible, though several problems are open to the future investigations including that from the statistical point of view.

Keywords: Mass Transport, Normal Distribution, Green's Function, Landform Change, Landform Equation, Ontake Landslide

GREEN'S FUNCTION FOR MASS TRANSPORT

Green's function in potential theory defines the effect of a point source to the surrounding area under a definite boundary condition. Thus, the concept of Green's function in broader sense is useful even for such an irreversible process as the heat conduction or mass diffusion as stated by Carslaw and Jaeger (1959). Considering a region with a particular condition on its boundary, we can introduce a Green's function for landform change corresponding to a unit mass of earth surface material at a particular point.

Transport of the earth surface material associated with diffusion brings a topographic change. The essential feature of this geomorphic process is described in terms of the transport distance and the area spreading of mass on slopes by the process concerned. Therefore, it is possible to state that the resulted distribution of debris is approximated at a first step by a normal distribution with the mean μ and the standard deviation σ given by

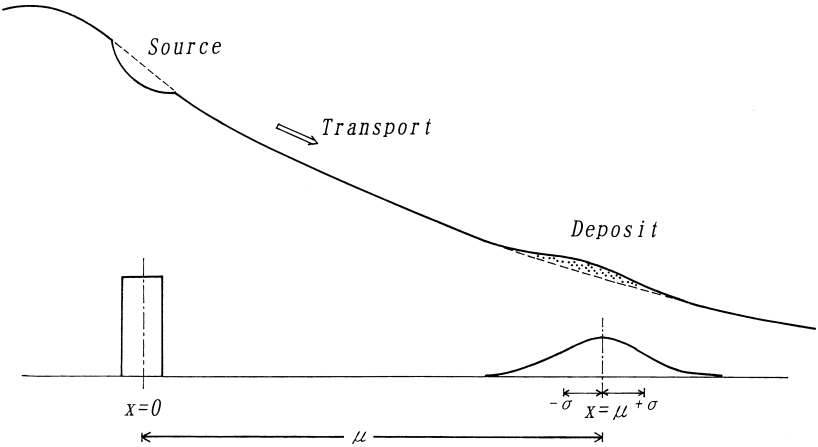


Fig. 1. Schematic presentation of fundamental feature of mass movement in terms of the transportation and diffusion of surface material on a slope. Travel distance is given by $\mu = bt$, and the spreading (diffusion) by $\sigma = \sqrt{2at}$.

$$N(\mu,\sigma) = \frac{1}{\sqrt{2\pi}\sigma} \exp\left\{-\frac{(x-\mu)^2}{2\sigma^2}\right\} \tag{1}$$

as shown by Fig. 1 with the origin $x = 0$ at the source. It is also noted here for further discussion on this account that the normal distribution is the approximation to the binomial distribution which does correspond to the debris distribution over a finite spatial range.

A unit mass on a slope moves at a rate b downward and spreads at a diffusivity a, simultaneously over the time t. Thus, we may introduce

$$u_* = \frac{1}{2\sqrt{a\pi t}} \exp\left\{-\frac{(x-bt-\xi)^2}{4at}\right\} \tag{2}$$

as a kind of Green's function for a unit mass as a unit instantaneous source situated at $x = \xi$ at $t = 0$ in one dimensional case with the boundary at infinity. We may put $\xi = 0$ in Eq. (2) for the comparison with Eq. (1) or Fig. 1, and this means that the source in Eq. (1) is at $x = 0$ as shown in Fig. 1. The function given by Eq. (2) defines the diffusion over the area at and the transportation over the distance bt during the time t. The constants a and b may change by the geomorphic processes.

The scheme shown in Fig. 1 concerns the mass movement chiefly, but it is possible to apply this even to the sediment transport based on its essential feature.

Thus, it is reasonable to consider that Eq. (2) concerns the mass transport in broader sense and is applied to various geomorphic processes including the landslide or sediment transport.

In general case, the mass distributes continuously along x-axis from $x = -\infty$ to $x = +\infty$ forming a slope, and the initial distribution can be expressed by $f(x)$ at $t = 0$. The function $f(x)$ may define the land surface elevation as the initial condition. Topographic change for the continuous masses is thus given by integration of Eq. (2), and we have

$$u(x,t) = \frac{1}{2\sqrt{a\pi t}} \int_{-\infty}^{+\infty} f(\xi) \exp\left\{-\frac{(x - bt - \xi)^2}{4at}\right\} d\xi \tag{3}$$

Equation (3) describes the redistribution of the continuous masses associated with the transportation and diffusion on the slopes, and the process brings topographic change.

It should be emphasized here additionally that the movement (transportation) is restricted to down-hill orientation on land surface, and this is an important difference of geomorphic mass transport from the usual diffusion. Derivation of the mass from a source (erosion) and its later settlement (deposition) are both directly connected with the change of land surface elevation.

LANDFORM EQUATION

The next problem is to know the differential equation which has the Green's function given by Eq. (2). By substitution of $b = 0$ and putting $u_* = h_*$, Eq. (2) reduces to

$$h_* = \frac{1}{2\sqrt{a\pi t}} \exp\left\{-\frac{(x - \xi)^2}{4at}\right\} \tag{2'}$$

which gives the effect of a point source without transportation, and this is the chief portion of Green's function for the equation of diffusion or heat conduction given by

$$\frac{\partial h}{\partial t} = a \frac{\partial^2 h}{\partial x^2} \tag{4}$$

for one-dimensional case in an infinite media (Carslaw and Jaeger, 1959). Equation (4) was first introduced by Culling (1960) to analyse the erosional process of hill slopes.

Introducing a new variable u given by

$$h = u\exp\{\alpha t + \beta x\} \text{ with } \alpha = \frac{b^2}{4a} \text{ and } \beta = \frac{-b}{2a}$$

Eq. (4) for h changes by this transformation to

$$\frac{\partial u}{\partial t} = a\frac{\partial^2 u}{\partial x^2} - b\frac{\partial u}{\partial x} \tag{5}$$

for which Eq. (2) is the Green's function. In other words, Eq. (2) is the solution of Eq. (5) corresponding to a unit instantaneous source on $x = \xi$ at $t = 0$. It is noted here that $\partial u/\partial x$ is positive for positive b as the surface elevation decreases with time by erosion usually.

Equation (5) is the landform equation proposed by Hirano (1966) in order to describe the landform change in one dimensional case and studied systematically (Hirano, 1968, 1975, 1976). The equation means geomorphologically that the rate of landform change concerns the slope gradient and curvature with the elevation u. Equation (5) is possible to be explained as a process response model (Hirano, 1990), though weathering of bed rock is still open as a future problem.

Equation (3) gives the general solution of Eq. (5) when the continuous mass distribution is given by $u = f(x)$ at $t = 0$, where $f(x)$ defines the initial land surface elevation. The simplest solution of Eq. (5) is obtained for the initial condition,

$$u = u_0,\ x > 0 \quad u = 0,\ x < 0$$

which means a vertical scarp at $x = 0$. Substituting this into Eq. (3), we have the solution,

$$u(x,t) = \frac{1}{2\sqrt{a\pi t}}\int_0^{+\infty} u_0 \exp\left\{-\frac{(x - bt - \xi)^2}{4at}\right\}d\xi = \frac{u_0}{2}\left\{1 + \operatorname{erf}\frac{x - bt}{2\sqrt{at}}\right\} \tag{6}$$

where the error function erf$x$ is defined by

$$\operatorname{erf} x = \frac{2}{\sqrt{\pi}}\int_0^x \exp\{-\xi^2\}d\xi$$

The solution shows the simultaneous retreat and subduing of a vertical scarp at $x = 0$ with time as shown in Fig. 2.

A variety of landforms is explained partly in relation to the initial and boundary conditions for the landform equation. Spatial distribution of the erosional coefficients corresponding to lithologic features also concerns such topographic features as structural bench land, cuesta, dyke ridge, etc. The variety

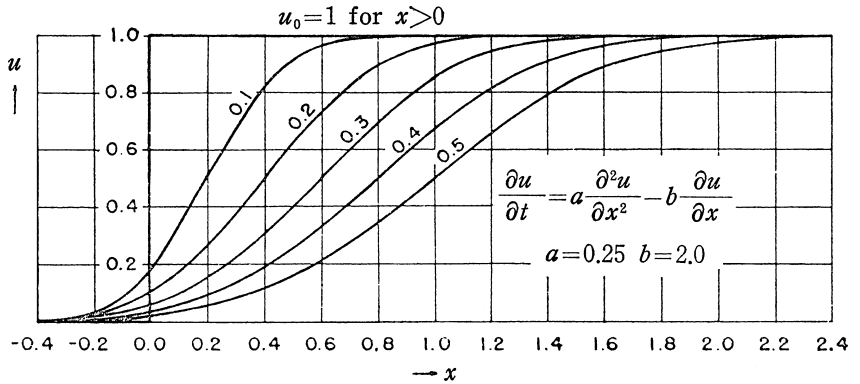


Fig. 2. Retreat and subduing of a vertical scarp at $x = 0$ with time derived from the landform equation. After Hirano (1968).

of morphology is derived too from the nature of tectonic movement which is given by the term $g(x, t)$ added to the right side of Eq. (5). The term $g(x, t)$ defines the rate of material supply above the base level, and possibly it takes the form of $X(x)\cdot T(t)$ corresponding to the separable space-time distribution of such tectonic movement as the case of uplift of block mountains.

LONG-TERM EVALUATION OF EROSIONAL COEFFICIENTS

The coefficients a and b in Eq. (5), the erosional coefficients together as they bring erosion, were called the subduing coefficient and the recessional coefficient, respectively, by Hirano (1968) based on their effects on landform change. A vertical scarp retreats and subdues with time as shown in Fig. 2, as the result of combined effect of these coefficients.

This fact is applied conceptionally to any kind of scarps in order to evaluate a and b quantitatively. Determination of the coefficients over geologic time scale is possible based on the morphometric feature, for instance, of fault scarps for which the fault line as the scaling origin is given, or of terrace scarps for which the age of formation is often given.

Normal distribution given by Eq. (1) concerns the determination of the coefficients a and b. Cumulative curve $\varphi(x)$ of a normal distribution with $\mu = 0$ and $\sigma = 1$ is given by

$$\varphi(x)=\frac{1}{\sqrt{2\pi}}\int_{-\infty}^{x}\exp\left\{-\frac{\xi^2}{2}\right\}d\xi$$

and this has a particular relationship to erf$x$ given by

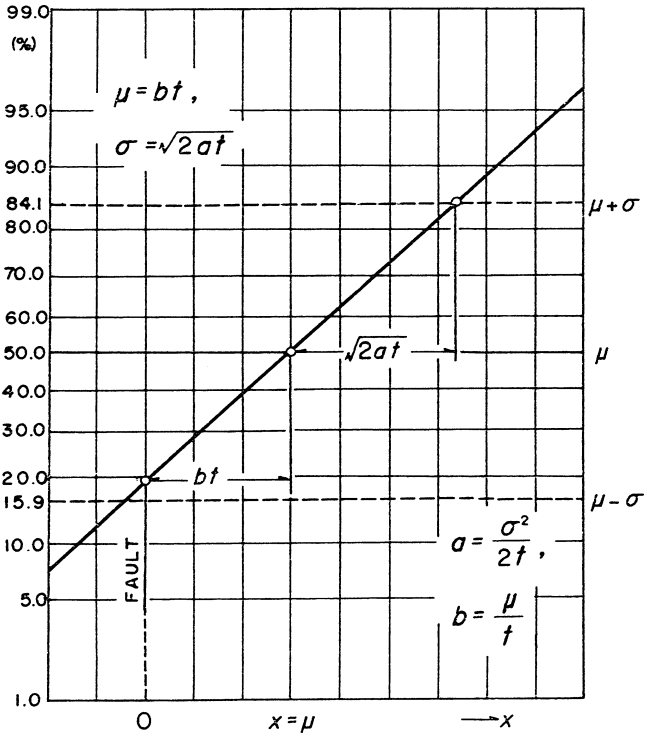


Fig. 3. Morphology of a scarp on a probability paper showing the simultaneous retreat and subduing during a given time span. After Hirano (1972).

$$\varphi(x) = \frac{1}{2}\left\{1 + \mathrm{erf}\left(x / \sqrt{2}\right)\right\}, \text{ or } \mathrm{erf}x = 2\varphi\left(\sqrt{2}x\right) - 1$$

Therefore, we have

$$\sigma = \sqrt{2at} \tag{7a}$$

$$\mu = bt \tag{7b}$$

for Eq. (6) by comparison. Cumulative curve of normal distribution is shown by a straight line on a probability paper (Fig. 3).

Morphometric data on fault scarps even be the volume preservative (Hirano, 1967) or the slope preservative (Hirano, 1972) are often approximated by straight lines on the probability paper with $x = 0$ at the fault line. The quantities μ and σ

Table 1. Estimated erosional coefficients where Rokko and Hira for fault scarps and Ontake for gigantic landslide. Numerals in parentheses were assumed.

Loc.	μ (km)	σ (km)	t	$a(=\sigma^2/2t)$	$b(=\mu/t)$
Rokko(1)	0.22～0.21	0.36～0.27	(10^6years)	0.065～0.036	0.21～0.22
Rokko(2)	0.37～0.38	0.64～0.48	(10^6years)	0.21～0.12	0.37～0.38
Hira	1.09～1.14	0.55～0.64	(10^6years)	0.151～0.205	1.09～1.14
Ontake-1	7	0.5	266～355sec	$1.48\sim1.11\times10^{10}$	$8.3\sim6.2\times10^{11}$
Ontake-2	10	1	(308～380sec)	$4.15\sim3.11\times10^{10}$	$(8.3\sim6.2\times10^{11})$

*a in m^2/year, b in mm/year.

are thus determined on the paper. If the age t since the scarp formation is known, though it be the Davisian concept on tectonism (Davis, 1912), the constants a and b are scaled, using Eqs. (7a) and (7b) for σ and μ obtained by morphometry.

Determination of t is often difficult for fault scarps as they move continuously or intermittently (the Penckian concept on tectonism as maintained in 1924) but the age of fresh fault scarps in Japanese island is probably 10^6 years or less (almost the later half of the Quaternary) in order of magnitude. As μ and σ for fault scarps have some 10^2~10^3 m in order of magnitude (Hirano, 1967, 1972), the constants b and a are thus to be 0.1~1 mm/year and 0.005~0.5 m^2/year, respectively in geologic time scale as shown in Table 1. Dimensionless parameter σ/μ gives the relative diffusivity to transport distance, and we have σ/μ almost equal to 1. It is a future problem to determine the constants more precisely. Even though, the result concerning the fault scarps suggests the conceptional applicability of Green's function given by Eq. (2) as well as Eq. (5) to the various types of mass transport including rapid mass wasting, as the fault scarps are shaped eventually by the combined or integrated geomorphic processes including the rapid mass movements.

APPLICATION TO PRESENT DAY MASS MOVEMENTS

It is appreciated to evaluate the erosional coefficients for the individual process in the present day space and time, directly from the transportational distance and the degree of diffusion. Diffusion or spreading by an actual event could be almost one-dimensional if the mass moves in a narrow linear channel, but it would be two-dimensional if the mass spreads over an open space. Diffusivity clearly depends on the processes concerned additionally, and several processes are mixed in the actual mass transport. Separation of the processes in addition to the dimensional reduction is, thus, appreciated to evaluate the parameters concerned there if possible.

When the elevation D_* is lost at the origin in one-dimensional profile, we have depositional thickness given by

$$D(x) = \frac{D_*}{2\sqrt{a\pi t}} \exp\left\{-\frac{(x-bt)^2}{4at}\right\} \tag{8}$$

from Eq. (2) for point source at $x = 0$ where the mass of surface material was concentrated before the event. For a planner spreading, debris moves to x-direction but spreads both in x- and y-directions and $(x - bt)^2$ in Eq. (8) is to be replaced possibly with $(x - bt)^2 + y^2$.

If we employ Eq. (8) for the sake of simplicity, we have

$$D(x) = \frac{D_*}{\sqrt{2\pi}\sigma} \exp\left\{-\frac{(x-\mu)^2}{2\sigma^2}\right\} \tag{8′}$$

by replacing $\sqrt{2at}$ with σ, and bt with μ, respectively. The intensity of point source D_* can be estimated from the maximum thickness of the accumulated debris along the central profile or from the volume at the source correlative to unit width. The parameters μ and σ are also estimated from the debris thickness distribution after the mass movement.

Here we investigate the case of Mt. Ontake as a representative and effective one where a part of the volcanic slope was destroyed by a gigantic landslide triggered by the 1984 earthquake. The volume in the source area obtained by photogrammetry exceeds 3.4×10^7 m^3 (Nagaoka, 1984). The failed mass moved downward along a channel, and the change of river-bed elevation by the accumulation of debris was detected by precise photogrammetry as shown in Fig. 4A by Okuda *et al*. (1985) and by morphometry from topographic maps in Fig. 4B. Though the debris flowed partly over ridges into other channels, we employ here one-dimensional model for the sake of simplicity.

Two remarkable accumulations of debris are detectable in Fig. 4. Depositional amount along the channel is approximated respectively by a normal distribution as shown in Fig. 4 by the broken lines, though the down stream extension of debris suggests the existence of other minor accumulation units. We have the approximate values of $\sigma_1 = 0.5$ km and $\mu_1 = 7$ km for upstream with $D_{*1} = 65$ m, and $\sigma_2 = 1$ km and $\mu_2 = 10$ km with $D_{*2} = 100$ m for downstream, respectively, where μ was measured from the approximate center of the source area. It is noted that the sum $D_{*1} + D_{*2}$ is almost correlative to the maximum depth 150 m of the landslide.

The time required for debris transport from the source to the confluence of Nigorizawa on the Ohtaki-gawa river shown by 0-km point in Fig. 4 is estimated to be 367 sec to 390 sec, and the average velocity ranges from 26.3 to 19.7 m/sec (Okuda *et al*., 1985), or 8.3 to 6.22×10^8 m/year, depending on the check-point specification. The values give the coefficient b_1 directly, and this is applicable to the first (up-stream) debris mound. From this fact, we have $t_1 = 266.2$ sec to 355.3 sec for $\mu_1 = 7$ km for upper mound, and thus $a_1 = \sigma_1^2/2t_1 = 469.9$~$351.8$ m^2/sec,

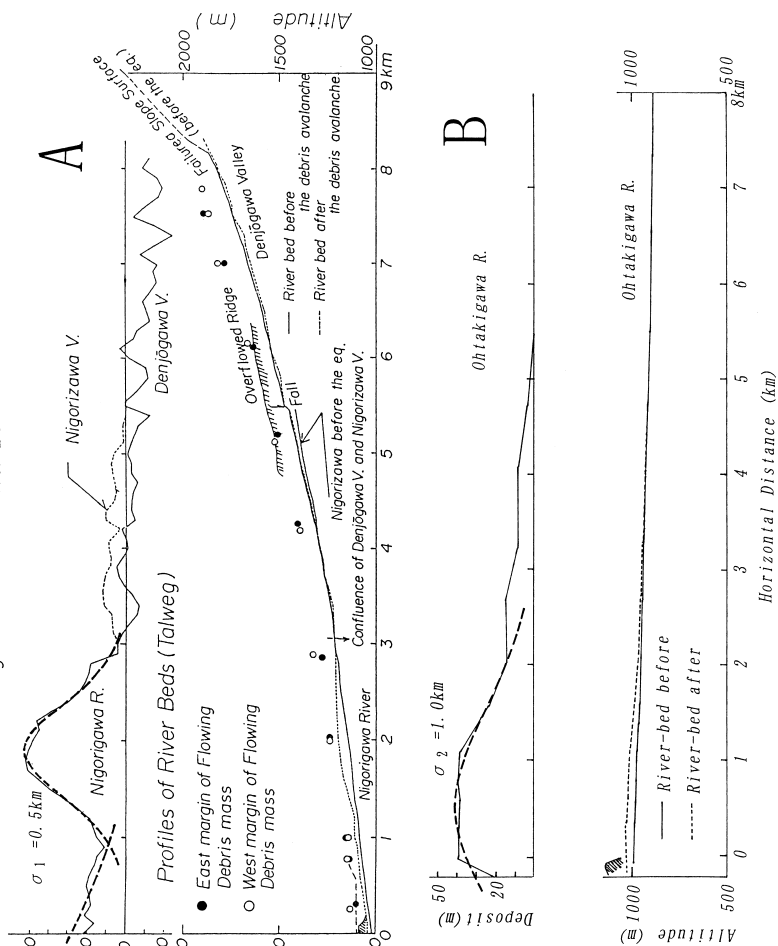


Fig. 4. Gigantic landslide at Mt. Ontake and debris transport where A (above) is simplified from Okuda *et al.* (1985) and B (below) by morphometry from maps. Change of river-bed elevation due to debris accumulation is approximated by a couple of normal distributions.

or 1.48~1.11 $\times$ 10^{10} m^2/year.

It is difficult to know exactly when the second (down-stream) debris mound stopped. A possible case is simultaneous freezing under the different moving velocity, and another case is successive freezing one after another presumably moving with almost same velocity. Estimation of the velocity just at the confluence point using super-elevation gives 17 m/sec (Okuda *et al*., 1985) which can be applied to the down-stream debris mound, and the value suggests the latter case as an approximation. Thus, we have t_2 = 380.2 to 507.6 sec for $b_2 = b_1$, and this brings a_2 = 1315~985 m^2/sec or 4.15~3.11 $\times$ 10^{10} m^2/year. The results are summarized in Table 1. It is true that a or b is extraordinarily large. However, the dimensionless parameter σ/μ is 0.07 for the up-stream and 0.05 for the down-stream, and no significant difference is detected.

FURTHER REMARKS

The concept of Green's function is applied to any landform change eventually. However, the long-term erosional coefficients obtained from the fault scarp morphology is much less than those obtained from the present day mass movement. Nevertheless, comparison of the dimensionless parameters, σ/μ, means that the material composing the fault scarps diffuses more easily through long time span. A possible way to overcome the contradictions is a statistical investigation.

It is probable to consider from statistical point of view that the erosional coefficients for wide area over long period give the average values for some ensemble of individual and discrete processes. Statistical investigation concerns the magnitude-frequency relationship and the return period of the events even in the case of landslide, in addition to the differential mobility of the debris characteristic to the respective process.

In order to compare the long-term diffusivity with that for single event, it is noted that a landslide as a source appears at a definite time, to say, $t = \tau$. This means in the statistical investigation that a point source begins to work at $t = \tau$, and that the frequency of source appearence or the return period of landslide has to be taken into account.

Moreover, a definite time span concerns the mass transport. The situation is shown in Fig. 5, where each of respective events has happened discretely over a long period, and has a specific duration time t_i for the movement. The average rate over the long period in which several events are included gives much less value than that of the individual event as shown in Fig. 5 with some exaggeration.

From spatial point of view, the relationship between a single event and a regional average is concerned. The area A_* and the volume V_* of a landslide are known for individual mass transport. Thus we may divide at first the whole area A into the unit area of A_*, and introduce a grid system. In other words, the whole area A is consists of n unit areas, and we have

$$A = nA_* \tag{9}$$

Probability of occurrence of an event once over the whole area brings the

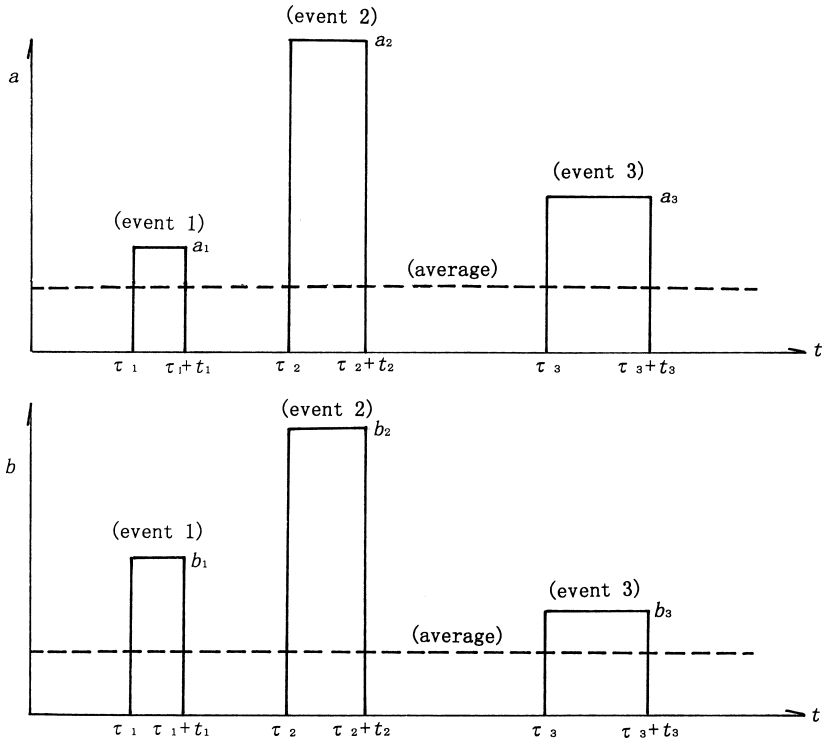


Fig. 5. Schematic relationship between the discrete unit events and the long-term average in the evaluation of coefficients. Coefficients obtained by application of Green's function for individual unit event can be extraordinarily larger than the average value.

frequency of $1/n$ for a grid point spatially. If the recurrence period of the event is m years, we have the frequency of $1/m$ for a year chronically at a grid. Therefore, we have the probability $1/mn$ for a year at a grid point. Lowering of the elevation by an event is thus given by

$$\delta u = D/mn \tag{10}$$

a year at a grid point in average, where D is the depth given by V_*/A_*.

If we apply this to the case of Ontake, the total area of Japanese Islands is ca. 3.7×10^5 km^2 though the area of mountainous region is less than A given here, and the area A_* is 0.65 km^2 for the Ontake landslide approximately. Thus, we have $n = 5.7 \times 10^5$. The landslide of Ontake class is estimated to be twice (another identical case is Mt. Bandai in 1888) or 4 times (with the additional Totsukawa hazard in 1889 and Hiedayama landslide in 1911) for recent 100 years in Japan, and this means $m = 50$~25. We have thus $1/mn = 0.36$~0.70×10^{-7}. The average depth of Ontake landslide is $D = 3.4 \times 10^7$ m^3/0.65 km^2 = 52.3 m, and we have the

Table 2. Ontake landslide and parameter estimation where b is for $|du/dx| = 0.3$ (total area of Japanese Islands, A; 3.7×10^5 km^2).

Volume (V_*);	3.4×10^7 (m^3)	
Area (A_*);	0.65 (km^2)	
Average depth (D_*);	52.3 (m)	
Frequency (f_*);	2/100	or 4/100 (years)
$\lvert \delta u/\delta t \rvert$	1.9×10^{-6}	or 3.7×10^{-6} (m/year)
recessional coefficient (b)	0.0063	or 0.012 (mm/year)

average lowering of $\delta u = 0.63 \sim 1.2 \times 10^{-2}$ m a year for the whole area.

In order to translate δu to b based on Eq. (5), the slope gradient $\partial u/\partial x$ must be introduced, even if $\partial^2 u/\partial x^2$ is very small and negligible. Assuming $I = |\partial u/\partial x| = 0.3$ (=16.7 deg.) in average, we have $b = 6.1 \times 10^{-3}$ mm/year from $b = |\partial u/\partial t|/I$, if the term including $\partial^2 u/\partial x^2$ is neglected (Table 2). Choice of another possible value of $\partial u/\partial x$ does not bring the remarkable change of order of magnitude.

Another approach based on the travel distance is possible, which may be more significant statistically than the instantaneous moving velocity, by analogy to Brownian movement evaluated by the resultant mean free path of molecules. Having distribute the value of $\mu = 7 \sim 10$ km at Mt. Ontake to all grid points and taking the average over the recurrence period, we have $b = 0.25 \sim 0.7$ mm/year at each grid for $1/mn = 0.36 \sim 0.70 \times 10^{-7}$. The value is correlative to that for fault scarps.

We face here some discrepancy especially in the first estimation that the long-term value for fault scarps is more than 10 times larger than the value in the first estimation. The discrepancy may comes first from the estimation of parameter values including A. Morphometric data based on digital elevation model over Japanese Islands may supply more improved estimates of slope gradient and curvature (Laplacian). The second reason of discrepancy comes from the magnitude-frequency relation of mass movement as discussed by Hirano and Ohmori (1989). Especially the latter concerns the total volume estimation by mass movements over long period, and it exhibits the fractal nature that the frequency decreases with the increasing magnitude (area or volume). Therefore, the geomorphic processes with small magnitude but high frequency may bring the superposition of δu, and b larger than those obtained here may be expected.

CONCLUSION

Any kind of mass movement on the slope is characterized by the transport distance and the degree of scattering of the debris. The debris thickness is approximated by a normal distribution eventually. Based on this fundamental features, it is possible to introduce a Green's function identical to the normal distribution with $\mu = bt$ measured form the source and with $\sigma = \sqrt{2at}$. The Green's function in broader sense explains the simultaneous transportation and diffusion

of a unit mass at a point source.

We of course face to the problem that the debris has to distribute from $-\infty$ to $+\infty$ logically if the normal distribution is applied. This is different from the actual debris distribution after the mass movements. It is well known however that the normal distribution is an approximation to the binomial distribution which shows a definite range of distribution. The normal distribution or the identical Green's function converges quickly leaving from the mean though it covers continuously from $-\infty$ to $+\infty$, and the convergence as well as the continuity plays such an important role as a special function to be a singular solution of partial differential equation from the analytical point of view.

The partial differential equation, namely the landform equation with the erosional coefficients, corresponding to the Green's function discussed here explains the features of landform evolution systematically. It is possible thus methodlogically to apply the concept to long-term landform change and to present day processes. In other words, the Green's function of mass transport gives a way to integrate the present day individual processes over the space and time on the basis of the corresponding landform equation.

Conclusively, Green's function for a point source can be a common scale to measure various kinds of present day mass transports and to evaluate their integrated effects over the long time and the large space. Application of this method to many more cases and evaluation of the features of mass transport processes in terms of the erosional coefficients are appreciated in the future, in addition to the precise statistical and kinetic investigations covering the individual mass movement. Of course, the limitation of one-dimensional treatment should be emphasized too, as the actual process is not the simple linear diffusion but it occurs on rugged topographic surface.

REFERENCES

Carslaw, H. S. and Jaeger, J. C. (1959) *Conduction of Heat in Solid* (2nd ed.). Oxford Univ. Press, London, 510 pp.

Culling, W. E. H. (1960) Analytical theory of erosion: *Jour. Geol*., **68**, 336–344.

Davis, W. M. (1912) *Die erklarende Beschreibung der Landforemen*. Teubler, Leipzig, Berlin, 565 pp.

Hirano, M. (1966) A study of mathematical model of slope development: *Geogr. Rev. Japan*, **39**, 36–48 (in Japanese with English abstract).

Hirano, M. (1967) Discussion on the two-dimensional morphometry of fault scarps: *Chikyu-kagaku*, **21-3**, 11–21 (in Japanese with English abstract).

Hirano, M. (1968) A mathematical model of slope development: *Jour. Geosci., Osaka City Univ*., **11**, 13–52.

Hirano, M. (1972) Quantitative morphometry of fault scarp with reference to the Hira Mountains, Central Japan: *Japan Jour. Geol. Geogr*., **XLII** (Nos. 1–4), 85–100.

Hirano, M. (1975) Simulation of developmental process of interfluvial slopes with reference to graded form: *Jour. Geol*., **83**, 113–123.

Hirano, M. (1976) Mathematical model and the concept of equilibrium in connection with slope shear ratio: *Z. Geomorph*., Supple. Bd., **25**, 50–71.

Hirano, M. (1990) Mass diffusion models in geomorphology and the related problem: *Trans. Japan Geomorph. Union*, **11-3**, 191–215 (in Japanese with English abstract).

Hirano, M. and Ohmori, H. (1989) Magnitude-frequency distribution for rapid mass movements and its geomorphic implications: *Trans. Japan Geomorph. Union*, **10**, 95–111 (in Japanese with English abstract).

Nagaoka, M. (1984) Disasters by Naganoken-seibu earthquake: *Sokuryo*, **34** (No. 12), 22–28 (in Japanese with English abstract).

Okuda, S., Okunishi, K., Suwa, H., Yokoyama, K. and Yoshioka, R. (1985) Restoration of motion of debris avalanche at Mt. Ontake in 1984 and some discussions on its moving state: *Bull. Disas. Prev. Inst., Kyoto Univ.*, **28**(B-1), 491–504 (in Japanese with English abstract).

Penck, W. (1924) *Die morphologische Analyse*. J. Engelhoruns Nachf., Stuttgart, 283 pp.

Concepts and Modelling in Geomorphology: International Perspectives,
Eds. I. S. Evans, R. Dikau, E. Tokunaga, H. Ohmori and M. Hirano, pp. 115–129.
© by TERRAPUB, Tokyo, 2003.

Towards Quantitative Modelling of Landform Evolution through Frequency and Magnitude of Processes: A Model Conception

Jochen SCHMIDT* and Nicholas James PRESTON**

Geographisches Institut, Universität Bonn,
Meckenheimer Allee 166, 53115 Bonn, Germany
e-mail: j.schmidt@niwa.co.nz

Abstract. In recent years, various process-based models for the evolution of regional landform systems have been developed (Coulthard, 2001). Quantitative models have considerable use in applied geomorphology, but also represent a good means we have for testing and developing theoretical models. Nevertheless, there remains a considerable gap between the detailed quantitative representation of individual process behaviour and its integration across spatial and temporal scales that are relevant to landform evolution (Hergarten and Neugebauer, 1999a). A major research issue that must be confronted is the differing frequencies and magnitudes of the various processes that contribute to regional landform evolution. A unifying concept that offers promise is that of the sediment cascade, i.e. viewing geomorphic processes as contributing to the general system of sediment flux through the landscape. In this paper, we present a formulation for modelling sediment flux at the Holocene timescale and at regional spatial scales (3rd/4th order drainage basin, Preston and Schmidt, 2003). The temporally integrated production of sediment from individual geomorphic units is derived through reference to frequency/magnitude distributions of process behaviour. The model operates at coarse spatial scales, providing a framework for linking individual geomorphic systems as components within a regional scale sediment flux model. The proposed modelling approach combines classical conceptualisation of landscapes into units with process-based flux modelling concepts and therefore represents an upscaling approach for models of landscape evolution. A series of issues with respect to contemporary geomorphologic research are discussed on the basis of the presented model approach.

Keywords: Landform Evolution, Sediment Cascade, Numerical Modelling, Conceptual Modelling, Frequency/Magnitude

INTRODUCTION

Models of landform evolution can be characterised as either qualitative or quantitative (Fig. 1). Qualitative approaches have involved geomorphogenetic and chronostratigraphic reconstruction of former landsurfaces and are often

*Present address: National Institute of Water and Atmospheric Research, PO Box 8602, Riccarton, Christchurch, New Zealand.

**Present address: Department of Physical Geography, Macquarie University, North Ryde, Sydney, New South Wales 2109, Australia.

based on dating results (Wasson *et al.*, 1998; Lang and Hönscheidt, 1999; Eriksson *et al.*, 2000). Alternatively, in recent years there has been an increase in the number of attempts to simulate landform development using numerical models of varying complexity (Armstrong, 1987; Kirkby, 1990; Willgoose *et al.*, 1991; Braun and Sambridge, 1997; Coulthard *et al.*, 1998; Hergarten and Neugebauer, 1999b). These models use more or less detailed descriptions of individual processes (e.g. gully erosion or fluvial sediment transport) ranging from simple threshold models (Kirkby, 1990) to differential equations describing sediment flux (Coulthard *et al.*, 1998). The individual process models are usually applied using artificial discretisation of the study area in space and time (often fixed grid cells and time steps), the size of which is determined by the maximum required resolution for the used process models and their interactions. Spatio-temporal scales and resolutions to which these models can be applied show a wide range (Preston and Schmidt, 2003).

Qualitative approaches can provide information about the development of small scale features, and insight into the underlying mechanisms. Their use for modelling of regional landform development, however, is limited by the scale transfer problem, i.e., larger scale systems are not simply larger versions of small scale systems. Further, because such reconstructions are often based on simple assumptions of geomorphic processes, they run the risk of being influenced by subjective interpretation. For these reasons, numerical/process-based models are more desirable, which are useful to explore process behaviour beyond the limits of individual locations (e.g. sensitivity studies) and therefore are applicable to large areas.

There are physically-based models for most if not all geomorphic processes and, on a small scale, they do indeed represent components of landform development. However, it is a research issue whether, and how, these models can be applied within the framework of regional landform development (Hergarten and Neugebauer, 1999a). In recent years, various models for the development of regional landform systems have been proposed (Coulthard, 2001). These models range from comparatively simple approaches (simplification of geomorphic processes) to complex models including detailed descriptions of individual processes (Coulthard, 2001; Preston and Schmidt, 2003). Generally, these approaches are based on process dependent formulations of sediment detachment, transport, and accumulation. Whereas the simple approaches of Armstrong (1987), Ahnert (1988), and Kirkby (1990) are based on parametric equations for sediment fluxes, the more complex recently developed models (e.g. Coulthard *et al.*, 1998) use common physically based formulations. However, obvious problems in both cases relate to model parameterisation and validation (see Schmidt, 2001; Preston and Schmidt, 2003). In the first case, the parameters used represent large scale process abstractions (e.g. denudation rates); in the second case, the spatio-temporal model parameterisation is normally impossible with respect to real world conditions. Usually both model types deliver temporal sequences of landform surfaces (either 2D or 3D). A main problem is how to verify these outputs and compare them with real world conditions. Therefore, most of the

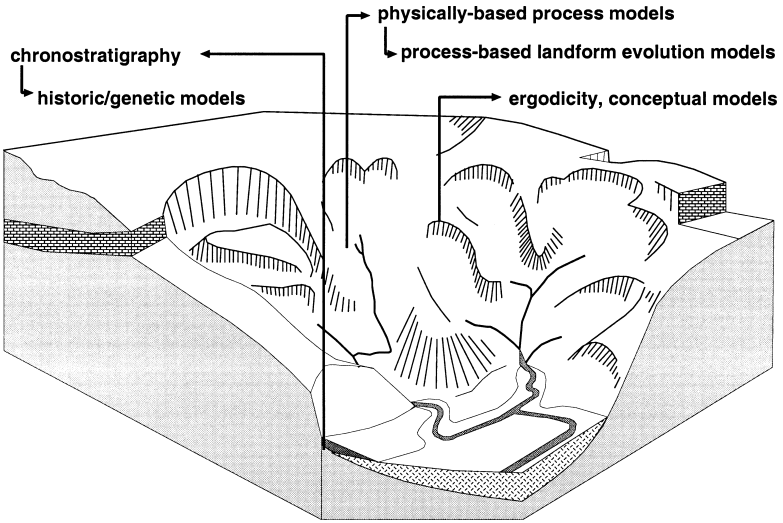


Fig. 1. Evidence and models used in understanding geomorphic systems: These range from detailed and small scale process models, principles and simplified models of landform evolution to singularily available field evidences.

modelling approaches remain speculative and unverified. Another problem relates to the various coupled processes within a landsystem, which operate at different magnitudes and with different frequencies. Understanding the interactions of these processes on longer timescales and the integration of these within landscape evolution models remains an unresolved issue. This present situation leaves a gap between numerical modelling of individual processes on the one hand and general landform evolution models on the other hand (Hergarten and Neugebauer, 1999a). It remains undetermined, if, and to which degree, detailed process modelling can contribute in modelling landform change, a system which acts on a different spatio-temporal scale. Much more research is needed in filling this gap and to come to a more fundamental understanding of landform systems and landform change on a physical basis. In general, it is questionable whether a landform surface, modelled with more or less spatial details can and should be compared with real world conditions; modelling and verifying plausible patterns may well be a more realistic objective of long term modelling (Beven, 1996; Preston and Schmidt, 2003).

Therefore, it might be more appropriate to view a landform as a composite system of landform units and to model their properties and interactions, rather than to model detailed surface development and pixelwise matter fluxes. Preston and Schmidt (2003) therefore argue for a hierarchical approach for modelling regional sediment flux over Holocene timescales. The model concept combines aspects from different scientific directions within geomorphology (Fig. 2). In this paper we present a model formulation of this concept, and the approach is used

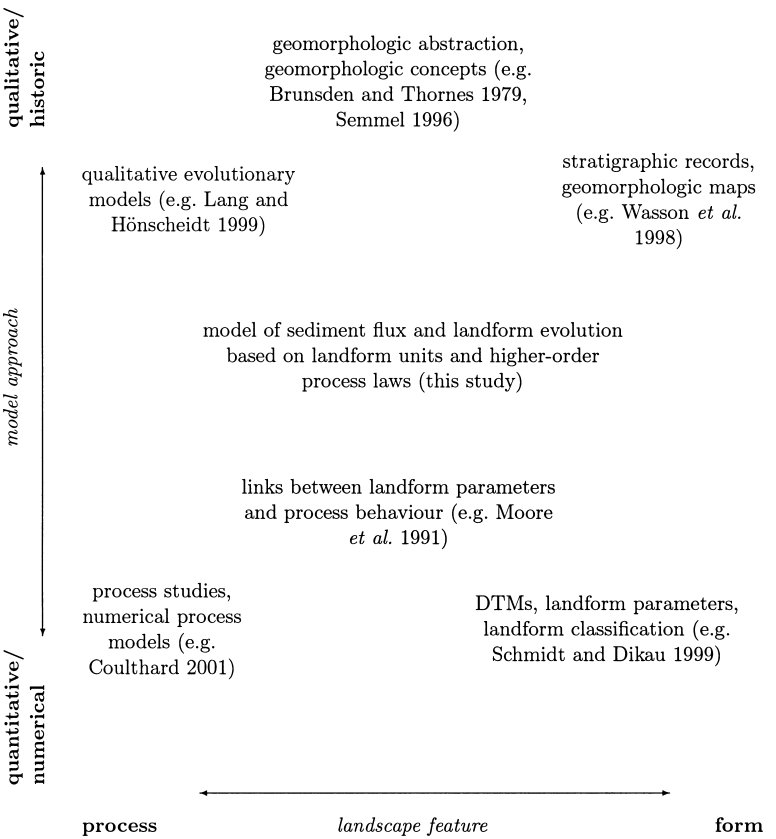


Fig. 2. Scientific position of the proposed model approach within the framework of model concepts (qualitative/quantitative) and modelled features (process/form). Quantitative approaches include process modelling and landform parameterisation. Some efforts have been made to find links between processes and parameters. Qualitative approaches include historic/genetic models, which are often based on stratigraphic records. Qualitative models include high degree of abstraction/expert knowledge. The model presented in this paper aims to find links between these approaches by higher-scale modelling of sediment flux based on a geomorphologic abstraction of land surface.

to discuss some key questions with respect to understanding regional landform systems.

WHAT IS REGIONAL LANDFORM EVOLUTION?

It has to be kept in mind that the *geomorphic evolutionary system* is highly complex, acting on different scales in space and time (Schumm, 1979; Chorley *et al.*, 1984). Therefore, system descriptions on different scales have to be developed. It is the purpose of this paper to introduce a conception and a modelling approach

for landform evolution at regional spatial scales (3rd/4th order drainage basins, approx. 10^8 m^2, scale of mesorelief according to Dikau (1990)). Typical landform systems within this respect include the Holocene development of the soft rock hill country on the east coast of New Zealand (Page and Trustum, 1997; Eden and Page, 1998; Trustum *et al.*, 1999) or the development of the Tertiary cuesta region in central Germany (Semmel, 1995; Preston, 2001). These systems, i.e. the related landform components (sediment storages), show residence times in the order of 10^3–10^4 a. Therefore, processes of sediment redistribution and sediment storages varying in timescales of tens to hundreds of years are considered, i.e. hillslope processes (soil erosion, mass movement) and colluvial storages, fluvial processes and alluvial storages. This means that the total timescale of interest is on the order of 10^4–10^5 a, and that the temporal resolution, determined by rates of major process activity, is in the range of 10^1–10^2 a. The typical regional landform system within this respect is illustrated in Fig. 1. It consists of sediment storages on the hillslopes and on the alluvial plains. Hillslope processes are dependent on hillslope form, but also change hillslope form on the other hand by creating erosive and accumulative form sequences (Fig. 1). These processes interact with fluvial processes which are dependent on channel morphology.

As one can see, the described system is a crude simplification of the complexity of landform systems. However, it is the purpose of this study to focus on the dominant forms, processes and interactions which characterise the study objective (Beven, 1996). We believe that this approach can more effectively assist in understanding regional landform systems than focusing on the complexity and possible variations and exceptions inherent in these systems types (Band *et al.*, 1993).

MODELLING LANDFORM COMPONENTS BY SEDIMENT FLUX

Landform is spatially and temporally hierarchical. The temporal scale of interest defines the appropriate spatial scale, and vice versa. Further, landform development involves a hierarchy of processes. While landform evolution occurs through processes of rilling, gullying, creep, landsliding, etc., modelling of these processes per se is not the objective of the present discussion; rather it is their net long term combined effect that is of interest, i.e. the “processes” of slope development and drainage development.

The link between individual processes and the morphologic evolutionary system of landform development is the *cascading* system of regional sediment flux. Chorley and Kennedy (1971) have argued that each process subsystem within the cascading system occurs with a different frequency/magnitude distribution resulting in a complex *process-response* system characterised by equilibrium and transient system stages and thresholds (Schumm, 1979; Preston and Schmidt, 2003). Indeed, it is these system characteristics that are the major focus of interest in modelling regional landform evolution, i.e. this is what can be expected from modelling of regional landform evolution rather than reconstructing the detailed development of three-dimensional surfaces. Modelling of landform evolution by sediment flux requires that a geomorphic system is separated into

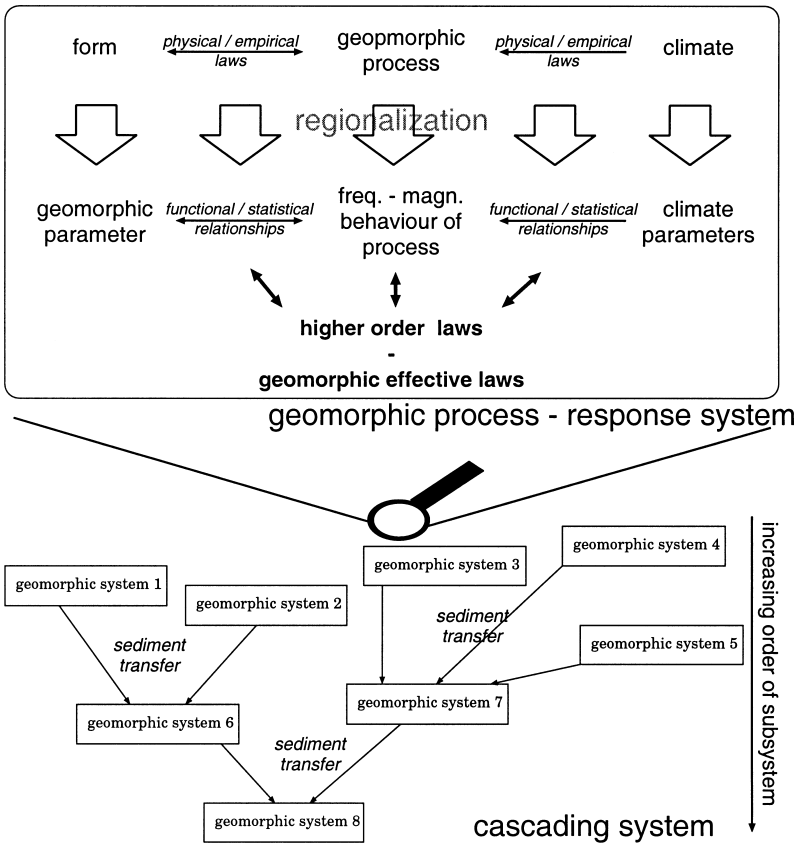


Fig. 3. Cascading system and geomorphic process-response system as parts of a geomorphic sediment cascade. Sediment transfer through the cascade can be easily described, if an appropriate topology of geomorphic subsystems is defined. Calculation of sediment produced by each subsystem is a problem, which cannot be solved in appropriate temporal and spatial scales by applying physically-based models. Hence, simpler geomorphic laws have to be found describing functional relationships between representative parameters and the frequency-magnitude characteristics of the processes.

individual components of the cascading system (and the related geomorphic components). The matter fluxes between the components should be modelled using process knowledge and scale transfer methodologies.

In the approach presented, the cascading system is simplified to a hierachical connected structure of geomorphic subsystems transfering sediment through the geomorphic cascade (Fig. 3). An example would be a system of drainage basins, from zero-order head water basins to the regional base level. Each subsystem can be viewed as a geomorphic process-response system with a geomorphic form, and geomorphic processes mainly determined by climatic regime, geomorphometry

and lithology. The subsystems include site-specific process behaviour in terms of form-process interactions and climatic impact on the acting geomorphic processes (Fig. 3). However, one issue considered in this paper is how the complex physical form-process and climate-process models can be simplified to functional relationships between geomorphic and climatic parameters and frequency-magnitude behaviour of geomorphic processes. Therefore, a basic requirement of the proposed model scheme is a discretisation of the continuous landscape into geomorphic components which are linked topologically by net sediment fluxes (Preston and Schmidt, 2003).

1. Model concept

The model structure is illustrated schematically in Fig. 4. It can be characterised as a simple tank model, in which sediment is routed through a series of storage components. The basic aims are to simplify complex landforms using a set of simple landform units and parameters and to describe temporal patterns of their long-term behaviour. This involves regionalisation and parameterisation steps.

- Regional scale landscapes are split up into process subunits (Fig. 3). These components are conceived as geomorphic process units or process domains, i.e. a spatial unit is defined in terms of its dominant geomorphic processes. They can be defined by a specific form-process relationship. These components can be seen as a landform unit producing a specific amount of sediment within a given timestep, related to their internal geomorphic properties, the climatic input, and the landcover conditions. These units can be described as *storage units* and/or *morphometric units*. This procedure can be seen as an analogy to the fixed cell-based discretisation of recent process-based landform evolution models.
- These geomorphic units are *linked topologically* to describe the transfer of sediments through the whole geomorphic evolutionary system and to model the spatio-temporal development of this system.
- A geomorphic unit is described by a set of *geomorphic parameters*. These parameters (i) describe the unit in terms relevant for evolution, and (ii) characterise corresponding *form-process relationships* of the cascading system (Fig. 3). Various landform components have to be considered, i.e. landform morphometry and material. In fact, there are numerous studies on effective geomorphometric parameters available (Schmidt and Dikau, 1999). The major issue is to integrate these within higher scale geomorphic models.
- The influence of climate and form on geomorphic processes can be quantified as functional relationships of geomorphic parameters (see above), climate parameters (see below) and frequency/magnitude characteristics of net sediment transport by geomorphic processes. This means that either (i) geomorphic processes act independently and can be modelled by separate equations or (ii) they have to be replaced by one integral process law. To complete the cascading system, functional *process-form relationships* are required, quantifying the influence of geomorphic processes on geomorphic forms (e.g. simplified sedimentation law).

• So far, only internal behaviour of the geomorphic system has been considered. External forcing processes, i.e. climatic input and landcover changes, are represented using *effective parameters* at timescales relevant for regional landform evolution. In order to simplify the temporal variability of these parameters (which is very uncertain, anyway), it is helpful to divide the continuous timescale into *climatic/landcover regimes* (Schmidt, 2001). These show comparatively high internal homogeneity in terms of their effects on geomorphic processes (which means their effective parameters). However, if the modelled temporal period is short enough (no major climatic variations), it might be reasonable to exclude climatic/landcover regimes from the model.

2. *Model formulation*

A mathematical formulation of the model is presented on the following pages (Fig. 4).

Step 1: Defining initial conditions by geomorphic regionalisation in space and feature scales to geomorphic process units

The continuous landscape is subdivided into n (i = 1, ..., n) geomorphic process units (slope units, zero-order basins etc.), where unit i delivers sediment to j:$i \rightarrow j$ (defined by surface topological relationship). Landform can be described by a set of geomorphic landform parameters $\vec{l} = (l_1, l_2, ...)$, which can vary with time t and unit i: $\vec{l} \doteq \vec{l_i}(t)$. These parameters describe dominant landscape characteristics and the sensitivity or susceptibility of a landform unit with respect to acting geomorphic processes (Crozier, 1999). Modern geomorphometric technology provide techniques assisting in these kinds of spatial regionalisation steps, e.g. algorithms for landform analysis (Schmidt and Dikau, 1999).

Step 2: Defining boundary conditions by aggregation to climatic/landcover regimes

Variations in the spatio-temporal continuous systems of climate and landcover are modelled by a set of climatic/landcover regimes, which means time intervals T_k: $t = [t_1, t_2]$, where variability in controlling conditions is relatively low and climate and landcover conditions are relatively homogeneous, i.e. the continuous timescale is discretised to time intervals $t \rightarrow T_1, T_2, T_3, ...$ (Preston and Schmidt, 2003). The time intervals are parameterised by a set of effective climate and landcover parameters $\vec{c} = (c_1, c_2, ...)$, which vary with unit i and time t, i.e. $\vec{c} \approx \vec{c_i}(t) \approx \vec{c}_{i,T_k}$ for $t = [t_1, t_2]$. Therefore the temporal dependency of the effective climate and landcover parameters can be reduced to a relationship between climatic and landcover regime and effective parameter. This step can be seen as a parameterisation of environmental conditions (forcing factors) in terms of their geomorphic effectiveness.

Step 3: Geomorphic process laws using frequency and magnitude

Power laws have frequently been used to describe temporal characteristics of geomorphic processes (Bak, 1996; Boardman and Favis-Mortlock, 1999; Hergarten and Neugebauer, 1999b). Therefore, the frequency-magnitude

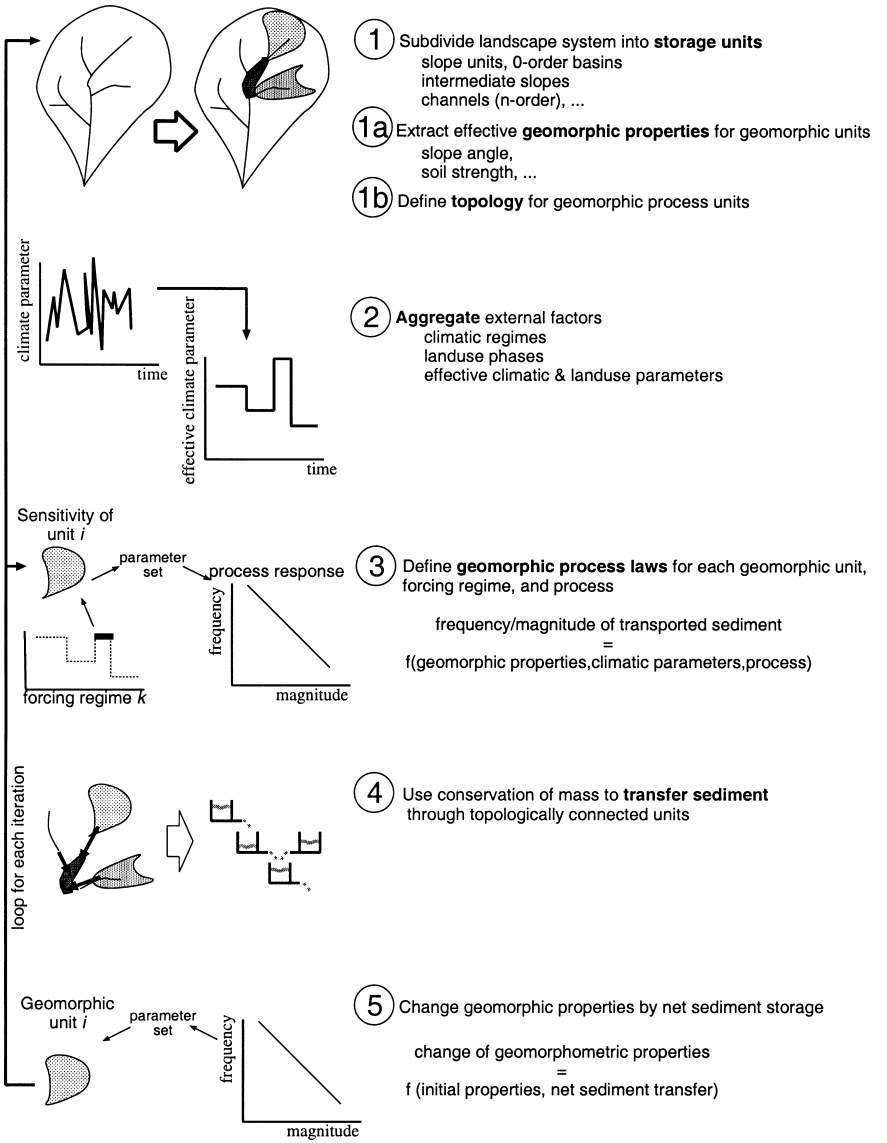


Fig. 4. Concept of a modelling approach for regional scale landform evolution (see text).

distribution of mobilised sediment (that is transfered from unit *i* to the topologically connected units) can be described as a power law between magnitude (unit: mass/time) and recurrence interval. This relation varies with geomorphic characteristics $\vec{l}$ (that means geomorphic unit *i*) and process and climatic/landcover conditions $\vec{c}$ (that means time interval T_k).

$$M = \left[M(R)\right]_{\vec{I},\vec{c},p} = \left[k \cdot R^b\right]_{i,T_k,p} \quad (1)$$

where M, magnitude of process p; R, recurrence interval of process p; k and b, power law parameters; i, geomorphic unit; p, geomorphic process and T_k, time interval.

The assumption is made, that the frequency-magnitude relationship of mobilised sediment is only dependent on (i) the geomorphic parameters $\vec{I}$, (ii) the climatic and landcover parameters $\vec{c}$, and (iii) the geomorphic process p. Therefore the parameters of Eq. (1) can be determined as:

$$\begin{pmatrix} k \\ b \end{pmatrix} = \vec{f}\left(\vec{I},\vec{c}\right)_p \quad (2)$$

where $\vec{I}$, effective geomorphic parameters of unit i, and $\vec{c} \approx \vec{c}_{i,T_k}$, effective climate parameters $\vec{c}$ of unit i for homogeneous time intervals T_k.

This means, the parameters of the frequency-magnitude relationship can be calculated as a function of geomorphometric properties and climate and landcover properties (i.e. landform sensitivity and effectivity of forcing factors).

Step 4: Sediment redistribution per time step

Based on the proposed dependency of frequency and magnitude of sediment production, a sediment flow law is established. This can be done by integrating the magnitude of processes for a given time span. However, finding appropriate time steps to route the sediment through the cascade is one crucial problem for the model solution.

$$V_i(t) = \sum_p \int_t^{t+\Delta t} (M)_{i,T_k,p}\, dt \quad (3)$$

where V_i is the total amount mobilised material in unit i (sediment flux out of unit i) by all geomorphic processes p acting in that unit within time interval t, $t + \Delta t$. The frequency magnitude relationship $M(R)$ can be calculated by Eqs. (1) and (2). However, a problem is identifiying the integral $\int_t^{t+\Delta t} M\,dt$. A possible solution is to estimate the contribution of an event magnitude by $\frac{M(R)\Delta t}{R}$. Then the total amount of sediment flux out of unit i within time interval t, $t + \Delta t$ can be calculated as

$$V_i(t) = \sum_p \int_{R=0}^{R=R_{\max}} M(R)_{i,T_k,p} \frac{\Delta t}{R}\, dR \quad (4)$$

However, because of divergence of the integral (and because of geomorphological considerations), this requires the introduction of a maximum recurrence interval R_{max} (i.e. exclusion of large events). The sediment budget S for unit i can be defined by the topology (as defined above) and the continuity equation from the sediment fluxes V:

$$S(i,t+\Delta t) = S(i,t) - V_i(t) + \sum_{j:j\to i} V_j(t) \tag{5}$$

Step 5: Recalculation of geomorphic properties

The change of geomorphic properties $\vec{l}$ for each unit i is a function $\vec{g}$ of initial conditions $\vec{l}$, mobilised sediment and sediment input in the system unit.

$$\vec{l}_i(t+\Delta t) = \vec{g}\left(\vec{l}_i(t), \sum_{k=i,\ j:j\to i} V_k(t)\right) \tag{6}$$

These step defines the initial conditions for the next modelling iteration (step 1, see Fig. 4).

DISCUSSION

The proposed model addresses topics that feature within contemporary geomorphologic research. A key problem is to devise methods and techniques in modelling geomorphologic evolutionary systems and to identify the role of process based models within that framework (Hergarten and Neugebauer, 1999a). This paper presented a conception for modelling geomorphic evolutionary systems based on the topology of sediment flux rather than individual process behaviour. To overcome the limitations inherent in raster and TIN based approaches (Coulthard, 2001), which represent an inappropriate spatial resolution for modelling evolutionary systems, it is proposed to represent space as a series of morphologically semantic *landscape units*; and to model landscape dynamics based on the *sediment fluxes*. This leads to models of landform evolution on a higher scale. The uncertainty in modelling landform evolution is treated by modelling evolution of landform structure rather than the height change of a three-dimensional surface. Therefore, configurational aspects in geomorphic systems are emphasised. Moreover, a *multiplicity of processes and related interactions* are modelled rather than details of behaviour of individual processes. Therefore, the proposed model approach simplifies process laws to relationships between frequency-magnitude spectra of processes and the environmental conditions which produce them, i.e. between the sensitivity of landscape units and the effectiveness of forcing factors (Brunsden and Thornes, 1979; Crozier, 1999).

However, the presented model framework also indicates a series of problems

and issues related to modelling approaches on higher scales. The approach is based on the modelling of landform structure and topology by storage units or geomorphic process domains. Therefore, a quantitative definition of *geomorphic process domains* has to be derived. Although there exist various specific approaches (e.g. hydrological response units (HRUs) or chemical response units (CRUs)), there is a need for a unifying and more rigorous definition for geomorphic units as a part of the cascading system (see the previous section). On the other hand, the definition of landscape units always involves a certain degree of abstraction and therefore subjectivity. However, this task could be done empirically, i.e. by mapping of process redistribution in association with the controlling factors. With geomorphometric progress this could replaced by semi-automatic GIS-supported expert systems on the basis of the controlling factors (Schmidt and Dikau, 1999).

Another problem relates to the definition of phases (regimes) of relatively homogeneous driving forces and landcover conditions. This involves landuse reconstruction, paleo climate analysis (e.g. using proxies), which is a research field in itself (Pfister and Lauterburg, 1992; Thompson *et al.*, 1993; Glaser *et al.*, 1999).

Another basic issue within the proposed generalised landform evolution model is the formulation of general *geomorphic process laws* based on frequency-magnitude spectra. The geomorphic process law as described in Eq. (2) might be simplified by functional separation of the independent variables into relationships (i) to the landscape sensitivity and (ii) to the effectiveness of forcing factors.

$$\begin{pmatrix} k \\ b \end{pmatrix} = \vec{f}\left(\vec{l},\vec{c}\right)_p \approx \left(\vec{h}\left(\vec{l}\right)\vec{i}\left(\vec{c}\right)\right)_p \tag{7}$$

Finding a functional separation like this could assist in identifying more generally valid formulations for relationships between the several factors. That means, the different functional relationships are independent and therefore universally applicable. Numerous empirical studies have been carried out, relating *landform properties* and geomorphic processes (Moore *et al.*, 1991; Schmidt and Dikau, 1999). However, universally applicable formulations of geomorphic process laws, as the relationship of process parameters and frequency and magnitude of processes to geomorphic parameters are missing. Geomorphometric parameters have been one major focus of interest (Moore *et al.*, 1991; Schmidt and Dikau, 1999). Moreover, physical process models can assist in deriving these relationships, in particular form-process interactions and effective parameters. Within this respect, various sensitivity studies have been carried out (Schmidt *et al.*, 1998, 2000) and several simple parameters that are currently applied within process models can be used (Beven and Kirkby, 1979). However, much more work is needed to establish more generally valid parameters and geomorphic laws.

Modelling of landform change by processes completes the circle of form-

process-form interaction. Whereas the influence of topographic properties on geomorphic processes has been investigated in many studies, a quantification of the impact of processes on landform has been rarely taken into account. Therefore, deriving adequate formulations for Eq. (6) (function $\vec{g}$), e.g. sedimentation laws, remain a problem in the model formulation. Moreover, appropriate iteration intervals for the proposed model approach have to be defined. These should certainly be considered in the context of frequency characteristics of the modelled processes that are thought to be most relevant.

Long-term processes such as weathering and tectonic uplift are not directly included in the current modelling concept. Weathering processes, which are dependent on soil hydrology, soil and bedrock properties, and climate (Cox, 1980) are considered to be spatio-temporal homogeneous for the model scale. However, weathering might be included as a spatio-temporal varying process like any other geomorphic process within the model concept (Eq. (2)). Tectonic activity might be included by adding a constant or varying change in surface height (or the effect of this change on the geomorphic parameters for each domain) and recalculating geomorphic process domains and geomorphic parameters for each timestep. The same issues apply to baselevel change. For highly active areas like New Zealand or Japan it might be appropriate to include details of spatio-temporal variations of tectonic displacements (e.g. to model fault scarps and rift valleys).

Landcover dynamics are treated as external factors, independent of the geomorphologic subsystem. However, in general and especially for specific environments, there are strong relations between these subsystems (parent material, landform, soil, vegetation).

CONCLUSIONS

The presented modelling approach focuses on modelling the regional scale sediment cascade. Individual process details are neglected or simplified. In terms of understanding the evolution of regional scale systems, it is argued that it is more appropriate to model the topology of the sediment cascade system rather that the exact behaviour of the single processes in the cascade, because of their stochastic nature in the context of higher order evolutionary systems. We argue that the inexactness and error in process description on the scale of process-response subsystems are averaged by diffusive effects of the cascading system. Moreover, at this scale interactions between process subsystems acting on different levels of frequency and magnitude may dominate the system. The proposed model offers potential for evaluating these effects using sensitivity analysis. The model structure is one possible solution for the necessary regionalisation step in changing scales from local process scales to scales of geomorphic evolutionary systems. It highlights the need for both detailed individual process studies to model net effects of process-response subsystem on the higher scale, and consideration of system scale by scaled system descriptors in terms of form (landscape units and parameters) and processes (frequency-magnitude spectra).

REFERENCES

Ahnert, F. (1988) Modelling landform change. In M. G. Anderson (ed.), *Modelling Geomorphological Systems*, pp. 375–400. Wiley, Chichester.

Armstrong, A. (1987) Slopes, boundary conditions, and the development of convexo-concave forms—some numerical experiments: *Earth Surface Processes and Landforms*, **12**(1), 17–30.

Bak, P. (1996) *How Nature Works: The Science of Self-Organized Criticality*. Springer, Berlin/Heidelberg/New York, 212 pp.

Band, L. E., Patterson, P. and Nemani, R. (1993) Forest ecosystem processes at the watershed scale: incorporating hillslope hydrology: *Agricultural and Forest Meteorology*, **63**, 93–126.

Beven, K. (1996) Equifinality and uncertainty in geomorphological modelling: In B. Rhoads and C. Thorn (eds.), *The Scientific Nature of Geomorphology*, pp. 289–313. Wiley, Chichester.

Beven, K. and Kirkby, M. (1979) A physically based, variable contributing area model of basin hydrology: *Bulletin of Hydrologic Sciences*, **24**, 43–69.

Boardman, J. and Favis-Mortlock, D. (1999) Frequency-magnitude distributions for soil erosion, runoff and rainfall—a comparative analysis: *Zeitschrift für Geomorphologie, N.F., Supplement Band*, **115**, 51–70.

Braun, J. and Sambridge, M. (1997) Modelling landscape evolution on geological time scales: a new method based on irregular spatial discretization: *Basin Research*, **9**(1), 27–52.

Brunsden, D. and Thornes, J. (1979) Landscape sensivity and change: *Transactions, Institute of British Geographers.*, New Series, **4**(4), 463–484.

Chorley, R. J. and Kennedy, B. A. (1971) *Physical Geography. A Systems Approach*. Prentice Hall, London, 370 pp.

Chorley, R., Schumm, S. and Sugden, D. (1984) *Geomorphology*. Methuen, London, 605 pp.

Coulthard, T. J. (2001) Landscape evolution models: a software review: *Hydrological Processes*, **15**, 165–173.

Coulthard, T. J., Kirkby, M. J. and Macklin, M. G. (1998) Non-linearity and spatial resolution in a cellular automaton model of a small upland basin: *Hydrology and Earth Sciences*, **2**(2–3), 257–264.

Cox, N. (1980) On the relationship between bedrock lowering and regolith thickness: *Earth Surface Processes*, **5**, 271–274.

Crozier, M. J. (1999) The frequency and magnitude of geomorphic processes and landform behaviour: *Zeitschrift für Geomorphologie, N.F.*, Supplement Band, **115**, 35–50.

Dikau, R. (1990) Geomorphic landform modelling based on hierarchy theory: In *Proceedings of the 4th International Symposium on Spatial Data Handling, July 23–27, 1990, Zürich*, Volume 1, pp. 230–239.

Eden, D. J. and Page, M. J. (1998) Paleoclimatic implications of a storm erosion record from late Holocene lake sediments, North Island, New Zealand: *Palaeogeography, Palaeoclimatology, Palaeoecology*, **139**, 37–58.

Eriksson, M. G., Olley, J. M. and Payton, M. G. (2000) Soil erosion history in central Tanzania based on OSL dating of colluvial and alluvial hillslope deposits: *Geomorphology*, **36**(1–2), 107–128.

Glaser, R., Brázdil, R., Pfister, C., Dobrovolný, P., Barriendos Vallve, M., Bokwa, A., Camuffo, D., Kotyza, O., Limanówka, D., Rácz, L. and Rodrigo, F. S. (1999) Seasonal temperature and precipitation fluctuations in selected parts of Europe during the sixteenth century: *Climatic Change*, **43**, 169–200.

Hergarten, S. and Neugebauer, H. (eds.) (1999a) *Process Modelling and Landform Evolution*, Volume 78 of *Lecture Notes in Earth Sciences*. Springer, Berlin/Heidelberg/New York, 305 pp.

Hergarten, S. and Neugebauer, H. (1999b) Self-organized criticality in landsliding processes: In S. Hergarten and H. Neugebauer (eds.), *Process Modelling and Landform Evolution*, Volume 78 of *Lecture Notes in Earth Sciences*, pp. 231–249. Springer, Berlin/Heidelberg/New York.

Kirkby, M. (1990) Landscape viewed through models: *Zeitschrift für Geomorphologie, N.F., Supplement Band*, **79**, 63–81.

Lang, A. and Hönscheidt, S. (1999) Age and source of colluvial sediments at Vaihingen-Enz, Germany: *Catena*, **38**, 89–107.

Moore, I., Grayson, R. and Ladson, A. (1991) Digital terrain modelling: a review of hydrological, geomorphological, and biological applications: *Hydrological Processes*, **5**(3), 3–30.

Page, M. J. and Trustum, N. A. (1997) A late Holocene lake sediment record of the erosion response to land use change in a steepland catchment, New Zealand: *Zeitschrift für Geomorphologie, N.F.*, **41**, 369–392.

Pfister, C. and Lauterburg, A. (1992) Spatial variability of climatic change in Europe 1780–1960: In B. Frenzel, C. Pfister, and B. Gläser (eds.), *European Climate Reconstructed from Documentary Data: Methods and Results*, Volume 7 of *Palaeoclimate Research*, pp. 177–192, Gustav Fischer, Stuttgart/Jena/Lübeck/Ulm.

Preston, N. J. (2001) Geomorphic response to environmental change: the imprint of deforestation and agricultural land use on the contemporary landscape of the Pleiser Hügelland, Bonn, Germany: Ph.D. Thesis, Department of Geography, University of Bonn, 136 pp.; http://hss.ulb.uni-bonn.de:90/ulb_bonn/diss_online/math_nat_fak/2001/preston_nicholas_james.

Preston, N. J. and Schmidt, J. (2003) Modelling sediment fluxes at large spatial and temporal scales. In A. Lang, K. Hennrich and R. Dikau (eds.), *Long Term Hillslope and Fluvial System Modelling*, Volume 101 of *Lecture Notes in Earth Sciences*, pp. 53–72. Springer, Berlin/Heidelberg/New York.

Schmidt, J. (2001) The role of mass movements for slope evolution—conceptual approaches and model applications in the Bonn area: Ph.D. Thesis, Department of Geography, University of Bonn, 313 pp.; http://hss.ulb.uni-bonn.de:90/ulb_bonn/diss_online/math_nat_fak/2001/schmidt_jochen.

Schmidt, J. and Dikau, R. (1999) Extracting geomorphometric attributes and objects from digital elevation models—Semantics, methods, future needs: In R. Dikau and H. Saurer, editors, *GIS for Earth Surface Systems—Analysis and Modelling of the Natural Environment*, pp. 153–173. Schweizbart'sche Verlagsbuchhandlung, Berlin/Stuttgart.

Schmidt, J., Merz, B. and Dikau, R. (1998) Morphological structure and hydrological process modelling: *Zeitschrift für Geomorphologie, N.F.*, Supplement Band, **112**, 55–66.

Schmidt, J., Hennrich, K. and Dikau, R. (2000) Scales and similarities in runoff processes with respect to geomorphometry: *Hydrologic Processes*, **14**(11–12), 1963–1979.

Schumm, S. (1979) Geomorphic thresholds: the concept and its application: *Transactions, Institute of British Geographers*, New Series, **4**, 485–515.

Semmel, A. (1995) Development of gullies under forest cover in the Taunus and Crystalline Odenwald Mountains, Germany: *Zeitschrift für Geomorphologie, N.F.*, Supplement Band, **100**, 115–127.

Semmel, A. (1996) The historic-genetic approach in applied geomorphology: *Zeitschrift für Geomorphologie, N.F.*, **40**, 289–303.

Thompson, W. I., Ruddiman, W. F., Steet-Perrott, F., Markgraf, V., Kutzbach, J. E., Bartlein, P. J., Wright, H. E., Jr. and Prell, W. L. (1993) Climatic changes during the past 18000 years: regional synthesis, mechanims, and causes: In H. E. Wright, Jr., J. E. Kutzbach, W. I. Thompson, W. F. Ruddiman, F. Steet-Perrott and P. J. Bartlein (eds.), *Global Climates since the Last Glacial Maximum*, pp. 514–535. University of Minnesota Press, Minneapolis.

Trustum, N. A., Gomez, B. and Page, M. J. (1999) Sediment production, storage and output: The relative role of large magnitude events in steepland catchments: *Zeitschrift für Geomorphologie, N.F.*, Supplement Band, **115**, 71–86.

Wasson, R. J., Mazari, R. K. and Starr, B. (1998) The recent history of erosion and sedimentation on the southern tablelands of southeastern Australia: Sediment flux dominated by channel incision: *Geomorphology*, **24**(4), 291–308.

Willgoose, G., Bras, R. L. and Rodriguez-Iturbe, I. (1991) Results from a new model of river basin evolution: *Earth Surface Processes and Landforms*, **16**, 237–254.

Concepts and Modelling in Geomorphology: International Perspectives,
Eds. I. S. Evans, R. Dikau, E. Tokunaga, H. Ohmori and M. Hirano, pp. 133–145.
© by TERRAPUB, Tokyo, 2003.

Planar Organization of River Networks: A Hidden Gamma Law Structure

Christophe CUDENNEC[1], Youssef FOUAD[1] and Irianto SUMARJO-GATOT[2]

[1]*Ecole Nationale Supérieure Agronomique de Rennes, Génie rural,*
65 rue de Saint Brieuc, 35042 Rennes Cedex, France
e-mail: cudennec@agrorennes.educagri.fr
[2]*Center for Soil and Agroclimate Research, Bogor, Indonesia*

Abstract. We consider the water path distribution from any point in a basin to the outlet through the river network. Using the Strahler ordering scheme (Strahler, 1957) we separate every hydraulic path length L as the sum $L = \sum_{i=1}^{n} l_i$ of the lengths of its different components l_i, where n is the basin's highest order. We obtain L and l_i ($\forall i$, $1 \le i \le n$) maps and probability distributions through a GIS-based analysis of the geographical and topological organization of river networks. It appears that the l_i probability distributions follow convex and rapidly decreasing shapes and have a strong scaling property, except for the highest orders. This scaling is consistent with river networks fractality (Rodriguez-Iturbe and Rinaldo, 1997) and its upper limit can be explained by the branched-out topology. Indeed, for a single basin, the highest order component l_n necessarily can not have a decreasing probability distribution. This is due to its particular position in the Strahler hierarchical network organization. For similar reasons, probability distributions for l_{n-1}, l_{n-2}, ... present a weaker scaling than for l_1, l_2, ... Thus, we consider the truncated hydraulic lengths $L' = \sum_{i=1}^{m<n} l_i$. The probability distributions of L' are negatively skewed and some of them can be described by a gamma law, whereas basin width functions are generally positively skewed (Rodriguez-Iturbe and Rinaldo, 1997). This shows how a gamma law underlies the river network self-similar organization, even if the shape does not obviously appear in the basin-scale geomorphological functions, due to hierarchical constraints.

Keywords: Hydro-Geomorphology, Scaling, Underlying Pattern, Branched-out Network, River Network Organization

INTRODUCTION

At the beginning of the nineteenth century, Playfair, quoted by Horton as an introduction to his famous article (Horton, 1945), noticed that <<every river appears to consist of a main trunk, fed from a variety of branches, each running in a valley proportionned to its size, and all of them together forming a system of valleys, communicating with one another, and having such a nice adjustment of their declivities that none of them join the principal valley either on too high or

too low level>>. Through this sentence Playfair expressed most of the fractal characteristics of the river network such as the similarity between the main trunk fed from branches and the branches fed from valleys', and the branching rules. Playfair's <<nice adjustment>> is in fact the network fractality. Indeed, since Mandelbrot's definition of the fractal geometry (Mandelbrot, 1982), some pioneer authors showed the fractal nature of river networks (La Barbera and Rosso, 1987; Tarboton *et al.*, 1988) and many works have been performed, which are well synthesized by Rodriguez-Iturbe and Rinaldo (1997) and Dodds and Rothman (1999).

The obvious characteristic of shape similarity between parts of networks was first studied, which led to the idea of self-similarity. Then many relations were found in terms of power laws, showing scaling properties, and expressions of the fractal dimension were proposed (La Barbera and Rosso, 1989; Liu, 1992). From their synthesis of the topic, Rodriguez-Iturbe and Rinaldo (1997) reached the conclusion that <<the search for invariance properties across scales as a basic hidden order in hydrologic phenomena is one of the main themes of hydrologic science>>. This means that this search is crucial for geomorphology in itself and also for geomorphology-related hydrology. For this reason, we focus on a geomorphological function and study how it is structured through the branched out drainage topology.

THE TOPOLOGICAL AND GEOMORPHOLOGICAL DESCRIPTION OF RIVER NETWORKS

Our work is motivated by two major aims. The first one is to describe the river network itself, seen as a fractal object within a basin considered as a two-dimensional planar object. Because this network is the particular topological network of all the lowest altitude points of the basin and because it is the result of complex geomorphological mechanisms, it appears to be a good indicator of the whole relief of the basin. More precisely, this network is itself oriented since there is one particular point of the lowest altitude, which is the outlet. The branched-out topology can thus be pointed out and used as a scale. The second aim is to lead a reasoning which can be fruitfull in hydrology, and we think as some other authors (Rodriguez-Iturbe and Valdès, 1979; Gupta *et al.*, 1980; Beven and Kirkby, 1993) that the hydrological response of a basin can be closely related to relevant basin-scale geomorphological functions.

1. The branched-out topology and scaling

The geographic unit at the scale of which the river network is organized is the basin. In a basin, besides the outlet, which is the only downstream extremity, the river network is made up of particular points: upstream extremities, called sources, and junctions. The part contained between two such successive particular points is a link. The Strahler ordering scheme (Strahler, 1957) permits the description of a link position in a river network (Fig. 1a). According to this ordering method, the stream, which is a set of successive links of same order, is

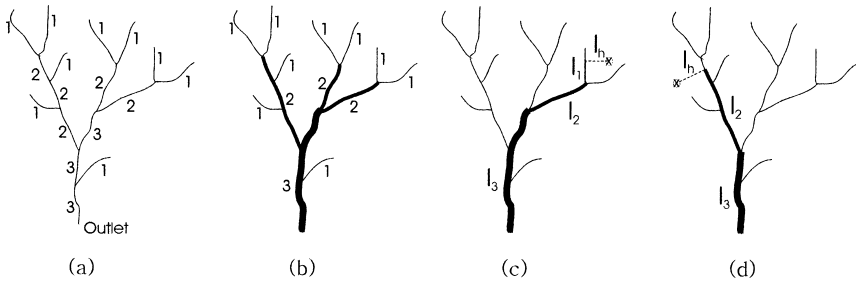


Fig. 1. Hypothetical network of order $n = 3$. (a) Strahler ordering of links. (b) Identification of streams of order 1 —, order 2 ▬ and order 3 ■. (c) and (d) Examples of paths run by a water drop from a point to the outlet. - - - is the path through the hillslope whose length is l_h. Identification of 1st (—), 2nd (▬) and 3rd (■) orders components whose lengths are respectively l_1, l_2 and l_3.

defined (Fig. 1b). The spectrum of orders represented in the network can be seen as a cascade, in the sense of Mandelbrot (1982), which is the first basement of fractality. Indeed, Horton laws (Horton, 1945) give the number of streams and the mean stream length through Strahler's ordering scheme (Schumm, 1956), on the basis of a bifurcation ratio $R_B = \frac{N_{i-1}}{N_i}$ and of a length ratio $R_L = \frac{\overline{L_i}}{\overline{L_{i-1}}}$—where N_i is the number and $\overline{L_i}$ the mean length of i-th order streams—, whose stabilities are statistically verified (Smart, 1968). According to Shreve (1966), Horton laws suggest that, if there is no geological control, the river network natural organization is ruled by general erosion processes and secondarily by local environmental factors. The Tokunaga law (Tokunaga, 1966) is similar, concerning the numbers $T_{i,j}$ of j-th order streams flowing into an i-th order stream from the side. These branching laws, as well as Hack's law (Hack, 1957) giving the basin mainstream length as a power function of its area, were the first implicit scalings found in a river network.

2. The basin-scale geomorphological functions

Then, in relation to the isochrone notion (Larrieu, 1957; Surkan, 1969), the area function (Foroud and Broughton, 1981; Snell and Sivapalan, 1994; Robinson *et al*., 1995) and the width function (Kirkby, 1976; Gupta and Waymire, 1983; Snell and Sivapalan, 1994) were introduced. The area function is <<the frequency distribution of contributing area with respect to flow distance from the outlet>> (Snell and Sivapalan, 1994). This function is also called area-distance function by Rodriguez-Iturbe and Rinaldo (1997) in their synthetic publication. Many authors approached this function by the width function $W(x)$ which gives the number of links in the network at a flow distance x from the outlet. Rodriguez-Iturbe and Rinaldo (1997) justify this in a DEM-use context, because <<in a system where a link is associated with every unit area used to discretize the catchment surface, the width function and the area-distance function are equal.

When the necessary support is the unit area, the network is space-filling because every pixel is assigned a link and no holes are allowed in the distribution of pixels covering the total drainage area.>> We agree with Rodriguez-Iturbe and Rinaldo (1997) who see in the width function an operator that maps the area of the basin, a two-dimensional object, onto a one-dimensional support, and who also think that <<the width function contains important information about the mechanisms of development of the drainage network and incorporates the essential characters of the hydrologic response through its linkage with residence time distributions>>, and we think that this is true even more with the area function.

NEW OBJECTS AND ORGANIZATION EVIDENCES

We think that considering the link as the elementary object for which the flow path is computed—with no relation to its position, draining area or length—takes the width function away from the area function. Indeed if there is a use of a DEM, the equivalence between the pixel and the link breaks the exact nature of the link. Secondarily, the idea of elementary-surfaces associated to the links over-simplifies the relation between the hillslopes and the thalwegs, both on geometrical and hydrological points of view, and this leads to a space-filling network which does not fit to actual observations (La Barbera and Rosso, 1989). Thus we consider a new geomorphological function and study its organization through the self-similar branched-out structure.

1. Original objects

From the flow path of a given point of the basin, which is the path followed by a water drop to reach the outlet, we consider separately the hillslope path and the hydraulic path through the river network. Within the hydraulic path, we call the "*i*-th order component" the part run through successive channels of the same order *i* (Figs. 1c and 1d). This definition has two important implications.

1) The *i*-th order component of a given hydraulic path is a set of successive links of the same order *i*—and eventually of a part of a link, for the first one—, which is not necessarily a whole *i*-order stream. For instance the 3rd order component on Fig. 1d is made up of two links of order 3, whereas the 3rd order component on Fig. 1c is the whole stream made up of three links. Moreover Figs. 1c and 1d show that the first link constituting the first component of the path (resp. 1st and 2nd orders) is partially run.

2) Because of the branching structure, a hydraulic path can present less than *n* components—*n* being the basin order—since the *i*-th order component flows into a *j*-th order component ($j > i$), which does not necessarily mean $j = i + 1$. For instance the hydraulic path drawn on Fig. 1c is made up of $n = 3$ components, whereas the hydraulic path drawn on Fig. 1d does not have any 1st order component.

Then we focus on the length of the hydraulic path, called the hydraulic length *L*. This appears to be an interesting variable characterizing the river network seen as a fractal object within the two-dimensional planar basin as well as a media

determining the drainage from hillslope and rapid dynamic transfer from up to downstream. The probability density function of this hydraulic length is equivalent to the area-hydraulic length function of the basin, which can be seen as a new concept derived from the one of area-distance function. Moreover, for any geographic point of the basin, the hydraulic length is the sum $L = \sum_{i=1}^{n} l_i$ where n is the basin order and l_i the length of the i-th order component.

We assume that the network scaling property applies to the components, of course to their mean lengths, but more generally to their probability density functions. Thus, besides the stream length ratio R_L (Horton, 1945), we define the component length ratio $r_l = \frac{\overline{l_i}}{\overline{l_{i-1}}}$ where $\overline{l_i}$ is the mean length of the i-th components, and propose to check its steadiness by a GIS-based analysis.

2. *A GIS-based analysis*

A georeferenced vector image of the river network is obtained from a human interpretation of 1/25000 scale maps, with the software ©ERDAS. This leads to realistic round shaped meanders and conjunctions, which are crucial for our issue. Then a topological analysis of the relationships between the vectors allows to build a binary branched-out tree. The interpretation of this tree leads to identify the links and their Strahler orders, the streams, and to estimate statistics of these constituents (Cudennec, 2000). Furthermore a square grid is used as a set of points to sample the basin territory, and for each of these points the hydraulic path is identified across the hillslope and the network, which means also across objects of increasing Strahler orders. Then one can evaluate the lengths of all the components l_i for each point and build georeferenced raster images of the obtained values: one image for each value $1 \leq i \leq n$. This multi-layer raster mapping of all the components allows then by image processing 1) to extract statistics and probability distributions of the lengths of components l_i; and 2) to study sums of lengths of components $L' = \sum_{i=1}^{m \leq n} l_i$, by combining raster images.

As the grid is square and represents a sampling of the basin surface, the actual normalized distribution of the hydraulic length is the area-hydraulic length function of the basin, defined above. But as far as a flow path enters the network at a given point, there is no artificial link assigned to an elementary surface like for the width function. Then the topological basic element is displaced from the network link or source to the surface sampling grid point and among the infinity of points along the network, all of them are not equivalent, but have a variable weight according to the proportion of flow paths entering the network through them.

3. *Experimental results*

The actual shapes, statistics and scalings of the components and of the area-



Fig. 2. Map of the Yvel river network for the whole basin and four sub-basins.

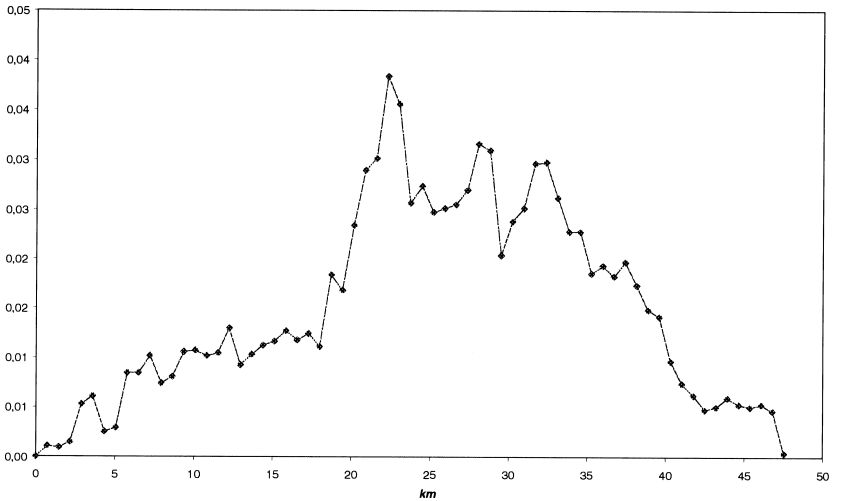


Fig. 3. Actual probability distribution of the hydraulic length *L* of the whole Yvel basin.

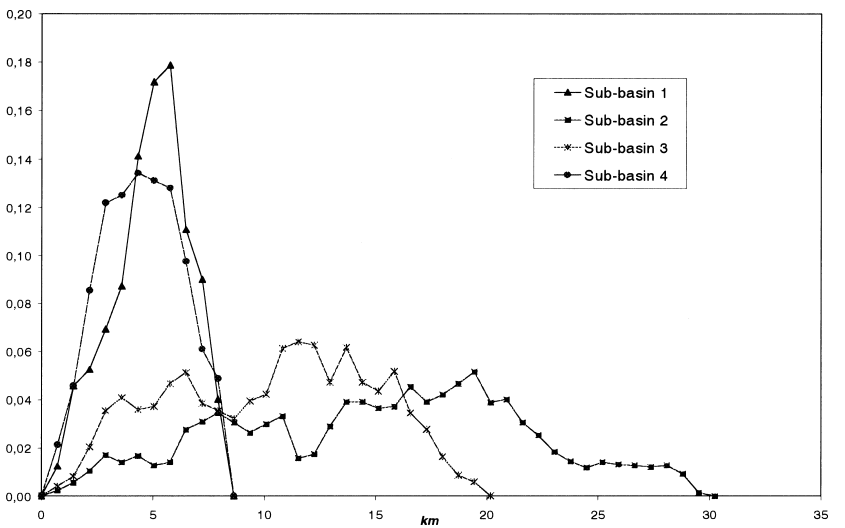


Fig. 4. Actual probability distributions of the hydraulic lengths *L* of the four sub-basins.

hydraulic length function are studied for the particular basin of the Yvel river (Lambert coordinates of the outlet: 248979/1043554; 302 km^2) whose river network is shown on Fig. 2. Figure 3 shows the probability distribution of the hydraulic length of the whole basin, and Fig. 4 the ones of the four sub-basins identified on Fig. 2. Despite big differences between the basins, in terms of size

Table 1. Horton's ratios and component length ratio of the whole Yvel basin.

Order i	2	3	4	5	6	7	Selected value	R^2
R_B	4.55	5.32	4.65	3.78	3	3	3.72	0.99
R_L	1.19	2.37	3.05	1.32	3.03	1.48	1.93	0.97
r_l	1.2	2.35	2.98	1.16	4.28	1.68	1.97	0.96

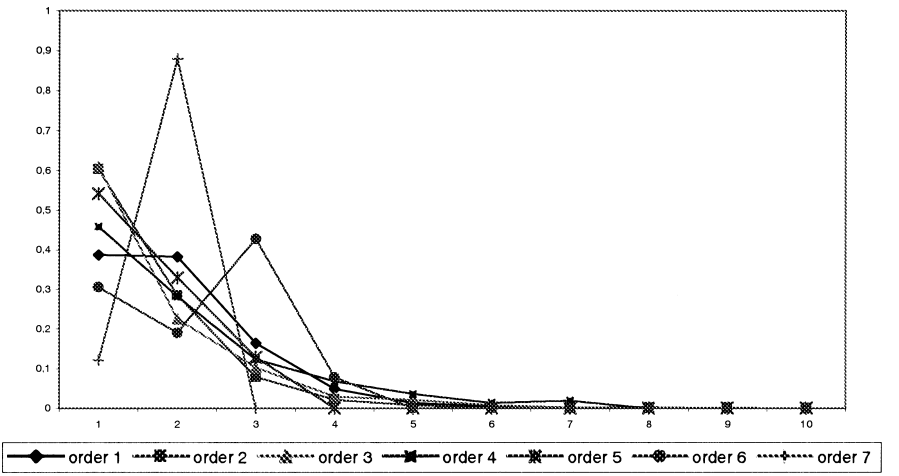


Fig. 5. Actual probability distributions of the reduced lengths of components $\frac{l_i}{r_l^{(i-1)}}$ of the whole Yvel basin, with r_l = 1.97. The results are grouped in 200 meters wide classes.

and Strahler order (n = 7, 5, 6, 6 and 5 respectively for the whole basin and for sub-basins 1, 2, 3 and 4), the five probability distributions on Figs. 3 and 4 are irregular and broadly positively skewed, which is relevant with the universal skewness of width functions (Rodriguez-Iturbe and Rinaldo, 1997).

More precisely, we then observe how the probability density function of the hydraulic length of the whole basin is structured and organized in terms of components. Table 1 presents the observed values of the Horton bifurcation and length ratios, and the values of the newly defined component length ratio r_l. The global values are obtained by logarithmic regressions, whose R^2 coefficients are indicated. It appears that the three ratios are steady, which shows that this particular basin presents a strong self-similarity of streams identified within the Strahler ordering scheme, and that this self-similarity is verified with components. Moreover one can notice that r_l and R_L values are close to each other.

Figure 5 presents the probability distributions of the lengths of the seven components, reduced by the scaling factor r_l identified in Table 1: $\frac{l_i}{r_l^{(i-1)}}$. The five

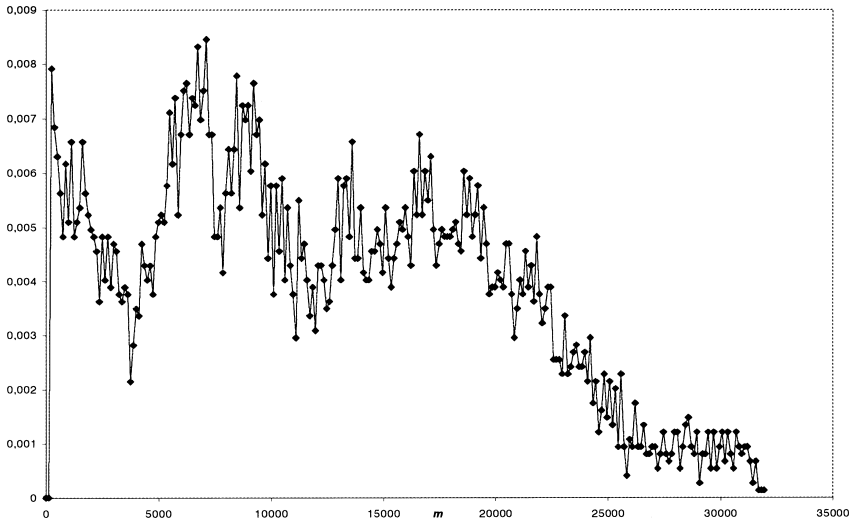


Fig. 6. Actual probability distribution of the truncated hydraulic length $L' = \sum_{i=1}^{m} l_i$ of the whole Yvel basin, with $m = 6$.

first curves (orders one to five) are very close together, convex and rapidly decreasing. This shows that the scaling of the components is not only verified in terms of geometric averages but also in terms of distribution. The two last curves are different since they are not decreasing and out of the envelop of the others. This shows a difference in the role and the representativity of the highest orders components, due to their particular hierarchical positions. Indeed the last order n is unavoidable and the $(n–1)$-th one is nearly unavoidable for hydraulic paths from anywhere in the basin to the unique outlet. Thus the probability distributions can necessarily not be decreasing, which would mean that avoiding is majority. This particular role of upper orders objects, that we call "hierarchy constraint", led us to consider the sub-system of the m ($m < n$) first Strahler levels, by defining the sum $L' = \sum_{i=1}^{m<n} l_i$, corresponding to the truncation of the highest orders components.

Experimental probability distributions of L', for any value of m, can be obtained through the GIS-based analysis. Figures 6, 7, 8, 9 and 10 show the actual probability distributions of L' for decreasing values of m, respectively 6, 5, 4, 3 and 2. It appears that the skewness is obviously becoming negative and that a regular shape is appearing. This is already true for $m = 6$ and $m = 5$, whereas the probability distributions of L for sub-basins of orders 6 and 5 (Fig. 4) are positively skewed. Nevertheless, we noticed and can here add that the truncated lengths L' present the same distribution shapes for any sub-basin.

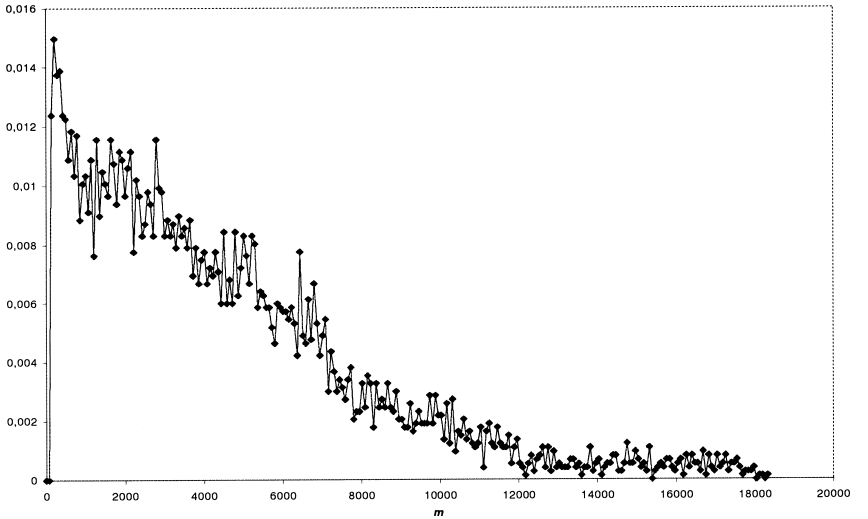


Fig. 7. Actual probability distribution of the truncated hydraulic length $L' = \sum_{i=1}^{m} l_i$ of the whole Yvel basin, with $m = 5$.

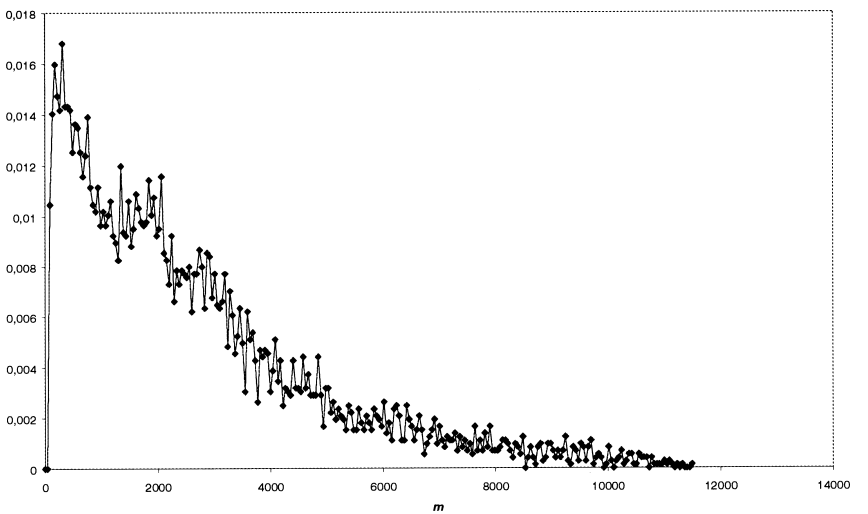


Fig. 8. Actual probability distribution of the truncated hydraulic length $L' = \sum_{i=1}^{m} l_i$ of the whole Yvel basin, with $m = 4$.

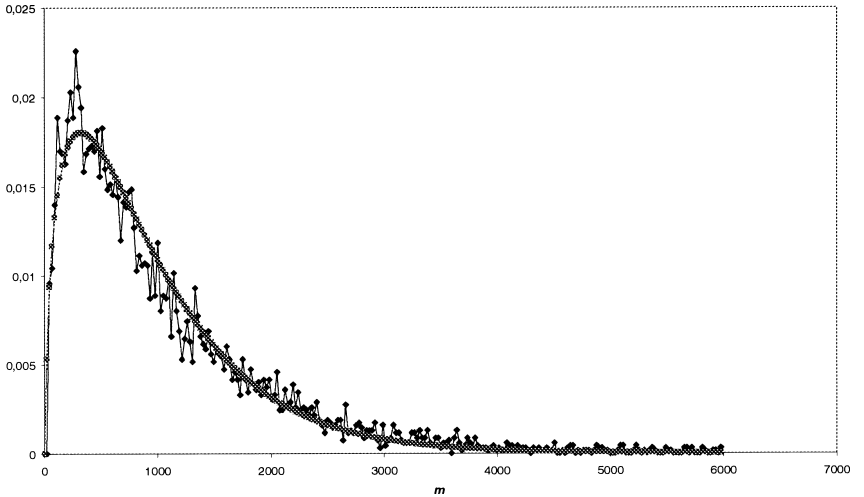


Fig. 9. Actual and theoretical $\left[g(L') = \left(\frac{m}{2 \cdot \overline{L'}} \right)^{\frac{m}{2}} \cdot \frac{1}{\Gamma\left(\frac{m}{2} \right)} \cdot L'^{\frac{m}{2}-1} \cdot e^{-\frac{m \cdot L'}{2 \cdot \overline{L'}}} \right]$ probability distributions of the truncated hydraulic length $L' = \sum_{i=1}^{m} l_i$ of the whole Yvel basin, with $m = 3$.

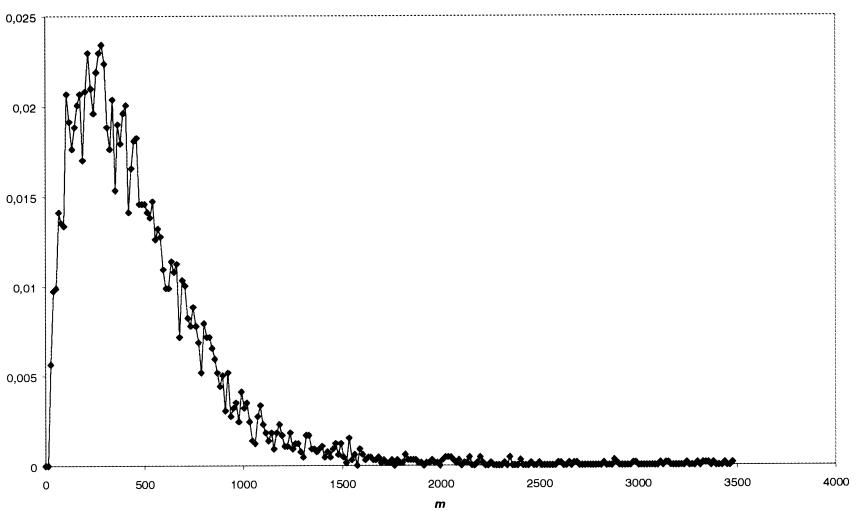


Fig. 10. Actual probability distribution of the truncated hydraulic length $L' = \sum_{i=1}^{m} l_i$ of the whole Yvel basin, with $m = 2$.

Moreover Fig. 9 shows how a gamma law fits very well to the actual distribution of L', for $m = 3$. This gamma law is not a statistical fitting but a theoretical proposal (Cudennec *et al.*, 2003):

$$g(L') = \left(\frac{m}{2\overline{L'}}\right)^{\frac{m}{2}} \cdot \frac{1}{\Gamma\left(\frac{m}{2}\right)} \cdot L'^{\frac{m}{2}-1} \cdot e^{-\frac{mL'}{2\overline{L'}}}$$

—where $\overline{L'}$ is the actual mean value of L'—, which has been obtained from a statistical physics reasoning based on a Strahler-components self-similar space identification. This confirms the idea of the hierarchy constraint and shows that a gamma law structure is underlying in the organization of the considered river network.

CONCLUSION

We consider new geomorphological objects within the river network of a basin, based on the Strahler ordering scheme: the hydraulic path and its components. The length of the hydraulic path L is thus the sum of the lengths of its n different components l_i, where n is the basin's highest order. It appears that the l_i probability distributions follow convex and rapidly decreasing shapes and have a strong scaling property, except for the highest orders. This scaling is consistent with river networks fractality and its upper limit can be explained by the branched-out topology. Indeed, for a single basin, the highest order component l_n necessarily can not have a decreasing probability distribution. This is due to its particular position in the Strahler hierarchical network organization. For similar reasons, probability density functions for l_{n-1}, l_{n-2}, ... present a weaker scaling than for l_1, l_2, ... The probability distributions of the truncated hydraulic lengths L' are negatively skewed and some of them can be described by a gamma law, whereas the probability distributions of L are positively skewed. This shows how a gamma law underlies the river network self-similar organization, even if the shape does not obviously appear in the basin-scale geomorphological functions, due to hierarchical constraints.

REFERENCES

Beven, K. and Kirkby, M. J. (1993) *Channel Network Hydrology*. Wiley, Chichester, 319 pp.

Cudennec, C. (2000) Description mathématique de l'organisation du réseau hydrographique et modélisation hydrologique. Ph.D. Dissertation, ENSAR, Rennes, 198 pp.

Cudennee, C., Fouad, Y., Sumarjo Gatot, I. and Duchesne, J. (2003) A geomorphological explanation of the unit hydrograph concept: *Hydrological Processes* (in press).

Dodds, P. S. and Rothman, D. H. (1999) A unified view of scaling laws for river networks: *Physical Review E*, **59**, 4865–4877.

Foroud, N. and Broughton, R. S. (1981) Flood hydrograph simulation model: *Journal of Hydrology*, **49**, 139–172.

Gupta, V. K. and Waymire, E. (1983) On the formulation of an analytical approach to hydrologic response and similarity at the basin scale: *Journal of Hydrology*, **65**, 95–123.

Gupta, V. K., Waymire, E. and Wang, C. T. (1980) Representation of an instantaneous unit hydrograph from geomorphology: *Water Resources Research*, **16**, 855–862.

Hack, J. T. (1957) Studies of longitudinal stream profiles in Virginia and Maryland. U.S. Geological Survey, Prof. Paper 294-13, 97 pp.

Horton, R. E. (1945) Erosional development of streams and their drainage basins; hydrophysical approach to quantitative morphology: *Bulletin of the Geological Society of America*, **56**, 275–370.

Kirkby, M. J. (1976) Tests of the random network model and its application to basin hydrology: *Earth Surface Processes*, **1**, 197–212.

La Barbera, P. and Rosso, R. (1987) Fractal geometry of river networks: *Eos Transaction AGU*, **68**, 1276.

Larrieu, J. (1987) Evaluation des crues catastrophiques par la méthode des hydrogrammes synthétiques: C.R. et Rapports Toronto, 3–14 Sept. 1957, IASH-IUGG, 160–173.

Liu, T. (1992) Fractal structure and properties of stream networks: *Water Resources Research*, **28**, 2981–2988.

Mandelbrot, B. B. (1982) *The Fractal Geometry of Nature*. W. H. Freeman and Co., San Francisco, 460 pp.

Robinson, J. S., Sivapalan, M. and Snell, J. D. (1995) On the relative roles of hillslope processes, channel routing, and network geomorphology in the hydrologic response of natural catchments: *Water Resources Research*, **31**, 3089–3101.

Rodriguez-Iturbe, I. and Rinaldo, A. (1997) *Fractal River Basins; Chance and Self-Organization*. Cambridge University Press, Cambridge, 547 pp.

Rodriguez-Iturbe, I. and Valdès, J. B. (1979) The geomorphologic structure of hydrologic response: *Water Resources Research*, **15**, 1409–1420.

Schumm, S. A. (1956) Evolution of drainage systems and slopes in badlands at Perth Amboy, N.J.: *Bulletin of the Geological Society of America*, **871**, 597–646.

Shreve, R. L. (1966) Statistical law of stream numbers: *Journal of Geology*, **74**, 17–37.

Smart, J. S. (1968) Statistical properties of stream lengths: *Water Resources Research*, **4**, 1001–1014.

Snell, J. D. and Sivapalan, M. (1994) On geomorphological dispersion in natural catchments and the geomorphological unit hydrograph: *Water Resources Research*, **30**, 2311–2323.

Strahler, A. N. (1957) Quantitative analysis of watershed geomorphology: *EOS Transactions AGU*, **38**, 913–920.

Surkan, A. J. (1969) Synthetic hydrographs: effects of network geometry: *Water Resources Research*, **5**, 112–128.

Tarboton, D. G., Bras, R. L. and Rodriguez-Iturbe, I. (1988) The fractal nature of river networks: *Water Resources Research*, **24**, 1317–1322.

Tokunaga, E. (1966) The composition of drainage network in Toyohira river basin and the valuation of Horton's first law: *Geophysics Bulletin Hokkaido University*, **15**, 1–19.

Concepts and Modelling in Geomorphology: International Perspectives,
Eds. I. S. Evans, R. Dikau, E. Tokunaga, H. Ohmori and M. Hirano, pp. 147–166.
© by TERRAPUB, Tokyo, 2003.

Tiling Properties of Drainage Basins and Their Physical Bases

Eiji TOKUNAGA

Faculty of Economics, Chuo University, Hachioji-shi, Tokyo 192-0393, Japan
e-mail: tokusan@tamacc.chuo-u.ac.jp

Abstract. Fractality of drainage basins is shown by their tiling properties with subbasins and interbasin areas. Drainage basin forms projected on the two-dimensional plane have mathematical properties similar to those of one-dimensional quasicrystals. Fractal drainage basins are divided into self-similar subbasins and interbasin areas to the infinitesimal limits of their sizes while one-dimensional quasicrystals are divided into segments of two lengths, namely, shorter ones and longer ones also to their infinitesimal limit. The law of stream numbers is expressed by a recurrence formula consisting of three terms. The total number of segments in the line of a quasicrystal is also given by a recurrence formula. In either case, one of the coefficients of them in the recurrence formula is given with the product of solutions of the quadratic equation and the other one with the sum the solutions. The stability of quasicrystals is discussed by using the concept of the Helmholtz free energy. Fractality of drainage basins is explained based on a statistical thermodynamics regarding potential energy expenditure of water in streams. The statistics to explain fractality of drainage basins are peculiar being different from BE, FD and MB statistics. It should be constructed as the nest of a most probable state in a most probable state in a most probable state and so forth.

Keywords: Fractality of Drainage Basins, Quasicrystal, Recurrence Formula, Statistical Thermodynamics, Nest of Most Probable States

INTRODUCTION

Projections of drainage networks on the two-dimensional plane have been recognized as possessing self-similar structures over a considerable range of scales. This self-similarity is an important basis on which drainage networks are regarded as fractals (Mandelbrot, 1977, 1983). There are numerous studies made by applying fractal geometry to analysis of drainage network composition. Such studies are synthesized by Rodoriguez-Iturbe and Rinaldo (1997). Many works are done by regarding Horton's law of stream numbers as expressing self-similarity of drainage networks (e.g. Tarboton *et al*., 1988; La Barbera and Rosso, 1989; Marani *et al*., 1991; Rosso *et al*., 1991; Liu, 1992). However, it has been proved that Horton's law of stream numbers is available in strict sense to express only self-similarity of structurally Hortonian networks (Tokunaga, 1966, 1975; Smart, 1967). Further more Horton's laws (including laws of stream lengths and basin areas) are inadequate in that they do not admit space-filling networks as shown by Tarboton (1996). Nevertheless we can use Horton's law of stream numbers redefining it as the asymptotic law of self-similar networks as shown by

Peckham (1995).

The space-filling problem is also the tiling problem. The latter problem has been extensively studied in the field of crystallography (e.g. Takeuchi, 1992) while the former one discussed rather in that of drainage basin geomorphology in connection with fractal geometry (e.g. Nikora *et al*., 1996; Rodoriguez-Iturbe and Rinaldo, 1997; Cui *et al*., 1999; Tokunaga, 2000). The stability of quasicrystals is discussed by using the concept of the Helmholtz free energy (e.g. Takeuchi, 1992). Many trials to explain drainage basin structures by applying concepts of thermodynamics have been made since Murray (1926). Such studies are also reviewed by Rodoriguez-Iturbe and Rinaldo (1997). The author, however, considers that they are not completely successful.

We deal with problems much more complex than those in crystallography. We, however, find mathematical formulas with the expressions common to tiling properties of drainage basins and quasicrystals which satisfy fractality of these objects considered to have natures physically different to each other. This suggests that there is a possibility to settle a firm theoretical basis for explanation of structures of drainage basins. This paper will show the mathematical natures common to these at first. Then it will be shown that the stability of drainage networks, which have natures more complex than those of quasicrystals, is explained by introducing a peculiar statistics different from Bose-Einstein (BE), Fermi-Dirac (FD) and Maxwell-Boltzmann (MB) ones. This means that we have to advance thermodynamics itself to settle a theoretically firm basis to fractality of drainage basins.

RECURRENCE FORMULAS FOR QUASICRYSTALS AND SELF-SIMILAR DRAINAGE BASINS

A simple model is used to demonstrate self-similarity of quasicrystals in books of crystallography (e.g. Takeuchi, 1992). Each line constructed with segments of length S and that of L in Fig. 1 is considered to be a one-dimensional quasicrystal. Let denote the number of segments in the nth line from the uppermost one by N_n. Then N_n expresses the Fibonacci Numbers when $L/S = (1 + \sqrt{5})/2$. The Fibonacci Numbers are produced by the recurrence formula

$$N_{n+2} = (P+Q)N_{n+1} - PQN_n$$

when $P + Q = 1$ and $PQ = -1$, where $N_1 = 1$ and $N_2 = 1$. Then $P = (1 - \sqrt{5})/2$ and $Q = (1 + \sqrt{5})/2$. These P and Q are the solutions of a quadratic equation. Each line has a self-similar structure as shown by the five lower lines in Fig. 1. Then,

$$\frac{L}{S} = \frac{(L+S)}{L} = \frac{(L+S+L)}{(L+S)} = \frac{(L+S+L+L+S)}{(L+S+L)}$$
$$= \frac{(L+S+L+L+S+L+S+L)}{(L+S+L+L+S)} = \cdots = \frac{\left(1+\sqrt{5}\right)}{2} \qquad (1)$$

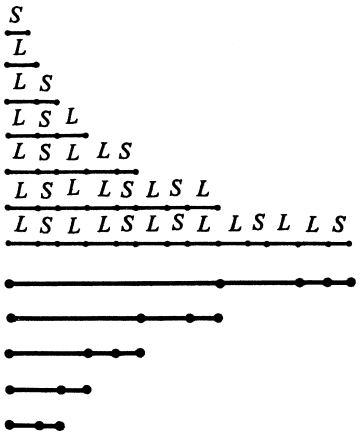


Fig. 1. One-dimensional quasicrystal and its self-similarity. The upper seven lines show the generating process of the Fibonacci sequence: $L/S = (1 + \sqrt{5})/2$. The lower five lines demonstrate self-similarity of the one-dimensional quasicrystal.

Here $(1 + \sqrt{5})/2$:1 is well known as the golden ratio.

Let denote a segment of length S by $\bar{S}$ and that of length L by $\bar{L}$, then the lines with self-similar structure are produced by the replacements $\bar{L} \rightarrow \bar{L} + \bar{S}$ and $\bar{S} \rightarrow \bar{L}$. We can also form a self-similar set of segments of two different lengths, namely longer one and shorter one, dividing line $\bar{L}_k$ of the finite length L_k by the following replacements

$$\bar{L}_k \rightarrow \bar{L}_{k-1} + \bar{S}_{k-1}, \quad \bar{S}_{k-1} \rightarrow \bar{L}_{k-2}$$

Therefore

$$\bar{L}_k \rightarrow \bar{L}_{k-1} + \bar{S}_{k-1} \rightarrow \bar{L}_{k-1} + \bar{L}_{k-2}, \quad \bar{L}_{k-1} \rightarrow \bar{L}_{k-2} + \bar{S}_{k-2} \rightarrow \bar{L}_{k-1} + \bar{L}_{k-3} \qquad (2)$$

where $S_{k-j} = L_{k-j-1}$ for $j = 1, 2, ..., (k-2)$. When $L_{k-j}/S_{k-j} = (1 + \sqrt{5})/2$ for $j = 1, 2, ..., (k-1)$, we can divide the line into segments which provide the Fibonacci Numbers. The reputation of replacements shown by Replacement (2) is also the process to form a one-dimensional Sierpinski space.

Recently Sakamoto (2000) showed that we can define lines with self-similar structure using $N_{n+2} = (P + Q)N_{n+1} - PQN_n$ for another conjugate values of P and Q (e.g. $P = 1 - \sqrt{2}$, $Q = 1 + \sqrt{2}$; $P = 2 - \sqrt{3}$, $Q = 2 + \sqrt{3}$).

The law of stream numbers for self-similar drainage basins is also expressed by using a recurrence formula. First we denote the number of side tributaries of order j entering into a stream of order k by $E_{k,j}$. When $E_{k,j}$ takes the same value for a certain value of $(k - j)$, independent of the individual values of k and j, we can

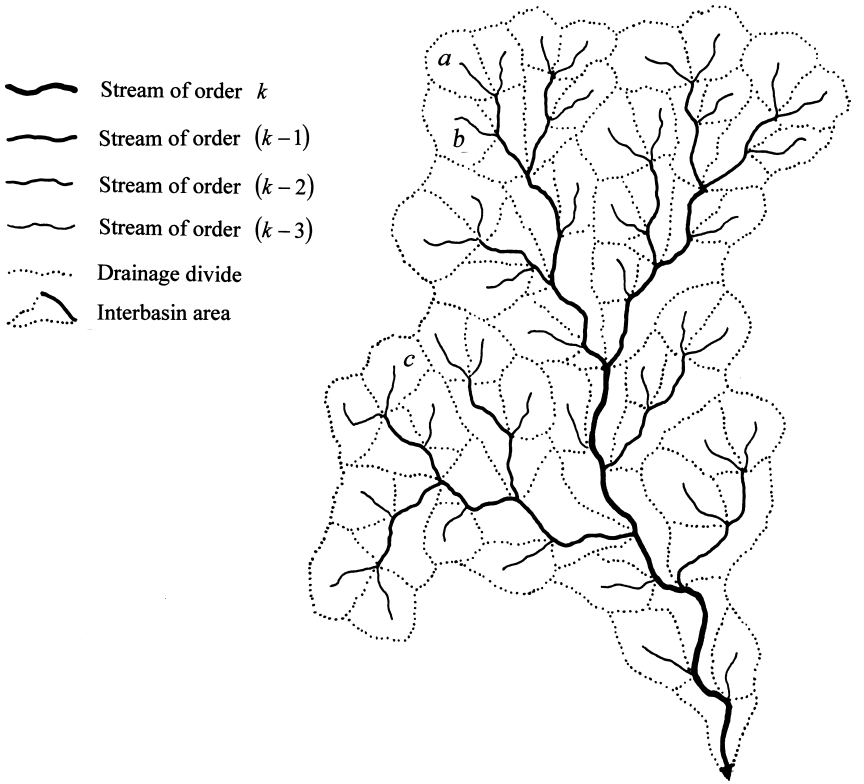


Fig. 2. Hypothetical drainage basin with $E_1 = 1$ and $K = 2$, after Tokunaga (2000). Streams of orders lower than $(k - 3)$ are ignored. Basin names, *a*, *b* and *c*, are used for explanation of relation of the law of stream fall by Yang (1971) to the most probable state of potential energy expenditure of running water.

put $E_{k-j} = E_{k,j}$. Then we can derive the recurrence formula for the number $N_{k,j}$ of streams of order j in a basin of order k when E_{k-j} satisfies $E_2/E_1 = E_3/E_2 = \cdots = E_{k-j}/E_{k-j-1} = K$ where K is constant. That is

$$N_{k,j} = (P+Q)N_{k,j+1} - PQN_{k,j+2} \tag{3}$$

where P and Q are given as follows (Tokunaga, 1966, 1978, 1994, 1998, 2000):

$$P = \frac{\left[2 + E_1 + K - \sqrt{(2+E_1+K)^2 - 8K}\right]}{2}$$

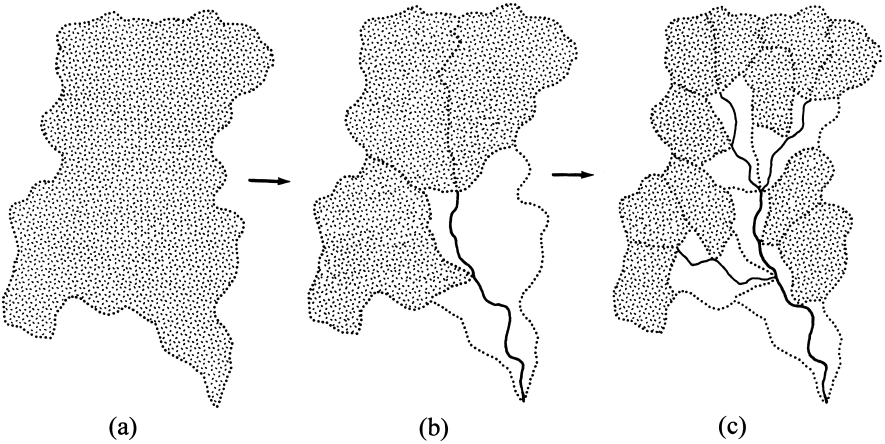


Fig. 3. A process to form a self-similar drainage basin with $E_1 = 1$ and $K = 2$ by replacements. A basin, dotted area, is replaced by three subbasins and three interbasin areas. A white area composed of three interbasin areas is replaced by two subbasins and five interbasin areas. The figures also show a process to form a two dimensional Sierpinski space.

$$Q = \frac{\left[2 + E_1 + K + \sqrt{\left(2 + E_1 + K\right)^2 - 8K}\right]}{2}$$

Here it should be noted that P and Q are the solutions of a quadratic equation. This type of recurrence formula can be transformed into a continued fraction (Tokunaga, 1994).

Put $T_{k,j} = T_{k-j} = E_1 K^{k-j-1}$. Then $T_{k,j}$ is called the tree generator (Veitzer and Gupta, 2000). We can derive an equation, which expresses $N_{k,j}$ in the form of the sum of a series (Tokunaga, 1966, 1978, 1994, 1998, 2000). Then

$$N_{k,j} = \frac{2 + E_1 - P}{Q - P} Q^{k-j} + \frac{2 + E_1 - Q}{P - Q} P^{k-j} \tag{4}$$

The drainage system expressed by Eq. (3) or (4) has been called Branching System I (Tokunaga, 1994, 1998, 2000). The law of basin areas of Branching System I is given by

$$A_k = A_j Q^{k-j} \tag{5}$$

where A_k is the area of a basin of order k and A_j that of order j. This equation is derived on the assumption that a basin of a given order is divided into subbasins

and interbasin areas of infinitesimal sizes in the ultimate. A hypothetical drainage basin with $E_1 = 1$ and $K = 2$ is illustrated in Fig. 2. Here let $N_{\mathrm{I},k,j}$ be the number of interbasin areas adjoining a stream of order k and $B_{k,j}$ be the area of such an interbasin area when streams of orders lower than j are ignored. Then the following replacements hold for Branching System I.

$$\left[A_k\right] \rightarrow \left[\left(2 + E_1\right)A_{k-1} + N_{\mathrm{I},k,k-1}B_{k,k-1}\right] \tag{6}$$

$$\left[N_{\mathrm{I},k,j+1}B_{k,j+1}\right] \rightarrow \left[E_1K^{k-j-1}A_j + N_{\mathrm{I},k,j}B_{k,j}\right] \tag{7}$$

where $N_{\mathrm{I},k,j} = 2 + E_1 + E_1K(K^{k-j-1} - 1)/(K - 1)$ and this relation is called the law of numbers of interbasin areas (Tokunaga, 1975, 1978, 2000). The values of E_1, K, $N_{\mathrm{I},k,j}$, A_j and $B_{k,j}$ are given by the statistical values, for examples, the average values for actual drainage basins (Tokunaga, 1966, 1975, 1978; Onda and Tokunaga, 1987; Peckham, 1995; Tarboton, 1996; Jämtnäs, 1999; Peckham and Gupta, 1999; Veitzer and Gupta, 2000).

Replacements (6) and (7) can be demonstrated by illustrations. Let the order of the three basins with $E_1 = 1$ and $K = 2$ in Fig. 3 be k, then the transition from Fig. 3(a) to Fig. 3(b) means Replacement (6). That from Fig. 3(b) to Fig. 3(c) means two replacements. One is Replacement (7) for $j = k - 2$ in the area occupied by interbasin areas in Fig. 3(b). The other is $[A_{k-1}] \rightarrow [(2 + E_1)A_{k-2} + N_{\mathrm{I},k-1,k-2}B_{k-1,k-2}]$ in each of the basins of order $(k - 1)$. This relation is obtained by substituting $(k - 1)$ into k in Replacement (6).

Moussa (1997) used at first a Sierpinski space to describe a fractal property of drainage basins. Figure 3 also shows that a two-dimensional Sierpinski space is generated by repetitions of a successive shift of indices in Replacements (6) and (7).

We can also demonstrate the replacements to form the Sierpinski space using the Peano basin. Natural drainage networks are modeled on a statistical basis as a system with branching number 2 (Peckham, 1995), binary tree, whereas streams form deterministically a regular triadic tree, system with branching number 3 (Peckham, 1995), in the Peano basin. Nevertheless the Peano basin is a good tool to explain the self-similar natures of drainage basins. If we regard a trifurcating point to consist of two bifurcating points, which are dislocated with an infinitesimal distance from each other, Strahler's ordering method is available for it and its stream network. Then $E_1 = 1$ and $K = 2$, $A_{k-1} = A_k/4$, and $B_{k,k-1} = A_k/8$ in the Peano basin. The law of numbers of interbasin areas in a basin with branching number 3 is given by $N_{\mathrm{I},k,j} = 1 + E_1 + E_1K(K^{k-j-1} - 1)/(K - 1)$ (Tokunaga, 2000). We can show the process to form the Sierpinski space substituting these values and relations into Replacements (6) and (7). The transition from Fig. 4(a) to Fig. 4(b) shows the replacement, $[A_k] \rightarrow [3A_{k-1} + 2B_{k,k-1} (=A_{k-1})]$. The transition of the area occupied by interbasin area in Fig. 4(c) to the corresponding area in Fig. 4(d) shows the replacement, $[2B_{k,k-1} (=A_{k-1})] \rightarrow [2A_{k-2} + 4B_{k,k-2} (=2A_{k-2})]$. These rules

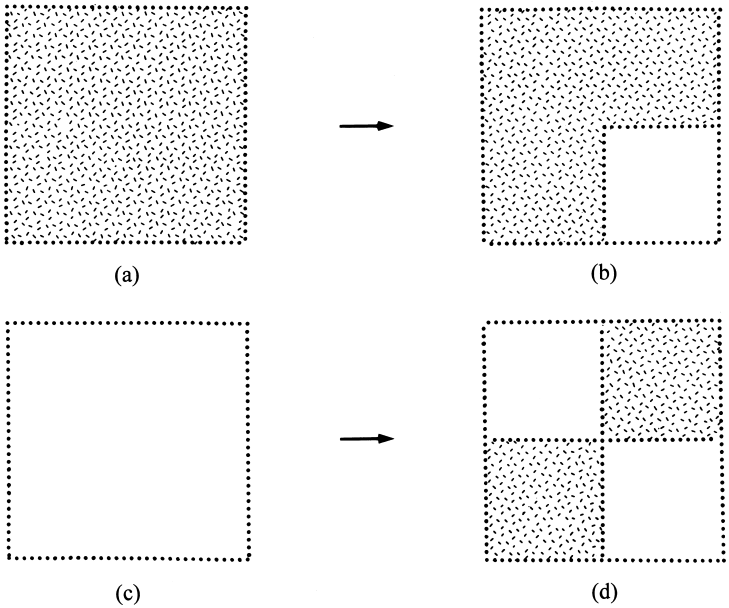


Fig. 4. The two rules to generate a Sierpinski space in a Peano basin. A dotted square is regarded as a basin and a white square as to be occupied by two interbasin areas.

to form the Sierpinski space, however, are entirely different from those demonstrated by Moussa (1997).

Now we find the terms, namely, recurrence formula, solutions of a quadratic equation, and Sierpinski space, common to the one-dimensional quasicrystal and the self-similar drainage basin. We can regard the one-dimensional quasicrystals as the one-dimensional drainage basins although such basins never exist in the actual world. Crystallographers regard one-dimensional quasicrystals as being quasi-cyclic (e.g. Takeuchi, 1992; Sakamoto, 2000) whereas geomorphologists use the term "cyclic" or "cyclicity" for the property of drainage basins expressed by Eq. (4) (e.g. Tokunaga, 1978; Tarboton, 1996; Veneziano *et al.*, 1997; Perera and Willgoose, 1998; Cui *et al.*, 1999). The author considers one-dimensional quasicrystals or one-dimensional drainage basins to be cyclic in geomorphological sense.

POTENTIAL ENERGY EXPENDITURE OF RUNNING WATER IN ALL STREAM CHANNELS IN A BASIN

The law of stream fall by Yang (1971) states that the ratio of the average stream fall between any two different order streams in the same basin is unity. Numerable data taken from actual drainage basins show their favorable conformity to the law (Yang, 1971; Yang and Stall, 1973; Shimano, 1978). Yang (1971) tried

to explain the physical basis of the law using the analogy of entropy in thermodynamics. His explanation is valid at least partly. Let denote the fall of a stream of order j by H_j and suppose water that flows into the stream of order (k – 3) at its uppermost reach in basin a in Fig. 2. The most probable state of potential energy expenditure per unit mass of water is certainly sustained when $H_k = H_{k-1} = H_{k-2} = H_{k-3}$, as shown by Yang (1971). We cannot, however, specify the condition to keep the most probable state using such an equation for water flowing into the stream of order (k – 3) in basin b within the traveling root from its inflow point to the uppermost reach of the stream of order (k – 1) whereas the relation $H_k = H_{k-1}$ sustains the most probable state of potential energy expenditure of a unit mass of water after flowing into the stream of order (k – 1). The relation $H_{k-1} = H_{k-2} = H_{k-3}$ also sustains the most probable state for a unit mass of water flowing into the stream of order (k – 3) in basin c at its uppermost reach up to the confluence point of the streams of order (k – 1) and order k. We cannot, however, specify the condition to keep the most probable state in the reach downward from the confluence point by using the relation regarding stream falls. Nevertheless let us regard provisionally the following relation as a necessary condition to sustain the most probable state of potential energy expenditure per unit mass of water supplied to a drainage basin of order k.

$$H_k = H_{k-1} = \cdots = H_j = \cdots = H \tag{8}$$

Here let $L_{k,h}$ be the length of a stream of order k measured by a ruler with length l_h and $L_{j,h}$ be that of order j, then the law of stream lengths for a self-similar network is expressed as follows:

$$L_{k,h} = L_{j,h} Q^{D_S (k-j)/D_B} \tag{9}$$

where D_S is the fractal dimension of individual streams, D_B that of individual basins, and l_h the straight-line length of a stream of order h for $j \geq h$ (Tokunaga, 1994, 1998, 2000). Then usually $D_B = 2$ for actual drainage basins. Combination of Eqs. (8) and (9) provides a self-affine stream network in three-dimensional space (Tokunaga, 1998). We can meditate on the most probable state of potential energy expenditure per unit mass of water in all stream channel of in a basin of a given order, which satisfies the condition of self-affinity of its steam network, using Eqs. (4), (5), and (8).

Let denote the quantity of water supplied as precipitation to a basin of order j in a given period of time by W_j. Then we may postulate the relation $W_j = \alpha A_j$ where α is constant regardless of the value of j. Let e_j^* be the potential energy expenditure per unit mass of water supplied to a basin of order j in the stream of order j. Then the following relation can be assumed between e_j^* and H.

$$e_k^* = e_{k-1}^* = \cdots = e_j^* = \cdots = \beta H \tag{10}$$

Table 1. Potential energy expenditure, e_{j-1}, per unit mass of water in all streams in a basin of order $(j-1)$. Streams of orders lower than i are ignored. In the basin, $E_1 = 1$ and $K = 2$. The third terms in the braces show the rapid convergence of them for decrease of i value.

	$i = j-2$	$i = j-3$	$i = j-4$
e_{j-1}	$\{(2/3)2 + (4/9) - (1/36)\}\beta H$	$\{(2/3)3 + (4/9) - (1/144)\}\beta H$	$\{(2/3)4 + (4/9) - (1/576)\}\beta H$

where β is constant. Here let e_k be the potential energy expenditure per unit mass of water supplied to a basin of order k in all streams in the basin. When we ignore streams of orders lower than i. Then we can give e_k by

$$e_k = \left[\sum_{j=i}^{k} e_j^* W_j N_{k,j}\right] \Big/ W_k = \left[\sum_{j=i}^{k} e_j^* A_j N_{k,j}\right] \Big/ A_k \tag{11}$$

From Eqs. (4), (5), (10), and (11),

$$e_k = \beta H \sum_{j=i}^{k} \left[C_1 + C_2 (P/Q)^{k-j}\right] = \beta H C_1 (k-i+1) + \beta H C_2 \frac{\left[Q - Q(P/Q)^{k-i+1}\right]}{(Q-P)} \tag{12}$$

where $C_1 = (2 + E_1 - P)/(Q - P)$ and $C_2 = (2 + E_1 - Q)/(P - Q)$. For a basin of order $(j-1)$, we have

$$e_{j-1} = \beta H C_1 (j-i) + \beta H C_2 \left[Q - Q(P/Q)^{j-i}\right] \Big/ (Q-P) \tag{13}$$

The average state of infinite topologically random channel networks satisfies Eq. (4) with $E_1 = 1$ and $K = 2$ (Shreve, 1969; Tokunaga, 1978). Therefore $P = 1$ and $Q = 4$. The values of e_{j-1} for $i = j-2$, $j-3$, and $j-4$ for $E_1 = 1$ and $K = 2$ are shown in Table 1. The values show that absolute value of the second term of the right side of Eq. (13) rapidly approaches $(4/9)\beta H$ with decrease of i. Therefore we can use

$$e_{j-1} \approx \beta H C_1 (j-i) + \beta H C_2 Q / (Q-P) \tag{14}$$

instead of Eq. (13) for a large value of $(j-i)$. Put $e_\infty = e_{j-1}$, then we derive the following equation for

$$e_k = \beta H C_1 (k-j+1) + e_\infty \tag{15}$$

We can regard e_∞ as constant for a very large value of $(j - i)$. Then Eq. (15) shows that e_k, e_{k-1}, ..., e_{j+1}, and e_j distribute equidistantly, increasing their values as the index value increases. This means that the amount of potential energy expenditure per unit mass of water in all streams in a basin of a given order increases equidistantly as the order increases when streams of orders lower than a certain value are ignored. Such a situation occurs in self-similar drainage basins when the law of stream fall is kept in them.

MOST PROBABLE STATE OF POTENTIAL ENERGY EXPENDITURE OF WATER IN SELF-SIMILAR DRAINAGE BASINS

Two streams of a given order join to form a stream of the next higher order in Strahler's ordering system. This designation inevitably divides the basin into two areas with topographically different natures. We can clearly demonstrate it using the example in Fig. 2. The drainage basin of order k is divided into the areas occupied by the two basins of order $(k - 1)$, which feed the streams entering into the stream of order k at its uppermost point, and the area occupied by the basins, which feed the side tributaries entering into the stream of order k, and the interbasin areas adjoining the stream of order k. We refer to the latter one a side area of the stream of order k and designate its area by A_k^*. Then $A_k^* = A_k - 2A_{k-1}$. This relation defines the side area of a stream of a given order. Therefore $A_k^* = A_k - 2A_{k-1}$, $A_{k-1}^* = A_{k-1} - 2A_{k-2}$, ..., $A_{j+1}^* = A_{j+1} - 2A_j$. Basins of order $(k - 1)$ are always structurally similar to that of order k in a self-similar drainage basin. Therefore, how to divide the side area to the stream of order k into subbasins of various orders decides the composition of the drainage network of order k. We can derive an equation for A_k^*, A_{k-1}, ..., A_j, and $B_{k,j}$ as follows:

$$A_k^* = E_1 \sum_{h=j}^{k-1} K^{k-h-1} A_h + N_{\mathrm{I},k,j} B_{k,j} \tag{16}$$

where $N_{\mathrm{I},k,j} = 2 + E_1 + E_1 K(K^{k-j-1} - 1)/(K - 1)$ as mentioned before. Let denote the potential energy expenditure of water supplied as precipitation to the side area of a stream of order k in all streams in the side area by U_k. Then U_k is given

$$U_k = E_1 \sum_{h=j}^{k-1} e_h K^{k-h-1} W_h = \alpha\beta C_1 H E_1 \sum_{h=j}^{k-1} K^{k-h-1}(h - j + 1) A_h + \alpha e_\infty E_1 \sum_{h=j}^{k-1} K^{k-h-1} A_h \tag{17}$$

when Eq. (15) is satisfied in all basins in the side area. We can eliminate the second term of the right side of Eq. (16) for a considerably large value of $(k - j)$ because of the small value of $(N_{\mathrm{I},k,j} B_{k,j} / A_k^*)$. Thus we obtain

$$A_k^* \approx E_1 \sum_{h=j}^{k-1} K^{k-h-1} A_h \tag{18}$$

Then we can also derive

$$U_k - \alpha e_\infty A_k^* \approx \alpha\beta C_1 H E_1 \sum_{h=j}^{k-1} K^{k-h-1}(h-j+1)A_h \tag{19}$$

from Eqs. (17) and (18).

Here let us replace the approximation signs in Eqs. (18) and (19) with equality signs respectively. Then we can derive the following equations for constant values of A_k^* and U_k.

$$A_k^* = E_1 \sum_{h=j}^{k-1} K^{k-h-1} A_h \tag{20}$$

$$D = H E_1 \sum_{h=j}^{k-1} K^{k-h-1}(h-j+1)A_h \tag{21}$$

where $D = (U_k - \alpha e_\infty A_k^*)/\alpha\beta C_1$ and therefore D is regarded as constant for a given value of $(j-i)$ in Eq. (14). Equation (20) means that the quantity of water supplied to the side area of the stream of order k in the given period is constant because $W_j = \alpha A_j$, and Eq. (21) that the amount of potential energy expenditure of water supplied to the side area in the given period is also constant, where the unit of mass of water can be given arbitrarily.

Let us regard a unit mass of water supplied to a unit area in the given period as a body and postulate that the amount of potential energy expenditure of each body differs from those of the other bodies in a basin in the side area. Then infinitesimally small difference in potential energy expenditure is postulated to be distinguishable. This means that all the bodies can be numbered by the amounts of their potential energy expenditure and therefore compose a numerable set in the basin. Let us divide a basin in the side area into two-dimensional cells of the unit area and postulate the state that all the cells can be numbered according to their positions in the basin. The number of all different arrangements of the numbered cells in a basin of order j is $A_j!$, where A_j is regarded as a natural number. Let denote the product of the numbers of all different arrangements of cells in respective basins in a side area by g. Then

$$g = (A_{k-1}!)^{E_1}(A_{k-2}!)^{E_1 K}(A_{k-3}!)^{E_1 K^2} \cdots (A_h!)^{E_1 K^{k-h-1}} \cdots (A_j!)^{E_1 K^{k-j-1}} \tag{22}$$

Let us decrease water supplied to a basin of order $(k-2)$ by two bodies and assume that the amounts of potential energy expenditure of these bodies in all streams in the basin approximate to the average value, e_{k-2}, respectively. And let us increase water supplied to a basin of order $(k-1)$ by one body, the amount of potential energy expenditure of which approximates to e_{k-1}, and that supplied to a basin of order $(k-3)$ by one, the amount of potential energy expenditure of which approximates to e_{k-3}. This procedure leaves U_k as well as A_k^* unchanged because

$$\begin{aligned} &e_{k-1} - 2e_{k-2} + e_{k-3} \\ &= \beta C_1 H(k-j) + e_\infty - 2\beta C_1 H(k-j-1) - 2e_\infty + \beta C_1 H(k-j-2) + e_\infty = 0 \end{aligned}$$

The product g' of numbers of all different arrangements of cells in the respective basins in the side area after the procedure is expressed by

$$\begin{aligned} g' = &\left(A_{k-1}!\right)^{E_1-1}\left(A_{k-1}+1\right)!\left(A_{k-2}!\right)^{E_1K-1}\left(A_{k-2}-2\right)!\left(A_{k-3}!\right)^{E_1K^2-1} \\ &\times\left(A_{k-3}+1\right)!\left(A_{k-4}!\right)^{E_1K^3}\cdots\left(A_j!\right)^{E_1K^{k-j-1}} \end{aligned} \tag{23}$$

The ratio g'/g is given by

$$\frac{g'}{g} = \frac{\left(A_{k-1}+1\right)!\left(A_{k-2}-2\right)!\left(A_{k-3}+1\right)!}{A_{k-1}!\,A_{k-2}!\,A_{k-3}!} = \frac{\left(A_{k-1}+1\right)\left(A_{k-3}+1\right)}{\left(A_{k-2}-1\right)A_{k-2}}$$

When a basin of order $(k-3)$ contains a very large number of cells, this expression may be replaced by

$$\frac{g'}{g} = \frac{A_{k-1}A_{k-3}}{{A_{k-2}}^2} \tag{24}$$

When g takes a maximum value, a small variation in the arrangements should leave it unchanged, then $g'/g = 1$ and thus $A_{k-1}/A_{k-2} = A_{k-2}/A_{k-3}$. A similar relationship applies to A_{k-2}, A_{k-3}, and A_{k-4}; ...; A_{j+2}, A_{j+1}, and A_j. Therefore the condition for the maximum value of g is

$$A_{k-1} / A_{k-2} = A_{k-2} / A_{k-3} = \cdots = A_{j+1} / A_j = Q \tag{25}$$

This relation is the law of basin areas itself. Let denote the numbers of water bodies supplied to all basins of order j in the side area of the stream of order k by W_j'. Then

$$W'_{k-1} / W'_{k-2} = W'_{k-2} / W'_{k-3} = \cdots = W'_{j+1} / W'_j = Q / K \tag{26}$$

because $W'_j = \alpha E_1 K^{k-j-1} A_j$. The relation of K to Q in Eq. (3) evidently shows that $Q/K > 1$.

A similar method is taken to obtain a most probable state under the restrictive conditions that the number of particles or oscillators and the total energy possessed by them are constant respectively in statistical thermodynamics (e.g. Reif, 1965). Equations (20) and (21) are apparently the restrictive conditions to sustain a most probable state of potential energy expenditure of water bodies in the side area of the stream of order k.

Statistics for potential energy expenditure of water bodies, however, differs from BE, FD, and MB statistics in some points. The number of quanta or particles decreases exponentially as their energy or energy level increases in BE, FD, and MB statistics. On the other hand, water bodies are clustered in respective basins and each clustered water bodies has the average value of their potential energy expenditure. The number of water bodies increases exponentially as the average value of their potential energy expenditure increases equidistantly as shown by Eqs. (15) and (26). The probability that a water body belong to the clusters, which produce an average value of potential energy expenditure, increases as the average value increases. This provides a distribution reverse to the canonical distribution, which expresses the relation between probability and energy in thermodynamics. We may refer to the distribution as the reverse canonical distribution for clustered bodies.

Equations (22) and (23) allow us to assume the state that in each basin the cells of unit area with different relative heights above its outlet distribute at random. This means that basins of higher orders have very rugged surfaces on which water does not flow at least smoothly. Random arrangements of the cells of different relative heights seldom form drainage divides. Conversely the marginal part of a cluster of cells ought to be occupied by ones relatively higher than those in the inner part to form a drainage network. Then the random process seems to be contradictive to the forming process of drainage basins. Altitudes of confluence points of side tributaries to a stream of a given order differ from each other in the side area of the stream. Consequently water bodies supplied to a basin have a base level different from those to the other basins with regard to potential energy expenditure in the side area of the stream, whereas the base level is given absolutely in BE, FD, and MB statistics. We need some additional settings to explain physical bases of the self-similarity of drainage basins.

NEST OF MOST PROBABLE STATES

A key concept to create the statistics with physical bases for drainage basin composition is a nest of most probable states. It will be shown in this chapter by using the Peano basin. As mentioned afore, $E_1 = 1$, $K = 2$, $P = 1$, and $Q = 4$ in it.

Let the lower half of the basin in Fig. 5(a) be the side area of the stream of

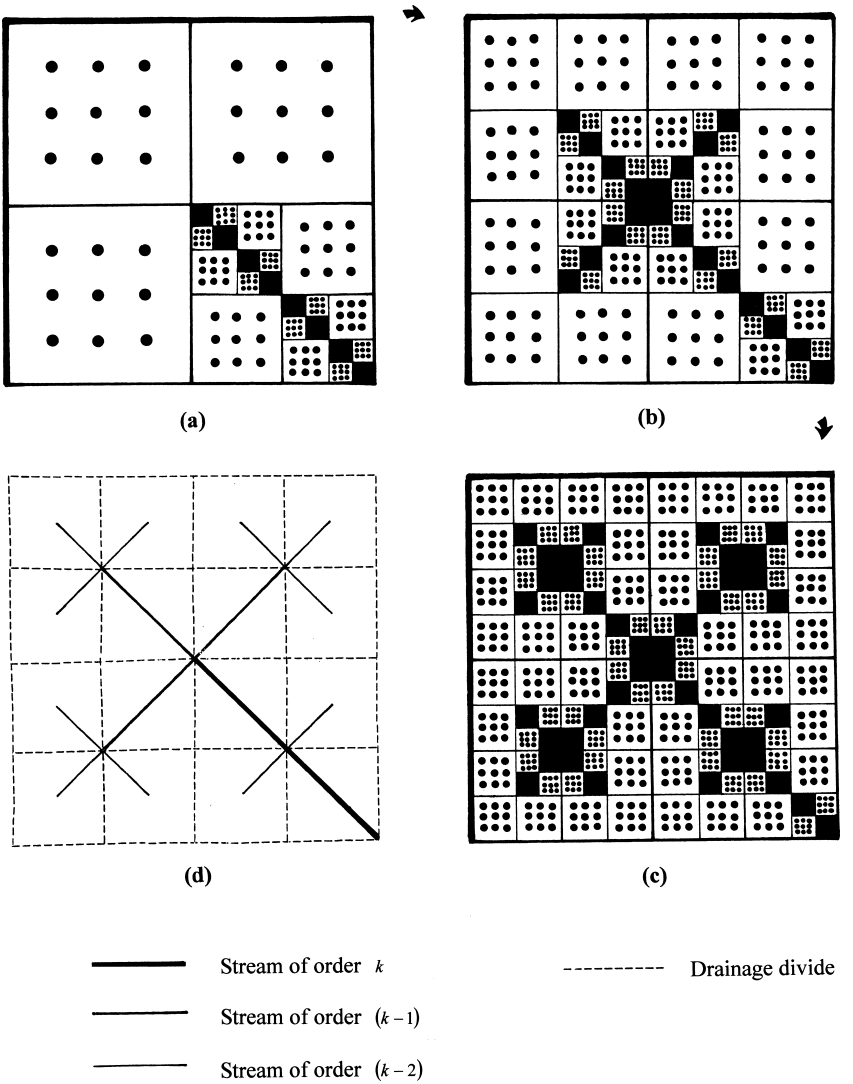


Fig. 5. The nest of most probable states of potential energy expenditure of water bodies in a Peano basin. Diameters of black circles show average values of potential energy expenditure per unit mass of water in respective basins qualitatively. The smallest right square consists of two interbasin areas with the shape of the right triangle. Streams of orders lower than $(k-2)$ are not drawn.

order k. Then there exist one basin of order $(k-1)$, two of order $(k-2)$, four of order $(k-3)$, eight of $(k-4)$, and sixteen interbasin areas in the side area when streams of order lower than $(k-4)$ are ignored. The number of interbasin areas adjoining a stream of a given order in a basin with branching number 3 is one less

than that in a basin with branching number 2 as mentioned before. A black right square in Fig. 5(a) consists of two right triangles and each one is an interbasin area adjoining the stream of order k. Let us assume the state that numbered cells with different heights above its outlet distribute at random regarding their positions in each basin. Water bodies supplied to the cells in a basin of order $(k-1)$ provides e_{k-1}, those to the cells in a basin of order $(k-2)$ provides e_{k-2}, and so forth. We may also assume that the relief of the basin of order $(k-1)$ is larger than that of the basin of order $(k-2)$, and then the relief of the basin decreases as the basin order becomes lower. This state should satisfy Eqs. (20), (21), (22), (23), (24), and (25). The diameter of black circles in Fig. 5 shows the size of the relief of each basin qualitatively.

We can depict a most probable state in each basin of order $(k-1)$ in a similar manner as to obtain Fig. 5(a). The result is shown as Fig. 5(b). The basins of order $(k-3)$ and of order $(k-4)$, and interbasin areas with relief smaller than that of the basin of order $(k-2)$ distribute alongside the stream of order k and those of order $(k-1)$, whereas the area adjoining the margin of the basin of order k except the part near its outlet is occupied by eleven basins of order $(k-2)$ with relatively large relief. Drainage divides can exist only in areas with relatively large relief.

We can also depict a most probable state in each basin of order $(k-2)$ in Fig. 5(b) as shown by Fig. 5(c). Then a stream of order $(k-2)$ appears with four interbasin areas in each of the basins of order $(k-2)$. All the streams are mostly surrounded by basins of order $(k-4)$ and interbasin areas with relatively small relief. The areas adjoining the margins of the basins of order k, order $(k-1)$ and order $(k-2)$ are occupied by the basins of order $(k-3)$ with relatively large relief except the part of their outlets. The surface of the basin designated by Fig. 5(c) is much smoother than that by Fig. 5(a). The three-dimensional form of the former basin is more systematic than latter one.

We can assume basins of $(k-5)$ in the basin shown by Fig. 5(c). Then an interbasin area is divided into one basin of order $(k-5)$ and two interbasin areas. This procedure makes the surface of the whole basin smoother and its three-dimensional form more systematic. Here let denote a system, in which A_k cells of a unit area with different heights distribute at random and the heights of the cells produce the average value corresponding to e_k, by S_k. We can assume a system at a most probable state in which cells of unit area with different heights above the outlet distribute at random in each of basins of orders lower than k. Then the heights of A_{k-1} cells in each of basins of order $(k-1)$ produce the average value corresponding to e_{k-1}, those in each of basins of order $(k-2)$ the average value corresponding to e_{k-2}, ..., and those in each of basins of order j the average value corresponding to e_j. Let us denote the system by $S_{k,k-1}$. Similarly we can define a system at a most probable state denoted by $S_{k,j}$ with a general index j in which the cells with different heights distribute at random in each of basins of orders lower than j. The following relation is derived for S_k, $S_{k,k-1}$, ..., $S_{k,j}$.

$$S_k \supset S_{k,k-1} \supset \cdots \supset S_{k,j} \tag{27}$$

This relation shows a nest structure of most probable states: a most probable state in a most probable state in a most probable state and so forth. Such a structure for the Peano basin is demonstrated by using Fig. 5. The basin illustrated by Fig. 5(c) exists as a most probable state in that by Fig. 5(b), which exists as a most probable state in that by Fig. 5(a). The basin illustrated by Fig. 5(a) is a most probable state of a regular square with the area same to that of the basins of order k in Fig. 5 in which cells with different heights distribute at random.

A mountain landscape is formed as a set of basins and interbasin areas. It looks to have a smooth surface cover completely different from those of rugged figures with Brownian relief by Mandelbrot (1983). The basin forming process is also one to form the mountain landscape with a smooth surface.

The nest of most probable states proposes a general idea that randomness can produce convergence. The principle that a form is produced as the nest of most probable states seems to be applicable to not only self-similar branching systems including diffusion limited aggregation (DLA), lightning, neural networks etc. but also to another systems with stable forms.

VALUES OF E_1 AND K

The nest of most probable states is defined by using Eqs. (20), (21), (22), (23), (24), (25), (26) and (27). There are no mathematical restrictions as to the values of E_1 and K themselves except $E_1 > 0$ and $K > 0$ when we treat them as statistical values. These equations are so comprehensive regarding the values of E_1 and K that we can define a self-similar system as the nest of most probable states for any large value of them. On the other hand it has been proved that Shreve's (1966, 1969) random topological model satisfies Eq. (4) with $E_1 = 1$ and $K = 2$ as a law which expresses the average state (Tokunaga, 1975, 1978). Empirical data, however, show a general tendency that E_1 and K as the average values are larger than 1 and 2 but not far from these values respectively in low order parts which provide reliable values because of large populations of streams in them (Tokunaga, 1966, 1978; Onda and Tokunaga, 1987; Peckham, 1995; Tarboton, 1996; Jämtnäs, 1999; Peckham and Gupta, 1999; Veitzer and Gupta, 2000).

There are some discussions on discrepancies between the empirical data and the random topological model on the values of E_1 and K (e.g. Tokunaga, 1978; Peckham, 1995; Cui *et al.*, 1999; Veitzer and Gupta, 2000). Tokunaga (1978) has stated that an equilibrium state of a drainage network is kept on the balance of randomness and non-random force. He also regarded the network, which satisfies Eqs. (4) and (5), as to be at the equilibrium state encompassing that of the maximum entropy with $E_1 = 1$ and $K = 2$ (Tokunaga, 1978). His consideration was made at that time without the physical bases demonstrated in this paper.

DISCUSSION

Theoretical studies on the values of E_1 and K have also advanced since the proposal of concept of self-similarity by Mandebrot (1977, 1983). Perera and

Willgoose (1998) examined the behavior of the cumulative area distribution based on the model defined by E_1 and K setting two different types of zeroth order hill slope flow patterns. Then they showed by simulation that the value of K is strongly related to the scaling exponent in the region of the catchment dominated by fluvial erosion. Cui *et al*. (1999) have considered the values of E_1 and K as representing the effects of regional controls and pointed out importance of a space-filling constraint to explain these values using their model, stochastic Tokunaga model. Peckham and Gupta (1999) discussed the value of $T_{k,j} = T_{k-j} = E_1 K^{k-j-1}$ presenting a reformation of Horton's laws on the basis of statistical self-similarity. Veitzer and Gupta (2000) analyzed this value and its variability introducing a new class of random self-similar networks. These studies have widened the horizon of study on drainage basin geomorphology. Further development of these studies might result in providing some statistical bases in connection with physical quantities. We can discuss some about the values of E_1 and K relating the nest of most probable states of potential energy expenditure of water bodies, Shreve's (1966, 1969) random topological model, and empirical data to each other.

Empirical data exhibit a general tendency that the value of E_1 is not far from 1 and that of K from 2 as mentioned in the previous chapter. This implies that actual drainage networks strongly controlled by randomness. Any constraints are not imposed on direction of streams in Shreve's (1966, 1969) random topological model. Streams merge each other completely at random in it. This means that no directionally systematic inclinations of streams are postulated. Water never flows in networks in which streams have no systematic inclinations. There is, however, no reason for us to abandon Shreve's (1966, 1969) random topological model. It should be considered to be an asymptotic base for theoretical consideraton of drainage network composition.

Water is drained from a basin through systematically inclined streams. Directionally systematic inclinations should impose a non-random bias on confluences of streams. Then the non-random bias probably acts as a force to raise the values of E_1 and K above 1 and 2 respectively. A stream with larger slope provides a stronger non-random bias. If so, the tree generator $T_{2,1}$ must tend to be larger than $T_{3,2}$ in actual drainage basins because Horton's (1945) law of stream slopes shows that the average slope of streams decreases geometrically as the order of streams increases.

Jämtnäs (1999) obtained tree generator matrices for 48 drainage basins in the United States, orders of which are equal to or higher than 6, after Peckham's (1995) study. Figures of the generators are shown to the two places of decimals. The values of $T_{2,1}$ and $T_{3,2}$ are regarded as relatively stable for their large numbers of samples. Then $T_{2,1} > T_{3,2}$ in 29 basins, $T_{2,1} = T_{3,2}$ in 4 basins, and $T_{2,1} < T_{3,2}$ in 15 basins. The difference $(T_{2,1} - T_{3,2})$ is evaluated small in all basins. The result is favourable to the conjecture mentioned above in statistical sense. The comparison of the values $T_{2,1}$ and $T_{3,2}$ in a basin, however, is almost meaningless because these values have wide ranges of distribution due to their stochastic property and also more or less influenced by regional difference of geologic controls, etc. It

must be still more difficult to prove that there exists the firm relation, $T_{k,k-w} < T_{k-1,k-w-1} < \cdots < T_{j+1,j-w+1}$ with a small difference between successive terms for $1 \leq w \leq j$, only using empirical data. If the existence of this relation is theoretically explained, the self-similar model defined by the constant values of E_1 and K will result in having a clear meaning as an asymptotic model with physical bases. Then drainage basins, which satisfy the relation mentioned above, are regarded as to be dislocated slightly from the self-similarity and at a quasi-equilibrium state.

Another asymptotic postulation was also used on the process to derive the nest of most probable states of potential energy expenditure of water bodies. We needed the assumption that a basin of a given order is divided into subbasins and interbasin areas of infinitesimal sizes to derive the law of basin area expressed by Eq. (5) (Tokunaga, 1978, 1994, 1998, 2000). The law of stream lengths expressed by Eq. (9) was derived from Eq. (5) (Tokunaga, 1994, 1998, 2000). Therefore the stream in a basin of an infinitesimal size should have the corresponding, namely infinitesimal, length. A stream with infinitesimal length and a finite fall given by Eq. (8) should be vertical. Such a stream never appears in nature. The assumption of subbasins and interbasin areas of infinitesimal sizes shows the asymptotic direction. We can presumably say that we need some asymptotic postulations, even if they are contradictive to each other in the ultimate, for modeling of complex systems such as drainage networks. Equations (20) and (21) are also derived by using the asymptotic property mentioned above.

FINAL REMARKS

Drainage basin forms projected on the two-dimensional plane have mathematical properties similar to those of one-dimensional quasicrystals. These properties are expressed by recurrence formulas consisting of three terms as well as by Sierpinski spaces. One of coefficients in the recurrence formulas is given by the product of the solutions of a quadratic equation and the other one by the sum of them. These expressions common to the quasicrystals and drainage basins describe their common properties, namely, cyclicity and self-similarity although the term, quasi-cyclic, is used in the field of crystallography.

The Helmholtz free energy should concern the stability of quasicrystals. The stability of self-similar drainage basins is explained by using the nest of most probable states of potential energy expenditure of water bodies. This must be considered an important physical base. The nest of most probable states never impose any constraints on the values E_1 and K except $E_1 > 0$ and $K > 0$. Empirical data, however, shows the general tendency that $E_1 > 1$ and $K > 2$ but these values are not so far from 1 and 2 respectively. This implies that confluences are fairly influenced by topological randomness in addition to any other forces than it. The author considers that stochastic theories combined with three-dimensional forms of basins and some explicit physical quantities in connection with them will explain the values of there are E_1 and K concretely. He also expects that the introduction of probabilistic theories into analysis of self-similarity of drainage basins (e.g. Cui *et al.*, 1998; Peckham and Gupta, 1999; Veitzer and Gupta, 2000)

will lead to discovery of such quantities. If there exists the relation, $T_{k,k-w} < T_{k-1,k-w-1} < \cdots < T_{j+1,j-w+1}$, for $1 \le w \le j$ with a small difference between successive terms in a basin of order k when streams of orders lower than j are ignored, the basin is regarded as to be at quasi-equilibrium state.

Any thermodynamic functions are not yet defined for the nest of most probable states. Established statistics for thermodynamics are defined in a unitary space. This study clarified that statistics in nested spaces is needed to define thermodynamic functions for self-similar or self-affine branching systems. The author feels some limitations to established principles of physics in investigations of complex systems. It is rather expected that new principles of physics will be discovered in objects of geomorphology and hydrology.

Acknowledgements—A part of this study was financially supported by Chuo University Grant Support from fiscal 1999 to 2000.

REFERENCES

Cui, G., Williams, B. and Kuczera, G. (1999) A stochastic Tokunaga model for stream networks: *Water Resour. Res.*, **35**, 3139–3147.

Horton, R. E. (1945) Erosional development of streams and their drainage basins: Hydrophysical approach to quantitative morphology: *Bull. Geol. Soc. Am.*, **56**, 275–370.

Jämtnäs, L. (1999) Recursive patterns in large-scale fluvial landscapes as extracted from digital elevation models: Master thesis, Dept. of Earth Sci., Uppsala Univ., Uppsala, 245 pp.

La Barbera, P. and Rosso, R. (1989) On the fractal dimension of stream networks: *Water Resour. Res.*, **25**, 735–741.

Liu, T. (1992) Fractal structure and properties of stream networks: *Water Resour. Res.*, **28**, 2981–2988.

Mandelbrot, B. B. (1977) *Fractals: Form, Chance, and Dimension*: W. H. Freeman, San Francisco, 365 pp.

Mandelbrot, B. B. (1983) *The Fractal Geometry of Nature*: W. H. Freeman, New York, 468 pp.

Marani, A., Rigon, R. and Rinaldo, A. (1991) A note on fractal channel networks: *Water Resour. Res.*, **27**, 3041–3049.

Moussa, R. (1997) Is the drainage network a fractal Sierpinski space?: *Water Resour. Res.*, **33**, 2399–2408.

Murray, C. D. (1926) The physiological principle of minimum work. I. The vascular system and the cost of blood volume: *Proc. Natl. Acad. Sci. USA*, **12**, 207–214.

Nikora, V., Ibbitt, R. and Shankar, U. (1996) On channel network fractal properties: A case study of the Hutt River basin, New Zealand: *Water Resour. Res.*, **32**, 3375–3384.

Onda, Y. and Tokunaga, E. (1987) Laws of the composition of dvide-segment systems and drainage basin morphology: *Geogr. Rev. Japan*, **60** (Ser. A), 593–612 (in Japanese with English summary).

Peckham, S. D. (1995) New results for self-similar trees with applications to river networks: *Water Resour. Res.*, **31**, 1023–1029.

Peckham, S. D. and Gupta, V. K. (1999) A reformulation of Horton's laws for large river networks in terms of statistical self-similarity: *Water Resour. Res.*, **35**, 2763–2777.

Perera, H. and Willgoose, G. (1998) A physical explanation of the cumulative area distribution curve: *Water Resour. Res.*, **34**, 1335–1343.

Reif, F. (1965) *Fundamentals of Statistical and Thermal Physics*: McGraw-Hill Kodansha, Tokyo, 651 pp.

Rodriguez-Iturbe, I. and Rinaldo, A. (1997) *Fractal River Basins: Chance and Self-Organization*: Cambridge Univ. Press, New York, 547 pp.

Rosso, R., Bacchi, B. and La Barbera, P. (1991) Fractal relation of mainstream length to catchment area in river networks: *Water Resour. Res.*, **27**, 381–387.

Sakamoto, K. (2000) One dimensional self-similar tilings generated by finite state automata: *Katachi no kagakukaishi*, **15**, 58–59 (in Japanese).

Shimano, Y. (1978) On the characteristics of the channel networks in Japanese drainage basins: *Geogr. Rev. Japan*, **51**, 776–784 (in Japanese with English summary).

Shreve, R. L. (1966) Statistical law of stream numbers: *J. Geol.*, **74**, 17–37.

Shreve, R. L. (1969) Stream lengths and basin areas in topologically random channel networks: *J. Geol.*, **77**, 397–414.

Smart, J. S. (1967) A comment on Horton's law of stream numbers: *Water Resour. Res.*, **3**, 773–776.

Takeuchi, S. (1992) *Junkessho* ("*Quasicrystals*"): Sangyotosho, Tokyo, 138 pp. (in Japanese).

Tarboton, D. G. (1996) Fractal river networks, Horton's laws and Tokunaga cyclicity: *J. Hydrol.*, **187**, 105–117.

Tarboton, D. G., Bras, R. L. and Rodoriguez-Iturbe, I. (1988) The fractal nature of river networks: *Water Resour. Res.*, **24**, 1317–1322.

Tokunaga, E. (1966) The composition of drainage network in Toyohira River Basin and valuation of Horton's first law: *Geophys. Bull. Hokkaido Univ.*, **15**, 1–19 (in Japanese with English summary).

Tokunaga, E. (1975) Laws of drainage composition in idealized drainage basins: *Geogr. Rev. Japan*, **48**, 351–364 (in Japanese with English summary).

Tokunaga, E. (1978) Consideration on the composition of drainage networks and their evolution: *Geogr. Rep. Tokyo Metrop. Univ.* **13**, 1–27.

Tokunaga, E. (1994) Selfsimilar natures of drainage basins: In R. Takaki (ed.), *Research of Pattern Formation*, pp. 445–468. KTK Scientific Publishers, Tokyo.

Tokunaga, E. (1998) Revaluation of Hack's relation by a self-similar model for drainage basins: *Trans. Japan. Geomorph. Union*, **19**, 77–90.

Tokunaga, E. (2000) Dimension of a channel network and space-filling properties of its basin: *Trans. Japan. Geomorph. Union*, **21**, 431–449.

Veitzer, S. A. and Gupta, V. K. (2000) Random self-similar river networks and derivations of generalized Horton's laws in terms of statistical simple scaling: *Water Resour. Res.*, **36**. 1033–1048.

Veneziano, D., Niemann, J. D., Tucker, G. and Bras, R. L. (1997) Self-similarity of fluvial topography: nature, origin, and scaling implications: *Supplementi di Geogrfia Fisica e Dinamica quaternaria*, Supplemento III, 391–392.

Yang, C. T. (1971) Potential energy and stream morphology: *Water Resour. Res.*, **7**, 311–322.

Yang, C. T. and Stall, J. B. (1973) Unit stream power in dynamic stream systems: In M. Morisawa (ed.), *Fluvial Geomorphology, Publications in Geomorphology*, pp. 285–297. State Univ. New York, New York.

Concepts and Modelling in Geomorphology: International Perspectives,
Eds. I. S. Evans, R. Dikau, E. Tokunaga, H. Ohmori and M. Hirano, pp. 167–182.
© by TERRAPUB, Tokyo, 2003.

Mathematical Modeling of Landforms: Optimality and Steady-State Solutions

Scott D. PECKHAM

INSTAAR, University of Colorado, 1560 30th Street, Boulder, CO 80309-0450, U.S.A.
e-mail: Scott.Peckham@colorado.edu

Abstract. The purpose of this paper is to first show how an Euler-Lagrange theorem can be applied to the steady-state fluvial landscape model, thereby allowing the geomorphic solution surfaces to be understood as those that globally optimize the difference between kinetic and potential energy dissipation (Hamilton's Principle) while conserving mass. It is then shown how this variational formulation of the steady-state problem makes it possible to exploit the well-known Ritz-Galerkin method for finding finite-element numerical solutions to partial differential equations. A "local equation" is derived that shows how elevations at a lattice node are related to the elevations of neighboring nodes. A variety of special solutions to this local equation are given that exhibit many of the at-a-point geometric features that characterize real fluvial landscapes, including peaks, ridges, saddles, hillslopes and forks. It is also shown that pits cannot occur as a solution to the local equation, so that numerical solutions will always be hydrologically sound.

Keywords: Fluvial Landscape Model, Steady-State Solutions, Optimality, Hamilton's Principle, Geomorphology

INTRODUCTION

More than three decades of work by many authors has resulted in a physically-based, mathematical model that can be used to model the time evolution of an idealized fluvial landscape. Despite fairly minor differences in formulation, there is widespread agreement on the basic components of this model, which will be referred to here as the standard model. A key feature of this model is that solution surfaces rapidly evolve from initial conditions to relatively stable dendritic channel networks. That is, after a (geologically) brief adjustment or transition period during which channels are formed and captured, the landscape enters into an "intermediate asymptotic" regime (Barenblatt, 1996; Smith *et al*., 1997, 2000) where the evolution is relatively slow and the branching structure of the river network is preserved as the elevations are gradually lowered. In previous work, Peckham (1995, 1999, 2003) has studied a steady-state version of the standard model in order to elucidate some of the relatively stable geometric forms that characterize this intermediate part of fluvial landscape evolution. In this paper, connections to optimality will be developed and explored in connection with a numerical solution scheme.

THE STANDARD MODEL

Contributions to the study of landscape evolution have been made by numerous authors over several decades, as reviewed by Peckham (2003). There is now considerable agreement on the basic set of equations that should be used to build a fluvial landscape model. The first two equations express conservation of mass for water and sediment

$$\nabla \cdot \underline{q} = R - d_t \tag{1}$$

$$\nabla \cdot \underline{q_s} = U - b_t \tag{2}$$

where $\underline{q}$ and $\underline{q_s}$ are 2D vector fields that give the unit-width discharge of water and sediment as a function of position in the landscape, R is the excess rainrate, U is the rate of tectonic uplift or the rate of soil production, d is the water depth and b is the landscape elevation. The second two equations are

$$\underline{q} = -q(\nabla f / S) \tag{3}$$

$$\underline{q_s} = -q_s(\nabla f / S) \tag{4}$$

and express the simple fact that the 2D flow direction is in the opposite direction of the water-surface gradient vector. Here $q(x, y)$ is the magnitude of the unit-width discharge vector, $f(x, y)$ is the water surface height (bed height plus water depth) and $S(x, y)$ is the slope, which is given by the magnitude of ∇f. The fifth equation is a generalized Manning-type flow resistance formula, typically written as

$$q = K d^p S^{1/2} \tag{5}$$

where $d(x, y)$ is the flow depth and $p \geq 5/3$ due to downstream fining of bed material. If the Manning's roughness parameter did not decrease in the downstream direction, as documented by Leopold *et al.* (1964, 1995, p. 244) then we would have $p = 5/3$ and K would simply be the reciprocal of the roughness parameter, n. Equations (3), (4) and (5) stem from conservation of momentum. Finally, the sixth equation is a generalized sediment transport law (which contains many of the well-known laws as special cases), usually written as

$$q_s = E q^m S^n \tag{6}$$

In some recent models, two different sediment transport laws are used, one for fluvial processes and one for hillslope processes. In addition, the formulas for

shear stress, τ_0, and unit stream power, P, are sometimes used to express these in terms of different variables. This set of five equations will be referred to here as the standard model. A more complete discussion of them is given by Smith *et al*. (1997a) and Peckham (2003). Taken as a coupled set of equations, they give a closed mathematical system that can, in principle, be solved for all of the variables of interest: $\underline{q}(x, y, t)$, $\underline{q_s}(x, y, t)$, $f(x, y, t)$, $v(x, y, t)$, $d(x, y, t)$ and $\tau_0(x, y, t)$ in terms of a specified $R(x, y, t)$ and $U(x, y, t)$. Here, v is the vertically-averaged flow velocity. Smith *et al*. (1997a) have obtained several important analytical results involving such things as the existence, uniqueness and stability of solutions. Smith *et al*. (2000) have also obtained several closed-form solutions to a time-evolving 1D version of the problem, subject to a wide variety of boundary conditions, and have clarified the concept of a graded stream.

AN EMPIRICAL SLOPE-DISCHARGE FORMULA

The hydraulic geometry equations (Leopold *et al*., 1964, 1995) express the width, depth, velocity and slope of channels as powers of the mean-annual river discharge, Q, and are given by $w = w_1 Q^b$, $d = d_1 Q^f$, $v = v_1 Q^m$, and $S = S_1 Q^z$, respectively. The subscript of 1 on the coefficients in these equations refers to the value obtained when Q equals one cubic meter per second and SI units are used. By defininition, $Q = vwd$, which implies that $w_1 d_1 v_1 = 1$ and $(b + f + m) = 1$. Typically observed values for the exponents are $b = 0.5$, $f = 0.4$, $m = 0.1$ and $z = -0.5$. Since the unit-width discharge is given by $q = Q/w$, the width-discharge and slope-discharge formulas can be combined to get

$$q = q_1 S^{\gamma} \tag{7}$$

as an alternate version of the slope-discharge formula. This implies that $\gamma = (1 - b)/z$, and $q_1 = 1/(w_1 S_1^{\gamma})$, with $\gamma = -1$ corresponding to the typical values of $b = 0.5$ and $z = -0.5$. The data given by Leopold *et al*. (1964, p. 244–246) suggests approximate values of $w_1 = 9.0$ meters, $S_1 = 0.0636$ (unitless), and $q_1 = 0.007$ square meters per second. Note that $\gamma = -1$ corresponds to spatially constant unit stream power, since $P = \rho g q S$. Similarly, the depth-discharge formula can be rewritten as a slope-depth formula

$$d = d_1 \left(\frac{S}{S_1} \right)^{f/z} \tag{8}$$

Comparing these to Eq. (5), we have

$$p = \frac{z}{f} \left(\gamma - \frac{1}{2} \right) \tag{9}$$

which for the typical values of z, f and γ gives $p = 15/8 = 1.875$. This is greater than $5/3 = 1.667$ due to the tendency for the Manning roughness parameter to decrease downstream due to fining of bed material. Note that the empirical equations of hydraulic geometry were obtained from data for mature drainage networks and they may not hold for the early, transient forms in the evolution of a fluvial landscape.

A STEADY-STATE FLUVIAL LANDSCAPE MODEL

In an effort to better understand how the geometric attributes of channels and channel networks depend on the physical parameters in the standard model equations, Peckham (1995, 1999) has studied a simplified steady-state version of the standard model. This model has three simple components: (1) steady-state mass conservation for water, $\nabla \cdot \underline{q} = R$, (2) $\underline{q}$ parallel to $-\nabla f$, and (3) a slope-discharge formula as given by Eq. (7). A known drawback of the slope-discharge formula is that it does not allow for a change in process dominance near hilltops, and may therefore give rise to cusp-like drainage divides, such as the ones that are often observed in badlands. Combining these three components leads to the following partial differential equation

$$\nabla \cdot \left(S^{\gamma - 1} \nabla f \right) = -R' \tag{10}$$

where $S = S(x, y) = |\nabla f|$ is the water-surface slope, and $R' = R/q_1$ is the rescaled "geomorphically-effective" rainrate with units of inverse length. As mentioned earlier, the exponent γ should be fairly close to –1. However, it would also be reasonable to use this equation to model convex hillslope forms, since hillslope processes are often modeled by a slope-discharge formula with $\gamma > 0$. Longitudinal profiles are concave down for $\gamma > 0$ (e.g. parabolic for $\gamma = 1$) and concave up for $\gamma < 0$ (e.g. logarithmic for $\gamma = -1$); see Peckham (1995, 1999, 2003). The type of this nonlinear, second-order equation can be shown to be hyperbolic for $\gamma < 0$, parabolic for $\gamma = 0$ and elliptic for $\gamma > 0$. The elliptic case of this equation is known as the p–Laplace equation ($p = \gamma - 1$), since it reduces to Laplace's equation for $\gamma = 1$ and $R' = 0$. The hyperbolic case does not appear to have received much prior attention in the literature. Its nonlinearity for $\gamma \neq 1$ presents a mathematical challenge.

AN EULER-LAGRANGE FORMULATION OF THE STEADY-STATE EQUATION

The Euler-Lagrange Theorem from the calculus of variations (Logan, 1987) establishes a correspondence between partial differential equations (PDEs) such as Eq. (10) and extremized functionals. One version of this theorem states that if $J(f)$ is a functional over the domain Ω of the form

$$J(f) = \iint_{\Omega} L\left(x, y, f, f_x, f_y\right) dx dy \tag{11}$$

where L depends on a function $f(x, y)$ and its first derivatives f_x and f_y, then the "extremal surfaces" (or stationary functions) that correspond to $\delta J = 0$ must satisfy the following partial differential equation (PDE):

$$\frac{\partial L}{\partial f} - \frac{\partial}{\partial x}\left(\frac{\partial L}{\partial f_x}\right) - \frac{\partial}{\partial y}\left(\frac{\partial L}{\partial f_y}\right) = 0 \tag{12}$$

The best-known example of this theorem is the case where $L = \sqrt{1 + f_x^2 + f_y^2}$ is the surface area functional and the surfaces which minimize the surface area for a given set of boundary conditions must satisfy the famous minimal surface equation:

$$\left(1 + f_y^2\right) f_{xx} - 2 f_x f_y f_{xy} + \left(1 + f_x^2\right) f_{yy} = 0 \tag{13}$$

As shown by Peckham (1995), a simple application of the Euler-Lagrange Theorem to the steady-state equation (10) implies that the modeled landscapes either minimize or maximize the following integral subject to boundary conditions on the boundary of the domain, Ω:

$$J(f) = \iint_\Omega \left[\frac{S^{\gamma+1}}{\gamma+1} - fR'\right] dxdy \quad (\gamma \neq -1) \tag{14}$$

$$J(f) = \iint_\Omega \left[\log(S) - fR'\right] dxdy \quad (\gamma = -1) \tag{15}$$

This result, and somewhat similar ones by Sinclair and Ball (1996) and Smith *et al*. (1997a, b), establish a firm connection between physically-based models and the concept of optimality. For $\gamma \neq -1$, the first term in the integrand that is being optimized is proportional to the unit stream power, since $q = q_1 S^\gamma$ and $P = \rho g q S$. Note that the first term is essentially the rate at which kinetic energy is dissipated by the channel network and the second term is the rate at which the system gains potential energy through the introduction of rainfall inputs at various elevations throughout the watershed. As a globally optimized difference between kinetic and potential energy dissipation, this may be interpreted as a continuous-system case of a famous theorem of classical mechanics known as Hamilton's Principle, as applied to fluvial landscapes. See Goldstein (1980, ch. 12) for a discussion of Hamilton's Principle in the context of continuous systems and fields.

Many previous authors have postulated that fluvial landscapes may evolve in such a way that local and global energy dissipation or stream power is minimized, and this is the basis of the optimal channel network (OCN) simulation models that have been studied by Howard (1990), Rinaldo *et al*. (1992, 1993),

Rigon *et al*. (1993), Rodriguez-Iturbe *et al*. (1992a, b, c) and Sun *et al*. (1994a, b). However, it is much more satisfying to start from first principles like mass conservation and then deduce optimality principles using an Euler-Lagrange theorem than to attempt to guess what quantity may be optimized and then validate this guess with the realism of simulations. To the author's knowledge, the potential energy generation component of Eq. (15) has not appeared in the previous OCN studies. Also, the logarithmic dependence on slope for $\gamma = -1$ (spatially constant unit stream power) is something that would be difficult to anticipate.

A FINITE-ELEMENT APPROACH TO THE STEADY-STATE EQUATION

For PDEs that can be written in a variational form, the well-known Ritz-Galerkin method (Dahlquist and Björck, 1974, p. 395) provides a numerical solution strategy. Solutions $f(x, y)$ to Eq. (10) must extremize the functional $J(f)$ that is given in Eq. (15). On a triangular lattice with N facets, $J(f)$ can be written as:

$$J(f) = \sum_{j=1}^{N} \iint_{\Delta j} \left[\frac{S^{\gamma+1}}{\gamma+1} - fR' \right] dxdy \quad (\gamma \neq -1) \tag{16}$$

$$J(f) = \sum_{j=1}^{N} \iint_{\Delta j} \left[\log(S) - fR' \right] dxdy \quad (\gamma = -1) \tag{17}$$

Since slope is constant over each triangle, the integrals can be approximated as

$$J(f) \approx \sum_{j=1}^{N} \left[\frac{S_j^{\gamma+1}}{\gamma+1} - \left(f_{j,1} + f_{j,2} + f_{j,3} \right) R_j' / 3 \right] A_j \quad (\gamma \neq -1) \tag{18}$$

$$J(f) \approx \sum_{j=1}^{N} \left[\log\left(S_j\right) - \left(f_{j,1} + f_{j,2} + f_{j,3} \right) R_j' / 3 \right] A_j \quad (\gamma = -1) \tag{19}$$

The set of node heights that extremize $J(f)$ must satisfy the equation:

$$\frac{\partial J}{\partial f_i} = 0, \quad \text{for every node index, } i \tag{20}$$

J is a sum over all triangles in the lattice, but a given node height, f_i, is only shared by 6 facets. Hence, there are only 6 nonzero terms in the expression for $(\partial J/\partial f_i)$. Let k be a second index that runs clockwise through the 6 neighbor nodes or facets

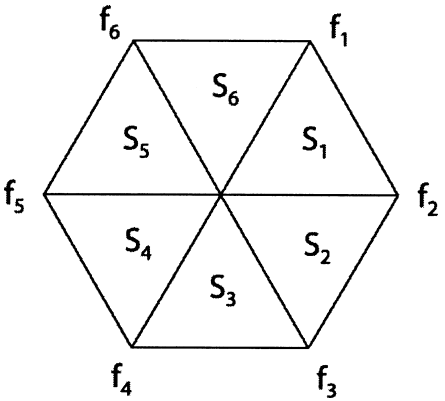


Fig. 1. Neighbor node elevations and facet slopes for a node in a lattice of equilateral triangles.

associated with node index i. We then have:

$$\frac{\partial}{\partial f_i}\left\{\sum_{k=1}^{6}\left[\frac{S_k^{\gamma+1}}{\gamma+1}-R_k'\left(f_i+f_k+f_{k+1}\right)/3\right]A_k\right\}=0 \quad (\gamma\neq -1) \tag{21}$$

$$\frac{\partial}{\partial f_i}\left\{\sum_{k=1}^{6}\left[\log\left(S_k\right)-R_k'\left(f_i+f_k+f_{k+1}\right)/3\right]A_k\right\}=0 \quad (\gamma=-1) \tag{22}$$

Note that the $(k + 1)$ index is cyclic (modulo 6). Both of the previous equations simplify to:

$$\sum_{k=1}^{6}A_k S_k^{\gamma}\left(\frac{\partial S_k}{\partial f_i}\right)=\frac{1}{3}\sum_{k=1}^{6}R_k A_k \tag{23}$$

In the general case, A_k can be computed as the determinant

$$A_k=\frac{1}{2}\begin{vmatrix}1 & 1 & 1\\ x_i & x_k & x_{k+1}\\ y_i & y_k & y_{k+1}\end{vmatrix}=\left[y_i\left(x_{k+1}-x_k\right)+y_k\left(x_i-x_{k+1}\right)+y_{k+1}\left(x_k-x_i\right)\right]/2 \tag{24}$$

where (x_i, y_i), (x_k, y_k) and (x_{k+1}, y_{k+1}) are the planar coordinates of the vertices of the kth triangle. However, for the remainder of this discussion we will specialize to the case of equilateral triangles and spatially uniform rain, so that $A_k = A$ and

$R'_k = R'$. This yields a "local equation" that must hold at each node (see Fig. 1):

$$\sum_{k=1}^{6} S_k^{\gamma}\left(\frac{\partial S_k}{\partial f_i}\right) = 2R' \tag{25}$$

For the 6 facets that touch node i, the slope can be expressed in terms of local node heights and the lattice scale, ε, as:

$$S_k = \frac{2}{\sqrt{3}\varepsilon}\left[f_i^2 + f_k^2 + f_{k+1}^2 - f_i\left(f_k + f_{k+1}\right) - f_k f_{k+1}\right]^{1/2} \tag{26}$$

This implies that

$$\frac{\partial S_k}{\partial f_i} = \frac{2}{S_k}\left[\frac{2f_i - \left(f_k + f_{k+1}\right)}{3\varepsilon^2}\right] \tag{27}$$

For the linear case of $\gamma = 1$, the local equation (25) is:

$$\sum_{k=1}^{6} S_k\left(\frac{\partial S_k}{\partial f_i}\right) = 2R' \tag{28}$$

Inserting the previous expressions for S_k and $(\partial S_k/\partial f_i)$ and simplifying, we get

$$f_i = \left(\frac{1}{6}\sum_{k=1}^{6} f_k\right) + \frac{R'\varepsilon^2}{4} \tag{29}$$

For $R' = 0$, the height of the center node is equal to the average height of the six equidistant neighbor nodes, a well-known result for Laplace's equation.

For the nonlinear case of $\gamma = -1$, the local equation (25) is:

$$\sum_{k=1}^{6} S_k^{-1}\left(\frac{\partial S_k}{\partial f_i}\right) = 2R' \tag{30}$$

Inserting the previous expressions for S_k and $(\partial S_k/\partial f_i)$ and simplifying, we get

$$\sum_{k=1}^{6}\left[\frac{f_k + f_{k+1} - 2f_i}{f_k^2 + f_{k+1}^2 + f_i^2 - f_i\left(f_k + f_{k+1}\right) - f_k f_{k+1}}\right] = -4R' \tag{31}$$

If we now make the change of variables $h_k = (f_k - f_i)$, we have

$$\sum_{k=1}^{6}\left[\frac{h_k + h_{k+1}}{h_k^2 + h_{k+1}^2 - h_k h_{k+1}}\right] = -4R' \tag{32}$$

This can be written in a number of different ways, such as

$$\sum_{k=1}^{6}\left[\frac{\left(h_k + h_{k+1}\right)^2}{h_k^3 + h_{k+1}^3}\right] = -4R' \tag{33}$$

and

$$\sum_{k=1}^{6}\left[\frac{h_k + h_{k+1}}{h_k^2 + h_{k+1}^2 + \left(h_k - h_{k+1}\right)^2}\right] = -2R' \tag{34}$$

This latter form of the local equation makes it easy to see that finite-element solutions for $\gamma = -1$ will be hydrologically sound or free of pits. If there were a pit at node i, then all 6 outer node heights would be higher than the center height, which would imply that $h_k > 0$ for all k. However, this would make every term on the left side positive, while the term on the right is negative for $R' > 0$. So pits cannot occur. The same argument applies to any value of γ. The analogous local equation for any value of γ is

$$\sum_{k=1}^{6}\left[\frac{h_k + h_{k+1}}{\left[h_k^2 + h_{k+1}^2 + \left(h_k - h_{k+1}\right)^2\right]^{p(\gamma)}}\right] = -R' 2^{p(\gamma)}\left(\sqrt{3}\varepsilon\right)^{1+\gamma} \tag{35}$$

where $p(\gamma) = (1 - \gamma)/2$. Note that $\gamma = -1$ is the only case where the equation is independent of the lattice scale parameter, ε. This represents a form of scale invariance.

If heights are known at the center node of a hexagon and 5 of the 6 outer nodes, then only two of the terms in the sum will contain the unknown node height and the other 4 terms can be evaluated. For example, if the unknown node has index $k = 2$, we can write Eq. (32) as

$$\left[\frac{h_1 + h_2}{h_1^2 + h_2^2 - h_1 h_2}\right] + \left[\frac{h_2 + h_3}{h_2^2 + h_3^2 - h_2 h_3}\right] = -4R' - K = G \tag{36}$$

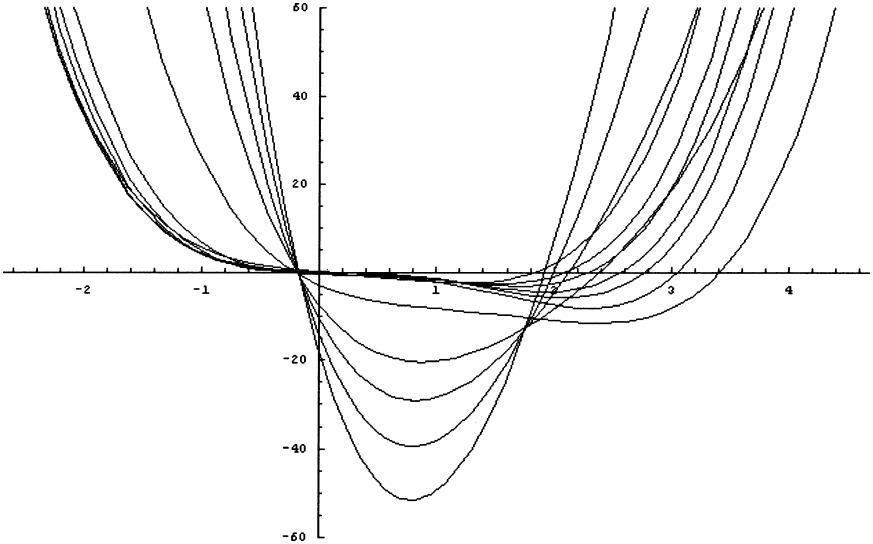


Fig. 2. Plot of the quartic for different combinations of u and w, showing the tendency for there to be two real roots.

where K is the sum of the four terms that do not contain h_2. When the value of G is nonzero, we can make the further change of variables $u = h_1G$, $v = h_2G$ and $w = h_3G$ to get

$$\left[\frac{u+v}{u^2+v^2-uv}\right]+\left[\frac{v+w}{v^2+w^2-vw}\right]=1 \tag{37}$$

Putting the two terms on the left over a common denominator and simplifying leads to a fourth-order polynomial for v, namely

$$P(v)=v^4+a_1v^3+a_2v^2+a_3v+a_4=0 \tag{38}$$

where

$$a_1=-(2+u+w)$$

$$a_2=\left(u^2+w^2+uw\right)$$

$$a_3=2uw-u^2(1+w)-w^2(1+u)$$

Table 1. Special solutions to the local equation for $R' = 1$, translated so $f_0 = 0$. Any of these can be rescaled to give a solution for $R' > 0$ by dividing all six node heights by R'.

Solution	f_1	f_2	f_3	f_4	f_5	f_6	Note
Isolated peak	-3	-3	-3	-3	-3	-3	or $f_3 = -\frac{3}{2}$
Symm. ridge	-2	-2	0	-2	-2	0	
Linear ridge	1	a	-1	-1	a	1	$a = -0.682328$
Desc. ridge	-2	-2	-1	-2	-2	2	or $f_3 = -2$
Simple saddle	-1	-1	1	-1	-1	1	
Monkey saddle	a	b	a	b	a	b	$\frac{-(a+b)}{a^2+b^2-a\,b} = \frac{2}{3}$
Monkey saddle	a	$-\frac{1}{2}$	a	$-\frac{1}{2}$	a	$-\frac{1}{2}$	$a = -1 \pm \sqrt{\frac{3}{2}}$
Hillslope	a	a	0	b	b	0	$a = \frac{-b}{1+b}$
Channel	b	0	a	0	b	b	$a = \frac{-b}{2\,b+3}$
Channel 1	1	0	$-\frac{1}{5}$	0	1	1	
Fork	1	0	$-\frac{1}{4}$	0	1	2	
Amphitheater	1	1	a	a	1	1	$a = -0.175971$

$$a_4 = uw(uw - u - w)$$

For the special case of $u = w$, the quartic reduces to a quadratic and we have

$$v_1 = (2 + u + B)/2 \tag{39}$$

$$v_2 = (2 + u - B)/2 \tag{40}$$

$$B = \sqrt{4 + 12u - 3u^2} \tag{41}$$

Preliminary results suggest that when $u \neq w$, 2 of the roots are always complex and 2 are real. This is supported by plotting the quartic as a graph for a wide variety of (u, w) pairs; see Fig. 2. With multiple real roots, one is faced with the issue of which one to use. Realizing that solutions make the functional $J(f)$ an extremum, it appears as though we should decide at the outset whether to minimize or maximize $J(f)$ and then select the roots that achieve this goal. It also seems likely based on results for optimal channel networks (OCNs) that roots should be chosen so as to minimize $J(f)$, both locally and globally over the problem domain

SPECIAL SOLUTIONS TO THE LOCAL EQUATION

The author has found several special solutions to the local equation for $\gamma = -1$ that demonstrate many of the local geometries that one wants to be able to reproduce and understand with a fluvial landscape model. These are summarized in Table 1. For each of these, the height of the center node, f_i, is zero and $h_k = f_k$;

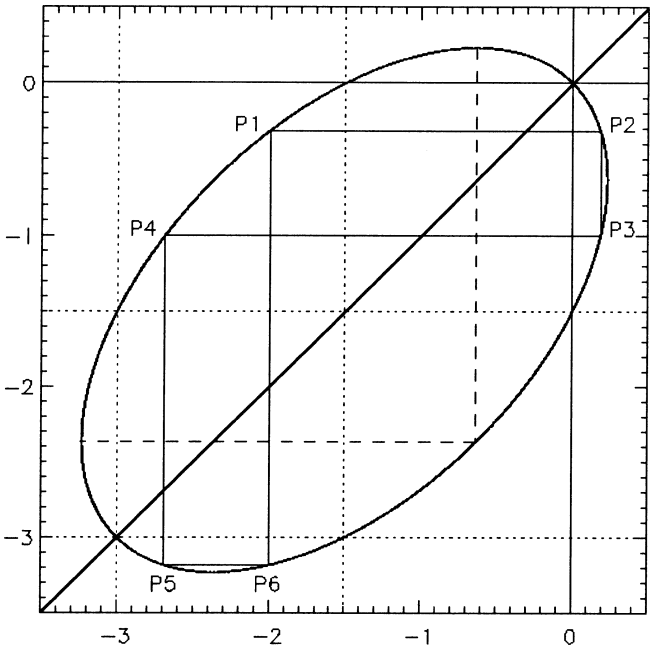


Fig. 3. Ellipse diagram showing a particular path through six points on the ellipse that produces a solution to the local equation.

see Fig. 1. The solutions given here all have a high amount of symmetry, but it should be kept in mind that Eq. (32) has an infinite number of solutions. The hillslope solution is always concave up. The linear ridge and hillslope solutions occur on the surfaces of Fig. 4. Notice also that both divergent and convergent flow geometries are represented. The rescaled excess rainrate, R', serves only to rescale solutions along the z-axis, as can also be seen from analyzing the scaling symmetries of the original PDE, Eq. (10). For the case $R' = 0$, it can be shown that if all of the node heights are chosen so as to lie on an arbitrary plane, they will also satisfy Eq. (10). This is true for any value of γ, and is to be expected since $f(x, y) = ax + by + c$ is a closed-form solution to the PDE for any value of γ when $R' = 0$. The local equation also has the translation property of the original PDE, in that if a set of f_k values provides a solution, then $f_k' = f_k + c$ is also a solution, where c is any constant

An infinite class of special solutions can also be obtained by the following algorithm. Let $\gamma = -1$ and

$$T_k = \frac{h_k + h_{k+1}}{h_k^2 + h_{k+1}^2 - h_k h_{k+1}} \tag{42}$$

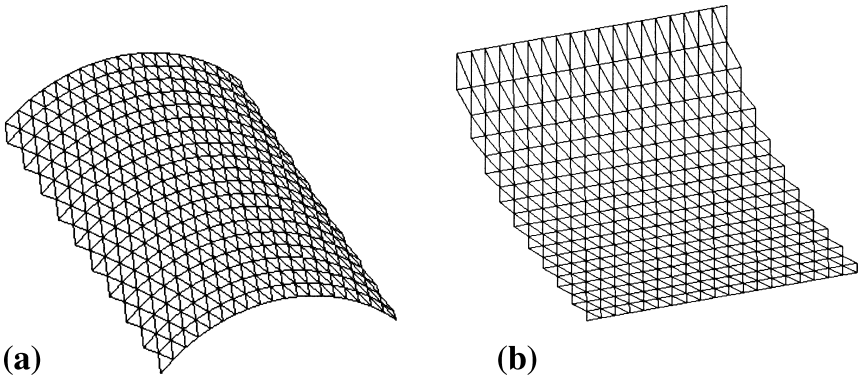


Fig. 4. (a) The numerical solution corresponding to a known analytic solution of the form $f(x, y) = A(x) + cy$, when $\gamma = -1$. Note that the ridge is concave down even though there is no term to model diffusive hillslope processes in the steady-state equation. This solution occurs as a periodic sequence of such shapes, as often seen in road cuts. (b) The numerical solution corresponding to the known analytic solution of a "logarithmic sheet".

so that the local equation is just

$$\sum_{k=1}^{6} T_k = -4R' \tag{43}$$

Now suppose that all of the T_k values are equal to $-2R'/3$. If we take $x = h_k$ and $y = h_{k+1}$, then the (x, y) pairs that satisfy $T_k = -2R'/3$ plot as an ellipse that is tilted by 45 degrees and passes through the origin; see Fig. 3 for which $R' = 1$. A sequence of six f_k values that satisfy the local equation can then be generated as follows.

(1) Choose any point, P_1, on the ellipse and let f_1 be its x-coordinate.

(2) Draw a horizontal line from P_1 to the other side of the ellipse to get a second point, P_2, and let f_2 be its y-coordinate.

(3) Draw a vertical line from P_2 to the other side of the ellipse to get P_3, and let f_3 be its x-coordinate.

(4) Continue this procedure, alternating between horizontal and vertical lines to get f_4, f_5 and f_6.

This procedure can also be summarized as follows: f_1, f_3 and f_5 are the ordered x-coordinates of the six points on the ellipse, and f_2, f_4 and f_6 are the ordered y-coordinates. Note that regardless of where you start, you will return to the starting point, P_1. Starting at certain special points, such as the points with the largest and smallest possible values of x and y or a point on the line $y = x$ yields high-symmetry solutions. In particular, the isolated peak and all monkey saddle solutions are in the class where $T_k = -2R'/3$. In general, however, the solutions of this method are asymmetric and tend to have only one node height that is positive.

The rules for moving around on the ellipse can be relaxed in various ways as long as you return to P_1 after six steps. For example, you can draw only four lines and then reverse direction and return to the starting point. Note that when the T_k values are not all equal, then the local equation has a geometric interpretation in terms of a closed path through six points on six ellipses.

A GENERAL SOLUTION METHOD FOR THE LOCAL EQUATION

A general method for generating solutions to the local equation when $\gamma = -1$ has also been found by the author. In the previous section it was noted that any solution to the $R' = 1$ case could be rescaled to give a solution for $R' > 0$ by dividing all six node heights by R'. Taking this idea further leads to the following general solution method. Begin by choosing any six numbers for the initial node heights. A random number generator can even be used. Compute the quantity $B = \sum_{k=1}^{6} T_k$ and let $R^* = -4/B$. Multiply each of the initial node heights by R^* to get a set of node heights that satisfy the local equation for $R' = 1$. As before, these node heights can be divided by R' to get a solution for any value of $R' > 0$. Realizing that $f_k = f_k(R')$, the scaling property can be stated as $R' f_k(R') = f_k(1)$. This method shows that most node height configurations that drain water can be vertically rescaled to give a solution that is valid for a given $R' > 0$. Initial node height configurations that do not drain, such as pits ($f_k > 0$, for all k) or flats ($f_k = 0$ and $f_{k+1} = 0$ for some k) do not yield valid solutions. Pits are converted to peaks by this method, and flats result in a division by zero. Another exceptional case is that of an inclined plane, e.g. $\{ f_k\} = \{a, a, 0, -a, -a, 0\}$, which is not a valid solution for $R' > 0$ and is converted by this method to $f_k = 0$ for all k. This method also shows how the "geomorphically effective rainrate," R can be estimated from any six node heights in a solution surface as $R = -4q_1/B$.

NUMERICAL SOLUTIONS

Laguerre's iteration method can be used to find the four roots to the "local equation" numerically. Starting from known values on top and side boundaries of a rectangular domain, this makes it possible, in principle, to iteratively solve for node heights at all interior nodes one-by-one, by marching across the domain. However, this simple numerical method is known to be unstable, even for the linear case of Poisson's equation ($\gamma = 1$). One must also be careful to consistently choose the real root that minimizes the integral of the functional over the domain. Figures 4(a) and (b) show two simple solution surfaces that were obtained by this method. Work is ongoing to find a stable numerical method for solving the coupled set of local equations simultaneously and efficiently for all values of γ.

CONCLUSIONS

In previous work (Peckham, 1999, 2003), a steady-state version of the standard fluvial landform evolution equation was analyzed as a model for understanding the relationship between function and form in highly-evolved or mature fluvial landscapes, with an emphasis on longitudinal profiles. The current

paper establishes an important reformulation of this steady-state partial differential equation as a variational or "optimality" problem. Moreover, it was shown how this variational formulation could be exploited as the basis of a finite-element numerical solution strategy, following the well-known Ritz-Galerkin method. While the solution strategy has been derived in detail, only preliminary applications of it have been presented here. In particular, the resulting "local equation" was analyzed to demonstrate that solution surfaces can have many of the key at-a-point geometric properties that one wishes to reproduce and understand in a fluvial landscape model, such as peaks, ridges, saddles, hillslopes, forks and sources. In future work, the author hopes to develop a stable numerical method for simultaneously solving the nonlinear local equation at all lattice nodes, while ensuring proper root selection. A simple application of a global Newton method does not work due to the root-selection issue. It is expected on the basis of the at-a-point results presented here that the resulting numerical solutions will exhibit dendritic valley networks that conserve mass and have realistic branching patterns and longitudinal profiles.

REFERENCES

Barenblatt, G. I. (1996) *Scaling, Self-Similarity, and Intermediate Asymptotics*. Cambridge Univ. Press, 386 pp.

Dahlquist, G. and Björck, Å. (1974) *Numerical Methods*. Prentice-Hall, Englewood Cliffs, NJ, 573 pp.

Goldstein, H. (1980) *Classical Mechanics*, 2nd ed. Addison-Wesley, Reading, MA, 672 pp.

Howard, A. D. (1990) Theoretical model of optimal drainage networks: *Water Resour. Res*., **26**(9), 2107–2117.

Leopold, L. B., Wolman, M. G. and Miller, J. P. (1995) *Fluvial Processes in Geomorphology*. Dover, New York (originally published in 1964).

Logan, J. D. (1987) *Applied Mathematics: A Contemporary Approach*. John Wiley, New York, 572 pp.

Peckham, S. D. (1995) Self-similarity in the three-dimensional geometry and dynamics of large river basins, Ph.D. Thesis, University of Colorado, Boulder.

Peckham, S. D. (1999) Solutions to nonlinear partial differential equations—A geometric approach: In O. E. Barndorff-Nielsen and E. B. Vedel Jensen (eds.), *Proceedings of the Conference on Geometry in Present-Day Science*, pp. 165–186. World Scientific, New Jersey.

Peckham, S. D. (2003) Fluvial landscape models and catchment-scale sediment transport: *Global and Planetary Change* (accepted).

Rigon, R., Rinaldo, A., Rodriguez-Iturbe, I., Bras, R. L. and Ijjasz-Vasquez, E. (1993) Optimal channel networks: a framework for the study of river basin morphology: *Water Resour. Res*., **29**(6), 1635–1646.

Rinaldo, A., Rodriguez-Iturbe, I., Rigon, R., Bras, R. L., Ijjasz-Vasquez E. and Marani, A. (1992) Minimum energy and fractal structures of drainage networks: *Water Resour. Res*., **28**(9), 2183–2189.

Rinaldo, A., Rodriguez-Iturbe, I., Bras, R. L. and Ijjasz-Vasquez E. (1993) Self-organized fractal river networks: *Phys. Rev. Lett*., **70**, 822–826.

Rodriguez-Iturbe, I., Rinaldo, A., Rigon, R., Bras, R. L. and Ijjasz-Vasquez, E. (1992a) Energy dissipation, runoff production, and the three-dimensional structure of channel networks: *Water Resour. Res*., **28**(4), 1095–1103.

Rodriguez-Iturbe, I., Ijjasz-Vasquez, E., Bras, R. L. and Tarboton, D. G. (1992b) Power law distributions of mass and energy in river basins: *Water Resour. Res*., **28**(4), 1089–1093.

Rodriguez-Iturbe, I., Rinaldo, A., Rigon, R., Bras, R. L. and Ijjasz-Vasquez, E. (1992c) Fractal structures as least energy patterns: the case of river networks: *Geophys. Res. Lett.*, **19**(9), 889–892.

Sinclair, K. and Ball, R. C. (1996) A mechanism for global optimization of river networks from local erosion rules: *Phys. Rev. Lett.*, **76**, 3360–3363.

Smith, T. R., Birnir, B. and Merchant, G. E. (1997a) Towards an elementary theory of drainage basin evolution: I. The theoretical basis: *Computers & Geosciences*, **23**(8), 811–822.

Smith, T. R., Merchant, G. E. and Birnir, B. (1997b) Towards an elementary theory of drainage basin evolution: II. A computational evaluation: *Computers & Geosciences*, **23**(8), 823–849.

Smith, T. R., Merchant, G. E. and Birnir, B. (2000) Transient attractors: towards a theory of the graded stream for alluvial and bedrock channels: *Computers & Geosciences*, **26**, 541–580.

Sun, T., Meakin, P. and Jøssang, T. (1994a) Minimum energy dissipation model for river basin geometry: *Phys. Rev. E*, **49**(6), 4865–4872.

Sun, T., Meakin, P. and Jøssang, T. (1994b) The topography of optimal drainage basins: *Water Resour. Res.*, **30**(9), 2599–2610.

Concepts and Modelling in Geomorphology: International Perspectives,
Eds. I. S. Evans, R. Dikau, E. Tokunaga, H. Ohmori and M. Hirano, pp. 185–197.
© by TERRAPUB, Tokyo, 2003.

A Simple GIS Model for Mapping Landslide Susceptibility

Richard J. PIKE, Russell W. GRAYMER and Steven SOBIESZCZYK

U.S. Geological Survey, 345 Middlefield Road, Menlo Park, CA 94025, U.S.A.
e-mail: rpike@usgs.gov

Abstract. Digital maps of geology, ground slope, and dormant landslides are combined statistically in a geographic information system (GIS) to identify sites of future landsliding over a broad area. The resulting index number, a continuous variable, predicts a range of susceptibility both within and between existing landslides. Spatial resolution of the index can be as fine as that of the slope map, and areal coverage is limited only by the extent of the input data. Susceptibility is defined for each geologic-map unit as the *spatial frequency* of the unit occupied by dormant landslides, adjusted locally by ground slope. Susceptibility of terrain between landslides is calculated for each one-degree slope interval as the percentage of grid cells that coincide with the failures. Susceptibility within landslides is the same percentage times the comparative frequency of recent failures within and outside the old landslides. We tested the model in an 872 km^2 urban area in California, using 120 geologic units, a 30-m digital elevation model, 6714 dormant landslide deposits, 1192 recent landslides, and ARC/INFO software. The method could generate a similar map for any area where the necessary digital-map data are available.

Keywords: Geomorphic Hazards, Landslide Susceptibility, Statistical Mapping, GIS, DEM

INTRODUCTION

Landslides pose a hazard to life and property worldwide. Improving public safety by predicting unstable slopes—in time or space, locally or regionally—is a complex problem in applied geomorphology for which many solutions have been proposed. One of the best clues to the location of future landsliding is the mapped distribution of past failures (Radbruch and Crowther, 1970; Nilsen and Wright, 1979). Such an *inventory* of landslides reveals the extent of prior movement and the probable locus of some future activity in the area, but it is discontinuous. An inventory does not indicate the likelihood of failure for the much broader expanses of terrain between landslides. By numerically (if manually) combining maps of geology, an inventory of Quaternary landslides, and generalized estimates of slope gradient, Brabb *et al*. (1972) first modeled the widely varying predisposition, or *susceptibility*, of hillside terrain to landsliding—both continuously and over a large area.

The semi-quantitative approach of Brabb *et al*. (1972) is extended here. Advances include higher-resolution data on geology and slope gradient, a fully numerical method implemented in a geographic information system (GIS), and a

uniformly high spatial resolution for the resulting hazard map. In the absence of guidelines for mapping landslide susceptibility, the model is predicated on six assumptions:

- The record of past landsliding can infer the location of future instability.
- Failures under climatic conditions that no longer prevail suggest the locus of future landsliding if not necessarily its abundance or temporal frequency.
- The areal percentage of past failure in a geologic unit reflects the combination of landslide-inducing conditions and processes unique to that unit.
- Geology, slope gradient, and areas of prior failure collectively serve as a proxy for materials-properties data needed to quantify susceptibility.
- Susceptibility of dormant landslides to later movement exceeds that of the terrain between them.
- A simple analysis of the spatial frequency of recent landslides can quantify the added likelihood of renewed activity in older landslides.

The model accommodates either specific types of slope movement or, as in this chapter, a mixture of types. Because the dormant landslides in our test area were identified by airphoto interpretation rather than by field mapping, the failures could not be attributed by type of movement. More recent inventories (e.g. Wilson *et al*., 2002) do not cover the area. Lacking detailed information, we term all dormant failures "non-debris flow landslides." "Landslide" or "slide" in this study connotes a topographically recognizable deposit (excluding its source area) probably formed in bedrock by one of the deeper mechanisms (Varnes, 1978). Few of these landslides are likely to be shallow debris flows, which leave a thin, ephemeral deposit (Dietrich *et al.*, 1993).

Figure 1D, a representative result of our regional-statistical analysis, shows 9 km^2 of a susceptibility map of the 872-km^2 test site, metropolitan Oakland in the San Francisco Bay region of northern California. To prepare the larger map, Pike *et al*. (2001) divided the Oakland area into 969,003 rectangular cells 30 m on a side, the spacing of the input digital elevation model (DEM), and created four digital raster-grid maps at this resolution: geology, presence-or-absence of old landslide deposits, slope gradient, and point locations of post-1967 landslides. Susceptibility was calculated at a 30-m resolution in the GRID module of version 7.1.1 of ARC/INFO, a commercial GIS, on a SUN/Solaris UNIX computer, from a two-step algorithm written in Arc Macro Language. We have since applied the model to a larger area in the San Francisco Bay region (Pike and Sobieszczyk, 2002).

INPUT TO THE MODEL

1. Geology

Hillside materials are the dominant site control over the larger, deeper types of slope movement worldwide (Aniya, 1985; Brunori *et al*., 1996; Jennings and Siddle, 1998; Irigaray *et al*., 1999). In the Oakland test area, prevalence of landsliding varies widely among the 120 lithologic units (Graymer, 2000). These

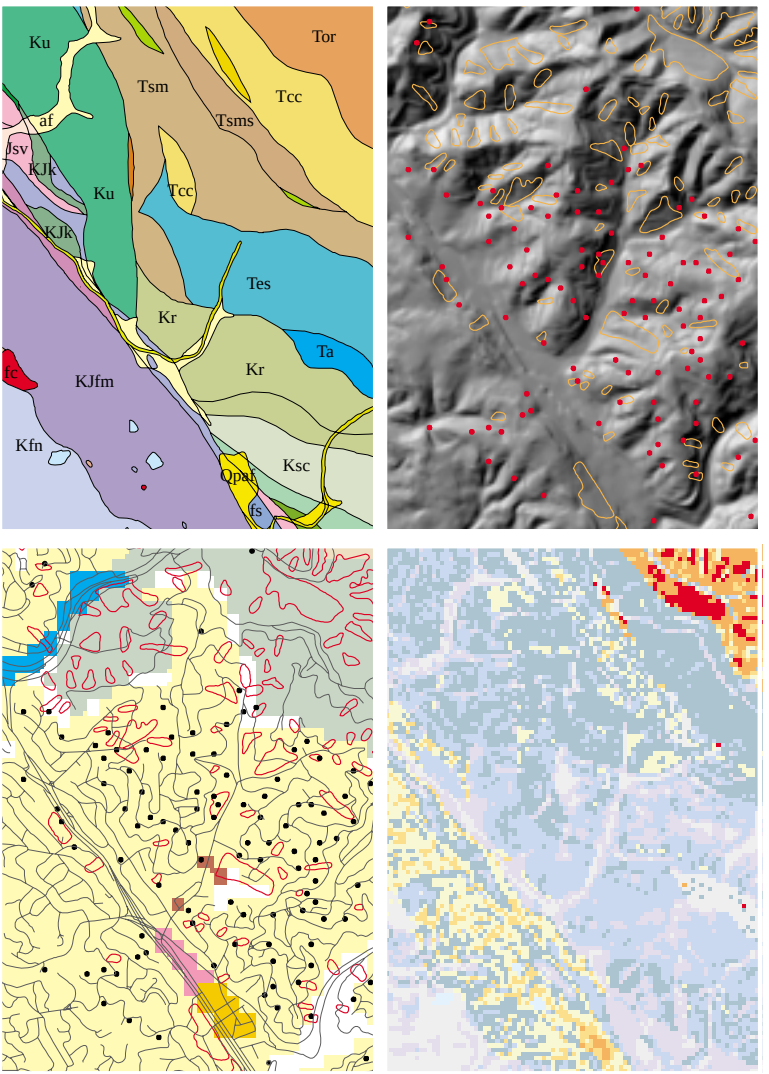


Fig. 1. Preparing a landslide-susceptibility map (after Pike *et al*., 2001). Maps for part of the city of Oakland, California, are about 2 km across. A, upper left. Geology; 19 units in Table 1. NNW-striking Hayward Fault Zone is at eastern edge of unit KJfm. B, upper right. Inventory of old landslide deposits (orange polygons) and locations of post-1967 landslides (red dots) on uplands east of the fault and on gentler terrain to the west. Shaded relief from 10-m DEM. C, lower left. Landslides and old deposits on 1995 land use (100-m resolution). Yellow, residential; green, forest; tan, scrub; blue, major highway; pink, school; orange, commercial; brown, public institution; white, vacant and mixed use; road net in gray. D, lower right. Values of relative susceptibility at 30-m resolution mapped in eight intervals from low to high as gray, 0.00; purple, 0.01–0.04; blue, 0.05–0.09; green, 0.10–0.19; yellow, 0.20–0.29; light-orange, 0.30–0.39; orange, 0.40–0.54; red, ≥0.55. Values 0.05–0.20 predominate in this small 9 km^2 sample of the Oakland study area.

Table 1. Data on dormant landslide deposits and post-1967 landslides for 20 selected geologic units in the Oakland metropolitan area, California—arrayed by mean spatial frequency. Spatial frequencies by slope gradient are shown for two units in Fig. 2.

GEOLOGIC UNIT			OLD LANDSLIDE DEPOSITS		POST-1967 LANDSLIDES	
Map symbol	Name (after Graymer, 2000)	All cells (number of 30-meter grid cells)	Landslide cells (number of grid cells)	Mean spatial frequency (Landslide cells / All cells)	Total number (one grid cell per landslide)	Number on old landslide deposits
Kfa	† Franciscan Complex - Alcatraz terrane	1002	820	***0.82***	6	6
Tor	Orinda Formation (Miocene)	35166	9682	***0.28***	83	27
KJfm	Franciscan Complex mélange - undivided	12212	2559	***0.21***	66	19
Tsm	unnamed glauconitic mudstone	3389	438	***0.13***	24	0
Tsms	x unnamed glauconitic mudstone - siltstone and ss	362	46	***0.13***	3	0
Tcc	Claremont Chert	10590	1177	***0.11***	4	0
Ksc	Shephard Creek Formation	5675	508	***0.09***	12	1
KJk	Knoxville Formation	8164	663	***0.08***	25	1
Jsv	keratophyre, qtz. keratophyre above ophiolite	15627	1212	***0.08***	50	6
Ku	Great Valley sequence - undifferentiated	12706	965	***0.08***	35	2
Kr	Redwood Canyon Formation (Cretaceous)	27503	1697	***0.06***	27	1
Tes	Escobar Sandstone (Eocene)	2513	141	***0.06***	43	3
fs	Franciscan Complex sandstone	3441	109	***0.03***	9	1
Ta	x unnamed glauconitic sandstone	163	3	***0.02***	4	0
Qpaf	Q alluvial fan and fluvial deposits (Pleistocene)	61867	1010	***0.02***	87	0
Kfn	Franciscan Complex - Novato Quarry terrane	7879	122	***0.02***	27	1
Ko	Oakland Conglomerate (Cretaceous)	20921	301	***0.01***	6	0
fc	x Franciscan Complex chert	323	1	***0.00***	0	0
Qhaf	Q alluvial fan and fluvial deposits (Holocene)	125014	254	***0.00***	38	0
af	Q artificial fill (Historic)	65934	15	***0.00***	5	0
	‡ Totals are for all 120 geologic units	**969,003**	**116,360**	***0.12***	**1192**	**183**

† Unit Kfa, the most highly susceptible unit in the Oakland study area, does not crop out in Figure 1A

x 3 of 32 hillside units with < 450 cells, for which distributions of spatial frequency are less regular than those of other units

Q 3 of the 20 Quaternary units in flatland terrain; most are less susceptible than the 20 (of 100 total) hillside units listed here

‡ Totals on last line are for entire Oakland study area, not just the small sample area in Figure 1 (Pike et al., 2001, Table 1)

differences are evident in the contrasting values of *mean spatial frequency*, the areal percentage of landslides in a geologic unit (see sample of 20 units in Table 1; the 19 in Fig. 1A plus unit Kfa). Failed hillsides are abundant (28%), for example, in the Miocene Orinda Formation (Tor) and similarly clay-rich rocks, but much less so (11%) in the Miocene Claremont Chert (Tcc)—which differs in composition, texture, and other properties (Nilsen *et al.*, 1976; Keefer and Johnson, 1983; Graymer, 2000).

The geologic input to our susceptibility model is a digital-map database compiled for the structurally complex Oakland area by Graymer (2000) at 1:24,000 scale (Fig. 1A). The uplands in and east of the city of Oakland comprise 100 bedrock units (16 shown in Fig. 1A) that occupy 62% of the study area, range in age from Jurassic to upper Tertiary, and cover between 0.01 km^2 and 90 km^2. Dormant landslides occur in all but eight of the 100 rock units. In contrast, of the 20 unconsolidated Quaternary deposits (3 in Fig. 1A) that occupy 38% of the area, largely in flatland terrain, only five units, among them alluvial fan and fluvial deposits Qpaf and Qhaf, contain old landslides (Table 1).

2. Old landslide deposits

Reconnaissance mapping of 6714 dormant landslides at 1:24,000 scale by Nilsen (1973, 1975) provides ample evidence of prior instability in Oakland hillsides. Figures 1B and 1C show part of the inventory identified by stereo-interpretation of 1:20,000-scale airphotos. Only landslide deposits were mapped; scarps and other source-area features upslope of the deposited masses were excluded. The inventoried slides were not visited in the field. Because failure mechanisms are difficult to interpret reliably from airphotos alone (Wills and McCrink, 2002), the landslide deposits were unattributed by type of movement (Varnes, 1978) and causal agent—earthquake or sustained rainfall. In the Oakland area, landslides large enough to be recognized on the photos Nilsen studied tend to be rock and debris slides, rock slumps, and large earth flows. Most shallow debris flows are too small or poorly preserved to have been mapped. In appearance, the 6714 deposits range from clearly discernible and uneroded features to indistinct and degraded forms recognizable only by their characteristic shapes (Nilsen, 1973). In size, deposits vary from about 1100 m^2 to 4 km^2 although most are <100 m in the longest dimension. Many medium-size and all large deposits coalesced from smaller slide masses and tend to be morphologically more complex with increasing size. Times of initial movement range from 35 years ago to possibly 200,000 years ago.

We compiled the landslide deposits as a digital database. The original linework inked on 1:24,000-scale plastic sheets by Nilsen (1975) was scanned, converted from raster to vector form, imported into ARC/INFO, hand edited, and combined in one file. The 6714 deposits occupy 12% of the Oakland study area (Table 1), mostly in the hills northeast of the Hayward Fault Zone. The deposits cover 19% of this hilly area, defined as the 100 bedrock units, and cluster in elongate patterns (not evident in the small sample in Fig. 1B) aligned with the

regional NW-SE trend (Fig. 1A).

Heavy rainfall (Nilsen *et al.*, 1976) and earthquake (Keefer *et al.*, 1998) frequently destabilize portions of landslide deposits in the San Francisco Bay area. Most dormant slides are unlikely to again move in their entirety, but smaller deposits and parts of large masses, e.g. the Mission Peak landslide (Coe *et al.*, 1999), often remobilize. Old landslide deposits thus are judged more susceptible to future movement than comparably sloping areas outside them (Nilsen and Wright, 1979; Wieczorek, 1984). This added potential for hazard can be incorporated into susceptibility estimates, based on the proclivity of recent movements for older slides.

3. Recent landslides

The only data from which to modify within-slide susceptibility in our test area are 1192 rainfall-induced failures that damaged the built environment (Nilsen *et al.*, 1976; Coe *et al.*, 1999). Because outlines of most of these post-1967 failures were not recorded, we compiled their locations as point data on 30-meter cells (Figs. 1B and 1C). The 1192 landslides are not an ideal sample because they are largely failures of cut-and-fill grading in urbanized areas, many of them in such otherwise "safe" materials as alluvial fan (Qpaf) and the Novato Quarry terrane (Kfn). These landslides thus overrepresent developed parts of the study area, especially land-use category 1 in Fig. 1C. An unbiased sample, which would include the many non-damaging (and unmapped) recent failures in the undeveloped uplands east of Oakland, is not available.

Despite this bias, distribution of the recent slides among the 120 geologic units largely mimics the prevalence of dormant landslide deposits (Pike *et al.*, 2001). The Orinda Formation (Tor) and Franciscan Complex mélange (KJfm) in Table 1 are two of the five bedrock formations that together host 40% of the 1192 recent landslides; all five have mean spatial frequencies of old slide deposits that exceed 20%. Similarly, the three Quaternary units that record the highest numbers of recent failures, including alluvial fan units Qpaf and Qhaf, are the same three surficial units with the most area in old landslide deposits. Recent failures are rare in geologic units that contain the fewest old landslide deposits; none of the Oakland area's 28 units with <6 grid cells on old landslide masses hosted any post-1967 failures (Pike *et al.*, 2001, Table 1).

4. Topography and slope gradient

Topography both influences and reflects slope instability. The extent of much past landsliding can be identified by a visual appraisal of ground-surface form at scales as coarse as 1:30,000 (Nilsen, 1973), but few of the geomorphic features that are diagnostic of a landslide or tract of landslide-prone terrain translate readily into numerical criteria from which an index of susceptibility might be computed. Among these few measures is slope gradient, arguably the best topographic predictor of landslide likelihood, although the relation of landsliding to slope is complex and differs according to failure process (Lanyon

and Hall, 1983; Dietrich *et al*., 1993).

To evaluate the role of topography in non-debris flow landsliding in the Oakland area, we assigned a value of slope gradient to each GIS grid cell. Graham and Pike (1998) computed these values, in one-degree increments from a 30-m DEM, as the maximum rate of change in height for a 30-m cell within a 3×3 cell subgrid. Failed and unfailed terrain in the study area differ dramatically (Pike *et al*., 2001). Unfailed slopes are strongly skewed toward low values (the mode is at zero), whereas slopes on old landslide deposits are near-normally distributed and peak at about 16°. This value might be somewhat higher if it were possible to identify potential source areas that have yet to fail. The distribution of slope gradient for the 1192 cells hosting post-1967 landslides has the same near-Gaussian shape, although the mode (about 12°) is slightly lower (Pike *et al*., 2001). The topography in Fig. 1B is from a 10-m DEM, which results in a smoother shaded-relief image than the 30-m data (but adds no useful information to the susceptibility calculations).

ESTIMATING SUSCEPTIBILITY

Radbruch and Crowther (1970) and Brabb *et al*. (1972) equated susceptibility of an area to landsliding with the amount of the area containing dormant failures. This quantity was computed for each of Oakland's 120 geologic units as the mean spatial frequency, the number of 30-m cells in landslide deposits divided by all cells in the unit (Pike *et al*., 2001). Resulting percentages range from 82% in the Alcatraz terrane (Kfa, part of the Franciscan Complex), to <1% in alluvial deposits Qhaf (and 25 other units in table 1 of Pike *et al*., 2001). The more susceptible of the 20 lithologies sampled here (Table 1) are bedrock units on steep upland slopes. Landslide deposits are rare in the Quaternary flatland units, among which the widespread alluvial-fan deposit Qpaf (spatial frequency only 2%) contains the most landslide cells (87, see Table 1).

1. Refined spatial frequencies

The mean spatial frequency of landsliding in a geologic unit (Table 1) is much less effective a predictor of future instability than an array of frequencies calculated for different values of ground slope (Brabb *et al*., 1972). Radbruch and Crowther (1970) compiled observations showing that prevalence (variously defined) of landsliding in California increases with slope gradient, but only up to a maximum—commonly 15° to 35°—depending on mode of failure and the underlying lithology. (Rock falls, topples, and some shallow landslides occur on steeper slopes; debris-flow source areas, for example, peak at about 30° slope; Ellen, 1988.) Similar slope maxima for deep-seated failures are documented elsewhere (Brunori *et al*., 1996; Jennings and Siddle, 1998; Irigaray *et al*., 1999).

The variation of spatial frequency of landsliding with slope gradient, in one-degree increments, is systematic and nonlinear in the Oakland area. Frequency distributions for all but the smallest geologic units are near normal, as evident in Fig. 2 for the Orinda Formation (unit Tor). Spatial frequency of past landsliding

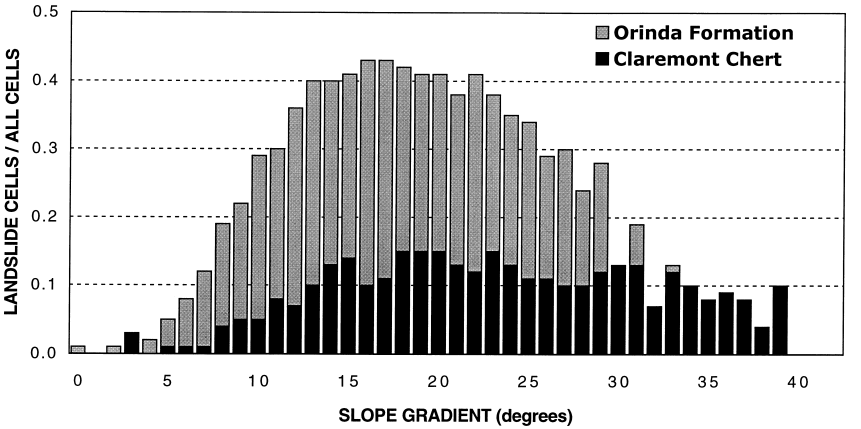


Fig. 2. Predisposition to landsliding can differ markedly by geology and slope gradient. Susceptibility, modeled as the number of 30-m grid cells on dormant landslide deposits divided by all cells, varies by 1° increments of slope in two of the 20 units in Table 1. The Claremont Chert (black, map unit Tcc) is much less susceptible than the Orinda Formation (gray, unit Tor). Mean spatial frequencies, respectively, are 0.11 and 0.28.

for unit Tor averages 28% (Table 1), but departs radically from the mean, rising from only 1% at zero slope to 43% at a slope of 16° and diminishing thereafter to <10% (Fig. 2). Collectively, the rising segments of all 120 such distributions include well over half the landslide cells in the study area, a correlation that supports some of the predictive capability claimed previously for slope gradient. The histogram for the 1192 post-1967 slides also has an overall bell-shape (Pike *et al.*, 2001). While frequencies of the steepest slopes in many units vary irregularly as the number of cells diminishes, these few aberrant values have little effect on later calculations. Distributions for the 32 units with <450 cells are more rectangular (Pike *et al.*, 2001) and resemble the histogram for steep slopes of the less susceptible (but overall steeper) Claremont Chert, unit Tcc in Fig. 2.

2. Between landslide deposits

We calculated susceptibility both between and within landslide deposits in the Oakland area. Susceptibility *S* for grid cells not underlain by old slide masses (88% of the study area and 81% of its hilly terrain, Table 2) is estimated directly from the 120 distributions of spatial frequency by slope gradient. In the Orinda Formation, for example, where 29% of the 30-m cells sloping at 10° are located on old landslide deposits (Fig. 2), *all other* cells in unit Tor with a slope of 10° are assigned that same susceptibility *S*, of 0.29. In the less-susceptible Claremont Chert (unit Tcc), by contrast, only 5% of the cells in the 10° slope interval lie on mapped slide masses, whereupon an *S* of 0.05 is assigned to *all* remaining 10° cells in the Claremont. Values of *S*, determined slope interval-by-slope interval,

Table 2. Distribution of GIS grid cells and their susceptibility values S_{ls} and S, by hillside or flatland sites and by location within or between old landslide deposits.

Terrain and Geology	Number of 30-meter grid cells		
	All cells	S_{ls} - within slide deposits	S - between slide deposits
Hillsides: the 100 bedrock units	604,973	114,543	490,430
Flatlands: the 20 surficial units	364,030	1,817	362,213
Entire study area: all 120 units	969,003	116,360	852,643

are unique to each value of slope gradient in each of the 120 units. The resulting frequency distribution of susceptibility (not shown) for the 852,643 cells that lie between mapped landslide deposits is severely skewed, even in the log domain. Values range from S = 0.00 for 300,000 cells in predominantly flat-lying Quaternary units to S = 0.90 for 14 cells in unit Kfa, Alcatraz terrane (Table 1).

3. Within landslide deposits

Obtaining susceptibility S_{ls}, for the much smaller fraction of the area that is in landslide deposits (Table 2) is more complex. We first calculated raw susceptibility S for the 116,360 cells within the deposits, by the same procedure as for cells between them. The highest S on landslide masses is 1.00, for 70 cells (15 in unit Kfa) that occur in 21 different units. To estimate the higher susceptibilities that characterize dormant landslide deposits S_{ls} we multiplied these 116,360 values of S by a factor a, based on the relative frequency of recent failures in the region,

$$a = (\#hist_{ls}/A_{ls})/(\#hist_{nls}/A_{nls}) \quad (1)$$

where $\#hist_{ls}$ and $\#hist_{nls}$ are the numbers of recent failures within and outside old landslide deposits, respectively, and A_{ls} and A_{nls} are the areas (in number of cells) of old deposits and the terrain between them. This correction, (183/116,360)/(1009/852,643) or 1.33, indicates that recent landslides in the area are about 1/3 more likely to occur within old landslide deposits than between them. Lacking historic documentation of landsliding for each geologic unit, we applied the 1.33 multiplier to all 120 units. The highest value of S_{ls} is 1.33, for the same 70 cells mentioned above. Because some S_{ls} values exceed 1.00, all susceptibilities are expressed as decimals rather than percentages. Figure 3 combines values of S and S_{ls} to yield the frequency distribution of susceptibility for all 969,003 grid cells in the Oakland metropolitan area.

EVALUATING THE MODEL

Landslide-susceptibility models are difficult to test; in actuality they can be "validated" only by the pattern of slopes that fail in subsequent storms and earthquakes. Two evaluations of our results for the Oakland area described in Pike *et al.* (2001) suggest that the model or a variant of it, with allowance for the effects of urbanization in Quaternary deposits, can estimate relative susceptibility, both within and outside the area in which the procedure was developed. Moreover, the modeled 33% higher incidence of recent failures within dormant slide deposits is of the magnitude noted previously for the area, about 55% to 70% in the more susceptible geologic units (Nilsen *et al.*, 1976, p. 19). Finally, Keefer *et al.* (1998, figure 4) found that 18 of the 20 largest landslides triggered in hills on the west side of San Francisco Bay by the 1989 Loma Prieta earthquake occurred within previous failures and occupied 55% of their area. Further development of the model is warranted. Distinguishing the inventoried landslides by triggering event (earthquake or precipitation) and type of movement, mapping a landslide's source area as well as its deposit (Wieczorek, 1984; Wilson *et al.*, 2002), and elaborating (if markedly complicating) the model by adding such variables as distance-to-nearest-road and terrain elevation, relief, aspect, and curvature from laser-generated DEMs are likely to strengthen the inferences.

THE SUSCEPTIBILITY MAP

Pike *et al.* (2001) displayed the 969,003 values of susceptibility between (S) and within (S_{ls}) dormant landslide deposits in the test area as an eight-color map. In Fig. 1D the continuous range of values from 0.00 to 1.33 is shown in shades of gray for the same eight intervals, which widen with increasing susceptibility and decreasing number of cells. We chose the unequal intervals from inspection of the frequency distribution (Fig. 3) and test plots (not shown) to yield a balanced-appearing map that emphasizes the spatial variability of the index. We assigned no exact level of hazard to the eight intervals, but simply an increasing susceptibility from white (0.00) to black (≥0.55). Which intervals to label "safe" or "dangerous" is subjective and remains a matter of interpretation; no reliable calibration is available at this time. However, from field study that has long identified certain rocks in the Oakland area as susceptible (Nilsen *et al.*, 1976; Keefer and Johnson, 1983), S and S_{ls} values at least as low as 0.20 indicate areas of potential instability—depending on the strength and duration of triggering events. Dense clusters of values >0.30 are likely to indicate hazardous terrain.

The spatial patterns on this experimental map are not random. Figure 1 reveals slope instability controlled by geology and the resulting slope contrasts in the NW-SE-trending topography, particularly distribution of the steeper, higher ridges. Low susceptibilities of 0.05–0.20 predominate in the small sample shown in Fig. 1D, but values >0.30, which indicate high potential hazard and occupy 19% of metropolitan Oakland (30% of its hillside areas; Pike *et al.*, 2001), are conspicuous in steep terrain underlain by the Orinda Formation (Tor) in Fig.

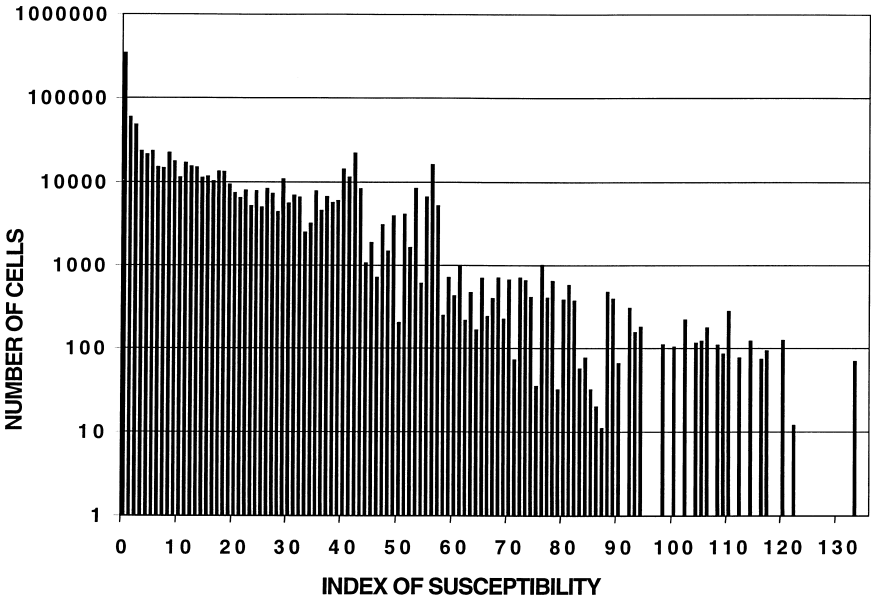


Fig. 3. Frequency distribution of susceptibility to large landslides for the 872 km^2 Oakland area, shown by log number of grid cells as a function of the modeled index number. This skewed histogram guided selection of the unequal intervals for mapping the susceptibility index (Fig. 1D).

1. Moreover, susceptibilities in the 0.10–0.29 range are common in Franciscan Complex mélange (KJfm) and other units (Table 1) that show evidence of failure (for more, see Pike *et al*., 2001). Most locations with the highest potential for hosting large landslides are steep and thinly settled, commonly in park land or tracts unlikely to be developed.

Areas of high susceptibility in Fig. 1D, while more likely to fail than locations with low values, also include local sites—scattered 30-m cells—that are not hazardous. More important for public safety, most low-susceptibility areas on the map are less prone to failure than areas of high value but are not without landslide hazard. Some of these locales slope steeply and are subject to debris flow (Ellen, 1988) and other types of failure—small landslides <60 m across, common in the area (Coe *et al*., 1999), were not included in the inventory on which Fig. 1D is based (Nilsen, 1975). Finally, landslide prediction remains something of an art, and the locus of much future landsliding cannot be identified with confidence. Slopes commonly fail from unanticipated blocking of surface drainage or other consequences of hillside development, as well as from random variation in the operation of landslide triggers and slope processes. Compiling Fig. 1D at a resolution coarser than 30 m might reflect some of these uncertainties.

CONCLUSIONS

Various methods for mapping the landslide hazard have been proposed (Radbruch and Crowther, 1970; Brabb *et al*., 1972; Nilsen and Wright, 1979; Aniya, 1985; Dietrich *et al*., 1993; Brunori *et al*., 1996; Jennings and Siddle, 1998; Irigaray *et al*., 1999). All have advantages and disadvantages. Drawbacks to our regional approach for estimating susceptibility to landsliding include the need for accurate digital-map information on geology, terrain, and prior failure over a large area. We believe that these constraints, of input data rather than of the model, are outweighed by the method's conceptual advantages:

- the model can be computed quickly over a large area;
- extent of the area is limited only by that of the input data;
- areal coverage is 100%;
- Spatial resolution can be as fine as that of the DEM;
- both method and data are 100% quantitative;
- the susceptibility index is a continuous variable;
- the model yields a range of values within, as well as between, existing landslides;
- the model is more "transparent" than "black-box"; values of the index can be related directly to field observations; and
- the method is portable; it applies anywhere the necessary data are available (e.g., Pike and Sobieszczyk, 2002).

Acknowledgements—Prof. Michio Nogami and Nihon University generously supported R. J. Pike's attendance at the 5th ICG in Tokyo. Comments by USGS colleagues Jeff Coe and Ray Wilson and by Prof. Eiji Tokunaga improved earlier drafts of this chapter.

REFERENCES

Aniya, M. (1985) Landslide-susceptibility mapping in the Amahata River basin, Japan: *Annals Assoc. American Geographers*, **75**, 102–114.

Brabb, E. E., Pampeyan, E. H. and Bonilla, M. G. (1972) Landslide susceptibility in San Mateo County, California: U.S. Geol. Survey Misc. Field Studies Map 360.

Brunori, F., Casagli, N., Fiaschi, S., Garzonio, C. A. and Moretti, S. (1996) Landslide hazard mapping in Tuscany, Italy—an example of automatic evaluation: In Slaymaker, O. (ed.), *Geomorphic Hazards*, pp. 56–67. Wiley, Chichester.

Coe, J. A., Godt, J. W., Brien, D. and Houdre, N. (1999) Map showing locations of damaging landslides in Alameda County, California, resulting from 1997–98 El Niño rainstorms: U.S. Geol. Survey, Misc. Field Studies Map 2325-B; http://pubs.usgs.gov/mf/1999/mf-2325-b/

Dietrich, W. E., Wilson, C. J., Montgomery, D. R. and McKean, J. (1993) Analysis of erosion thresholds, channel networks, and landscape morphology using a digital elevation model: *J. Geology*, **101**, 259–278; http://socrates.berkeley.edu/~geomorph/shalstab/

Ellen, S. D. (1988) Description and mechanics of soil slip/debris-flows in the storm: In Ellen, S. D. and Wieczorek, G. F. (eds.), *Landslides, Floods, and Marine Effects of the Storm of January 3–5, 1982, in the San Francisco Bay Region, California*: U.S. Geol. Survey Prof. Paper 1434, pp. 63–112.

Graham, S. E. and Pike, R. J. (1998) Slope maps of the San Francisco Bay region, California; a digital database: U.S. Geol. Survey Open-file Report 98-766, 17 pp.; http:wrgis.wr.usgs.gov/open-file/of98-766/index.html

Graymer, R. W. (2000) Geologic map of the Oakland Metropolitan Area, California: U.S. Geol. Survey, Misc. Field Studies Map 2342; http://geopubs.wr.usgs.gov/mapmf/mf2342/

Irigaray Fernández, C., Fernández del Castillo, T., El Hamdouni, R. and Chacón Montero, J. (1999) Verification of landslide susceptibility mapping—a case study: *Earth Surface Proc. and Landforms*, **24**, 537–544.

Jennings, P. J. and Siddle, H. J. (1998) Use of landslide inventory data to define the spatial location of landslide sites, South Wales, UK: In Maund, J. G. and Eddleston, M. (eds.), *Geohazards in Engineering Geology*, Eng. Geol. Spec. Publ. 15, Geological Society London, pp. 199–211.

Keefer, D. K. and Johnson, A. M. (1983) Earth flows-morphology, mobilization, and movement: U.S. Geol. Survey, Prof. Paper 1264, 56 pp.

Keefer, D. K., Griggs, G. B. and Harp, E. L. (1998) Large landslides near the San Andreas fault in the Summit Ridge area, Santa Cruz Mountains, California: In Keefer, D. K. (ed.), *The Loma Prieta, California, Earthquake of October 17, 1989—Landslides*: U.S. Geol. Survey, Prof. Paper 1551, C71–C128.

Lanyon, L. E. and Hall, G. F. (1983) Land-surface morphology 2, predicting potential landscape instability in eastern Ohio: *Soil Science*, **136**, 382–386.

Nilsen, T. H. (1973) Preliminary photointerpretation map of landslide and other surficial deposits of the Concord 15′ quadrangle and the Oakland West, Richmond, and part of the San Quentin 7.5′ quadrangles, Contra Costa and Alameda Counties, California: U.S. Geol. Survey Misc. Field Studies Map 493.

Nilsen, T. H. (1975) Preliminary photo-interpretation maps of landslide and other surficial deposits of 56 7.5-minute quadrangles, Alameda, Contra Costa, and Santa Clara Counties, California: U.S. Geol. Survey Open-File Report 75-277.

Nilsen, T. H. and Wright, R. H. (1979) Relative slope stability and land-use planning in the San Francisco Bay region, California: U.S. Geol. Survey Prof. Paper 944, 16–55.

Nilsen, T. H., Taylor, F. A. and Dean, R. M. (1976) Natural conditions that control landsliding in the San Francisco Bay region—an analysis based on data from the 1968–69 and 1972–73 rainy seasons: *U.S. Geol. Survey Bull.*, 1424, 35 pp.

Pike, R. J. and Sobieszczyk, S. (2002) A digital map of susceptibility to large landslides in Santa Clara County, California: *Eos Trans. American Geophys. Union*, **83**, 47 (Supplement), F557; http://www.agu.org/meetings/fm02/fm02-pdf/fm02_Hl2D.pdf

Pike, R. J., Graymer, R. W., Roberts, S., Kalman, N. B. and Sobieszczyk, S. (2001) Map and map database of susceptibility to slope failure by sliding and earthflow in the Oakland area, California: U.S. Geol. Survey, Misc. Field Studies Map 2385, 37 pp.; http://geopubs.wr.usgs.gov/map-mf/mf2385/

Pike, R. J., Howell, D. G. and Graymer, R. W. (2003) Landslides and cities—an unwanted partnership: In G. Heiken, R. Fakundiny and J. F. Sutter (eds.), *Earth Science in the City—A Reader*, American Geophys. Union Special Publication 56, pp. 187–254.

Radbruch, D. H. and Crowther, K. C. (1970) Map showing areas of relative amounts of landslides in California: U.S. Geol. Survey, Open-file Report OF 70-270, 36 pp.

Varnes, D. J. (1978) Slope movement and types and processes: In Schuster, R. L. and Krizek, R. J. (eds.), *Landslides—Analysis and Control, Special Report 176*, pp. 11–33. Transportation Research Board, National Academy of Sciences, Washington, D.C.

Wieczorek, G. F. (1984) Preparing a detailed landslide-inventory map for hazard evaluation and reduction: *Bull. Assoc. Eng. Geologists*, **21**, 337–342.

Wills, C. J. and McCrink, T. P. (2002) Comparing landslide inventories—the map depends on the method: *Environmental and Engineering Geoscience*, **8**, 279–295.

Wilson, R. I., Wiegers, M. O., McCrink, T. P., Haydon, W. D. and McMillan, J. R. (2002) Earthquake-induced landslide zones: In *Seismic hazard zone report for the Oakland East 7.5-minute quadrangle, Alameda County, California*, Seismic Hazard Zone Report 080, California Geological Survey, pp. 25–43 and Plate 2.1.

Concepts and Modelling in Geomorphology: International Perspectives,
Eds. I. S. Evans, R. Dikau, E. Tokunaga, H. Ohmori and M. Hirano, pp. 199–220.
© by TERRAPUB, Tokyo, 2003.

Eigenvector Analysis of Digital Elevation Models in a GIS: Geomorphometry and Quality Control

Peter L. GUTH

Department of Oceanography, U.S. Naval Academy,
Annapolis, Maryland 21402-5026, U.S.A.
e-mail: pguth@usna.edu

Abstract. Digital elevation models (DEMs) cover a wide range of scales, and allow statisticalanalysis of geomorphometric parameters. At global or continental scale, DEMs covering rectangular quadrangles can be considered random samples. Average quadrangle values can be compared at different DEM scales, and for different physiographic provinces. Three independent variables provide valuable descriptions of terrain: average elevation, average slope, and the degree of terrain organization. DEMs with spacings of 30″ (global coverage), 3″ (continental United States), and 30 m (local United States) provide almost perfect correlations for average quadrangle elevation and slope, although the slope values increase as the DEM spacing decreases. The degree of terrain organization also correlates across DEM scales, but with lower correlation coefficients, especially in areas of lower relief. Terrain variables computed from 10 m and 30 m USGS Level 2 DEMs are essentially identical. Slope algorithms perform differently in different physiographic provinces, and the aspect algorithm performs poorly in low relief areas. Geomorphometric analysis can provide a rapid and effective assessment of DEM quality control, and should be integrated into the DEM production process.

Keywords: Digital-Elevation-Model, Geomorphometry, Slope-Algorithm, Aspect-Algorithm

INTRODUCTION

Digital elevations models (DEMs), rectangular grids of elevation values, provide an unparalleled tool for geomorphometry. DEMs now cover a wide range of scales, from global through continental and regional to local and almost point scales. Analysis can extract a wide variety of parameters relating elevation, slope, aspect and terrain organization. Conversely, geomorphometry provides an ideal tool for assessing the quality of DEMs. Outliers on histograms or bivariate plots of geomorphometric parameters almost always represent flawed DEMs.

At small scales DEM data cover the entire world, but at large scale data availability reflects a bias toward the United States. This bias results from two factors: (1) the United States government has one of the most aggressive programs in the world to produce DEMs, and (2) almost unique in the world, the United States national mapping agencies place no restrictions on their digital data. DEMs with 30 m spacing cover almost all of the United States, and increasing numbers of 10 m DEMs are coming on line. With data spacing ranging

from almost 10 km to 10 m, available DEMs span 4 orders of magnitude. Experimental 1 m resolution LIDAR (Light Detection and Ranging) DEMs cover areas almost point-like with vast quantities of data (NOAA Coastal Services Data Center, 2001), and will add another order of magnitude to range of scales when they become widely available.

DATA

This study used DEMs from continental scale (30″ spacing, about 1 km), regional scale (3″ spacing, 60–90 m), and local scale (10–30 m spacing). Table 1 summarizes the free data obtained from the www. These data sets will now fit comfortably on hard disks of mainstream personal computers. All of these data sets use binary 2 byte elevations. The continental data sets are stored uncompressed, whereas the other data sets are stored with the same standard UNIX compressed file structure obtained from the USGS web site. Because compression varies with the type of terrain and the amount of smoothing from the DEM creation process, the estimates below should be viewed only as rough estimates for the order of magnitude of the DEM sizes. Further, if future large scale DEMs use 4 byte values for elevation as the USGS is starting to implement, file sizes might double.

Three different United States government mapping agencies have created quasi-independent continental 30″ DEMs: DTED Level 0 (NIMA, 2000), GLOBE (NOAA National Geophysical Data Center, 2001), and GTOPO30 (USGS EROS Data Center, 2001). After downloading, the GLOBE and GTOPO30 datasets were converted to 1° tiles to match the DTED, and provide a good statistical sampling unit for comparisons. With 1° elevation tiles each data set will fit on a single CD-ROM, if some of the interior cells in Antarctica are removed. The flatness of the ice sheet and the convergence of the meridians make the 30″ DEM a poor choice for the polar regions.

The 250K DEM (USGS, 2001) was originally created by a precursor of NIMA and contains many processing anomalies but remains a valuable regional data resource because of its availability. The current NIMA product, DTED Level 1, provides a much better demonstration of what this data resolution can achieve but is unfortunately not publicly available. The DEMs used in this study cover all of the United States and Puerto Rico except for Alaska. The SRTM mission

Table 1. DEMs available for comparison.

Name	DEMs in Sample	Tile	Spacing	Sample Storage	Full US	Full World
ETOPO5 TerrainBase	1		5’	20 MB		20 MB
DTED0 GLOBE, GTOPO30	17,680 21,803 20,151	1°	30”	650 MB		650 MB
USGS 250K	940	1°	3”	1 GB	1 GB	20 GB
USGS 24K	50,279 (42,921 unique)	7½’	30 m	6.2 GB	6.2 GB	150 GB
USGS 24K	1066	7½’	10 m	1 GB	50 GB	1 TB

should produce this world-wide data set for public use (Jet Propulsion Laboratory, 2001), and the first samples covering some of the United States appeared in early 2002 and South America in the summer of 2003. The SRTM data appeared too late to include in this analysis, and will require careful consideration on how to handle the data voids when conducting statistical analyses.

Over 51,000 24K DEMs were downloaded from the same USGS site along with the 250K DEM (USGS, 2001) in the summer of 2000, before the 24K DEMs were removed. USGS allowed an automated download process, the only practical way to obtain such a large sample. This data, and an increasing number of 10 m DEMs, must now be downloaded free from two commercial sites that restrict the speed or number of DEMs that can be, and which forbid the use of automated ftp, or in a reprojected format from the National Elevation Dataset (NED, Gesch and others, 2002). While the data considered here have elevations stored as 2 byte integers with foot or meter resolution, some newer DEMs now use 2 byte integer decimeters and others use 4 byte floating point values.

The 24K DEMs have two characteristics relevant to a discussion of geomorphometry. The "Level" of the DEM assesses its quality: Level 1, no longer being produced, used profiling or similar photogrammetric methods to produce lower quality DEMs, whereas the newer Level 2 DEMs used interpolation from scanned contour lines (USGS National Mapping Division, 1997/1998). Except for contour line "ghosts" where elevations corresponding to the source map contour lines are overrepresented in the DEM (Guth, 1999c), the Level 2 DEMs provide a much better representation of the terrain. In addition, some DEMs have both 10 m and 30 m resolution. Ten meter resolution provides much greater visual detail in representations of the terrain.

At 30 m spacing the data set includes 42,921 (80%) of the 53,873 24K quadrangles in the continental United States, plus 81 DEMs in Puerto Rico and the Virgin Islands, and provides an excellent sample for this scale data at continental resolution. Hawaiian data were not available on the USGS web site, and Alaska was not mapped at this scale. The SRTM mission (Jet Propulsion Laboratory, 2001) should produce this world-wide data set for US military use, although the radar's smoothing might make the effective resolution lower than the nominal resolution. The data set includes about 1000 10 m level 2 DEMs, or about 2% of the total area of the continental United States.

The following tests on the differences in calculated statistical parameters will be conducted using these DEMs for geomorphometry:

1. How do the different 30″ continental DEMs differ?
2. How do the 30″ continental and 3″ regional DEMs differ?
3. How do the 3″ regional and 30 m local DEMs differ?
4. How do the Level 1 and Level 2 local DEMs differ?
5. How do the 10 m and 30 m Level 2 local DEMs differ?

GEOMORPHOMETRIC PARAMETERS

Pike (1988) introduced the concept of a geometric signature, a multi-variate description of topography using a suite of measures, and later expanded the

concept with a listing of 49 variables that could be grouped into 22 attributes (Pike, 2001). He considered roughness and height the two most important attributes, with two measures of texture in seventh and eleventh position. Fifteen different variables contribute to roughness.

This analysis will focus on three geomorphic parameters: average elevation, average slope, and organization strength. These parameters reflect the interaction of climate, lithology, and topography. Average elevation, combined with latitude, represents a primary control on climate for both precipitation and temperature. Slope depicts the ruggedness and dissection of the landscape. Organization values measure the processes responsible for terrain formation; the most highly organized regions are in folded mountain belts or glacial drumlin fields. Average elevation and average slope coincide with Pike's (2001) most important attributes, but none of his experimental measures fully capture this organization parameter.

Computation of average slope requires selection of a slope algorithm; a number have been proposed, and about a half dozen widely used (recent summaries in Skidinore, 1989; Guth, 1995; Hodgson, 1998; Jones, 1998). Results for average regional slope correlate very strongly among the various methods, although the absolute values vary. This analysis uses the steepest adjacent neighbor algorithm, but comparisons between the steepest adjacent neighbor and four nearest neighbor methods show how the choice of slope method affects geomorphic results.

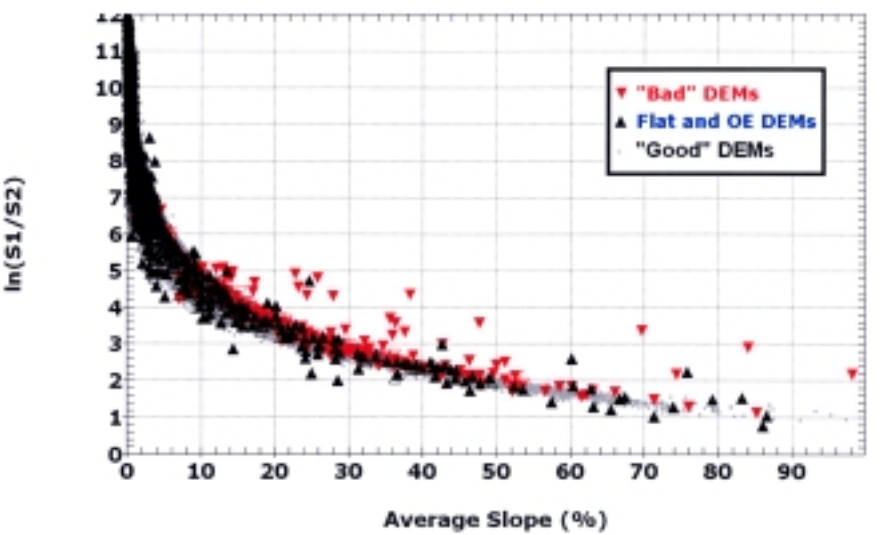


Fig. 1. Average slope versus flatness parameter ln(S1/S2) for the 51,000 24K USGS DEMs. The "good" DEMs show the high correlation. Outliers consist of "bad" DEMs (visually examined to verify processing anomalies) and flat and overedge DEMs (identified by small compressed file sizes).

Eigenvector methods can retrieve a flatness parameter and organization parameter. Chapman (1952) proposed a graphical method using a stereo net to characterize terrain orientations. Woodcock (1977) described an eigenvalue method for fabric shapes in structural geology. The two methods can be combined for automatic characterization of terrain organization (Guth, 1999a, 1999b, 2001). Direction consines of the landscape surface were computed from the slope and aspect at each point, and then eigenvectors were obtained. The eigenvalue method extracts two independent parameters from the distribution of normals to the earth's surface calculated from the DEM, both logs of the ratios of eigenvalues. The ratio ln(Sl/S2) reflects a flatness parameter, and it correlates almost perfectly with the average slope (Fig. 1). The correlation is negative because the log ratio is flatness and not steepness, and is not linear because of the log ratio. This correlation should not be surprising, since the eigenvalue method starts with the slope and aspect at each point and the orientation of the first eigenvector is the average normal to the earth's surface.

The ratio ln(S2/S3) reflects the strength of the preferred orientation shown by Fig. 2. No previously defined geomorphic parameters replicate its power in quantifying the degree of organization of the terrain. Other parameters attempt to measure the spatial dimensions of periodic landforms, with "grain" representing the distance between repeating landforms. Based on analysis of over 50,000 30 m DEMs, Fig. 2 shows the three most highly organized quadrangles in the United States. The figure shows the dominant direction of the fabric, defined by the orientation of one eigenvector, and shows how it swings around as the folded ridges change orientation along strike.

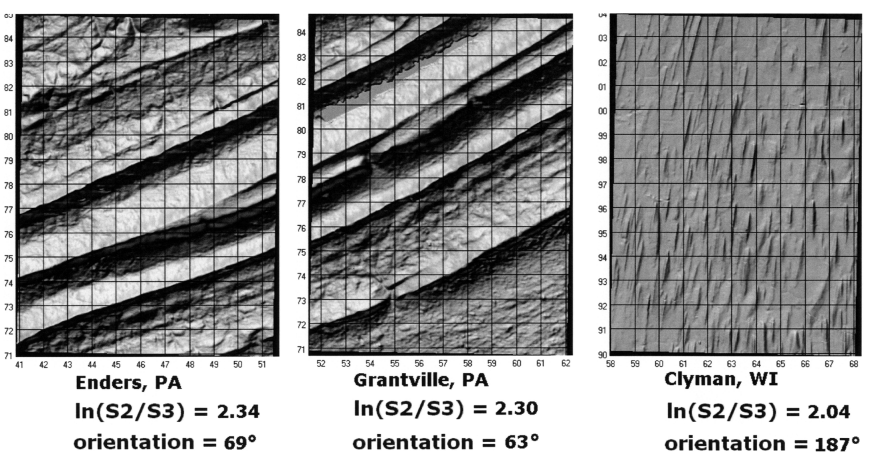


Fig. 2. The three most highly organized quadrangles in the United States. The two on the left are adjacent Level 1 DEMs in the folded Appalachians, and the level 2 DEM on the right contains a drumlin field in Wisconsin. One km UTM grid provides scale.

Elevation is a true point parameter, defined at every grid location in the DEM. While slope is also a point parameter, it requires consideration of the neighboring elevations and various algorithms use from 2 to 8 adjacent neighbors. The most commonly used algorithm uses four neighbors and actually ignores the elevation of the central point to which the slope is assigned. The eigenvector method uses a region and probably requires at least 100 points for reasonable statistical accuracy. While organization can be calculated as a point parameter for a particular region size about a point with a sliding window over the DEM (Guth, 1999b, 2001), this study will concentrate of calculations with a 1° region size for global scale or 7 1/2′ region for continental scale. This quadrangle geomorphometry introduces arbitrary aspects to the study, but sample sizes are large enough that quadrangles represent reasonable sampling areas.

METHODS

All analyses used the MICRODEM program (Guth and others, 1987; Guth, 1995). This program predates commercial GIS programs for personal computers, and while MICRODEM has now become a full-feature GIS program it retains a greater emphasis on DEMs and geomorphometry than any commercial program. While scripting within a GIS might duplicate the operations described here (e.g. contour line ghosts or terrain organization), I prefer embedding the capabilities within MICRODEM where I have complete control of the operations and displays. With object-oriented programming, the DEM object contains methods to calculate geomorphic parameters of the terrain.

MICRODEM indexes the DEMs, and sequentially processes them to calculate geomorphic parameters. For the 30″ global DEMs the program used 1° tiles. For the 3″ 250K DEM, the comparison used 1° tiles to compare with the 30″ data, and 7 1/2′ tiles to compare with the 24K DEM. The program computed five variables for each tile: average slope, average elevation, the eigenvalue flatness and organization parameters, and the direction of terrain organization. The database contains five additional fields for the DEM name and its bounding geographic rectangle. The program computed 28 additional parameters for the 24K DEM: duplicate variables to compare slope algorithms, DEM quality measures like the ghost ratio (Guth, 1999c), and additional geomorphometric parameters which will not be discussed here but which could be used for a geometric signature (Pike, 2001).

The GIS database files for the geomorphic parameters allows summary statistics, bivariate scatter plots, and map displays, with options to filter the display—for example, to only show terrain organization for regions with greater than a specified average slope. The interactive nature of the GIS allows clicking on a point on the graph to show tabular data for that point and its location on the map. For the large data sets considered in this effort, the power of the GIS represents the most effective way to explore the data.

Drawing on earlier work of Fenneman dating to 1917, the Fenneman and Howard (1946) map of the United States has 8 major divisions, 25 provinces, and 86 sections representing distinctive areas having common topography, rock types

and structure, and geologic and geomorphic history. A digital version of the map (Hitt, 2002) was converted to geographic coordinates, and then each quadrangle in the United States was assigned to the corresponding section. This allows the GIS to compute statistics based on the Fenneman physiographic regions.

Many of these analyses omit 24K DEMs identified as containing "bad" data, and those with a compressed file length less than 50 kb. Small file sizes occur in two cases: coastal "overedge" DEMs where standard quadrangles leave a small bit of land in what would be the next quadrangle, and extremely flat quadrangles in regions like the coastal plains. These DEMs account for a disproportionate number of the outliers on statistical plots. Overedge DEMs have an insufficient number of points for reliable statistics, and the DEMs do not have adequate vertical resolution for good statistics in very flat regions. The GIS also contains a percent ocean field for the global data sets; often the coastal DEMs should be ignored for the eigenvector analysis. The 30″ 1° tiles contain only about 1400 elevations, and when a significant proportion are missing the resulting statistics represent outliers compared to full data sets.

SLOPE ALGORITHMS

While different slope algorithms correlate highly, they produce different results. Guth (1995) suggested using a steepest adjacent neighbor algorithm, while the most popular algorithm appears to be the four nearest neighbors (e.g. Hodgson, 1998; Jones, 1998), although Evans (1998) makes a convincing case for the superiority of an eight neighbors algorithm. Because the steepest adjacent neighbor and four nearest neighbors have the greatest differences among the common methods, a detailed analysis of their differences highlights the effect of slope algorithm on geomorphic parameters. Because slope and aspect provide the raw input to the eigenvector algorithm, the slope algorithm might affect the organization calculations.

With an eight point neighborhood about the central point, eight partial slopes can be calculated in each of the eight principal cardinal directions. If the point elevations are considered accurate, these represent the only unambiguous slopes that can be determined. The challenge for the slope algorithm is to use these values to estimate a single slope at the central point. The steepest adjacent neighbor algorithm uses the steepest of the eight slopes: this slope exists, it is measured over the DEM spacing (or the diagonal), and in many applications the steepest slope is most important. The four nearest neighbors algorithm uses just four neighbors: it is measured over twice the DEM spacing, and it smooths the results by using twice the slope distance and not using the diagonal neighbors.

Figure 3 shows a comparison of the average quadrangle slope computed from these two algorithms for 30 m DEMs (28,479 level 2 and 18,689 level 1). This analysis omits DEMs identified as containing bad data, and those with a compressed file length less than 50 kb.

Several observations are clear from the two graphs: (1) the two slope algorithms are highly correlated; (2) the steepest adjacent neighbor algorithm produces consistently larger average slopes; (3) the level 2 DEMs appear to be

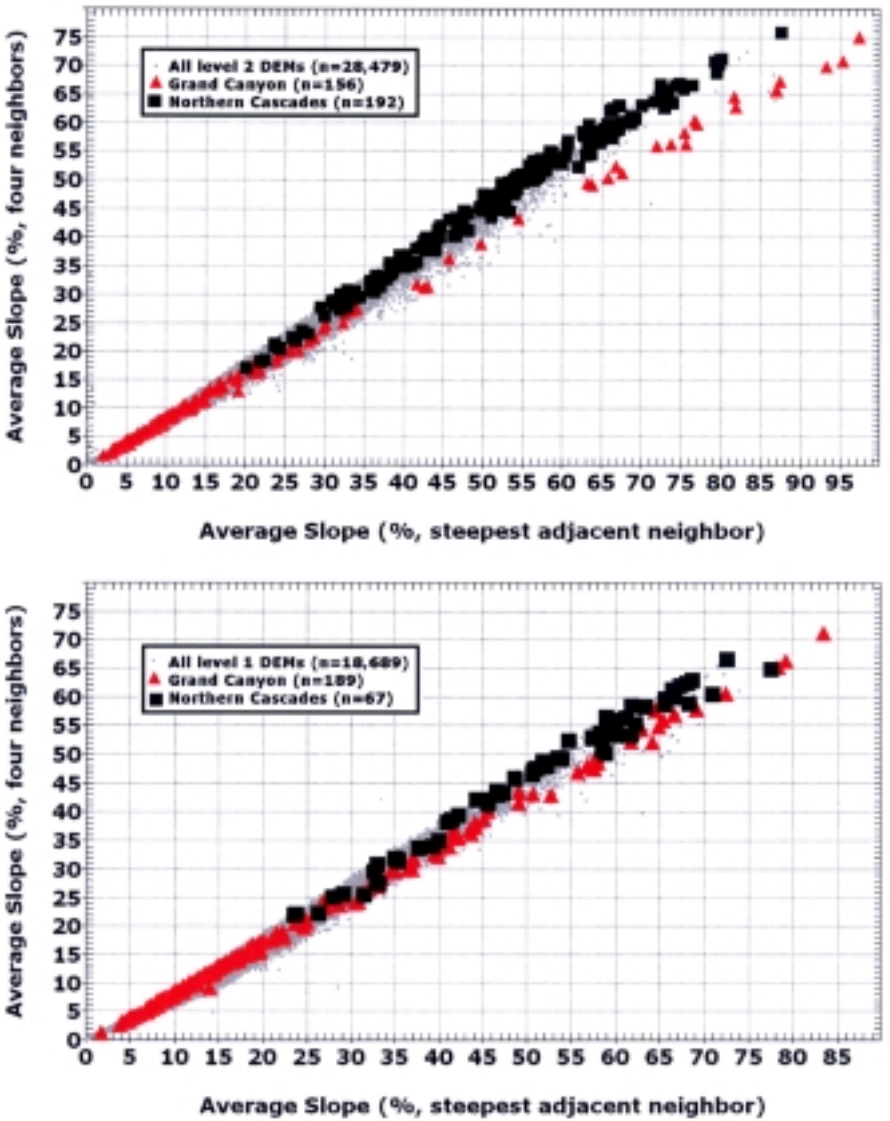


Fig. 3. Average slope computed by two different algorithms, for both Level 1 and Level 2 USGS 24K DEMs. DEMs from two Fenneman physiographic provinces indicated.

steeper than the level 1 DEMs, with both algorithms (this is not proven by these graphs because the DEMs in the two samples are not the same, but it will be proven later); (4) the wide scatter about the trend lines suggests that additional factors affect the slopes.

Table 2. Comparison of slope algorithms for two mountainous quadrangles.

	Temple of Sinawava, Utah		Cascade Pass, WA	
	Steepest Neighbor	Four Neighbors	Steepest Neighbor	Four Neighbors
Entire DEM	86.7%	63.8%	87.5%	75.7%
Peaks	101.2	33.4	130.7	35.8
Other	86.0	64.6	87.6	75.7

Table 3. Comparison of correlation coefficient *r* for geomorphometric parameters.

DEM scales compared	Average Elevation	Average Slope	Organization ln(S2/S3)
DTED0 vs GLOBE, n=17,559	r=0.992	r=0.975	r=0.598
DTED0 vs GTOPO30, n=17,547	r=0.992	r=0.950	r=0.516
GLOBE vs GTOPO30, n=20,114	r=0.999	r=0.979	r=0.906
DTED0 vs USGS 250K, n=946	r=1.000	r=0.983	r=0.680
GTOPO30 vs USGS 250K, n=938	r=0.999	r=0.987	r=0.701
GLOBE vs USGS 250K, n=941	r=0.999	r=0.987	r=0.670
USGS 250K vs 24K, n=51,345	r=0.997	r=0.951	r=0.496
USGS 24K, Level 2, 10 vs 30 m, n=472	r=1.000	r=0.998	r= 0.960
USGS 24K, Level 1 vs 2, 30 m, n=6476	r=1.000	r=0.968	r=0.545

To investigate the effect of additional factors on the computed average slopes, two level 2 DEMs were selected from the steeper side of the graph. Both had similar average slopes using the steepest adjacent neighbor method, but greatly different slopes for the four adjacent neighbors method (Table 2).

As noted by Guth (1995), these two algorithms will differ most for peaks, pits, ridges and valleys. Pits are extremely rare, both in nature and the DEMs, but the other terrain types occur about in 5–6% of the points in these DEMs. While the differences in these points can be huge (see the results for peaks in Table 2), it is the other points that make the difference—the 95–96% of the points classified as "other" have average slopes almost identical to the averages for the entire DEM (Table 3). On this measure these two DEMs differ significantly.

Analysis of the graphs in Fig. 3 revealed that the high slope DEMs occurred primarily in two geomorphic provinces, the Grand Canyon and the Northern Cascades. A few equally steep DEMs occur in other provinces, including the Temple of Sinawava DEM in the High Plateaus of Utah Section adjacent to the Grand Canyon. Highlighting those provinces on the graph showed two very distinct trends: the four adjacent neighbors method produces gentler slopes in the Grand Canyon than in the Northern Cascades, for DEMs that the steepest adjacent neighbor method considered equally steep. Figure 4 shows shaded relief depictions of these two DEMs. The Temple of Sinawava quadrangle has more youthful dissection. More points have extreme slopes along one of the diagonals, and these influence the average slope of the quadrangle only with the steepest adjacent neighbor. The commonly used four neighbors slope algorithm behaves differently

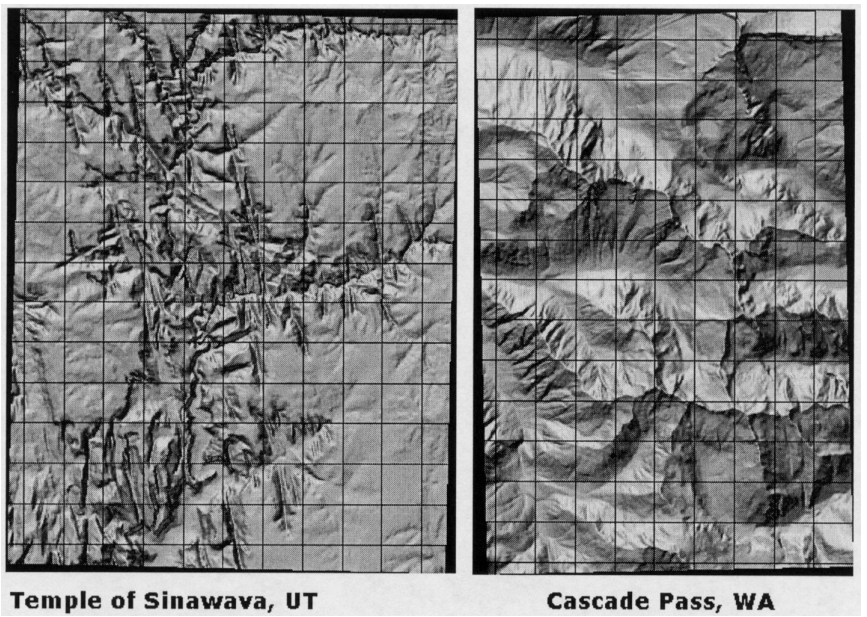


Fig. 4. Shaded relief views to Level 2, 30 m USGS DEMs of Temple of Sinawava and Cascade Pass.

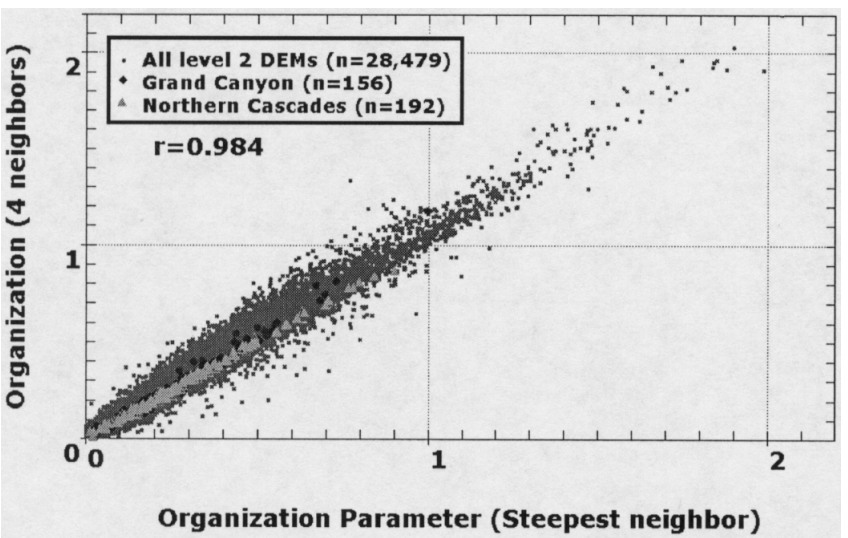


Fig. 5. Organization parameter for 30 m Level 2 USGS DEM calculated with two different slope methods.

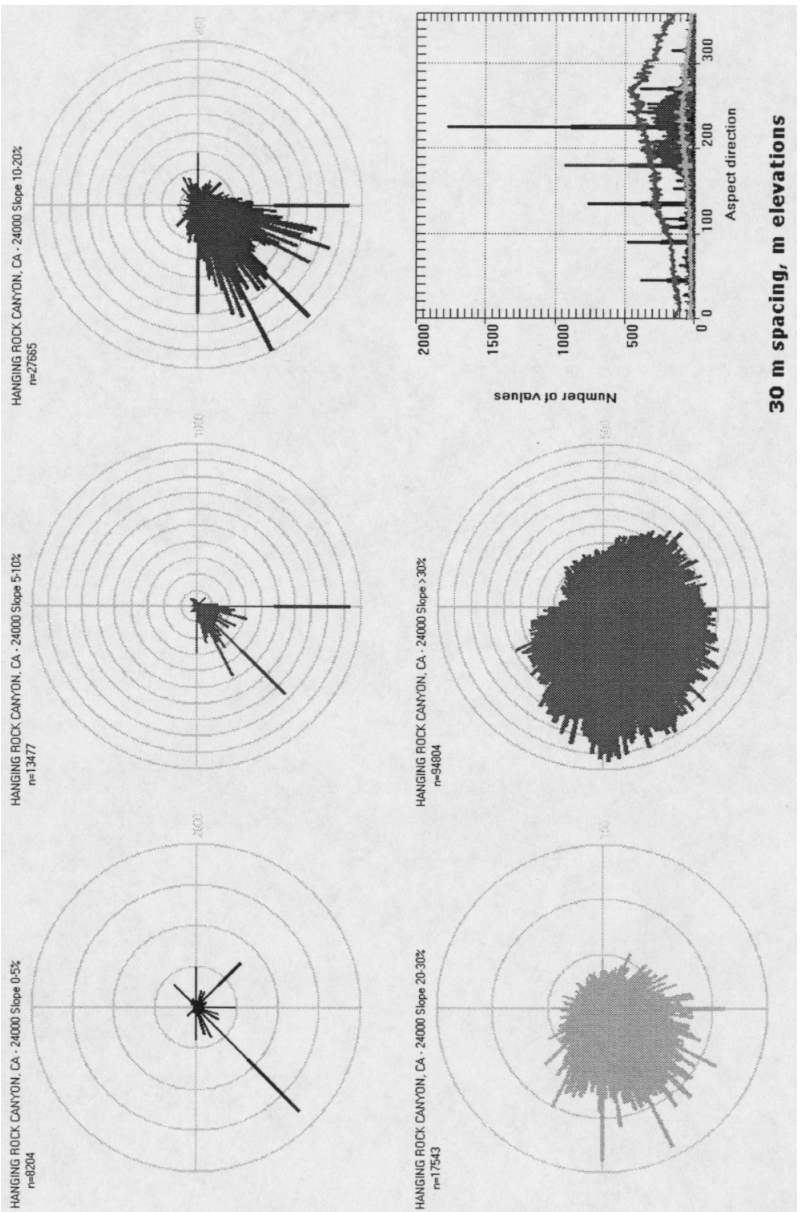


Fig. 6. Aspect distributions for the Level 2 Hanging Rock Canyon 30 m DEM, divided by slope class. This DEM has elevations in meters.

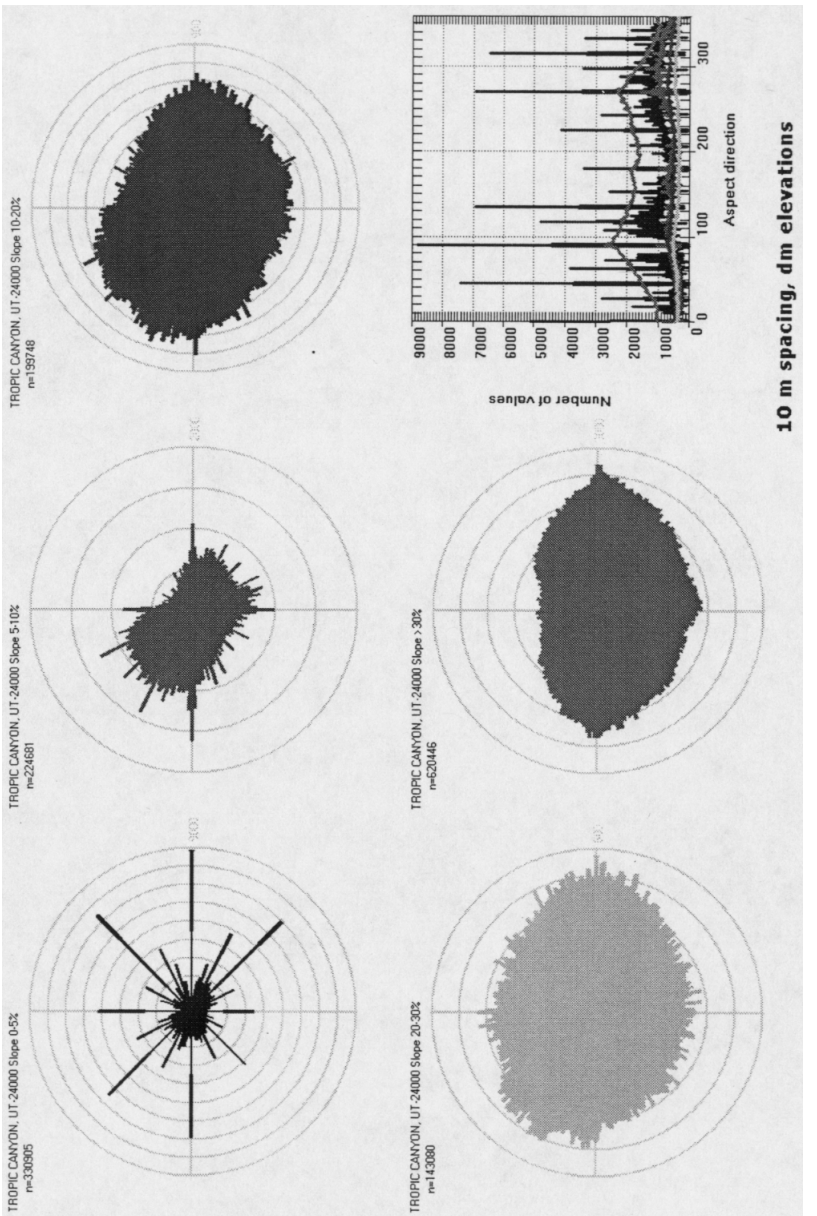


Fig. 7. Aspect distributions for the Level 2 Tropic Canyon 10 m DEM, divided by slope class. This DEM has elevations in decimeters.

in different physiographic provinces, compared to the steepest adjacent neighbor algorithm.

Since the eigenvector technique relies on the slope as input, Fig. 5 shows the organization parameter for level 2 DEMs calculated with the two slope algorithms. Scatter is minimal, the graph's slope is close to 1, and the differences do not correlate with the physiographic province. The eigenvector technique appears to extract organization independent of the slope algorithm use.

ASPECT ALGORITHM

Selection of an aspect algorithm presents much less choice than that of a slope algorithm, because extending many of the slope algorithms would result in a very limited number of possible aspect directions. Guth (1995) suggested use of the eight nearest neighbors with even weighting, and that algorithm has been used here. However, this algorithm does not provide an even or uniform distribution of aspects.

Figure 6 shows the aspects for a 30 m DEM. Note the spikes in the aspect distribution, especially prominent for the low slope parts of the DEM. Aspects at 45° intervals are overrepresented, and the algorithm appears to work well only when the slope exceeds 30%. The problem originates in the discrete nature of the elevations: with meter elevation resolution and 30 m spacing, the basic slope values only change by 1/30. To verify this assumption, Fig. 7 shows the aspect distributions for a 10 m DEM with elevations in decimeters. This allows slope values to change by 1/100, and in this case the algorithm appears to produce uniform and natural aspect distributions if the slope is steeper than 10%.

RESULTS

Table 3 summarizes the results of the comparisons of DEMs at different scales or sources. The correlation coefficients for both average slope and average elevation exceed 0.95 for all the comparisons, but with these sample sizes such correlation coefficients still allow some scatter and some significant anomalies. The organization parameter shows more scatter and lower correlations.

1. Continental data sets

The continental data sets agree with each other extremely well for average slope and average elevation, and less well for organization level. Table 3 shows correlation coefficients greater than 0.99 for elevation and 0.95 for slope, and as low as 0.51 for organization. GTOPO30 and GLOBE show the strongest correlation, and both have complete coverage of the world. DTED level 0 does not include Antarctica, and still has a large gap in the Amazon Basin.

Despite correlation coefficients for average elevation exceeding 0.99, differences in average elevation for 1° cells can exceed 2000 m. Six cells in the Andes of Peru and Bolivia have differences this large between DTED and GLOBE, and one has a difference exceeding 3000 m. This suggests that for parts of the world the continental data sets still have significant problems.

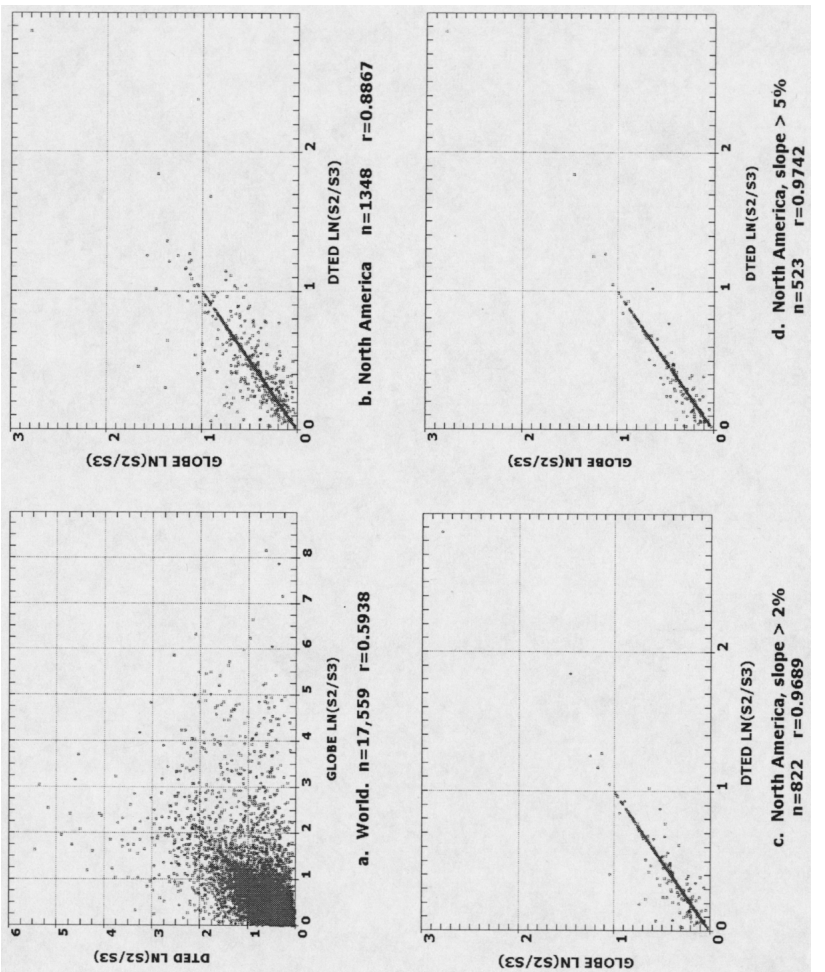


Fig. 8. Comparison of the organization parameter ln(S2/S3) calculated from DTED Level 0 and GLOBE for 1° cells. Note that (a) has a different scale than the others.

To investigate how well the continental data sets work in regions with good digital representations of topography, Fig. 8 shows the scatter plots for organization plotted from DTED and GLOBE. Figure 8a shows the global data, with a great deal of scatter and a correlation of 0.594. With the data restricted to part of North America (N23–N54, and W130–W73), Fig. 8b shows much less scatter and an improved correlation of 0.887. Restricting the data to regions with slopes greater than 2% and 5% in Figs. 8c and 8d increases the correlation even further to 0.97. Organization values have the least reliability in regions of low slope.

Assessing the accuracy of DTED Level 0 versus GLOBE or GTOPO30 remains beyond the scope of this work, because it likely varies regionally. The tremendous differences in average elevation noted above occur on the eastern flank of the Andes, where DTED shows the average elevation in one cell to be over 2000 m higher than the cell immediately to the east, and neighboring cells do not even remotely match along their common edge. Only a few of the cells in that region used higher resolution DTED as their source, and most of the others show only the grossest outlines of topography. GTOPO30 and GLOBE improve the elevation picture somewhat in that region, but clearly show which cells had high resolution source data available. The SRTM 30″ global set has just been released (summer 2003), and should now be used for this scale analysis.

2. Continental versus regional DEMs

This comparison must be restricted to the United States because of the lack of publicly available data elsewhere. Table 3 shows the comparison of about 940

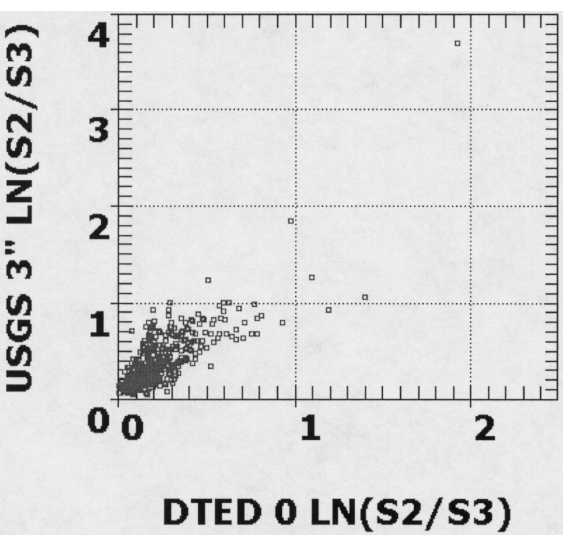


Fig. 9. Comparison of the organization parameter between DTED 0 and the USGS 3″, 250K DEM. This shows the 432 cells covering the United States with an average slope in the USGS DEM greater than 5%.

Table 4. USGS 250K versus 24K, 7 1/2′ tiles.

Average slope	Number of 7½' tiles	Organization Parameter Correlation Coefficient r
All data	34,887	0.473
>2%	23,241	0.612
>5%	13,026	0.757
>10%	7,956	0.818
>20%	3,598	0.818
>30%	1496	0.835

1° tiles for DTED 0, GLOBE, and GTOPO30 with the USGS 250K DEM. The three continental data sets have slightly different numbers of tiles because of differences in continental masking. Average elevation and average slope correlate almost perfectly, showing that the continental DEMs accurately capture this aspect of topography.

Organization correlates less well, with correlation coefficients around 0.68. As with the comparison among the continental DEMs, the disagreements tend in occur in the flatter DEMs. For the DTED 0 comparison with the USGS 3″ 250K DEM, the correlation coefficient increases from 0.6802 (n = 946) for all data, to 0.7314 for DEMs with an average slope greater than 2% (n = 642), and to 0.7875 for DEMs with an average slope greater than 5% (n = 432, Fig. 9). Areas of different slope will occur within 1° cells, so that low slope areas will produce different estimates of organization when aggregated over the entire cell.

3. Regional versus local DEMs

Table 3 shows that the USGS 250K and 24K DEMs show almost perfect correlations in average elevation and slopes. At the quadrangle level, despite severe contour line ghosts, the 250K DEM accurately depicts average terrain characteristics. The organization parameter between the two series correlates less well, but as Table 4 shows, the flat DEMs account for most of the poor correlations.

4. Scale in local DEMs 10 m versus 30 m

Somewhat surprisingly, Tables 3 show that for these geomorphic parameters the 10 m DEMs do not provide increased precision. The 10 m DEMs are visually vastly superior in the fine details they provide, but produce essentially identical statistical results. Even the organization parameter shows a high correlation coefficient, and it only increases from 0.954 to 0.981 as average slope increases from 2% to greater than 30%.

5. Quality in local DEMs

USGS produces two levels of DEMs, and in this sample they were present in almost equal numbers. Table 5 shows how the calculated organization parameters correlate as the average slope in the DEM increases.

Table 5. USGS 24K, 7 1/2′ tiles, Level 1 versus Level 2.

Average slope	Number of 7½' tiles	Organization Parameter Correlation Coefficient r
All data	6476	0.545
>2%	6454	0.544
>5%	5940	0.606
>10%	4695	0.706
>20%	2909	0.757
>30%	1586	0.890

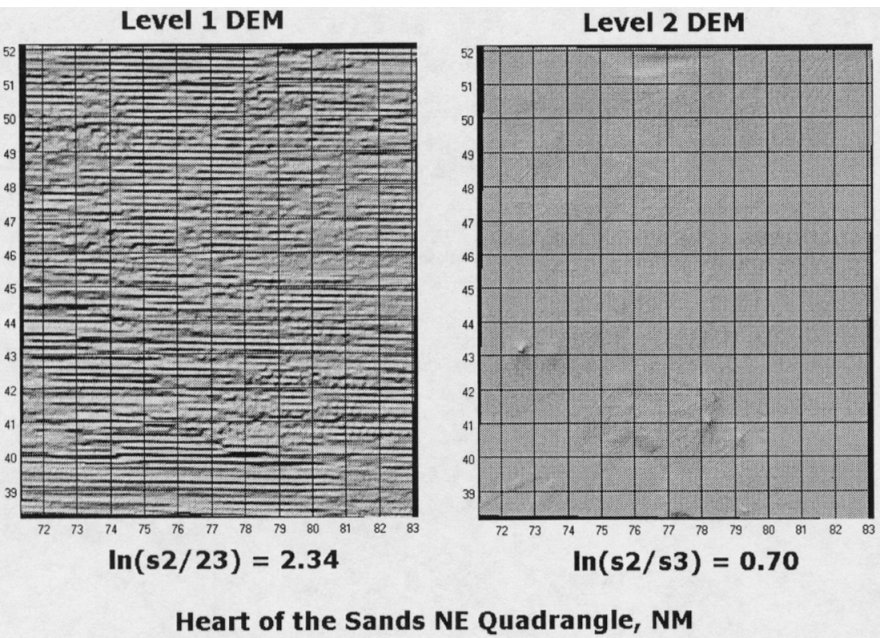


Fig. 10. Shaded reflectance maps of Level 1 and Level 2 DEMs of the same quadrangle in New Mexico.

One reason for the scatter in this comparison is the wide range in quality of the level 1 DEMs. Figure 10 shows the level 1 and level 2 DEMs for a very flat region, and the Level 1 DEM is one of the worst examples available. Its calculated organization parameter would rank it as one of the most organized in the country, but as the Level 2 DEM shows, the organization is entirely an artefact of the DEM creation process.

6. Average slope at different DEM scales

As has been determined in previous studies, computed slope increases as the

Table 6. Comparison of average slope from different scale DEMs.

Small Scale DEM and Tile Size	Sample Size	Slope Ratio to Large Scale DEM
GLOBE Slope (1° tiles)	n=941	78% 250K slope
250K Slope (7½' tiles)	n=51,345	86% 24K Slope
24K level 1 Slope (7½' tiles)	n=6476	85% 24K Level 2 slope
24K (30 m) level 2 Slope (7½' tiles)	n=472	100% 24K (10 m) level 2 Slope

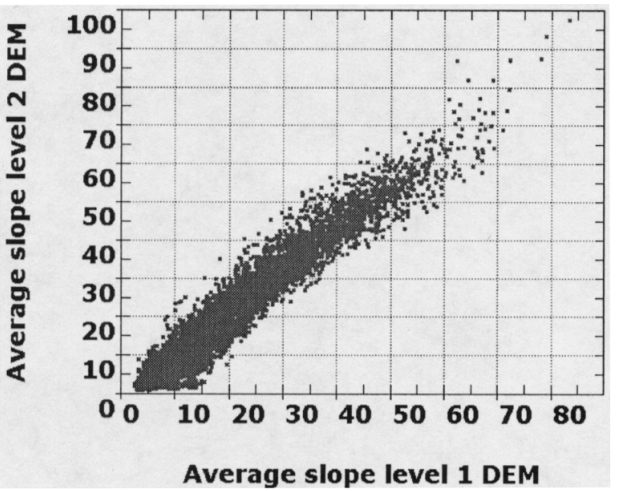


Fig. 11. Comparison of the average slope (steepest adjacent neighbor method) for 6226 30 m DEMs with both Level 1 and level 2 coverage.

size of the sampling region decreases. This study quantifies that relationship, using large samples of real DEMs. Table 6 shows the relationship observed, and Fig. 11 shows the relationship between independent level 1 and level 2 DEMs of the same quadrangle. Much of the scatter is likely due to a minority of very poor quality Level 1 DEMs (such as that in Fig. 10). The only surprise was that 10 m and 30 m DEMs produced identical average slopes.

7. DEM quality control

First attempts to create bivariate plots of geomorphic parameters from the USGS 24K DEMs led to the recognition that (1) overedge and extremely flat DEMs produced Door statistics, and (2) most outliers on the plots represent problems in the source DEMs. This problem was severe enough that a "BAD_DEM" field was added to the database, and a quick way to flag these DEMs was incorporated into MICRODEM. Figure 10 shows one particularly bad DEM, identified with striping (Oimoen, 2000) when it was visually inspected as a candidate for the most organized DEM in the United States.

Table 7. "Bad" 24K DEMs by series.

DEM Series	Number Available	Number "Bad"	Percent "Bad"
Level 1, 30 m	19,444	256	1.31%
Level 2, 30 m	30,835	68	0.22%
Level 2, 10 m	1066	6	0.56%

Average quadrangle slope initially revealed the most defective DEMs, because the bad elevations are usually so much larger than the others that they affect the average. Figure 1 shows the strong relationship between average quadrangle slope and the flatness parameter. After first flagging flat and overedge DEMs, a number of outliers remained. These had a higher average slope than their flatness parameter would indicate. Clicking the point on the graph brings up the database table for that record, and a click there opens the DEM. When visual analysis confirms that the DEM is defective, it can be flagged and ignored for further analysis. This pair of variables works because bad values affect the arithmetic mean used for average slope more than they affect the vector average used for the flatness parameter.

The following errors have been identified: (1) large rectangular regions of the DEM with uniform, erroneous elevations (probably a flag representing regions of no data, appropriate to processing software but not to the SDTS DEM profile); (2) a single partial row or column of bad elevations along one margin of the DEM (often one or two bad postings); (3) a single spike elevation, in some cases where a posting in feet was inserted into a DEM in meters; (4) snaking "lines" of bad elevations within the DEM; (5) DEMs mislabeled as feet or meters instead of the correct value, which show up in regional maps of average elevation where they are either three times or one third the elevation of their neighbors; (6) lakes with a uniform elevation that does not match the surroundings, or the height on the topographic map. The striping artefacts in some level 1 DEMs (Oimoen, 2000) are not included, because I have not been able to automate their identification, and assessing their severity remains a very subjective process.

At present at least 330 of the 51,345 DEMs downloaded from the USGS have been flagged as defective; this is a minimum estimate because only the most obvious statistical outliers have been examined visually to confirm the DEM quality. After redownloading a sample of these, it is clear the files posted on the web were defective and not the download process. With compressed downloads, a faulty download is more likely to produce a file that will not decompress rather than one with erroneous elevations. Table 7 suggests that over 1% of the Level 1 DEMs have errors, and that for Level 2 DEMs the error rate has decreased. This analysis may not reflect the current status of the USGS data because (1) the USGS performed a major reprocessing effort in the summer of 2001 to correct registration problems with some DEMs, (2) increasing numbers of 10 m DEMs are now available, and (3) it is not currently feasible to duplicate collection of the 50,000 DEM data set.

Maximum point slope is probably the single best parameter for flagging bad DEMs. While a few DEMs have valid huge point slopes, like the volcanic neck at Ship Rock, New Mexico (slope 1561%) or the cliff face of Half Dome in Yosemite National Park (slope 1553%), excessive point slope values over 1000% almost always represent bad postings in the DEM (at least 291 of 364 bad DEMs in this sample). While many of the errors in these DEMs are not severe and would not significantly affect most uses of the DEM, they could be eliminated with a simple quality control step. The DEM should be displayed as a shaded reflectance map, the location of the steepest point slope flagged, and the elevations of the postings surrounding the point displayed. The maximum slope could be compared to the distribution of maximum slope with the Fenneman province, and if the maximum slope in the DEM occurs in a pit, the point almost certainly represents an error. The DEM could then be accepted, or additional edits performed. While this sample was downloaded in the summer of 2000, some of the bad DEMs are still present on the commercial servers now distributing the USGS data. Osborn and others (2001) describe the challenges faced by USGS in developing quality control methods for the DEMs.

CONCLUSIONS

- Different slope algorithms behave differently depending on the physiographic province. Most of the difference between the steepest adjacent neighbor algorithm and the four nearest neighbors algorithms is not due to the small number of peaks, ridges, and valleys, which can have huge differences, but to the vast majority of points which cannot easily be categorized over a nine point region.
- Aspect algorithms do not work well in low relief regions, producing too many aspects at 45° intervals. They never work well at very low slopes, and the steepness at which they begin to produce uniform results appears to be related to the ratio of vertical resolution to horizontal resolution in the DEM.
- Different scales of DEMs accurately capture average elevation, which correlates very strongly across scales.
- Different scales of DEMs accurately capture average slope, which correlates very strongly across scales. The absolute value of average slope increases as the resolution of the DEM increases (post spacing decreases), although there appears to be no change between data spacings of 10 and 30 m.
- Different scales of DEMs accurately capture terrain organization, both in orientation and magnitude. The correlation is weakest in low slope regions, probably because of problems with the aspect algorithms, and is strongest in moderate to high relief areas.
- Geomorphic parameters can provide quality control for DEMs. Experience with the USGS DEMs suggests that a simple maximum point slope check should be performed on all DEMs, with excessive values over 1000% almost always representing bad postings in the DEM. This procedure should be implemented in the DEM production process.

Acknowledgements—I thank Richard Pike for his roles in organizing the Tokyo symposium, inviting me to attend, and generally encouraging me to pursue this work. The openness of U.S. government mapping agencies in sharing digital data on the web made this work possible, because without huge samples of free data this analysis would not have been possible.

REFERENCES

Chapman, C. A. (1952) A new quantitative method of topographic analysis: *American Journal of Science*, **250**, 428–452.

Evans, I. S. (1998) What do terrain statistics really mean?: In S. N. Lane, K. S. Richards and J. H. Chandler (eds.), *Landform Monitoring, Modelling and Analysis*, Ch. 6, pp. 119–138. J. Wiley, Chichester.

Fenneman, N. M. and Johnson, D. W. (1946) Physical divisions of the United States: United States Geological Survey, Map, Scale 1:7,000,000.

Gesch, D. B., Oimoen, M., Greenlee, S., Nelson, C., Steuck, M. and Tyler, D. (2002) The national elevation dataset: *Photogrammetric Engineering & Remote Sensing*, **68**, 5–11.

Guth, P. L. (1995) Slope and aspect calculations on gridded digital elevation models: Examples from a geomorphometric toolbox for personal computers: *Zeitschrift für Geomorphologie N.F.*, Supplementband, **101**, 31–52.

Guth, P. L. (1999a) Quantifying topographic fabric: eigenvector analysis using digital elevation models: In R. J. Merisko (ed.), *27th Applied Imagery Pattern Recognition (AIPR) Workshop: Advances in Computer-Assisted Recognition*, 14–16 Oct. 1988, Washington, D.C., *Proceedings of SPIE [The International Society for Optical Engineering]*, Vol. 3584, pp. 233–243.

Guth, P. L. (1999b) Quantifying and visualizing terrain fabric from digital elevation models: In J. Diaz, R. Tynes, D. Caldwell and J. Ehlen (eds.), *Geocomputation 99: Proceedings of the 4th International Conference on GeoComputation, Fredericksburg, Virginia, USA, 25–28 July, 1999*, CD-ROM ISBN 0-9533477-1-0. Available online at http://www.geovista.psu.edu/geocomp/geocomp99/index.htm

Guth, P. L. (1999c) Contour line "ghosts" in USGS Level 2 DEMs: *Photogrammetric Engineering & Remote Sensing*, **65**, 289–296.

Guth, P. L. (2001) Quantifying terrain fabric in digital elevation models: In J. Ehlen and R. S. Harmon (eds.), *The Environmental Legacy of Military Operations*, **14**, Chapter 3. Geological Society of America Reviews in Engineering Geology.

Guth, P. L., Ressler, E. K. and Bacastow, T. S. (1987) Microcomputer program for manipulating large digital terrain models: *Computers & Geosciences*, **13**, 209–213.

Hitt, K. J. (2002) Metadata for physical divisions of the United States, digital version of Fenneman map: http://water.usgs.gov/GIS/metadata/usgswrd/physio.html

Hodgson, M. E. (1998) Comparison of angles from surface slope/aspect algorithms: *Cartography and Geographic Information Systems*, **25**, 173–185.

Jet Propulsion Laboratory (2001) Shuttle Radar Topography Mission: http://www.jpl.nasa.gov/srtm/ (last update on page listed as 12/6/2001, accessed 1/3/2002).

Jones, K. H. (1998) A comparison of algorithms used to compute hill slope as a property of the DEM: *Computers & Geosciences*, **24**, 315–324.

NIMA (2000) Geospatial Engine: http://164.214.2.59/geospatial/digital_products.htm (last update on page listed as 12/14/2000, accessed 12/22/2001).

NOAA Coastal Services Data Center (2001) Topographic change mapping: http://www.csc.noaa.gov/crs/tcm/index.html (last update on page listed as 12/14/2000, accessed 12/22/2001).

NOAA National Geophysical Data Center (2001) The Global Land One-km Base Elevation (GLOBE) Project: Get GLOBE Data: http://www.ngdc.noaa.gov/seg/topo/globeget.shtml (last update on page listed as 2/27/2001, accessed 12/22/2001).

Oimoen, M. J. (2000) An effective filter for removal of production artifacts in U.S. Geological Survey 7.5-minute digital elevation models: *Proceedings of the 14th International Conference, Applied Geologic Remote Sensing, 6–8 November 2000, Las Vegas, Nevada*, pp. 311–319.

Osborn, K., List, J., Gesch, D., Crowe, J., Merrill, G., Constance, E., Mauck, J., Lund, C., Caruso, V. and Kosovich, J. (2001) National digital elevation program (NDEP): In D. F. Maune (ed.), *Digital Elevation Model Technologies and Applications: The DEM Users Manual*, pp. 83–120. American Society for Photogrammetry and Remote Sensing, Bethesda, MD.

Pike, R. J. (1988) The geometric signature: quantifying landslide-terrain types from digital elevation models: *Mathematical Geology*, **20**, 491–512.

Pike, R. J. (2001) Geometric signatures-experimental design, first results: In H. Ohmori (ed.), *DEMs and Geomorphometry, Special Publications of the Geographic Information Systems Association, Proceedings of the symposia on New Concepts and Modeling in Geomorphology and Geomorphometry, DEMs and GIS, held 24–26 August, 2001, Tokyo, Fifth International Conference on Geomorphology*, **1**, pp. 50–51.

Skidmore, A. K. (1989) A comparison of techniques for calculating gradient and aspect from a gridded digital elevation model: *International Journal of Geographical Information Systems*, **3**, 323–334.

USGS EROS Data Center (2001) GTOPO30, Global Topographic Data: http://edcdaac.usgs.gov/gtopo30/gtopo30.html (last update on page listed as 7/19/2001, accessed 12/22/2001).

USGS (2001) USGS Geographic Data Download: http://edcwww.cr.usgs.gov/doc/edchome/ndcdb/ndcdb.html (last update on page listed as 10/29/2001, accessed 12/22/2001).

USGS National Mapping Division (1997/1998) Standards for digital elevation models: http://rockyweb.cr.usgs.gov/nmpstds/demstds.html

Woodcock, N. H. (1977) Specification of fabric shapes using an eigenvalue method: *Geological Society of America Bulletin*, **88**, 1231–1236.

Concepts and Modelling in Geomorphology: International Perspectives,
Eds. I. S. Evans, R. Dikau, E. Tokunaga, H. Ohmori and M. Hirano, pp. 221–237.
© by TERRAPUB, Tokyo, 2003.

Multiresolution Spline Models and Their Applications in Geomorphology

Jan Rasmus SULEBAK and Øyvind HJELLE

SINTEF Applied Mathematics, P.O. Box 124, Blindern, N-0314 Oslo, Norway
e-mail: Jan.R.Sulebak@sintef.no

Abstract. Digital terrain models are valuable tools for studying landforms on computers. Since a landscape consists of a mix of landforms at many scales, an analysis of all these landforms using a terrain model at constant resolution is not appropriate. To fully model and analyse the complexity of the landscape a multiresolution approach for terrain modelling should be emphasised. During the last decades, different mathematical methods for building data structures for multiresolution terrain models have been developed. Most of them are, however, based on triangulations and optimised for real-time visualisation and are less suitable for digital terrain analysis and landscape studies. In this paper we use spline based techniques to effectively build multiresolution terrain models that are more appropriate for terrain analysis. These methods can handle millions of data points over huge areas as input and create a hierarchy of spline surfaces at different levels of resolution as output. The surfaces can easily be evaluated at different scales for terrain analysis in GIS applications.

Keywords: Multiresolution, Terrain Modelling, Splines, Terrain Analysis, Geomorphology

INTRODUCTION

When modern aerial photography and satellite remote sensing started to provide continuos surface information by means of optical cameras, radar or laser beams, and the derivation of terrain elevation was made possible by stereoscopy and interferometry, topography gained a whole new meaning in spatial studies. Of special interest are how different scales of topography influence ongoing processes and how different processes result in landforms of different space-scale characteristics. The topography consists of a mix of landforms at different time and space scales. Their existence is the result of the ongoing work of a variety of geological as well as geomorphological processes (hydrological, glacial, periglacial). To fully investigate the process-form relationships among landforms at varying scale, multiresolution terrain models could be a valuable tool. If so, an absolute requirement to such models is that they are based on a data structure which in a flexible and effective manner makes it possible to extract and evaluate surface models at varying resolution to produce topographic parameters (e.g. slope, aspect, plan curvature and profile curvature). Based on such parameters, a classification process (relief classification) can be carried out to produce

combinations of topographic parameters that define topographic regions (relief units) (Dikau, 1989; Sulebak *et al*., 1997). These relief units can represent the dominance of certain surface processes during a specific time period resulting in landforms identified at a specific scale. The latter is important due to the growing recognition that process rates themselves may be better estimated from observation of morphological change, particularly if measurement of process rate is difficult to achieve at relevant space and time scales (Lane *et al*., 1995; Ashmore and Church, 1998). The close relationship between a range of hydrological processes and the morphometry of the land surface has made topographic parameters and indices a useful tool in modelling the spatial variation of, i.e., soil water content, evaporation, soil erosion and land slides (Beven and Kirkby, 1979; Moore *et al*., 1991).

Today, elevation information is represented on computers as elevation data in a digital format. This format is usually called digital elevation models (DEM). Thus, a DEM is a computerised representation of the Earth's relief. Different formats exist, among the most commonly used are triangulated irregular networks (TIN), regular grids, contour lines and scattered data points. A DEM is usually described either by a wire frame model or an image matrix in which the value of each pixel is associated with a specific topographic height. These models represent the terrain at a fixed resolution and their capability for effective analysis of landscapes at different scales is therefore limited.

The main objective of this paper is to present (briefly) the theory behind B-spline surfaces in general, and to show how a hierarchy of B-spline surfaces constituting a multiresolution model can be calculated from scattered measurement data and used in topographical analysis. The topographic parameters slope, profile curvature and planform curvature can easily be calculated at any point in the terrain by evaluating the mathematical spline model of the terrain. The advantage of the multi-resolution approach is that the topographic parameters can be more easily analysed at different resolutions. This can give valuable insight into the relationships between data density and the calculated topographic attributes and how this further can be linked to the morphometry of the landscape and presence of specific landform types. The results may give valuable information when analysing both the more general surface and relief characteristics of a landscape and the more underlying complex process-form relationship in an area. For example, assuming that a general flattening of the landscape occurs due to the presence of erosional processes, the multi-resolution terrain model can be used as a model of the overall landscape development in an area through time.

THE STUDY AREA AND TEST DATA

The spline algorithms are tested on scattered elevation data sampled from a mountainous area in Norway called Jotunheimen. Jotunheimen is situated in the centre of South-Norway (Fig. 1). Most of the terrain in Jotunheimen is shaped by glaciers thousands of years ago. This means that most of the terrain consists of valleys where the elevation is between 800–1400 meters, steep hillsides and peaks where the elevation is 2000–2500 meters above sea level. All the highest

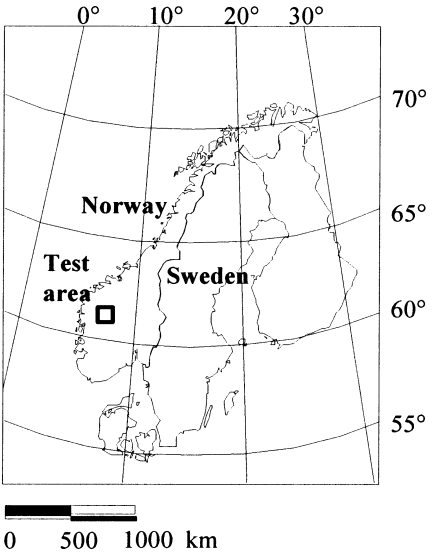


Fig. 1. The location of the test area in Jotunheimen.

peaks in Norway are in Jotunheimen. The highest is Galdhøpiggen at 2469 meters. The geomorphological processes dominating this area are mainly due to hydrological, glacial and periclacial processes and mass movement due to debris-flow, rock falls and avalanches. The data set covers an area of 625 km^2 and is sampled and structured in a regular 250 × 250 grid with 100 meter spacing (635,000 data points). Note that the algorithms presented in the following also accept input data that are randomly distributed.

THEORY AND METHODS

1. Spline surfaces defined on regular grids

A B-spline surface representing a terrain over a rectangular domain Ω in the plane can be defined by a regular grid of coefficients $\Phi = \{\phi_{kl}\}_{k,l=1}^{m,n}$ overlaid on Ω. Each coefficient ϕ_{kl} associated with a grid point (k, l), is a real value that must be determined, e.g. by least squares approximation as outlined in the next section. We also say that each ϕ_{kl} has a position (x_k, y_l) in Ω. The coefficient grid is similar to an ordinary digital elevation model (DEM), but the coefficients of a B-spline surface are not necessarily points that lie in the terrain surface. More specifically, a *bi-cubic* B-spline surface, which is used in our implementation, can be described by the function,

$$f(x,y) = \sum_{q=0}^{3}\sum_{r=0}^{3} M_{qr}(s,t)\phi_{(k+q,l+r)} \qquad (1)$$

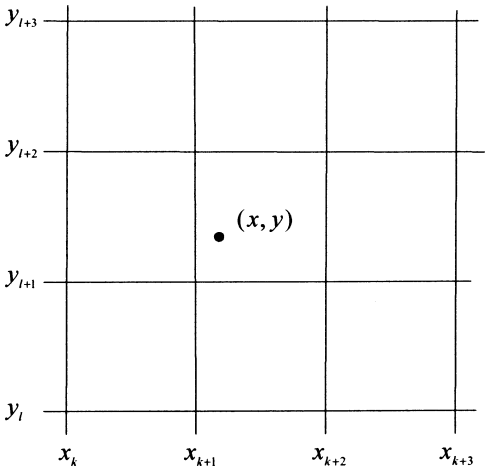


Fig. 2. The (4×4)-neighbourhood of grid points around a point (x, y).

where the sixteen $M_{qr}(s, t)$ are smooth (piecewise) polynomial basis functions, and $(k + 1, l + 1)$ is the lower left corner of the grid cell containing (x, y). Moreover, $s = x - x_k + 1$ and $t = y - y_l + 1$, where (x_{k+1}, y_{l+1}) is the coordinate associated with the grid point $(k + 1, l + 1)$; see Fig. 2. Thus, the function value $f(x, y)$, or the altitude of the terrain in position (x, y), depends only on a (4×4)-neighbourhood of coefficients in Φ.

Let us assume without loss of generality that the grid spacing in x and y-direction is of unit length. Then s and t are in the interval $[0, 1)$. The *bi-cubic* basis functions in Eq. (1) are defined as products of univariate cubic polynomials as follows:

$$M_{qr}(s, t) = B_q(s)B_r(t), \quad q, r = 0, 1, 2, 3$$

where

$$B_0(s) = (1 - s)^3/6$$

$$B_1(s) = (3s^3 - 6s^2 + 4)/6$$

$$B_2(s) = (-3s^3 + 3s^2 + 3s + 1)/6$$

$$B_3(s) = s^3/6$$

Since B_0, B_1, B_2 and B_3 are smooth polynomial functions, M_{qr} is also smooth, and the linear combination in Eq. (1) is smooth such that f models the terrain as a smooth surface.

B-splines are "standard" for representing curves and surfaces in visualization and applications such as CAD (Computer Aided Design). A nice guide to B-splines can be found in Farin (1997).

2. Spline surfaces from scattered data

Given a set of scattered data $P = \{(x_i, y_i, z_i),\ i = 1, ..., N\}$, we seek a B-spline surface f that is an approximation to P. Loosely speaking, we say that f approximates P if $f(x_i, y_i) \approx z_i$, $i = 1, ..., N$. In the following we explore two schemes for calculating a B-spline surface from a set of scattered data; a CPU extensive global scheme and a fast local scheme.

2.1 Method of least squares with smoothing

We may choose an approximation to the scattered data in the *least squares* sense and seek coefficients $\Phi = \{\phi_{kl}\}_{k,l=1}^{m,n}$ in Eq. (1) such that the function f minimises the sum of squared errors, $\sum_{i=1}^{N} (f(x_i, y_i) - z_i)^2$. Clearly, if this sum is small and $\max_{(i = 1, ..., N)} |f(x_i, y_i) - z_i|$ is small, then the deviation of f from the points P is small. In particular, if the sum is zero then f interpolates the data, that is, $f(x_i, y_i) = z_i$, $i = 1, ..., N$.

It can be shown that the equation system that arises from this least squares problem does not have a unique solution in general (Golitschek and Schumaker, 1990). There are also other reasons why this basic least squares method is not appropriate. The data may contain noise and outliers in which case the surface will be attracted towards the outliers and cause anomalies and visual artefacts. The most common method to deal with lack of uniqueness and noisy data is to augment the sum of squared errors by one or more smoothing terms. In our implementation we have chosen an energy term that involves second order partial derivatives of f such that the functional to be minimised takes the form

$$F(\Phi) = \sum_{i=1}^{N} \left(f(x_i, y_i) - z_i \right)^2 + \alpha \iint_{\Omega} \left[f_{xx}^2 + 2 f_{xy}^2 + f_{yy}^2 \right] dxdy \qquad (2)$$

where Ω is the rectangular domain where f is defined (the xy-area of the terrain surface), and α is a real positive value that determines the degree of smoothness of the surface f. The smoothing term in Eq. (2) is known as the *thin plate spline energy*.

A minimum of $F(\Phi)$ occurs where all the partial derivatives $\partial F / \partial \phi_{kl}$ are zero. This gives rise to an equation system with mn equations in mn unknown coefficients,

$$(\mathbf{B}^T\mathbf{B} + \alpha\mathbf{E})\Phi = \mathbf{B}^T\mathbf{z} \qquad (3)$$

Here $\mathbf{B}$ is a sparse $N \times (mn)$ matrix with elements constructed from the positions $\{(x_i, y_i)\}$ of the input points, $\mathbf{z} = (z_1, ..., z_N)^T$, and $\mathbf{E}$ is an $(mn) \times (mn)$ matrix that originates from the smoothing term and involves first and second order partial

derivatives of the basis functions $\{M_{qr}\}$. Note that since we use bi-cubic basis functions that are twice differentiable, the partial derivatives are well defined such that divided differences are not required for the smoothing term. The unknown coefficients $\Phi = \{\phi_{kl}\}_{k,l=1}^{m,n}$ are now interpreted as a vector, $\Phi = (\phi_{1,1}, \phi_{2,1}, ..., \phi_{m,1}, \phi_{1,2}, ..., \phi_{m,n})^T$. The interested reader is referred to Golitschek and Schumaker (1990) and Floater (1998) for more details and hints on implementation.

If the underlying grid of coefficients is large, for example, if $m = n = 1000$, then Eq. (3) is a system with one million equations in one million unknowns. This requires a fast equation solver. Since the system matrix $(\mathbf{B}^T\mathbf{B} + \alpha\mathbf{E})$ is sparse, symmetric and positive definite, an iterative solver like the conjugate gradient method would be a natural choice (Hestenes and Stiefel, 1952). But due to an extremely ill-conditioned system matrix*, we found that even the conjugate gradient method was far too slow in most cases when Φ was large. We implemented a scheme based on the *full multigrid method* (Briggs *et al.*, 2000) to overcome these numerical challenges. This proved to be extremely fast compared to the conjugate gradient method. In the current implementation the memory usage limits the size of the system that can be solved in reasonable time. Note that the size of the equation system does not depend on number of scattered data points.

2.2 Local methods

There are other methods for calculating a B-spline surface f from a set of scattered data P that are much faster than that of the (global) least squares method above. While the least squares method solves a large equation system for finding the unknown coefficients, there are local schemes that determine each spline coefficient ϕ_{kl} of Φ locally from only those points of P that are in a neighbourhood of the grid position (x_k, y_l) of ϕ_{kl}. In (Lee *et al.*, 1997) they use a local scheme founded on the following basic idea that we describe by a pseudocode.

Algorithm 1

1. *For each point $p_i = (x_i, y_i, z_i)$ in P*
2. *Calculate the contribution from p_i to (4×4) coefficients of Φ in a neighbourhood around p_i*
3. *For each coefficient ϕ_{kl} in Φ*
4. *Compromise between the contributions from the different points in P where the local neighbourhoods overlap*

The reason why a point p_i only contributes to a (4×4)-neighbourhood of coefficients is that this is exactly the coefficients that determine the function value $f(x_i, y_i)$, where (x_i, y_i) is the position of p_i (see Section 1). Figure 3 shows two (4×4)-neighbourhoods of coefficients associated with two points p_1 and p_2 where the neighbourhoods overlap. We see that six of the coefficients receive

*An ill-conditioned matrix $\boldsymbol{A}$ is one where the solution to the equation system $Ax = b$ is sensitive to pertubations in A and b. The consequence is that iterative equation solvers like the conjugate gradient method will converge very slowly. In our particular problem the convergence rate also depends heavily on the distribution of the data $P = \{(x_i, y_i, z_i)\}$.

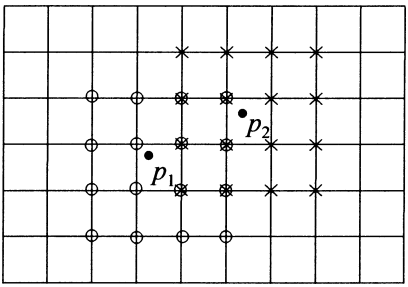


Fig. 3. Two overlapping (4×4)-neighbourhoods of B-spline coefficients for two points p_1 and p_2.

contribution from both p_1 and p_2. There are many ways of implementing Step 2 and 3 above. Some choices based on minimizing local approximation errors can be found in Lee *et al*. (1997) and Hjelle (2001). It is easy to see that the time complexity of Algorithm 1 is $O(N + mn)$. Thus, it is linear both in the number of scattered data N and in the number of coefficients mn of the coefficient grid Φ.

Several notes are in order. Regardless of the actual implementation of Step 2 and 4 of the algorithm, the local calculation of a coefficient ϕ_{kl} heavily relies on the distribution of the scattered data, and in particular on the number of points with a (4×4)-neighbourhood that contain ϕ_{kl}. For example, if the (4×4)-neighbourhood of a point p_i does not overlap with other neighbourhoods, then ϕ_{kl} is calculated from p_i only and it would be natural to require exact interpolation of p_i. But, if p_i is an outlier, then the surface would get an artificial extreme value at p_i. In particular, suppose that a coefficient ϕ_{kl} does not belong to any (4×4)-neighbourhood of points in P. Then there is no obvious choice of how to determine ϕ_{kl}, though a value based on the average of all points in P may be used, or if the z_i's of P are overall small, then zero may be assigned.

If a grid of coefficients Φ_0 is suffciently coarse and the points in P are evenly distributed in the domain, the problems stated above will be less severe since many points from P contribute to each coefficient in Φ_0 and Algorithm 1 produces a surface f_0 that is smooth. On the other hand, the differences $z_i - f_0(x_i, y_i)$ at the data points in P might be unacceptably large when Φ_0 is coarse. In the multiresolution model presented in the sequel, we model the differences $\{(x_i, y_i, z_i - f_0(x_i, y_i))\}$ as a new B-spline surface f_1 on a finer grid Φ_1 that can be added to f_0, and thus obtain a surface $f_0 + f_1$ that is more accurate than f_0. This is done repeatedly for finer and finer grids until the desired accuracy is reached by a sequence $f_0 + f_1 + \cdots + f_h$.

3. The multiresolution model

The multiresolution model is defined as a sequence of grids over uniform partitions such that a B-spline surface f representing a terrain is defined as a sum of B-spline surfaces,

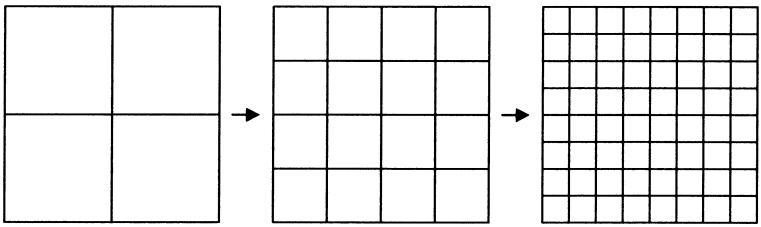


Fig. 4. The first three levels, Φ_0, Φ_1 and Φ_2 in the hierarchy of B-spline coefficient grids in the multiresolution model.

$$f(x, y) = f_0(x, y) + f_1(x, y) + \cdots + f_h(x, y) \tag{4}$$

Each f_j on the form of Eq. (1) is defined over a grid Φ_j for $j = 0, ..., h$, where each Φ_j is uniform, or regular, in the sense that the grid spacing is constant in each direction (as for a digital elevation model). Moreover, the surfaces f_j are defined at dyadic scales in the sense that they constitute a hierarchy where a grid Φ_k at a level k in the hierarchy is obtained by inserting grid lines halfway between the grid lines of Φ_{k-1} at the previous level $(k-1)$. Figure 4 shows an example of grids Φ_0, Φ_1 and Φ_2 at the first three levels of the hierarchy.

A common scheme for calculating the multiresolution model in Eq. (4) from a set of scattered data $P = \{(x_i, y_i, z_i)\}$ is as follows. First the coarse grid Φ_0 of B-spline coefficients are calculated from P such that f_0, which is defined on Φ_0, is a smooth surface, possibly with low accuracy with respect to P. For example, f_0 may be calculated by the equation system in Eq. (3), or f_0 may be calculated by the local scheme in Algorithm 1. Since Φ_0 is a coarse grid, f_0 possibly leaves large discrepancies at the data points in P. Let $P_1 = \{(x_i, y_i, z_i^1)\}$ be a new data set, now with z-values as the deviations between f_0 and the data points in P, $z_i^1 = z_i - f_0(x_i, y_i)$. The surface f_1 in Eq. (4) with coefficients Φ_1 is calculated from P_1 and is thus an approximation to the deviations that f_0 leaves at the data points. Since Φ_1 is a finer grid than Φ_0, the surface $g_1 = f_0 + f_1$ leaves a smaller deviation $z_i - f_0(x_i, y_i) - f_1(x_i, y_i)$ at each data point and is thus a better approximation to P than f_0 is.

In general, for each level k in the hierarchy, the point set $P_k = \{(x_i, y_i, z_i^k)\}$ is approximated by a function f_k defined by the coefficient grid Φ_k, where $z_i^k = z_i - \sum_{j=1}^{k-1} f_j(x_i, y_i) = z_i^{k-1} - f_{k-1}(x_i, y_i)$, and $z_i^0 = z_i$. As more levels are included in the hierarchy, the approximation errors z_i^k of the function $g_k = f_0 + \cdots + f_k$ get smaller and smaller. Finally we get the approximation $f = g_h$ in Eq. (4) defined by the sequence of grids Φ_j, $j = 0, ..., h$.

If we keep the representation of f on the form of Eq. (4), we have a *level of detail* (LOD) model where, for a given k, we have a surface $g_k = f_0 + \cdots + f_k$ at detail level k. This can also be defined as the *smoothing level* k since adding a term f_{k+1} adds details (or high frequencies) to the surface f_k and makes it less smooth. Although the surface $g_{k+1} = f_0 + \cdots + f_{k+1}$ is a better approximation to P than g_k,

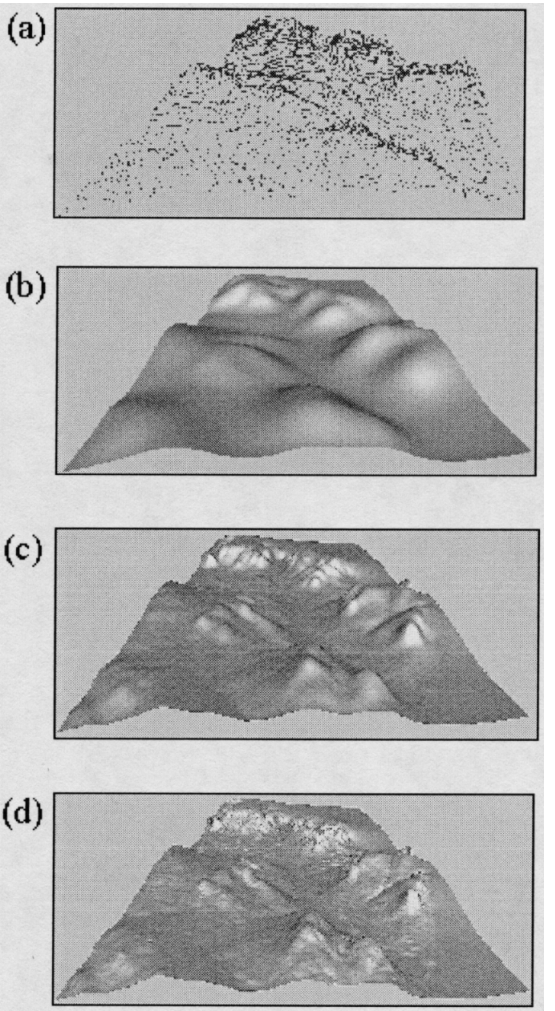


Fig. 5. Contour data of a terrain model in (a), and B-spline surfaces at three different levels of resolution in (b), (c) and (d).

it is less smooth, and using g_k instead g_{k+1} may be preferred in many cases when calculating slopes and curvatures in terrain analysis. We will return to this later. Figures 5(b), (c) and (d) show surfaces of the LOD model at three different levels of resolution. The surfaces were generated from the contour data shown in Fig. 5(a).

There is another important aspect of the LOD model concerning data compression. Since the differences z_i^k get smaller and smaller with increasing k, the coefficients of Φ_k also get smaller. If we assign zero to those coefficients of

Φ_k that are below a specified small threshold value, this will not change g_k or f much. Moreover, if the local scheme in Algorithm 1 is used, then one may assign zero to coefficients of Φ_k that do not belong to any (4×4)-neighbourhood of points in P_k. Thus, the number of zero-coefficients in Φ_k increases with increasing k. Instead of storing the Φ_k's as full matrices we store only the non-zero coefficients. The coefficients are stored compactly in linear arrays such that huge surfaces with, for example, (1 million) $\times$ (1 million) grid points at the finest level can be handled easily.

Evaluating altitude, slope or curvature of a terrain surface represented by Eq. (4), requires at least h times the CPU time for evaluating a surface in the standard B-spline format of Eq. (1). Thus, if the LOD capabilities are not needed and if the finest grid Φ_h is not too large, then it would be more appropriate to represent the surface as in Eq. (1) with one single grid of coefficients. There is a feature called B-spline refinement that transfers a grid Φ_k to a finer grid Φ_{k+1} such that the B-spline surface g_{k+1} defined by Φ_{k+1} represents exactly the same surface as g_k defined by Φ_k (Cohen *et al.*, 1980). Thus, by successive B-spline refinement the sum in Eq. (4) can be transferred to one single function on the standard form of Eq. (1).

Lastly, we mention that even in a multiresolution setting as presented here, the local scheme in Algorithm 1 may produce surfaces that have bumps and artefacts near noisy data and outliers. On the other hand, if the data are "clean" without noise, and if the data are suffciently dense and evenly distributed in the domain, the results from the local scheme is comparable to the results from the global least squares scheme. But in general, results from the (slow) least squares scheme is better than the (fast) local scheme.

4. Calculation of topographic parameters

B-spline surfaces defined by Eq. (1) are C^2-continuous when the basis functions are bi-cubic as used in our implementation. That is, the first and second order partial derivatives f_x, f_y, f_{xy}, f_{xx}, and f_{yy} are continuous and well defined everywhere where f is defined. These are the only partial derivatives used for calculating the topographic parameters slope, aspect, profile curvature and plan curvature (Zevenbergen and Thorne, 1987). For example, the profile curvature at any point (x, y) in the terrain surface is defined by

$$(\cos\theta, \sin\theta)\begin{pmatrix} f_{xx} & f_{xy} \\ f_{xy} & f_{yy} \end{pmatrix}(\cos\theta, \sin\theta)^T$$

where the partial derivatives are evaluated in (x, y) and θ is the aspect direction (direction of flow) in (x, y) defined by

$$\cos\theta = \frac{f_x}{\sqrt{f_x^2 + f_y^2}}, \quad \sin\theta = \frac{f_y}{\sqrt{f_x^2 + f_y^2}}$$

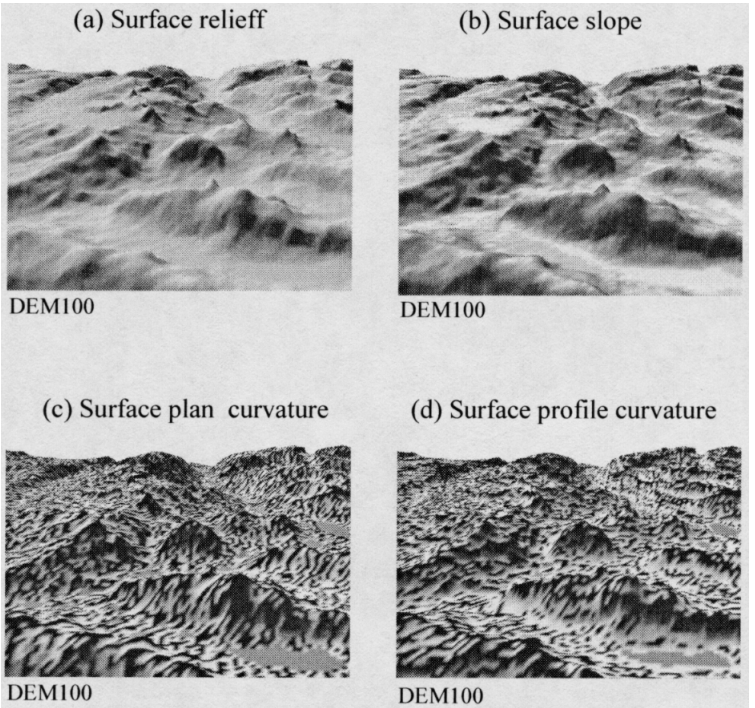


Fig. 6. (a): The relief surface based on a regular grid (DEM100), (b): the surface slope parameter overlaying the relief surface, (c): the plan curvature parameter overlaying the relief surface, and (d): the profile curvature parameter overlaying the relief surface. For the slope model, darker shade represents steeper areas while for the curvature models, black colour represents convex areas and white colour represents concave areas.

Contrary to the discrete approach in Zevenbergen and Thorne (1987) where a 3×3 submatrix of a digital elevation model is used to compute topographic parameters, we calculate these parameters at any point (x, y) in the terrain directly from the underlying mathematical definition of the terrain.

RESULTS

1. The software application

The spline algorithms has been implemented and a software application developed that was able to read scattered elevation data and create both regular grid elevation models (DEM) and spline models. The basic spline algorithms were implemented in a C++ library, while Java 3D was used to build the software application with 3D visualisation. Java 3D is based on the Open GL library and uses triangulations for visualising the surface models. The algorithms for computing the topographic parameters slope, profile curvature and plan curvature

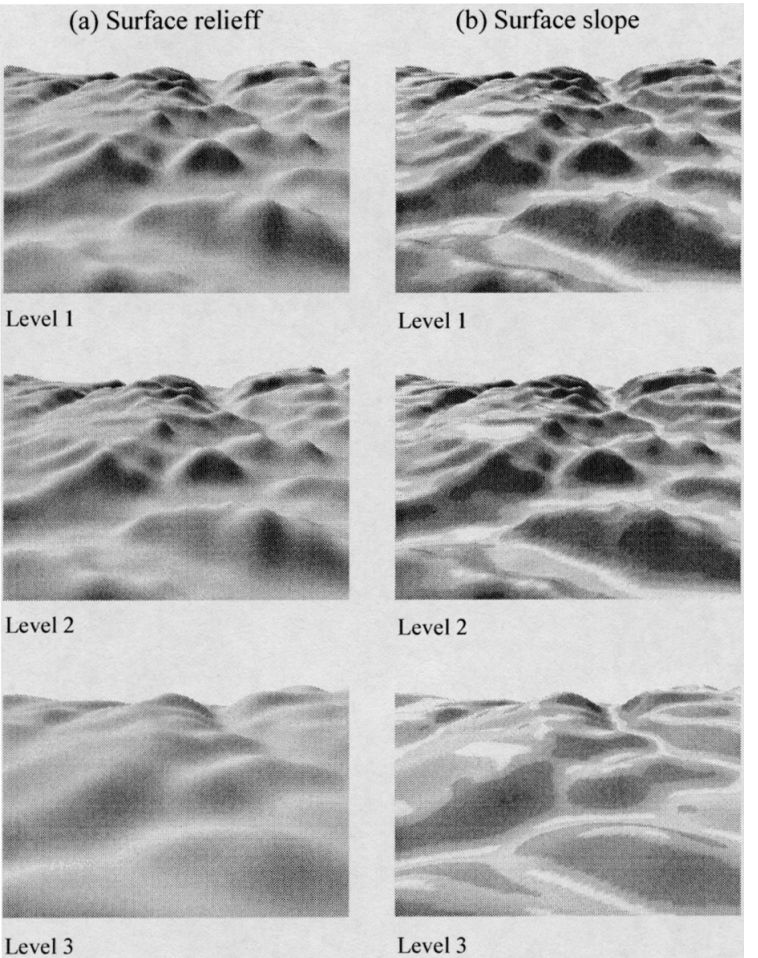


Fig. 7. (a): Relief surface based on a regular grid for the spline models (Level 1–Level 3), and (b): the surface slope parameter overlaying the relief surface. For the slope model, darker shade represents steeper areas.

were also implemented in Java. The parameters are visualised by overlaying the parameter grids on the 3D-relief model. The program was used to produce four different surface models based on the test data set that we denote “DEM100”, “Level 1”, “Level 2” and “Level 3”. DEM100 is a simple raster model based on a regular grid representation of the input elevation data, while Level 1–Level 3 represent different levels in the hierarchy of spline surfaces in the multiresolution spline model. The parameter h in Eq. (4) was 10, 8, and 6 for Level 1, Level 2 and Level 3 respectively.

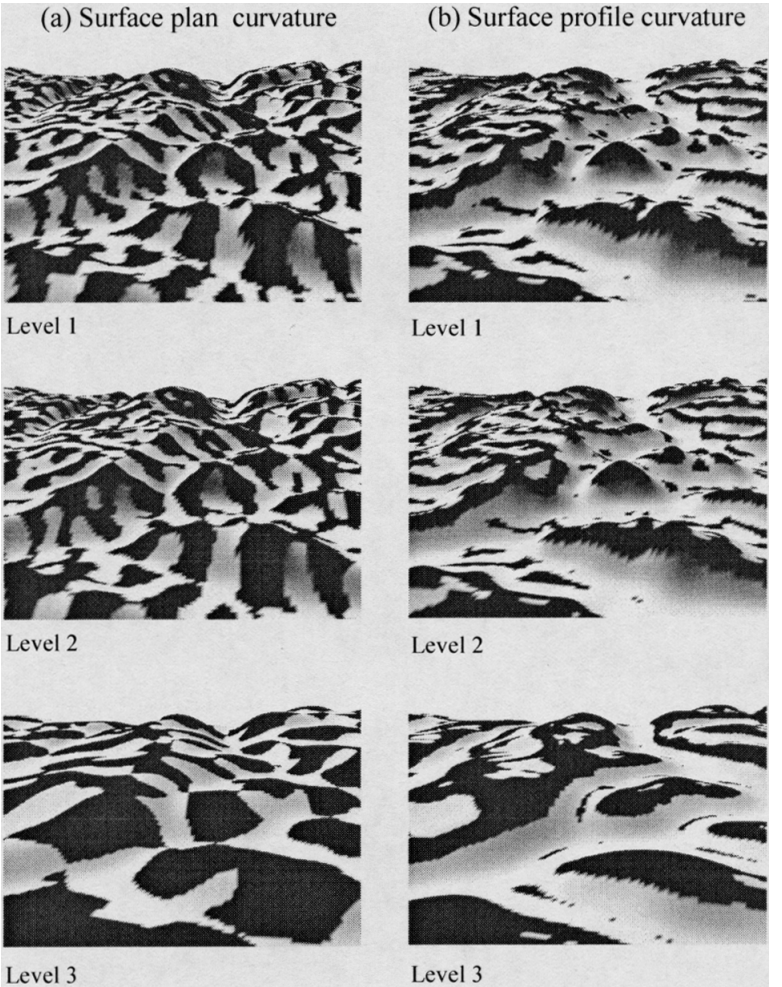


Fig. 8. (a): The plan curvature parameter overlaying the relief surface for Level 1–Level 3, and (d): the profile curvature parameter overlaying the relief surface. For the curvature models black colour represents convex areas while white colour represents concave areas.

2. *Calculated surface models and elevation statistics*

Figure 6(a) shows the resulting elevation model from the Jotunheimen area where the data is represented in a regular grid structure (DEM100), while Figs. 6(b)–(d) show the respective derived topographic parameters slope, plan curvature and profile curvature. Figure 7(a) presents the surface relief and the surface slope of Level 1 to Level 3, while the plan curvature and profile curvature are presented in Figs. 8(a) and (b). Table 1 shows the general elevation statistics of the four surface models.

Table 1. Calculated elevation statistics from the frequency distribution of elevation for the four surface models. The last column is the elevation-relief ratio E (Wood and Snell, 1960), a measure of the local relief, or vertical dispersion of elevation.

	Elevation statistics					
	Mean	*Std*	*Min*	*Max*	*Range*	*E*
DEM100	1520	289	520	2469	1949	0.51
Level 1	1521	292	543	2422	1879	0.52
Level 2	1521	293	554	2416	1862	0.52
Level 3	1521	277	661	2248	1587	0.54

Upon only a visual inspection of the surface relief models in Figs. 6(a) and 7(a), it seems that DEM100 better models the detailed relief including small-scale features of the landscape, and thus, it better visualises the alpine characteristics of the study area. Only minor differences exist between Level 1 and Level 2 in the surface relief model, while a greater difference can be observed between Level 2 and Level 3. This is reflected in elevation statistics calculated for each surface model (Table 1). The difference in the range value between Level 1 and Level 2 is 17 m, while the difference is 275 m between Level 2 and Level 3. The statistics reflect the overall smoothing of the land surface when reducing the h-parameter. Both the mean value and the range are reduced for Level 1–Level 3. An interesting observation is the constant value of the mean for the different surfaces. This indicates a more scale independent measure than the other statistical measures. From the slope surfaces in Fig. 7(b) most of the gradient values are below 30 degrees. With increasing smoothness the gradient is reduced. For Level 3 no gradient values exist above 10 degrees.

3. General relief properties and roughness

The term relief is usually used to describe the vertical dimension or amplitude of topography, while roughness refers to the irregularity of a topographic surface (Mark, 1975). According to Evans (1972), the standard deviation of elevation provides one of the most stable measures of the vertical variability of a topographic surface. From Table 1, both Level 1 and Level 2 show a higher standard deviation value than DEM100, and hence a surface with more relief. A second relief measure is the elevation-relief ratio E (Wood and Snell, 1960), where

$$E = \frac{\text{elevation mean} - \text{elevation min}}{\text{elevation max} - \text{elevation min}}$$

A higher E-value indicates a smoother surface. Thus, the lower value calculated for DEM100 (0.51) than for Level 1 (0.52) and Level 2 (0.52), indicates a more rugged surface for DEM100.

DISCUSSION

1. The general topographic characteristics of the surface models

The more realistic looking model provided by DEM100 (Fig. 6(a)) compared to the smoother spline models (Fig. 7(a)), can be explained by the general nature of B-splines. DEM100 is defined by a regular grid of input points while the spline models (Level 1–3) are smooth piecewise polynomial functions Eq. (1). This results in a model that flattens out the small-scale topographic irregularities of the surface. Also, a decrease of h from Level 1 to Level 3 is reflected by a surface including less detailed terrain information and emphasising landforms of larger scale. This smoothing effect can also be observed in Table 1 where the range of elevation decreases from Level 1 to Level 3.

2. Differences in the relief measures

The results showed differences between the DEM100 model and the spline models concerning the two relief measures, standard deviation of elevation and elevation-relief ratio (E). Based on the standard deviation measure, the spline surfaces Level 1 and Level 2 obtained higher values than DEM100 indicating a surface with more relief. This is surprising after the visual interpretation of the two models since DEM100 seems much less smooth then Level 1 and Level 2. However, E indicates that DEM100 has more local relief than Level 1 and Level 2, and this is more in accordance with our visual interpretation. The explanation may be that the standard deviation is more a measure of large-scale relief. This is more dependent on the domination of larger landforms emphasised by the spline algorithm, while the elevation-relief ratio shows the local relief that is better adopted with this measure.

3. Plan curvature versus profile curvature

Interesting differences can be observed when comparing the surface models with plan curvature and profile curvature in Figs. 8(a) and (b). For Level 1 in Fig. 8, the plan curvature identifies better topographic features located at the slopes, like talus cones and talus scars. These are landforms produced by the events of slope processes like debris flow, rock falls and avalanches. Such landforms have certain space scale characteristics and can therefore only be identified in a surface model of higher resolution. The same pattern can, however, be observed for Level 3 in Fig. 8(a), but this pattern probably indicates the presence of a different type of landform; a landform of larger scale, e.g., a glacier cirque or a hanging valley. When decreasing resolution and thus increasing smoothness, the profile curvature (Level 3) shows landforms at a larger scale like large U-shaped valley systems and rolling hills and ridges. That is, by decreasing the resolution of the spline model, the resulting surface model and calculated topographic parameters can be used to identify and emphasise landforms at a larger and broader scale. Landforms at this scale may be difficult to identify in surface models at higher resolution

since their interpretation is easily disturbed by small-scale landforms (DEM100 or Level 1).

4. Multiresolution terrain models in a time-space perspective

By relating time to the sequence of continuous levels in a multiresolution terrain model, these levels can be looked upon as time slices modelling the topography at different time periods during landscape development. A level with low resolution and less accuracy may model a period when the landscape was characterised as a flat, smooth and undulating surface dominated by relatively large landforms. A level with higher resolution with more details picked up from the underlying input data may represent a younger period after erosional and denudating forces have dominated and dissected the landscape. Connecting time to the different levels may result in two different development scenarios. 1) Level 1 represents a younger and more dissected landscape than Level 2 and Level 3. 2) Level 1 is the oldest, and due to erosion processes and mass transportation, the surface is levelled out and has become smoother as represented by Level 2 and Level 3. Due to the general lowering of the relief by the approximation properties of splines, the latter scenario may be the most appropriate. More investigation of the different process-form relationships and the properties of the spline algorithms are needed to verify this.

CONCLUSIONS

A multiresolution spline model has been presented and its implementation has been tested on elevation data from a mountainous area. The multiresolution model provides a fast and efficient tool for both visual inspection and quantitative analysis of surface topography and associated topographic properties. The combination of Java 3D for visualisation and the C++ spline library made it easy to develop a powerful application for moving around in a 3D landscape and visualise the different topographic properties on the relief model. The smoothing effect of splines may be both positive and negative. It may remove noise and errors in the input data, but can also remove irregularities caused by real small-scale landforms in the landscape. A large potential exists in using multiresolution terrain models as a tool in geomorphology and quantitative terrain analysis to increase insight into the complexity of landscapes and landscape development processes. However, further research is needed to explore the strengths and weaknesses of the different modelling approaches and how their results can be linked to observations of the behaviour of real world processes and phenomena at different scales.

Acknowledgements—This work was supported by the Research Council of Norway under the research program 117644/223, “DYNAMAP II, Management and Use of Geodata”. The Norwegian Mapping Authority provided the elevation data from the Jotunheimen area. The authors thank Vegard Røyne Stenerud and Geir Anker for developing the Java 3D application.

REFERENCES

Ashmore, P. E. and Church, M. (1998) Sediment transport and river morphology: A paradigm for study: In P. Klingeman, R. L. Beschta, P. D. Komar and J. B. Bradley (eds.), *Gravel-Bed Rivers in the Environment*, pp. 115–148. Water Resources Publications, Highlands Ranch.

Beven, K. J. and Kirkby, M. J. (1979) A physically based, variable contributing area model of basin hydrology: *Hydrological Sciences*, **24**(1), 43–69.

Briggs, W. L., Henson, V. E. and McCormick, S. F. (2000) *A Multigrid Tutorial*. 2nd ed. Society for Industrial and Applied Mathematics (SIAM), Philadelphia.

Cohen, E., Lyche, T. and Riesenfeld, R. (1980) Discrete B-splines and subdivision techniques in computer aided geometric design and computer graphics: *Computer Graphics and Image Processing*, **14**(2), 87–111.

Dikau, R. (1989) The application of a digital relief model to landform analysis in geomorphology: In J. F. Raper (ed.), *Three Dimensional Applications in Geographical Information Systems*, pp. 51–77. Taylor and Francis, London.

Evans, I. S. (1972) General geomorphometry, derivatives of altitude, and descriptive statistics: In R. J. Chorley (ed.), *Spatial Analysis in Geomorphology*. Mathuen & Co. Ltd., London.

Farin, G. (1997) *Curves and Surfaces for Computer-Aided Geometric Design: A Practical Guide*. 4th ed. Academic Press, New York.

Floater, M. S. (1998) How to approximate scattered data by least squares. Technical Report STF42 A98013, SINTEF, Oslo.

Golitschek, M. and Schumaker, L. L. (1990) Data fitting by penalized least squares: In J. C. Mason and M. G. Cox (eds.), *Algorithms for Approximation II*, pp. 210–227. Chapman & Hall, London.

Hestenes, M. and Stiefel, E. (1952) Methods of conjugate gradients for solving linear systems: *J. Res. Nat. Bur. Stand.*, 409–436.

Hjelle, Ø. (2001). Approximation of scattered data with multilevel B-splines. Technical Report STF42 A01011, SINTEF Applied Mathematics, Oslo.

Lane, S. N., Richards, K. S. and Chandler, J. H. (1995) Morphological estimation of the time-integrated bed load transport rate: *Water Resources Research*, **31**, 761–772.

Lee, S., Wolberg, G. and Shin, S. Y. (1997) Scattered data interpolation with multilevel B-splines: *IEEE Transactions on Visualization and Computer Graphics*, **3**(3), 229–244.

Mark, D. M. (1975) Geomorphometric parameters: A review and evaluation. *Geografiske Annaler* **57A**, 165–177.

Moore, I. D., Grayson, R. B. and Ladson, A. R. (1991) Digital terrain modelling: A review of hydrological, geomorphological, and biological applications: *Hydrological Processes*, **5**, 8–34.

Sulebak, J. R., Etzelmuller, B. and Sollid, J. L. (1997) Landscape regionalization by automatic classification of landform elements: *Norsk Geogr. Tidsskr.*, **51**, 35–45.

Wood, W. and Snell, J. (1960) A quantitative system for classifying landforms. Technical Report EP-124, US Army Quartermaster Research and Development Center.

Zevenbergen, L. W. and Thorne, C. R. (1987) Quantitative analysis of land surface topography: *Earth Surface Processes and Landforms*, **12**, 47–56.

AUTHOR INDEX

B

Blair, R. W., Jr. 33

C

Cudennec, C. 133

E

Evans, I. S. 61

F

Fouad, Y. 133

G

Graymer, R. W. 185
Guth, P. L. 199

H

Hirano, M. 101
Hjelle, Ø. 221

I

Ilyin, A. V. 43

N

Nishimori, H. 87

O

Ohmori, H. 3

P

Peckham, S. D. 167
Pike, R. J. 185
Preston, N. J. 115

S

Schmidt, J. 115
Sobieszczyk, S. 185
Sulebak, J. R. 221
Sumarjo-Gatot, I. 133

T

Tanaka, H. 87
Tokunaga, E. 147

SUBJECT INDEX

1984 earthquake, 108
2D flow direction, 168
3-D nature, 72

abyssal hill, 76
acoustic basement, 52, 54, 56
actual normalized distribution, 137
advection
  flux, 90
  process, 89, 90
aeolian bedform, 63
alluvial
  fan, 11, 13, 22, 62, 71
  plain, 119
altitude, 7, 9, 14, 16, 17, 18, 20, 21, 22, 23, 25, 26, 27, 28
  dispersion, 9, 10, 11, 12, 14, 16, 17, 18, 19, 20, 22, 26, 27
amphitheater, 177
analogy of entropy, 154
analytic solution, 179
annual
  rainfall, 11
  sedimentation rate, 7
antidune, 65
apatite-type rock, 55
arbitrary plane, 178
area
  function, 135, 136
  spreading, 101
area-distance function, 135, 137
area-hydraulic length function, 137
artificial crater, 77
aspect, 221, 229, 230
  algorithm, 199, 211, 218
asthenospheric diapir, 74
asymptotic
  base, 163
  direction, 164
  law of self-similar networks, 147
  model, 164
  postulation, 164
  property, 164
at-a-point
  geometric feature, 167
  geometric property, 181
  result, 181
avalanche, 223, 235

average
  elevation, 199, 202, 204, 211, 213, 218
  quadrangle slope, 205
  slope, 199, 202, 203, 211, 213, 218
  transport length, 90
axial volcano, 76
  zone, 47

B-spline
  coefficient, 227, 228
  coefficient grid, 228
  refinement, 230
  surface, 222, 223, 225, 226, 227, 229, 230
barchan, 64, 92, 97, 98, 99
basaltic flow, 75
base level, 5
basic altitude dispersion, 9, 17, 20, 26
basin, 138, 162
  territory, 137
basin-scale geomorphological function, 135, 144
bedform, 62, 63, 65
bi-cubic, 224, 226
  B-spline surface, 223
  basis function, 224, 226
bifurcating point, 152
bifurcation ratio, 135
bimodality, 78
binary
  branched-out tree, 137
  tree, 152
binomial distribution, 102, 113
block mountain, 105
bomb, 78
Bose-Einstein (BE), 148, 159
Bouguer reduction, 49
boundary
  concept, 41
  condition, 122
  surface, 34, 36, 38, 40
  surface interplay, 38
branched-out topology, 134, 144
branching
  law, 135
  number 2, 152, 161
  number 3, 152, 160
  pattern, 181
  structure, 136

Branching System I, 151, 152
Brownian
  motion, 89
  movement, 112
  relief, 162

CAD (Computer Aided Design), 225
caldera, 73
canonical distribution, 159
cascade, 124, 135
cascading system, 119, 120, 121, 126, 127
catchment surface, 135
causal agent, 189
Cenozoic, 44, 54, 57
  volcanic rock, 10
central
  peak, 76, 77
  rebound, 77
centripetal slumping, 77
channel, 177
  density, 70, 71
  initiation, 71
  morphology, 119
  network, 171
chemical response unit, 126
cinder cone, 75
cirque, 62, 66
  length, 67
climate parameter, 124
climate-process model, 121
climatic change, 11, 12, 21
climatic/landcover regime, 122
clint, 67
closed-form solution, 169, 178
cohesion, 38
colluvial storage, 119
complex
  geomorphological mechanism, 134
  system, 164, 165
component, 135, 136, 137, 140, 141, 144
  length ratio, 137, 140
concave up, 170
concept
  graded stream, 169
  optimality, 171
  self-similarity, 162
conceptual model, 4
conical composite volcano, 73
conjugate gradient method, 226
conservation
  equation, 89
  law, 89
  mass, 168
  momentum, 168
constant uplift rate, 19
continental
  crust contamination, 56
  lithosphere, 56
  subduction zone, 74
  trappean magmatism, 54
continuous system, 171
contraction of plate, 48
convergent
  flow geometry, 178
  plate boundary, 38
convex
  hillslope form, 170
  surface, 39
cover ratio, 94
crater, 77, 78
creep, 89
crest, 90
Cretaceous, 53, 54, 55, 56, 57, 74
crevasse, 39
critical
  altitude, 19, 20, 21, 25, 27
  shear stress, 71
  vegetation density, 94
crucial problem, 124
crust rupture, 56
crustal density, 7
crystallography, 148, 164
cuesta, 119
culminating stage, 19, 22, 24, 26, 27
cumulative
  area distribution, 163
  vertical displacement, 21
curvature, 229, 230, 231, 233
Cycle of Erosion, 5
cyclicity, 153, 164

Davisian
  concept on tectonism, 107
  end-peneplain, 4, 27, 28
  model, 3, 4, 5, 6, 24, 25, 27, 28
  scheme, 5, 6
  sequence, 24
debris
  distribution, 102, 113
  flow, 70, 186, 189, 191, 195, 223, 235
  slide, 189
declining stage, 19, 20, 22, 27
deep-sea ocean floor, 53
dendritic
  channel network, 167
  valley network, 181
density
  boundary interface, 39

plant, 93
denudation
process, 4, 5, 6, 18
rate, 6, 7, 8, 9, 10, 11, 12, 13, 14, 15, 16, 17, 18, 19, 21, 23, 25, 27, 28, 116
surface, 26
unloading, 22
depth-discharge formula, 169
desc. ridge, 177
desert dune, 89
detail level, 228
developing stage, 19, 21, 27
differential solution, 37
diffusion, 101, 107, 112, 113
limited aggregation, 162
diffusional flux, 94
diffusivity, 107, 110
digital
database, 189
elevation model (DEM), 9, 63, 135, 186, 199, 222, 223, 231
map, 185
raster-grid map, 186, 189, 196
terrain analysis, 221
terrain model, 221
discharge, 71
dispersion
altitude, 8, 73
potential energy, 9
divergent flow geometry, 178
doline, 62, 67
dome, 77
dormant landslide, 185, 186, 189
drainage
area, 136
basin, 7, 8, 9, 10, 11, 12, 16, 22, 25, 26, 119, 120, 164
basin composition, 159
basin form, 147
basin geomorphology, 148, 163
basin structure, 148
channel network, 70
density, 72
development, 119
divide, 159, 160
network, 147, 156, 159, 162, 163, 164
system, 151
topology, 134
draining area, 136
drift, 90
driving force, 38
drumlin, 62, 65
DSDP material, 55
DTED Level 0, 200, 211, 213
dune, 63, 65, 87
dynamic equilibrium, 17, 19, 24

earth
boundary surface, 34
crust contamination, 56
crust's second layer, 48
flow, 189
surface morphology, 34, 41
earthquake, 190, 194
effective shear stress, 37
effusion, 75
eigenvalue, 203, 204
eigenvector, 203, 204, 211
analysis, 199
ejecta, 77
electromagnetic force, 37
elevation-relief ratio, 234, 235
ellipse diagram, 178
elliptic, 170
elongate parabolic dune, 96, 97, 98
end-peneplain (Endrumpf), 4, 5, 6, 20, 25, 27
endogenic process, 34
endogenous
energy, 35, 40
landform, 39
media surface, 38
medium, 35, 37
process, 40
environmental condition, 122
Eocene, 56
episode, 5
equilateral triangle, 173
equilibrium
form, 62
state, 162
erosional
coefficient, 105, 107, 110, 113
form, 63
error function, 104
Euler-Lagrange
Formulation, 170
Theorem, 170, 171, 172
evolutionary system, 121, 125, 127
exogenic process, 33, 35
exogenous
medium, 35, 37
process, 38, 40
exponential
frequency distribution, 76
model, 78
extremal surface, 171
extremized functional, 170

failure, 185
  threshold, 38, 186, 190, 191, 193, 194
fast-spreading ridge, 76
fault
  block, 76
  scarp, 76, 105, 106, 107, 112
Fermi-Dirac (FD), 148, 159
Fibonacci Numbers, 148, 149
  sequence, 149
finite-element
  approach, 172
  numerical solution, 175
  numerical solution strategy, 181
flatness parameter, 202, 203, 217,
flexural rigidity, 73
flow
  depth, 168
  distance, 135
  path, 136
flute, 65
fluting, 65
fluvial
  dune, 65
  landscape, 171
  landscape model, 168, 177, 181
  process, 119, 168
  slope, 70
foraminfera, 54
fork, 177, 181
form of scale invariance, 175
form-process
  interaction, 126
  relationship, 121
fractal, 147
  dimension, 72, 76, 134, 154
  geometry, 134, 147, 148
  nature of river networks, 134
  object, 136
  property of drainage basins, 152
  surface, 72
fractality, 148
  drainage basin, 148
free air
  gravity anomaly, 49
  reduction, 49, 50
frequency and magnitude, 122, 124, 126, 127
frequency distribution, 67, 78, 80
frequency-magnitude, 120
  distribution, 79, 122
  relationship, 124
  spectrum, 125, 126, 127
friction, 38
frictional (or diffusion) process, 89
frost action, 73
full
  mature stage, 21
  maturity, 5, 25
  multigrid method, 226

gamma law, 144
Gaussian
  distribution, 65
  frequency distribution, 69
Gaussian-linear geostatistical model, 75
general method for generating solution, 180
generalized Manning-type flow resistance formula, 168
genetic model, 5
geographic information system (GIS), 185, 186, 193, 204, 221
Geographical Cycle, 4, 5
geologic unit, 190, 191, 194
geometric
  attributes of channels and channel networks, 170
  signature, 201, 204
geomorphic
  cascade, 120
  effectiveness, 122
  evolutionary system, 118, 127
  parameter, 121, 122, 124, 127
  process, 116, 121, 124, 126, 127
  process law, 122, 126
  process unit, 122
  process-response system, 120
  surface, 41
  system, 117, 122, 125
  unit, 121, 126
geomorphically effective rainrate, 170, 180
geomorphologic
  abstraction, 118
  evolutionary system, 125
geomorphological function, 134, 136
geomorphometric parameter, 199, 204, 207
geomorphometry, 199
georeferenced
  raster image, 137
  vector image, 137
ghost, 201, 204, 214
GIS-based analysis, 137, 141
glacial
  cirque, 65
  process, 11
glaciation, 73
glacier cirque, 235
global
  energy dissipation, 171
  Newton method, 181

GLOBE, 200, 211, 212, 213, 214
golden ratio, 149
grain, 72
  transfer, 90
grandiose relief form, 54
granitic rock, 10, 11
gravitational segregation, 34
gravity, 37, 38
  anomaly, 48, 50, 51
  force, 36
Green's function, 101, 104, 107, 110, 111, 112, 113
grike, 67
ground
  slope, 191
  surface form, 190
GTOPO30, 200, 211, 213, 214
gully, 71
gypsum, 67

Hack's
  diagram, 95
  law, 135
  phase diagram, 98
Hamilton's Principle, 171
hanging valley, 235
hazard map, 186
heat flow, 48, 51, 74
heavy rainfall, 190
height transfer, 90, 94
Helmholtz free energy, 147, 164
hierarchy, 64
  approach, 117
  constraint, 141, 144
high-symmetry solution, 179
highly-evolved landscape, 180
hillslope, 72, 103, 177, 181
  development, 22
  form, 119
  path, 136
  process, 119, 168, 170
  solution, 178
histogram, 66, 67, 74
Holocene, 63, 117, 119
horizontal
  dimension, 71
  ruggedness, 45
horn, 64
Horton
  bifurcation and length ratios, 140
  laws, 135, 147, 163
Horton's
  law of stream numbers, 147
  law of stream slopes, 163
  ratio, 140
hot-spot, 51, 55, 76
  track, 74
  volcano, 74
hydraulic
  geometry equation, 169
  length, 137, 139, 140
  length function, 139
  path, 136, 141, 144
hydrologic science, 134
hydrological response, 126, 134
hydrology, 134, 165
hyperbolic, 170

i-order stream, 136
i-th order component, 136, 137
ice creep, 37
Ideal Geographical Cycle, 5
idealized fluvial landscape, 167
ill-conditioned system matrix, 226
image processing, 137
impact crater, 62, 76
inertial process, 89
infinite topologically random channel networks, 155
initial
  altitude, 19, 20, 25, 28
  condition, 104, 122, 125
  form, 3
  landform, 6
  movement, 189
inselberg, 34
instability, 186, 189, 194
inter-media dynamics, 35
interbasin area, 151, 152, 153, 156, 160, 161, 162, 164
interferometry, 221
interfluve, 21, 26
interior node, 180
intermediate asymptotic regime, 167
internal
  heat, 38
  kinetic energy, 37
interruption, 5
intra-plate rise, 57
invariance property, 134
isolated peak, 177, 179
isostasy, 22, 40, 73
isostatic compensation, 51

Java, 232
Java 3D, 231, 236
junction, 134
Jurassic, 54

Jurassic-Cretaceous, 56

karst, 67
  depression, 67
  tower, 67

kinetic energy, 37, 40, 171
Kronecker's delta, 90

Laguerre's iteration method, 180
landform
  equation, 103, 104, 113
  evolution, 115, 119, 125
  evolution model, 126
  parameterisation, 118
  property, 126
  size, 79
  structure, 125, 126
  system, 117, 119
  type, 78
landscape
  elevation, 168
  evolution model, 117
  sensitivity, 126
  unit, 125, 126, 127
landslide, 39, 62, 67, 70, 107, 109, 110, 111, 112, 185, 186, 189, 190, 193, 194, 196
  deposit, 189, 192, 193, 194
  mass, 69
  susceptibility model, 194
landsliding, 73
landsystem, 117
landuse, 126
Laplace's equation, 170, 174
Last Glacial Age, 11
lateral moraine, 71
lattice of equilateral triangle, 173
lava flow, 75
law
  basin areas, 147
  horizontality, 36
  numbers of interbasin areas, 152
  stream fall, 153, 156
  stream lengths, 164
  stream numbers, 149
least
  square, 223, 225
  squares method, 225, 226
lee side, 90
length ratio, 135
level of detail (LOD) model, 228
LIDAR (Light Detection and Ranging), 200
limestone, 67
linear
  dune, 96, 98
  geostatistical model, 75
  magnitude, 80
  ridge, 177, 178
lineation, 71, 75
link, 134, 136, 137
liquifaction, 39
lithologic unit, 186
lithosphere
  block, 52
  thickness, 74
lithospheric
  plate, 50, 51
  thickness, 74
local
  equation, 174, 175, 177, 178, 179, 180, 181
  relief, 5, 6, 7, 8, 9, 11, 17, 18, 19, 21, 22, 24, 25, 26, 27
LOD
  capability, 230
  model, 229
log-Gaussian probability distribution, 62
log-normal
  distribution, 69, 75
  frequency distribution, 69
  model, 78
log-normality, 62
long-term
  denudation rate, 13
  process, 127
longitudinal profile, 180, 181
Love wave, 39
Lower Cambrian, 40
lowland, 22

macroscale
  geomorphology, 3
  landscape, 4, 6, 7
magma
  column, 73
  production rate, 75
magmatic process, 48
magmatism, 75
magnetic anomaly, 46
magnitude, 123
  frequency, 112
  frequency relationship, 110
  process, 124
Manning roughness parameter, 168, 170
mantle plume, 48
mare crater, 78
marine dune, 65

mass
  conservation, 172
  diffusion, 101
  movement, 102, 107, 112, 119, 223
  transfer, 36
  transport, 101, 107, 110, 113
mathematical model, 167
mature
  drainage network, 170
  fluvial landscape, 180
  stage, 5
maturity, 3
maximum
  entropy, 162
  recurrence interval, 125
Maxwell-Boltzmann (MB), 148, 159
mean
  altitude, 9, 12, 16, 17, 18, 19, 20, 22, 24, 25, 26, 27
  annual rainfall, 10
  annual river discharge, 169
  basic altitude dispersion, 9, 10, 11, 13, 16, 26
  denudation rate, 10, 11
  Quaternary tectonic uplift rate, 26
  short-term denudation, 10, 11
  surface gradient, 9
  uplift rate, 20, 21
  weighted uplift rate, 20
mega and mesoscopic scale, 36, 41
mega-yardang, 63
megadune (draa), 64
megageomorphic surface, 34
megascopic scale, 38
mesogeomorphic surface, 34
mesoscopic landform, 35
Mesozoic, 44, 53, 54, 55
Mesozoic-Palaeozoic sedimentary rock, 10
Metamorphic rock, 10
microcontinent, 44
MICRODEM program, 204
micromorphology, 40
microscopic
  plucking, 37
  scale, 38
  surface, 35, 40
microtopographic, 36, 37
microtopography, 40
mid-ocean ridge (MOR), 43, 45, 46, 47, 49, 50, 51, 52, 53, 54, 55, 57, 75, 76
minimal surface equation, 171
Miocene, 74
model
  diffusive hillslope process, 179
  parameterisation, 116
Moh's hardness, 37
molecular force, 36
molecular scale, 41
monkey saddle, 177, 179
MOR
  axial zone, 51
  lithosphere, 54
  relief, 50
  rift zone, 51, 56
  segment, 52
  spreading zone, 56
  strike, 52
moraine, 71
Morphological Analysis, 4
morphometric
  analysis, 11, 13, 21, 45, 46, 47
  unit, 121
morphostructure, 43, 45, 52, 54, 57, 58
morphotectonic
  division, 14
  terrain, 12, 22
most probable state, 154, 159, 161, 162
mountain landscape, 162
multi-layer raster mapping, 137
multi-ring basin, 77
multiple ring, 77
multiplicity of process, 125
multiresolution, 221, 222, 227, 230, 236

National Elevation Dataset, 201
negatively skewed, 144
neighbor algorithm, 205
Neogene sedimentary rock, 10
nest of most probable states, 159, 160, 162, 163, 164, 165
net sediment flux, 121
network scaling property, 137
node height configuration, 180
non-debris flow landslide, 186
non-equilibrium form, 62
non-random
  bias, 163
  force, 162
nonlinear local equation, 181
nonlinearity, 170
normal
  distribution, 101, 102, 105, 106, 112, 113, 109
  fault, 75
Northeast Trades, 63
numerable set, 157
numerical
  model, 116

process-based model, 116
solution scheme, 167
solution strategy, 172

oberes Denudationsniveau, 19
ocean
basalt, 48
earth's crust, 47
floor, 40, 43, 75, 76
floor spreading, 56, 57
oceanic
crust, 76
rise, 53, 57
volcano, 73, 74
old
age, 3
stage, 20
Oligocene, 74
one-dimensional
drainage basin, 153
quasicrystal, 149, 153, 164
Sierpinski space, 149
support, 136
optical camera, 221
optimal channel network (OCN), 171, 172, 177
optimality, 172
problem, 181
organic entity, 35
organization
strength, 202
value, 202
orogenesis, 6, 7, 20, 27, 28
orogenic
period, 6
process, 26, 27
zone, 27
orogeny, 3, 4, 6, 7, 24, 25, 28
overland flow, 71

Palaeozoic, 63
paleo climate analysis, 126
parabolic, 170
dune, 87, 96, 97, 98
parallel retreat of slope, 19, 20
parallelism, 65
parameterisation, 121, 122
parasitic cone, 73
Pareto (power function) distribution, 62
partial differential equation, 113, 170
path through the hilslope, 135
peak, 180, 181
Peano basin, 152, 159, 160, 162
pediment, 34
Penckian
concept on tectonism, 107
diagram, 23, 24
model, 3, 4, 5, 6, 22, 27, 28
primary peneplain, 4, 26, 27, 28
primary peneplain sequence, 24
peneplain, 3, 4, 5, 6, 26, 27
periglacial process, 11
Phanerozoic, 54
physical
boundary surface, 34
form-process model, 121
process model, 126
pingo, 79
pit, 180
plan curvature, 221, 230, 231, 233, 235
planform curvature, 222
plants density, 93
plate motion, 18, 22
Pleistocene, 11, 13, 21, 22,
Pliocene, 21
plume, 52
volcanism, 57
plutonism, 40
point source, 101, 103, 108
Poisson's equation, 180
positively skewed, 140, 141, 144
potassic rock, 55
potential energy, 73, 171, 172
expenditure, 153, 154, 155, 156, 157, 158, 159, 160, 164
power
flow law, 37
function, 70, 135
law, 70, 75, 76, 134
precipitation, 8
primary peneplain, 4, 6, 7, 24, 25, 26, 27
Primärrumpf, 6
probabilistic theory, 164
probability
density function, 137, 140, 144
distribution, 137, 139, 140, 141, 144
distribution of the truncated hydraulic lengths, 141, 142, 143, 144
process
abstraction, 116
domain, 121
form relationship, 121
model, 126
response, 104, 120
response subsystem, 127
response system, 119
subunit, 121
profile curvature, 221, 230, 231, 233, 235

property of drainage basin, 153
protobasin, 77
p–Laplace equation, 170

quadratic, 177
quantile-quantile plot, 67, 69
quartic, 176, 177
quasi
  cyclic, 153, 164
  equilibrium state, 164, 165
  power-law relationship, 70
quasicrystal, 148, 164
quasistatic process, 17
Quaternary, 12, 13, 14, 26, 107
  uplift rate, 12

RAD model (Relief-Altitude-Denudation model), 22, 24, 25
rainfall-induced failure, 190
random
  arrangement, 159
  number generator, 180
  process, 159
  self-similar network, 163
randomness, 162, 163
rate of soil production, 168
Rayleigh wave, 39
recessional coefficient, 105
recurrence
  formula, 148, 149, 150, 151, 153, 164
  interval, 123, 124
  period, 110, 112
reduced length of components, 140
regional
  control, 163
  difference of geologic control, 163
  landform development, 116
  landform system, 116, 118
  scale system, 127
regionalisation, 121
regression line, 72
relief, 73, 222
  amplitude, 45
  anomaly, 50
  ratio, 22
  ruggedness, 46, 47, 52
  surface, 231, 232, 233
  unit, 222
representative elementary area, 80
reptation, 89
rescaled excess rainrate, 178
residence time distribution, 136
resistance, 38
resisting force, 38
resolution, 116, 185, 200, 201, 211, 213, 218, 221, 229
restrictive condition, 159
retreat, 104, 106
return period, 110
reverse canonical distribution, 159
ridge, 181
  axis, 76
  flank, 75
  spacing, 72
rift, 45
  valley, 52
  zone, 43, 44, 46, 47, 57
  zone relief, 48
  zones' strike, 45
rift-geneous relief, 52, 57
rift-genesis, 52
right-skewed distribution, 62
rigidity, 37
rim, 77
  floor, 76
  wall, 77
ripple, 89
Ritz-Galerkin method, 172, 181
river
  channel, 62
  network, 134, 135, 136, 137, 144, 167
  network self-similar organization, 144
  networks fractality, 144
river-bed elevation, 108, 109
rock
  avalanche, 70
  contamination, 56
  fall, 191, 223, 235
  slide, 189
  slump, 189
  type, 8, 10, 11, 12
  weathering, 11
root-two times diameter, 77
rotational slump, 70
roughness, 202, 234
  parameter, 168
rugged
  form, 47
  relief, 47
ruggedness, 48, 53

saddle, 181
safety ratio, 38, 39
saltation, 88, 89
  flux, 91, 94, 95
  length, 90
sand
  dune, 63

flux, 95
ribbon, 65
wave, 65
saturation value, 93
scale
dependence, 80
specificity, 73, 75, 80
scale-dependency, 62, 78
scale-free, 78
fractal model, 63, 72
scale-specific, 62, 70, 74, 75, 77, 79, 80
feature, 72
landform, 80
nature, 61
scale-specificity, 62, 63, 65, 70, 71, 73, 74, 75, 76, 77, 79, 80
scaling
factor, 140
property, 134, 144, 180
scattering, 112
scour mark, 36
sea mountain, 57
seamount, 44, 53, 76
sediment
budget, 125
cascade, 127
delivery rate, 7
density, 7
flow law, 124
flux, 116, 117, 118, 119, 124, 125
sedimentation ratio, 7
seif dune, 92
seismic
body wave, 39
energy, 35
seismo-acoustic profile, 52
self-affine stream network, 154
self-affinity, 154
self-similar
branched-out structure, 136
branching system, 162, 165
drainage basin, 148, 149, 151, 153, 156
model, 164
network, 154
structure, 147, 148, 149
self-similarity, 140, 147, 149, 159, 164
shape similarity, 134
shear stress, 169
shield volcano, 73
shoreline, 35
Shreve's random topological model, 162, 163
side
area, 156, 157, 158, 159, 160
tributary, 156
Sierpinski space, 152, 153, 164
silicic flow, 75
simple
saddle, 177
solution surface, 180
sinkhole, 67
depth, 67
skewness, 65, 141
width function, 140
slide, 186, 190, 192
slip face, 64
slope, 103, 168, 185, 191, 192, 194, 221, 222, 230, 231, 232
algorithm, 199, 202, 204, 205, 207, 218
development, 119
effect, 89
failure, 38
gradient, 112, 185, 186, 190, 191, 192, 193
stability, 38, 71
slope-depth formula, 169
slope-discharge formula, 169, 170
slump terrace, 76
small scale feature, 116
smooth
polynomial basis function, 224, 235
surface, 162, 224, 228
smoothing level, 228
term, 225, 226
snow-patch, 66
snowline (ELA), 73
sodium chloride, 67
soil erosion, 119
solar energy, 35
solution
flute (Rillenkarren), 67
quadratic equation, 148, 153, 164
surface, 167, 181
source, 134, 137
space-filling, 136
constraint, 163
network, 136
problem, 148
spatial
frequency, 185, 186, 189, 191, 192
regionalisation, 122
specific
landform, 62
scale, 75
spline, 221, 236
algorithm, 222, 231, 235, 236
coefficient, 226
model, 221, 222, 231, 232, 235, 236
surface, 221, 223, 235
spreading, 107

center, 47, 50, 57
rate, 76
spreading-plate boundary, 75
SRTM, 200
stability
quasicrystal, 164
self-similar drainage basin, 164
stable
form, 162
geometric form, 167
numerical method, 180
standard
deviation, 65
fluvial landform evolution equation, 180
model, 37
star dune, 64, 92
statistical
self-similarity, 163
thermodynamics, 159
statistics in nested space, 165
steady state, 6, 19, 20, 21, 27, 170
equation, 170, 171, 172, 179
fluvial landscape model, 167, 170
mass conservation, 170
partial differential equation, 181
process, 6
version, 180
steepest adjacent neighbor algorithm, 202, 205, 211, 218
stereoscopy, 221
stochastic
property, 163
theory, 164
Tokunaga model, 163
storage unit, 121, 126
Strahler
level, 141
order, 137, 140
ordering of link, 135
ordering scheme, 134, 140, 144
Strahler-component, 144
Strahler's
ordering method, 152
ordering scheme, 135
ordering system, 156
straight-line length, 154
strain rate, 37
stratovolcano, 73
stream
channel, 153
length, 135
length ratio, 137
power, 171
strong force, 37
strong/electromagnetic force, 38
structural
discontinuity, 37, 38
process, 51
relief, 47, 48
structurally
Hortonian network, 147
similar, 156
sub-aqueous dune, 89
subbasin, 138, 139, 141, 151, 164
subduction zone, 74
subdued landscape, 20, 27
subduing, 104, 106
coefficient, 105
submarine topography, 40
subsurface volatile, 77
summit level, 19
super-elevation, 110
suppression factor, 93, 94
surface
altitude, 8, 9
area functional, 171
boundary, 38
gradient, 6
relief, 233, 234
slope, 231, 232, 233
susceptibility, 185, 191, 192, 193, 194, 195
index, 196
suspension process, 89
symm. ridge, 177
sympathetic boundary, 38, 41
system of valleys, 133
systematic inclination, 163

tabular data, 204
talus
cone, 235
scar, 235
tank model, 121
tectonic
stress, 73
uplift, 6, 127, 168
uplift rate, 6, 18, 19, 20, 22, 24, 26, 27
tectonics, 4, 5
tectonism, 63, 73
temporary denudation rate, 10
terrace scarp, 105
terrain
analysis, 221, 229, 236
model, 221, 222, 229, 236
organization, 199, 203, 204, 218
orientation, 203
surface, 223, 225, 230
Tertiary, 26, 119

thermal
  conductivity, 49
  contraction, 49, 50, 51
  contraction curve, 50, 51
  contraction hypothesis, 51
  energy, 35, 37
  spalling, 40
thermodynamic function, 165
thermodynamics, 148, 154, 159, 165
thin plate spline energy, 225
three-dimensional
  form, 161, 164
  space, 154
threshold, 62, 65, 71, 77, 80, 119
  drainage area, 71
  model, 116
tiling problem, 148
time interval, 124
time-independent landscape, 19
Tokunaga law, 135
topographic parameter, 221, 222, 230, 233
topological
  analysis, 137
  basic element, 137
  network, 134
  randomness, 164
TOR-1 type, 48
total sediment volume, 7, 8
transition period, 58
transport
  distance, 101, 107, 112
  length, 90
transverse dune, 87, 92, 96, 97
trap efficiency, 7
tree generator, 151, 163
triadic tree, 152
triangular lattice, 172
triangulated irregular net-work, 222
trifurcating point, 152
triple junction, 57
truncated length, 141
turbulent boundary layer, 99
two-dimensional
  object, 136
  planar, 134, 136
  plane, 147, 164
  Sierpinski space, 152
two-ring basin, 77

U-shaped valley, 235
unit
  instantaneous source, 102, 104
  mass, 101, 112
  mass of water, 157
  stream power, 169, 171, 172
unit-width discharge, 168, 169
unitary space, 165
unvegetated dune, 87, 88
upland crater, 78
uplift rate, 17, 21, 24, 27
uplifted
  initial landform, 5
  peneplain remnant, 21, 26

variational problem, 181
variogram analysis, 72
vegetated dune, 87, 88, 91
vegetation density, 95
vertical
  dimension, 72
  ruggedness, 45
vertically-averaged flow velocity, 169
viscosity, 37, 75
volatile, 77
volcanic, 73
  basalt, 48
  block, 43
  cone, 62
  edifice, 74
  growth fault, 76
  massif, 57
  relief, 57
volcanism, 55, 75, 76
volcano, 73, 74, 75, 76

warm ice, 77
water
  storage capacity, 7
  surface height, 168
water-surface
  gradient vector, 168
  slope, 170
weak force, 37
weathering, 127
width function, 135, 136, 137
width-discharge formula, 169
wind ripple, 36

xenolith, 56

yardang, 62, 63
youth, 3
youthful stage, 26

PLACE INDEX

Addis Ababa, 74
Aeolis region, 63
Afar rise, 74
African rifts, 55
Agulhas Plateau, 56
Akaishi Range, 69
Alaska, 200, 201
Alberta, 65
Alps, 72
Amazon Basin, 211
Andean Mountain chain, 38
Andean mountain system, 39
Andes, 73, 211
Antarctica, 40, 200
Appalachian, 80
Appalachians, 203
Asia, 73
Atlantic, 54, 57
Atlantic Ocean, 47, 53, 55, 56
Atlantic Ocean's rift zone, 48
Australia, 73
Azores, 47, 48, 50, 51, 55, 57, 74
Azores ridge, 45
Azores rift zone, 57
Azores segment, 51

Bárcena Volcano, 71
Bendor range, 66
Bermuda rise, 57
Bolivia, 211
Bowe Island, 57
Britain, 66
British Columbia, 66

California, 71, 72, 185, 186, 187, 188, 191
Callisto, 77
Cameroon, 74
Cape Verde, 74
Cape Verde Islands, 55, 56
Cayoosh Range, 66
central Europe, 72
central Germany, 119
central Japan, 12, 21, 71
central Japanese mountain ranges, 12
central Pacific Ocean, 55
Chad, 63
Chinese Himalayan, 40
Chugoku Mountains, 26

Dhaulagiri, 73
Dubbi, 74

Earth, 40, 73, 77
East Pacific Rise, 47, 51, 53, 75, 76
East-Indian ridge, 54
eastern Africa, 74
eastern Uganda plateaux, 74
Ecuador Rift, 76
England, 66
equatorial Pacific, 51
Erta-ali, 74
Estonia, 40
Ethiopian Plateau, 74
Ethiopian Rift, 74
Europa, 77
Europe, 65

Galapagos, 51, 74
Galapagos Islands, 55
Galdhøpiggen, 223
Ganymede, 77
Georgia, 72
Grand Canyon, 207
Greece, 71
Gregory Rift, 74

Half Dome, 39
Hanging Rock Canyon, 209
Harar, 74
Hawaii, 73, 74, 201
Hawaii-Emperor chain, 74
Hawaiian, 75
Hayward Fault Zone, 187, 189
Henry Mountains, 38
Hiedayama, 111
Himalaya, 71, 73
Hira, 107
Hokkaido, 12

Iberia, 71
Iceland, 55
Indian Ocean, 54, 55
Indochina, 77
Irish basin, 56

Japan, 4, 7, 9, 10, 11, 12, 13, 14, 15, 16, 18, 21, 22, 25, 26, 27, 127

Japanese Alps, 70
Japanese Islands, 107, 111, 112
Japanese mountain ranges, 16, 18
Jotunheimen, 222, 223, 233
Juan de Fuca Ridge, 75
Jupiter, 77

Kentucky, 67
Kharga, 63

Lake District, 66
Line Islands, 55
Line rise, 55
lunar maria, 77

Majorca, 67
MAR rift zone, 47, 48, 50, 52
MAR tropical zone, 50, 51
MAR, 47, 48, 49, 50, 51, 52, 54
Marcus-Necker arch area, 55
Mars, 40, 63, 73, 74, 77, 78
Martian plain, 77
Mercury, 77
Mexico, 71
Mid-Atlantic Ridge (MAR), 44, 46, 50
Mission Peak, 190
Montara Mountain, 72
Moon, 76, 77, 78
Mt. Bandai, 111
Mt. Ontake, 108, 109

Namib draa, 64
Namib Desert, 64
Nanga Parbat, 73
New England, 72
New England seamounts, 74
New York, 72
New Zealand, 70, 119, 127
Nigorizawa, 108
North America, 73, 75,
North Atlantic, 45, 47, 48, 50, 51, 52, 54, 56, 57
North Atlantic rift zone, 48
north-western California, 72
Northeast Japan, 12
Northern Cascades, 207
northern Sahara, 64
Norway, 222

Oakland, 186, 187, 188, 189, 190, 191, 192, 193, 194
Ohtaki-gawa river, 108
Ontake, 107, 111, 112
Oregon, 70, 71

Pacific Mid-Ocean Ridge, 75
Pacific Ocean, 53, 54, 55
Pacific Ocean basin, 53
Pacific Ocean floor, 54, 57
Peru, 211
Puerto Rico, 67, 200

Red Sea, 74
Reykjanes Ridge, 45, 47, 48, 50, 51, 55, 57
Rockoll Rise, 56
Rokko, 107

San Francisco Bay, 186, 190, 194
San Mateo County, 72
South America, 73, 201
South Atlantic, 52
South Vietnam, 77
south-central Japan, 68, 69
South-Norway, 222
southern France, 71
Southwest Japan, 12, 26

Taiwan, 70
Temple of Sinawava, 207
Tharsis region, 63
Tibesti massif, 63
Tibetan Plateau, 73
Tropic Canyon, 210

United States, 199
USA, 65, 72
Utah, 207
Uzbekistan, 67

Venus, 40, 73
Virgin Islands, 201

Wake atoll, 55
Wales, 66
western USA, 80
western Washington, 70
Wisconsin, 203
World Ocean, 53, 54, 55, 56

Yosemite National Park, 39
Yvel basin, 139, 140, 141, 142, 143
Yvel river, 138, 139